JAERI-Research
98-039

REVIEW OF JT-60U EXPERIMENTAL RESULTS IN 1997

August 1998

JT-60 Team

日本原子力研究所
Japan Atomic Energy Research Institute

本レポートは，日本原子力研究所が不定期に公刊している研究報告書です。
入手の問合わせは，日本原子力研究所研究情報部研究情報課（〒319-1195　茨城県那珂郡東海村）あて，お申し越しください。なお，このほかに財団法人原子力弘済会資料センター〒319-1195　茨城県那珂郡東海村日本原子力研究所内）で複写による実費領布をおこなっております。

This report is issued irregularly.
Inquiries about availability of the reports should be addressed to Research Information Division, Department of Intellectual Resources, Japan Atomic Energy Research Institure, Tokai-mura, Naka-gun, Ibaraki-ken 319-1195, Japan.

© Japan Atomic Energy Research Institute, 1998

編集兼発行　日本原子力研究所

Review of JT-60U Experimental Results in 1997

JT-60 Team*

Department of Fusion Plasma Research
and
Department of Fusion Facility
Naka Fusion Research Establishment
Japan Atomic Energy Research Institute
Naka-machi, Naka-gun, Ibaraki-ken

(Received July 7, 1998)

The JT-60U experiments in 1997 focused mainly on the steady-state tokamak research with the newly installed W-shaped pumped divertor and the negative ion based neutral beam (NNB) in addition to the existing profile and shape control techniques developed in JT-60U. In particular, the research on divertor physics was accelerated under the new divertor system with many of fine diagnostics: Detachement characteristics, pumping control, impurity control, recycling characteristics, etc. in the W-shaped divertor were investigated in detail. The onset density of X-point MARFE in ELMy H-mode was reduced to 50-70% of Greenwald limit density from about 70% in the previous open divertor. On the generation of X-point MARFE, electron density increased locally near the X-point and electron temperature decreased to 20eV. The ratio of recombination to ionization in Balmer series was about 1%. Probability of the inner-leg pumping was estimated to be 0.6-2% of total recycling. In the steady (5s) helium pumping experiment using the core fueling helium beams to model the helium ash, $\tau_{He}^*/\tau_E \sim 4$ satisfying the ITER requirement was obtained. With the 'gas and pump' technique, it became possible to control divertor radiation loss, neon concentration and divertor neutral pressure. The main purpose of confinement and stability studies in 1997 was to improve steadiness of high confinement plasmas with the new divertor. Since a long heating time with 203MJ of the total heating energy became possible without harmful increase in impurity and particle recycling, the DT equivalent

fusion gain $Q_{DT}^{eq} \sim 0.1$ was sustained for 9 sec in a ELMy H-mode discharge. The progress in the high confinement reversed shear operation was demonstrated by a quasi-steady sustainment of the internal transport barrier with an ELMy H-mode edge. Researches progressed also for the formation conditions of the internal and the surface transport barriers in the high-β_p mode, the reversed shear mode and the H-mode. Toward the advanced feedback controls of multiple parameters, the JT-60U started new feedback controls of central line density and divertor neutral gas pressure in addition to the existing controls of off-axis line density, radiation power and neutron production rate. The JT-60U team also carefully studied characteristics of halo current during disruptions. Optimization of NNB operation progressed steadily and injection power increased up to 4.2MW. The NNB-driven current was identified directly from the internal magnetic measurement and driven current profile was confirmed to be consistent with the ACCOME calculation. The current profile control with LHCD successfully sustained the internal transport barrier in reversed shear plasmas. Continuous TAE modes were observed with NNB for the first time as beam-driven TAE modes.

Keywords: JT-60U, Plasma Control, Halo Current, Confinement, Stability, Long Pulse, Reversed Shear, Current Drive, N-NBI, High Energy Particle, W-shaped Divertor, Heat and Particle Exhaust, Radiative Divertor, Diagnostics

※ The JT-60 Team

H.Adachi, H.Akasaka, N.Akino, K.Annou, T.Arai, K.Arakawa, N.Asakura, M.Azumi, M.G. Bell[9], C.D. Challis[10], C.S. Chang[14], C.Z. Cheng[9], S.Chiba, O. Dacosta[4], S. A. Dettrick[5], N.Ebisawa, G.Y. Fu[9], T.Fujita, T.Fukuda, H.Fukuda[1], A.Funahashi, H.Furukawa[1], X. Gao[18], L. Grisham[9], K.Haga[1], K.Hamamatsu, T.Hamano[1], Y.Hasegawa[1], T.Hatae, N.Hayashi[20], S.Higashijima, K. Hill[9], S.Hiranai, H.Hiratsuka, T.Hirayama, T.Hiroi[1], M.Honda, A.Honda, N.Hosogane, L. Hu[18], S. Hudson[5], H.Ichige, S.Ide, Y.Ikeda, M.Isaka, A.Inoue[1], A.Isayama, N.Isei, S.Ishida, Y.Ishii, K.Ishii[1], T. Ishijima[3], K.Itami, T.Itoh, M.Iwase[2], S.C.Jardin[9], M.Kabazawa, E.Kajiyama[1], Y.Kamada, A.Kaminaga, T.Kashiwabara[1], M.Kawai, Y.Kawamata, Y.Kawano, M.Kikuchi, T.Kimura, V. Kiptily[13], H. Kishimoto, Y.Kishimoto, S.Kitamura, K.Kiyono, K.Kodama, Y.Koide, M.Koiwa[1], S.Kokusen[1], K.Komuro[1], T.Kondou, S.Konoshima, J.Koog[2], G.J. Kramer[6], H.Kubo, A. Kumagai[3], K.Kurihara, G.Kurita, M.Kuriyama, Y.Kusama, L. L. Lao[11], A. Makhankov[15], J. Manickam[9], K.Masaki, T.Matsuda, M.Matsukawa, T.Matsumoto, Y. Meng[18], D.R. Mikkelsen[9], Y.M.Miura, K.Miyachi, H.Miyata[1], Y.Miyo, K.Mogaki, M.Mori, M.Morimoto[1], A.Morioka, S.Moriyama, M.Nagami, K.Nagashima, A.Nagashima, S.Nagaya, O.Naito, Y.Nakamura, R. Nazikian[9], M.Nemoto, H.Nemoto[1], S.V. Neudatchin[12], Y.Neyatani, T.Nishitani, H.Nobusaka[1], T.Ohga, M. Ohsawa, K.Ohshima[1], T.Oikawa, M. Okabayashi[9], T.Okabe, J.Okano, S.Omori, Y.Omori, K.Omori, T.Ooba[1], H.Oohara, T.Oshima, T.Ozeki, A. Polevoi[7], P. Politzer[11], G. Rewoldt[9], J.A. Romero[8], M.Saidoh, N.Saito, A.Sakasai, S.Sakata, T.Sakuma[1], S.Sakurai, T.Sasajima, N.Sasaki[1], M.Sato, Y.Seimiya, M.Seki, H.Seki[1], M.Shimada, K.Shimizu, M.Shimizu, M.Shimono, K.Shinohara, S. Shinozaki, H.Shirai, M.Shitomi, A.Sugawara, T.Sugie, H.Sunaoshi, M.Suzuki[1], S.Suzuki[2], S.Takahashi[1], S.Takano[1], S.Takeji, H.Takenaga, T.Takenouchi, T.Takizuka, H.Tamai, Y.Tanai[1], T.S. Taylor[11], T.Terakado, M.Terakado, K.Tobita, S.Tokuda, T.Totsuka, R.Toyokawa[1], N.Toyoshima, K.Tsuchiya, T.Tsugita, Y.Tsukahara, K.Uehara, Y.Uramoto, K.Ushigusa, K.Usui, E. Wang[17], J. Xie[16], J.Yagyu, M.Yamagiwa, T.Yamamoto, H.Yamazaki[1], K.Yokokura, H.Yoshida, R.Yoshino, J. Zhao[18], C. Zhou[19]

1) Staff on loan
2) Post-Doctoral Fellow
3) JAERI-Tukuba Univ. Doctor Cource
4) STA Fellow Ecore Polytech, France
5) STA Fellow, Australian Nat. Univ.
6) STA Fellow, Netherlands
7) STA Fellow, Kurchatov Institite
8) STA Fellow, Spain
9) PPPL, USA
10) JET Undertaking
11) GA, USA
12) Kurchatov Institute, RF
13) Ioffe Institute, RF
14) New York Univ. USA
15) D.V. Efremov Scientific Research Institute RF
16) ASIPP China
17) SWIP China
18) STA Exchange, ASIPP China
19) STA Exchange, SWIP China
20) Fellow of Advanced Science

1997年におけるJT-60U実験結果のレビュー

日本原子力研究所那珂研究所
炉心プラズマ研究部・核融合装置試験部
JT-60チーム*

（1998年7月7日受理）

1997年におけるJT-60Uの実験はトカマクの定常化に係わる研究に主眼を置いた。そこでは、これまでJT-60Uで開発してきた分布・形状制御手法に加えて、新たに設置したW型排気付きダイバータや負イオン源中性粒子ビームを活用した。特に、高性能計測機器を備えた新ダイバータによって、ダイバータ物理の研究が加速し、デタッチメント特性、排気制御、不純物制御、リサイクリング特性等の詳細を明らかにすることができた。ELMのあるHモードにおけるX点MARFEの発生密度はグリーンワルド限界密度の50-70%であり、従来の開ダイバータにおける約70%に比べて低下した。X点MARFEの発生時、X点付近に局所的な電子密度の上昇があり、電子温度は約20eVに下がる。Balmer系列の再結合／電離の比は1%であった。内側排気による排気割合はリサイクリングの0.6-2%と評価される。中心粒子供給のヘリウムビームでヘリウム灰の発生を模擬した準定常的（5秒）な排気実験において、ITERの要求する$\tau_{He}^*/\tau_E \sim 4$を得た。ガス注入と排気により、ダイバータ放射損失、ネオン混入量、ダイバータ部の中性子粒子圧力等の制御が可能になった。一方、閉じ込め及び安定性研究の主目的は、新ダイバータの元で高閉じ込め放電の定常性を向上することであった。長パルス放電において、全加熱入力203MJであっても閉じ込めを阻害する不純物の発生や粒子リサイクリングの無い放電が得られ、DT等価エネルギー増倍率～0.1を、ELMのあるHモードで9秒間維持した。また、内部輸送障壁を伴う高閉じ込め負磁気シア放電においても、ELMのあるHモードとの複合に成功し、準定常維持が可能となった。高β_pモードや負磁気シアモードにおける内部輸送障壁やHモードにおける周辺輸送障壁の形成物理、また、ディスラプション時のハロー電流挙動の研究も進んだ。帰還制御については、中心線密度及びダイバータ部中性粒子圧力の制御を、従来からの周辺線密度、放射パワー及び中性子発生率の制御に加えることで、先進的な複合帰還制御を目指した研究を開始した。負イオン源中性粒子ビーム（NNB）装置の運転最適化も順調に進展し、入射パワー4.2MWを得た。また、内部磁場の測定からNNBによる非誘導駆動電流分布を明らかにし、ACCOMEコードによる計算値と一致することを示した。一方、低域混成波電流駆動による電流分布制御では、内

那珂研究所：〒311-0193　茨城県那珂郡那珂町向山801-1

部輸送障壁を伴う負磁気シアプラズマの維持に成功した。また、NB励起TAEモードとして初めて、NNB入射による連続TAEモードを観測した。

※ JT-60チーム

赤坂 博美，秋野 昇，朝倉 伸幸，安積 正史，安達 宏典[1)]，新井 貴，荒川喜代次，安納 勝人，池田 佳隆，井坂 正義，諫山 明彦，石井 和宏[1)]，石井 康友，石島達夫[3)]，石田 真一，伊世井宣明，伊丹 潔，市毛 尚志，井手 俊介，伊藤 孝雄，井上 昭[1)]，岩瀬 誠[2)]，上原 和也，牛草 健吉，薄井 勝富，浦本 保幸，海老沢 昇，及川 聡洋，大賀 徳道，大澤正哉，大島 貴幸，小関 隆久，大場 俊夫[1)]，大原比呂志，大森 俊造，大森 栄和，大森憲一郎，岡野 潤，M. Okabayashi[9)]，岡部 友和，X. Gao[18)]，梶山 英一[1)]，柏原 庸央，桛澤 稔，鎌田 裕，神永 敦嗣，河合視己人，河野 康則，川俣 陽一，菊池 満，岸本 泰明，岸本 浩，北村 繁，V. Kiptily[13)]，木村 豊秋，清野 公広，鞠 重山[2)]，草間 義紀，久保 博孝，熊谷 晃[3)]，L. Grisham[9)]，栗田 源一，栗原 研一，栗山 正明，G.J. Kramer[6)]，小出 芳彦，小岩 素直[1)]，石仙 茂晴[1)]，児玉 幸三，木島 滋，小室 健一[1)]，近藤 貴，斉藤 直之，西堂 雅博，逆井 章，坂田 信也，佐久間 猛[1)]，櫻井 真治，佐々木 昇[1)]，笹島 唯之，佐藤 稔，蔀 守正，篠崎 信一，篠原 孝司，嶋田 道也，清水 正亜，清水 勝宏，下野 貢，S.C.Jardin[9)]，白井 浩，J. Xie[16)]，菅原 章博[1)]，杉江 達夫，鈴木 光博[1)]，鈴木 慎悟[2)]，砂押 秀則，清宮 宗孝，関 宏[1)]，関 正美，C. Zhou[19)]，高野 正二[1)]，高橋 昇竜[1)]，滝塚 知典，竹治 智，竹永 秀信，竹之内 忠[1)]，O. Dacosta[5)]，棚井 豊[1)]，玉井 広史，C.Z. Cheng[9)]，千葉 真一，C.D.Challis[10)]，C.S.Chang[14)]，J. Zhao[18)]，塚原 美光，次田 友宣，土屋 勝彦，T.S. Taylor[11)]，S. A. Dettrick[5)]，寺門 恒久，寺門 正之，徳田 伸二，戸塚 俊之，飛田 健次，豊川 良治[1)]，豊島 昇，内藤 磨，永島 圭介，長島 章，永見 正幸，中村 幸治，永谷 進，R. Nazikian[9)]，西谷 健夫，根本 正博，根本 博文[1)]，閨谷 譲，S.V.Neudatchin[12)]，信坂 裕通[1)]，芳賀 浩一[1)]，長谷川幸弘[1)]，波多江仰紀，S. Hudson[5)]，濱野 隆[1)]，浜松 清隆，林 伸彦[20)]，東島 智，平塚 一，平内 慎一，平山 俊雄，K. Hill[9)]，広井 俊和[1)]，G.Y. Fu[9)]，L. Hu[18)]，福田 弘幸[1)]，福田 武司，藤田 隆明，船橋 昭昌，古川 弘[1)]，M.G. Bell[9)]，細金 延幸，P. Politzer[11)]，A.Polevoi[7)]，本田 正男，本田 敦，A. Makhankov[15)]，正木 圭，松川 誠，松田 俊明，松本 太郎，三浦 友史，D.R. Mikkelsen[9)]，J. Manickam[9)]，宮田 寛[1)]，宮地 謙吾，三代 康彦，Y. Meng[18)]，藻垣 和彦，森 雅博，森岡 篤彦，森山 伸一，森本 将明[1)]，柳生 純一，山極 満，山崎 晴幸[1)]，山本 巧，横倉 賢治，吉田 英俊，芳野 隆治，L.L. Lao[11)]，G. Rewoldt[9)]，J.A. Romero[8)]，E. Wang[17)]

1) 業務協力員
2) 博士研究員
3) 連携大学院生（筑波大学）
4) STAフェロー, Ecore Polytech, France
5) STA フェロー, Australian Nat. Univ.
6) STAフェロー, Netherlands
7) STA フェロー, Kurchatov Institite
8) STAフェロー, Spain
9) PPPL, USA
10) JET Undertaking, U.K.
11) GA, USA
12) Kurchatov Institute, RF
13) Ioffe Institute, RF
14) New York Univ. USA
15) D.V. Efremov Scientific Research Institute RF
16) 中国科学院プラズマ物理研究所
17) 中国核工業公司西南物理研究所
18) 原子力交流制度, ASIPP China
19) 原子力交流制度, SWIP China
20)特別研究生

Contents

目　　次

1. Overview of the Experiment in 1997

1.1 Confinement, Stability and Plasma Control

The main experimental purpose for confinement and stability studies in 1997 was to improve steadiness of high confinement plasmas with the new w-shaped pumped divertor. The key operational factors such as plasma volume, shape, position relative to neutral beam lines, ramp up speed of plasma current, gas fueling rate etc. had to be optimized for the new first wall boundary and particle supply and exhaust. To study changes in H-mode characteristics by the divertor modification was also an important topic. Concerning the disruption research, construction of halo current data base was raised as the key subject. In addition to these tasks related to the divertor modification, understandings of profile effects on transport and stability were continuously emphasized as the most important physics target. Through these works, issues of plasma control were clarified toward our final goal of steady-state high integrated performance with simultaneous achievement of high confinement, high β, noninductive current drive with high bootstrap fraction and high efficiency of heat and particle exhaust.

After the divertor modification, a long heating time (9sec) of high power NB (20 -25MW) became possible without harmful increase in impurity and particle recycling. The total energy input reached 203MJ. The DT equivalent fusion gain Q_{DT}~0.1 was sustained for 9 sec (triangularity δ =0.16) and Q_{DT} ~0.16 for 4.5 sec (δ=0.30) in high β_p ELMy H-mode discharges at I_p=1.5MA by optimizing the pressure profile and electron density. In the latter case, H-factor ($=\tau_E/\tau_E^{ITER89PL}$)~2.3, β_N~2 and β_p~1.6 were sustained with 60-70% of noninductive current drive (NB driven and bootstrap). The new extension of pulse length accelerates understanding of roles of parameters with long time constants such as the current profile and particle recycling. Concerning the former, appearance of low-n resistive modes limits the sustainable β_N in a long pulse (~ 2 for 5- 9sec). The detailed measurement of electron temperature by the heterodyne radiometer with high spatial resolution of 2cm showed growth and saturation of island width (~5cm). The neoclassical tearing mode is the candidate of this instability.

The remarkable progress in the high confinement reversed shear operation was demonstrated by its long time sustainment with an ELMy H-mode edge. By using power step-down technique, the β-collapses were avoided and a favorable performance with H-factor=1.8-2.5 and β_N=1.5-1.8 were sustained for 1.5s (~4-5xτ_E) in a discharge with high triangularity (B_t=3.5T, I_p=1.5MA, δ=0.28) where the internal transport barrier (ITB) for both electron and ion channels were sustained in addition to the edge transport barrier by the H-mode. A longer sustainment reaching 4.3s was also demonstrated in the ELMy discharge

(H-factor ~1.7, β_N ~1.5) using feedback control of the NB heating power to maintain a fixed neutron production rate. Compared to the L-mode edge discharges, the high β stability in the H-mode edge discharges was improved in the low-q_{min} region (β_N ~2.3 at q_{min}~1.5-1.9). The remaining issue for the confinement improvement in reversed shear H-mode is the relatively small ITB radius (~50% of the minor radius).

Concerning the ITB formation physics, two improved modes with ITBs viz. the high-β_p mode and the reversed shear mode were carefully compared. The high-β_p mode has the ITB at positive magnetic shear. Although these two modes have clear ITBs for the ion channel, only the reversed shear mode has the clear ITB for the electron channel. In reversed shear discharges, the radial location of the ITB propagates outward and then stagnated near or just inside the radius of q_{min}. The reduction of the electron thermal diffusivity was also observed in case of electron heating by ICRH, where a steep density gradient does not seem to be essential for the ITB formation.

The above experimental results suggest us to advance or expand the theoretical treatment of transport and stability. Concerning the ion transport in reversed shear discharges, the thermal diffusivity is close to the neoclassical value. However, the conventional theories do not give an accurate formula for the ion thermal diffusivity valid for arbitrary shape, aspect ratio and impurity content. We have applied the so called Matrix Inversion (MI) method to calculate the neoclassical ion thermal diffusivity for the JT-60U discharges including the above effects. The diffusivity from the MI method is two times smaller than that from the Chang-Hinton formula. Concerning the MHD stability of the reversed shear discharges, we found that the Mercier criterion can be violated. In the negative shear region, the stabilizing terms due to the parallel current and the magnetic well produced by the poloidal current change to the destabilizing terms.

For the ITER physics R&D, we conducted detailed analyses of the H-transition. In order to correlate the edge quantities with the H-mode power threshold, an exploratory work was undertaken with the edge nondimensional quantities, namely ρ^{*95}, β^{95} and ν^{*95}. Another approach to the H-transition physics is to find "hidden" variables. We reported that increase in edge neutral pressure reduces the edge collisionality required for the transition. According to the result, a change of the threshold power was expected by the divertor modification. It was found, however, that the amount of reduction in the threshold power in the modified divertor geometry was subtle (~10%), in comparison with the open divertor. The density exponent also remained in the range of 0.5 to 0.75, whilst it was 0.5 for the open divertor. For understanding of the effects of neutral pressure, we have to resolve where in the edge poloidal location being the most influential on the H-transition.

The JT-60U team also carefully studied characteristics of halo current during disruptions for the ITER R&D. Ranges of the measured total halo current normalized by the initial plasma current (I_h/I_{p0}) and the toroidal peaking factor (TPF) were 0.05 - 0.26 and 1.4 - 3.6 respectively

in the range of I_p=0.7 - 1.8 MA, B_t=2.2 - 3.5T, κ=1.3-1.6, q_{95}= 2.8 - 7.0. The maximum local halo current (I_h/I_{p0} x TPF) was 0.52. This value is smaller than that of the present design value of 0.58 in ITER. The value of I_h/I_{p0} x TPF decreases with increasing line integrated electron density at the time of the peak of halo current.

Finally, toward the advanced feedback controls of multiple parameters with multiple actuators, the JT-60U started two new feedback controls, namely the central line integrated electron density and the divertor neutral gas pressure in addition to the existing controls of off-axis line density, radiation and neutron production rate.

1.2 Current Drive and High Energy Particle Behavior

Optimization of the operation of Negative-ion-source Neutral Beam Injector (NNBI: designed parameters of 500 keV and 10 MW with two ion sources) progressed and the injection power of 3.2 MW/source at 350 keV was achieved. The maximum injection power increased up to 4.2 MW using two ion sources. Utilizing the NNB, lower hybrid (LH) waves and ion cyclotron range of frequency (ICRF) waves, following new results were obtained in studies of the Current Drive and High Energy Particle Behavior in a campaign of 1997. These results contributed significantly to activities of ITER Physics R&D.

Concerning the NNB current drive (CD), a centrally-peaked profile of plasma current driven by the negative-ion-based neutral beam (NNB) was confirmed by reconstruction of the current density and loop voltage profile using the equilibrium code (EFIT) and the motional Stark effect spectroscopy (MSE) measurements. The total driven current and a current density profile are consistent with the predictions with ACCOME code.

The coupling of LH waves to plasmas in the newly installed W-shaped divertor was investigated in order to examine the applicability of LH to new plasma configuration. The plasma current profile during LHCD was investigated directly with MSE measurement and a broader profile of the driven current was confirmed with LHW with larger refractive index parallel to the magnetic field ($N_{//}$). The lower hybrid current drive (LHCD) was applied in reversed shear plasmas to sustain the internal transport barrier (ITB) together with the sustainment of the R/S configuration. The ITB was sustained for about 2 s while the R/S was maintained by LHCD forming a broader driven-current profile.

Enhancement in the ionization cross-section of NNB was evaluated at 350 keV. Measured shine-through of NNB was lower than that calculated by assuming the single-step ionization process. This shows that the multi-step ionization process is needed to be taken in to account. The experimental enhancement factor agrees with that predicted using enhanced cross-section evaluated by Janev.

The Toroidicity-induced Alfvén Eigenmodes (TAE modes) were excited with NNB. Both burst and continuous modes with low toroidal mode numbers were observed in a low bh regime of $<\beta_h>\leq 0.1$-0.2%. The amplitude of magnetic fluctuations of the burst modes is about ten times as large as that of the continuous modes. Accompanying these bursting activities were 2-3% drops in the neutron emission rate. This small drop indicates that the loss of co-injected NNB ions is small. The growth of continuous modes were compared with temporal evolution of volume-averaged NNB-ion beta calculated using an orbit following Monte Carlo code.

The TAE mode study using the ICRF heating also progressed. TAE modes and high frequency modes observed in ICRF-heated low-q discharges were analyzed in detail using NOVA-K code (PPPL). The analysis shows that TAE modes appear before giant sawtooth crash are excited inside q=1 surface and high frequency modes observed after the crash are shown to be Ellipticity-induced Alfvén Eigenmodes (EAE modes) and Noncircular triangularity-induced Alfvén Eigenmodes (NAE modes). The interaction between TAE modes and EAE/NAE modes and NNB-injected ions was investigated, and the EAE/NAE modes were shown to be stabilized with NNB. An analysis using NOVA-K code suggested that the stabilization mechanism was beam ion Landau damping. It is also shown that the q-profile derived from a change in TAE mode frequency agrees with that obtained from MSE measurement. Chirping modes were observed in ICRF-heated weak magnetic shear plasmas.

The ICRF coupling with plasmas in the W-shaped divertor was optimized by adjusting a gap between the first wall and the separatrix. The coupling resistance similar to that in the open divertor was obtained and the ICRF power of ~4 MW was applied to reversed-shear plasmas. By changing the NB power and the ICRF power and by replacing the ICRF power by the NB power, formation of the ITB was investigated. It was shown that NB power of 4-5 MW was necessary to sustain the ITB in electron density. Magnetic shear effect on electron temperature in ICRF-heated reversed and normal shear plasmas was also observed, suggesting a hollow heating profile due to an expansion of banana orbits and/or enhanced ripple transport.

A new scaling including plasma current was obtained for temperatures of ICRF-driven tail ions based on a diffusion model of fast ion losses and measured tail temperatures were well described by the scaling. Ripple loss of super-thermal ions in the reversed shear discharge, where $Q_{DT}^{eq}=1.05$ was achieved, was calculated and was found to be small enough to neglect in the estimation of Q_{DT}^{eq}.

1.3 Divertor Peformance

summarized by N. Hosogane

In JT-60U, the previous open divertor was modified to a W-shaped divertor with pumps from February to May in 1997(Fig. 1). The aim of this modification is to investigate effects of divertor geometry and control on divertor functions and to realize radiative divertor compatible with good confinement simultaneously. The W-shaped divertor is characterized by inclined targets and a dome in the private flux region and pumping from the inboard side in the private flux region, which has never been found in other tokamaks. Therefore, divertor performance obtained in this divertor will have strong influence on the determination of divertor structure of future tokamaks like ITER.

Partially detached divertor operation is considered as a promising concept for realizing radiative divertor and good core plasma confinement simultaneously as is taken into the design of ITER divertor. The operational density in ITER is $1x10^{20}$ m^{-3}, corresponding to 1.2x (Greenwald density). This means that partially detached divertor compatible with good core plasma confinement should be demonstrated at about Greenwald density in the present machines.

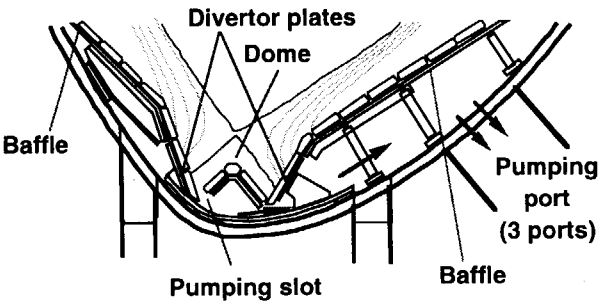

Fig. 1 Structure of W-shaped divertor

Divertor experiment in 1997 was firstly focused on producing high density ELMy H-mode plasmas with good confinement as targets for divertor studies. However, H-factor of ELMy H-mode obtained with gas puff turned out to be similar in the previous open divertor. H-factor was decreased as electron density was increased, and degraded to almost unity at 0.8x(Greenwald density). In the W-shaped divertor, to obtain high density plasma, several times stronger gas puff were necessary than in the open divertor. To reduce influence of gas puff and to find a way of producing good ELMy H-mode, tokamak operations with and without divertor pumping, with NBI heating during ramp-down of electron density just after switching off gas puff, with high X-point or low X-point configuration etc., were tried. However, significant improvement was not obtained. Detailed study on a relationship between recycling characteristics(including neutral particle behavior) and edge confinement characteristics was considered to be necessary to understand confinement degradation. On the other hand, detailed studies of divertor functions such as particle pumping, heat flux reduction, impurity reduction etc. are very important not only to find a key to simultaneous realization of radiative divertor and good confinement but also to understand roles of divertor geometry as physics R&D for ITER. Therefore, the latter half of divertor experiments was concentrated on studying fundamental divertor functions rather than exploring radiative divertor compatible with core plasma confinement. The main results are briefly summarized here.

Plasma detachement

In the W-shaped divertor, partially detached divertor with enhanced divertor radiation loss larger than 70% of input power was always accompanied by X-point MARFE. The X-point MARFE onset density of H-mode plasmas in the W-shaped divertor was reduced to 50-70% of Greenwald density, whereas that in the open divertor was about 70%

for H-mode plasmas with small current of Ip = 1-1.2 MA. Taking account of the experimental result in C-mod, the reduction in X-point MARFE onset density observed in the W-shaped divertor may be attributed to the effectiveness of inclined targets on formation of dense and cold divertor plasma.

In small or medium size tokamaks such as C-mod, DIII-D, ASDEX-U, electron temperature of divertor plasmas smaller than a few eV has been observed in partially detached divertor states. In these states, volume recombination process of deuterium atoms is dominant. However, in JT-60U, even in a partially detached divertor with X-point MARFE, electron temperature estimated from the intensity ratio of Balmer continuum(364 nm) and Paschen continuum(400 nm), which is an average temperature along the line of sight of spectrometer, was higher than 10 eV[1]. Recombination flux(recombination process for particle flux) estimated from intensity of DI(n=2-7) was only about 1 % of ionization flux estimated from D_α intensity. The region where recombination process is dominant is considered to be small.

Divertor pumping

As shown in Fig. 1, particle pumping in the W-shaped divertor is done from the inboard side of the private flux region divided by the dome(inner pumping). A good feature of inner pumping is that high pumping efficiency is expected even with relatively small pumping speed(Sp=13 m3/s at the pumping slot) in attached divertor, because the neutral pressure at the inner divertor region is enhanced compared with the outer divertor region due to in-out asymmetry of particle recycling in the usual discharges with ion grad_B drift toward the divertor. In fact, the pumping probability for the particle flux to the divertor in discharges with ion grad_B drift toward and away from the divertor were about 0.6-2% and about 0.2% respectively, showing the importance of pumping location. Also, the inner pumping worked well to achieve good efficiency of helium exhaust described later.

In partially detached divertor with X-point MARFE, the neutral pressure at the outer divertor region without pumping slot became larger than that at the inner divertor region with the pumping slot. This means that the inner and outer divertor regions are well separated by the dome, and the inner pumping becomes less effective than expected in the extension from attached divertor though the throughput by the inner pumping actually does not decrease. This tendency was clear in L-mode discharges compared with H-mode discharges.

These results suggest that pumping from both sides is necessary in the detached divertor. This was expected to some extent from the beginning. The employment of inner pumping was determined by the following reasons: Besides strong in-out asymmetry of particle recycling, 1) a relationship between particle recycling and pumping will be easy to be understood by fixing the pumping slot at the inner side only, 2) if pumping slots are arranged at both sides, particles at the higher pressure side will go to the lower pressure side, which may lead to low pumping efficiency. At this point, further study is necessary to understand the results obtained in the inner pumping. Furthermore, comparison of experiments with inner pumping with those with pumping from both sides would make it easy to understand a relationship between particle recycling and pumping.

He exhaust

Remarkable progresses has been achieved in helium exhaust study[2] as follows:
1) Good helium exhaust characteristics has been obtained in the pumping scheme from the private flux region like ITER. $\tau_{He}^*/\tau_E=4$ has been obtained, well satisfying $\tau_{He}^*/\tau_E<10$ in

ITER. H-factor of this discharge was about 1.3.
2) Helium exhaust characteristics could be studied in the quasi-steady state(5 s) with helium beam simulating helium ash for the first time, owing to cryopumps with a large pumping capacity and argon frost processing properly done before shots.
3) Enrichment coefficient defined by $(n_{He}/n_e)/(P_{He}/2P_{D2})$ was about 1, whereas 0.2 was required in the design of ITER divertor. The pumping speed required for helium exhaust depends on enrichment coefficient, so that this result will have strong influence on ITER design.

Feedback control of divertor radiation power and neutral pressure

Feedback control of radiation power, neutral pressure etc. is important for developing operational scenarios of radiative divertor.

By the modification to the divertor with pumps which play a role as an active particle sink term, capability of feedback control for the divertor radiation power has been increased. A feedback control experiment was carried out in hydrogen L-mode plasma with constant beam heating power of 6.5 MW[3]. A step wise radiation power with 3.4, 4.7, 5.9 and 5 MW, corresponding to 50-90% of input power, was well controlled by hydrogen gas puff and divertor pumping. Effect played by divertor pumping was obvious both when X-point MARFE occurred and when the preprogrammed radiation power was lowered at the final phase. The radiation power went down rapidly when gas puff was switched off. Such control was impossible in the previous open divertor without pump. When the radiation power was near X-point MARFE level, the radiation power was observed to fluctuate corresponding to a sequence of occurrence and elimination of X-point MARFE.

Feedback control of main electron density and divertor neutral pressure by main gas puff and divertor gas puff has been tried to investigate a possibility of independent control of main plasma and divertor plasma[4]. It was found that this system was a strong interacting one, and simultaneous controllability depended on the operational region. In a certain operational region, both main electron density and divertor neutral pressure were controlled, but in other regions, they were out of control. The important finding relating to the geometrical property of the W-shaped divertor is the difference in response of couplings between main electron density and divertor gas puff and between divertor pressure and main gas puff (cross term coefficients). It was found that contribution from main gas puff to divertor pressure is higher than that from divertor gas puff to main electron density.

Impurity reduction

As expected by the simulation analysis of impurity transport[5], experimental results showing geometrical effects of the dome on carbon impurity reduction have been obtained in the W-shaped divertor. In the W-shaped divertor, CD band intensity near the X-point, which comes from methane produced by chemical sputtering in the private flux region, was found to remain low when the density was increased to the density just below the MARFE onset. In contrast, in the previous open divertor, CD band intensity near the X-point increased as electron density was increased. This difference is explained as that the dome impedes free upstream motion of hydrocarbon gas in the private flux region, resulting in reduction of direct penetration of carbon impurities to the X-point vicinity.

A SOL flow generated by a combination of gas puff and pumping is expected to drag impurities to the divertor by frictional force, and is potentially an effective method of

impurity shielding. Effectiveness of this method for carbon impurities has been studied in the W-shaped divertor. Comparing carbon impurity behavior in ELMy H-mode discharges with gas puff only from the main chamber and only from the divertor chamber, CIV intensity at the inner divertor showing carbon transport became small in the former case though CII intensity showing carbon generation was unchanged, and carbon density in the main plasma was reduced by about 20%. This suggests that SOL flow was generated by main gas puff and divertor pumping, and was effective in impurity shielding.

Experimental results obtained in 1997 are presented in this review. However, as for divertor study, experiments were done in February and early March. To understand the performance of the W-shaped divertor, theses results should be included. Therefore, in this summary, experimental results till March 1998 are also inferred though some of these are not presented in the following section.

References

[1] H. Kubo et al., Section 7.5 in this review.
[2] A. Sakasai et al., Section 6.2 in this review.
[3] S. Konoshima et al., Section 7.4 in this review.
[4] H. Tamai et al., Section 6.4 in this review
[5] K. Shimizu et al., J. Nucl. Mater., 241-243(1997)167

1.4 New Diagnostics

1.4.1 Diagnostics for Compact W shaped Divertor

Several new diagnostics[1] have been equipped for the divertor plasma investigations with the Compact W shaped divertor. Some of them are briefly reviewed as follows.

1) A ***mm-wave interferometer*** [2] newly installed for measuring line integrated electron density (n_{el}) in the modified W-shape divertor region has found a clear density drop in the divertor region at the L-H transition. Furthermore a relation between the n_{el} in the divertor region and that in the main plasma has been investigated.

2) ***Fast ionization gauges*** [3] installed behind the inside/outside baffle tiles and the dome tiles, in the pumping duct, and at the midplane port have measured the neutral pressure at each point. Some gauges are used for an active control of the divertor neutral particle pressure, where a moderate neutral pressure in the divertor region has been successfully kept constant by the feedback control of the gas puffing rate into the divertor region.

3) A ***midplane reciprocating probe*** [4] has been modified to attach a Mach probe head, so particle flow in SOL has been measured in addition to the SOL electron density and temperature. A new ***X-point reciprocating probe*** [5] with the same probe type has clarified the plasma parameters in the divertor region. Two sets of 18 channel divertor target ***Langmuir probe arrays*** [4] have confirmed the location of the separatrix line on the divertor plate. These systematic measurements of SOL at the up-stream to the plasmas at the target plate will clarify the divertor plasma performance.

4) Four sets of ***bolometer cameras*** [6] have been installed at the divertor chamber. Many channels unfortunately had damages at the early phase of the operation. Thus a horizontal chord with 4ch. was replaced by a ceramic window type for thermal and electric isolations at the last maintenance period (Nov. - Dec./1997), and no serious damage has occurred for this chord yet. Two dimensional tomographic reconstruction is planned in the next step.

5) 32 channel optical fiber array viewing divertor region for C II emission profiles in the modified divertor region were obtained. Now we are analyzing data and planning to make two dimensional contour plots of intensities.

6) New ***Rogowski-coil type probes*** [7] have been installed in the divertor region at 6 points in the toroidal direction for measuring the halo-current with its toroidal asymmetry. Halo current measurement for I_p of 0.7~1.8 MA has shown that the ratio of the total halo current with the initial I_p is lower than 25% and this ratio decreases with the initial I_p.

1.4.2 Diagnostics Development for the Main Plasma

Diagnostics for the main plasma are also under the development. Some of them are presented as follows.

1) Tangential CO_2 laser polarimeter [8]

This system is necessary to measure the electron density for large tokamaks with the steady state, so its development is one of urgent items in ITER Physics R&D. The mid-plane Faraday rotation of CO_2 laser wave in a tokamak plasma has been successfully detected for the first time, where feasibility of a newly designed infrared-polarimeter has been demonstrated for stable measurement during the tokamak operation.

2) Reflectometer

4 channel correlation reflectometer is planned to be installed in the head of F.Y. 1998 with the collaboration with PPPL. A special window for this reflectrometer has been installed to JT-60U. Microwave electronics and transmission line have been fabricated under the leadership of PPPL. Using this reflectometer, we will get the information of fluctuations in a core plasma, which will help to understand the transport in the core plasma region (especially at the internal transport barrier for reversed shear plasmas).

3) Collective Thomson scattering

The bio-shield penetration study for the CO_2 laser beam and scattered beam propagation is in progress. The pre-arranging of the penetration has been done in the torus hall, where the ventilating duct has been modified to avoid the shield structure of the beam penetration optics. The development of a detector to decrease the noise or to increase quantum efficiency is now being done in the US detector company and one order of magnitude improvement is expected within F.Y. 1998.

REFERENCE

1) see "Diagnostics in JT-60" in http://www-jt60.naka.jaeri.go.jp

2) H. Takenaga, etal., 、 8.2 in this review.

3) H. Tamai, et al., 、 6.4, 8.4 in this review.

4) N. Asakura, et al., 、 7.2 in this review.

5) S. Sakurai, et al., 、 8.5 in this review.

6) S. Kohnoshima, et al., 、 8.3 in this review.

7) Y. Neyatani, et al., 、 2.1 in this review.

8) Y. Kawano, et al., 、 8.1 in this review.

2. Operation Physics and Disruption

2.1 Halo Current in JT-60U [1)]

Y. Neyatani, R. Yoshino, Y. Nakamura, S. Sakurai

1. Introduction

A current flowing directly into a vacuum vessel from a plasma (called halo current) was observed during disruptions in tokamak. This halo current produces a strong electromagnetic force to the in-vessel components, such as the blanket module and the divertor cassette. Therefore, the halo current amplitude is one of the critical issue for designing ITER. The design value for ITER is mainly determined from the data base for the medium and small sized tokamaks. Thus, further investigation for the characteristics of the halo current in large tokamaks, especially the confirmation of its parameter dependence and the establishment of the mitigation and/or avoidance methods in order to extrapolate them toward ITER are desired. In JT-60U, The sensors for halo current (Rogowski coils) were newly installed during the divertor modification in May 1997 and the measurement of its toroidal and poloidal distribution was started. These halo current sensors were installed to round off the support structures of baffle plates, divertor basements and dome supports.

2. Experimental Results

For the halo current study, the most dangerous disruption caused by vertical displacement event (VDE) was experimentally simulated, in which a plasma was actively controlled to move downward (Fig.1). In this case, the halo current flew into the inside baffle plate and went back to the plasma at the outside baffle plate as was expected. A toroidal distribution had an n = 1 structure, and its peak position rotated with the rotation frequency of 500 ~ 700 Hz. The halo current data base for the amplitude and toroidal peaking factor (TPF = maximum/average amplitude of the toroidal direction) was constructed by scanning the plasma parameters just before the disruption in the ranges of I_p = 0.7 ~ 1.8 MA, B_T = 2.2 ~ 3.5 T, κ = 1.3 ~ 1.6 and q_{95} = 2.8 ~ 7.0 respectively. Ranges of the measured total halo current normalized initial plasma current (I_h/I_{p0}) and TPF were 0.05 ~ 0.26 and 1.4 ~ 3.6 respectively (see figure 2). The maximum TPF*I_h/I_{p0}, which indicated the maximum local halo current, was 0.52 so far, which was lower than that of the maximum value of the ITER data base of 0.75, and was also smaller compared with the present design value of ITER divertor cassette of 0.58.

3. Parameter Dependencies

The upper boundary of TPF*I_h/I_{p0} tended to decrease with the increase in I_{p0}. Other parameter dependencies of TPF*I_h/I_{p0} to B_T, κ and q_{95} were not clear. The driving forces of the halo current are considered to be an electric field generated by the decrease in toroidal and poloidal magnetic fluxes in a plasma caused by the vertical shift velocity ($-dZ_j/dt$) and the plasma current decay time ($I_p/(-dI_p/dt)$). Since the magnitude of the halo current is considered to be determined by the induced electric field and the resistance in the halo region, the effects of the driving forces and the resistance have been verified. We confirmed that the upper boundary of TPF*I_h/I_{p0} decreased with the decrease in $-dZ_j/dt$. On the other hand, the TPF*I_h/I_{p0} clearly decreased with the increase in the stored energy just before the energy quench ($W_{dia}^{e\cdot q\cdot}$). This dependence was consistent with the dependence of the upper boundary of TPF*I_h/I_{p0} against the plasma current. The TPF*I_h/I_{p0} clearly decreased with the increase in the line integrated electron density at the time of the peaked halo current as shown in Fig. 3. To confirm the relation, preliminary analysis of the tokamak simulation code (TSC) has been performed. The simulated amplitude of the halo current decreased with the decrease in the temperature in the halo region as well as the indication of experiments. The analyses for the effect of the electric field produced by changing the internal magnetic fluxes are under preparation.

These stored energy and density dependencies of the halo current can be considered as the following process. When the released plasma energy at the energy quench increases with $W_{dia}^{e\cdot q\cdot}$, a large amount of impurity is generated at the divertor plates by a large heat load. After that, the electron density increases and the electron temperature decreases in the halo region (the resistivity increases), then the halo current decreases. These results support the concept that the magnitude of halo current is small when the electron temperature in the halo region is low.

4. Avoidance and Reduction of Halo current

Based on the previous results, avoidance and reduction methods of the halo current have been investigated. For the reduction of the temperature in the halo region, a strong pulse gas puff has been attempted. When hydrogen gas was applied with 50 Pam^3/s x 0.1s during VDE, the magnitude of the halo current decreased about by 40%. In order to reduce the driving forces stationary current termination technique to keeping a divertor configuration [2] has been attempted, and the avoidance of the halo current was experimentally confirmed.

REFERENCE

1) Y. Neyatani, R. Yoshino, et al., submitted to Nucl. Fusion

2) R. Yoshino, Y. Nakamura, Y. Neyatani, Nucl. Fusion **36** (1996) 295.

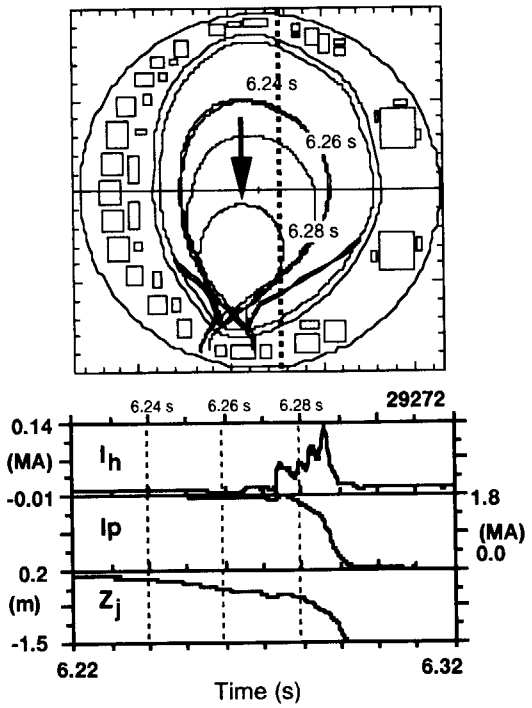

Fig. 1 Waveforms of the halo current during a simulated VDE. A plasma is shifted downward actively to simulate the VDE. The dotted line in an upper figure indicates the line of sight of FIR measurement. Halo current starts to flow from t = 6.265 s and peaks at t = 6.286 s.

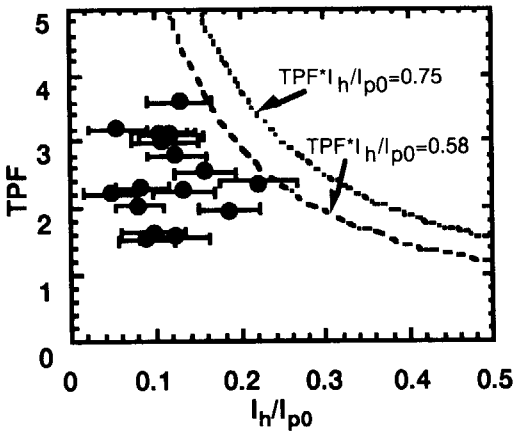

Fig. 2 Toroidal Peaking Factor (TPF) versus normalized halo current defined by I_h/I_{p0}. Where I_{p0} is a plasma curren just before the current quench.

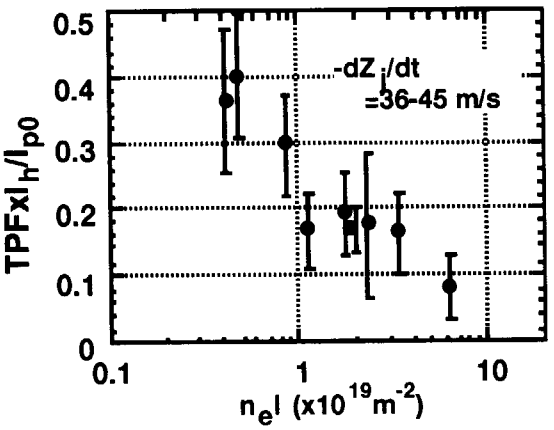

Fig. 3 The TPF*I_h/I_{p0} versus line integrated electron density ($n_e l$) at the time of the maximum halo current with the fixed vertical shift velocity (-dZj/dt).

2.2 Realtime processing of CO_2 laser interferometer for density feedback control

S.Chiba, Y.Kawano, and A.Inoue

The main purpose of the CO_2 laser interferometer is to measure line electron density at the central part of JT-60U plasma [1]. A realtime processing system of CO_2 laser interferometer has been developed in order to realize electron density feedback using density data along a tangential chord [2]. Figure 1 shows the schematic diagram of the realtime processing system. The phase signals measured by the CO_2 laser interferometer are processed into realtime density data using UNIX Workstation computer. The UNIX Workstation computer can provide data including various signal correction and smoothing for reliable feedback control. Then, the density data are transmitted for every 500 μs to the ZENKEI computer and are used for feedback control of electron density of JT-60U. Figure 2 shows the statistical analysis of realtime density data obtained during JT-60U discharges. As shown in Fig.2 , data for 147 discharges out of data for 177 discharges (83%) show good results. It is found that the remainder 30 data (17%) were suffered from electric noises. The noises are supposed to be originated from break-down of NBI and NNBI. Those noises can be reduced by further improvement of electric components of the interferometer. Figure 3 shows typical waveforms of density feedback control using CO_2 laser interferometer signal. During the feedback period, the electron density is successfully controlled by control of gas puffing. The results shown above indicate that the realtime processing system using the UNIX Workstation computer has feasible performances for density feedback control.

References

1) Y. Kawano, et al., Journal of Plasma and Fusion Research,**73**, 870 (1997).

2) S. Chiba, et al., to be submitted to JAERI report.

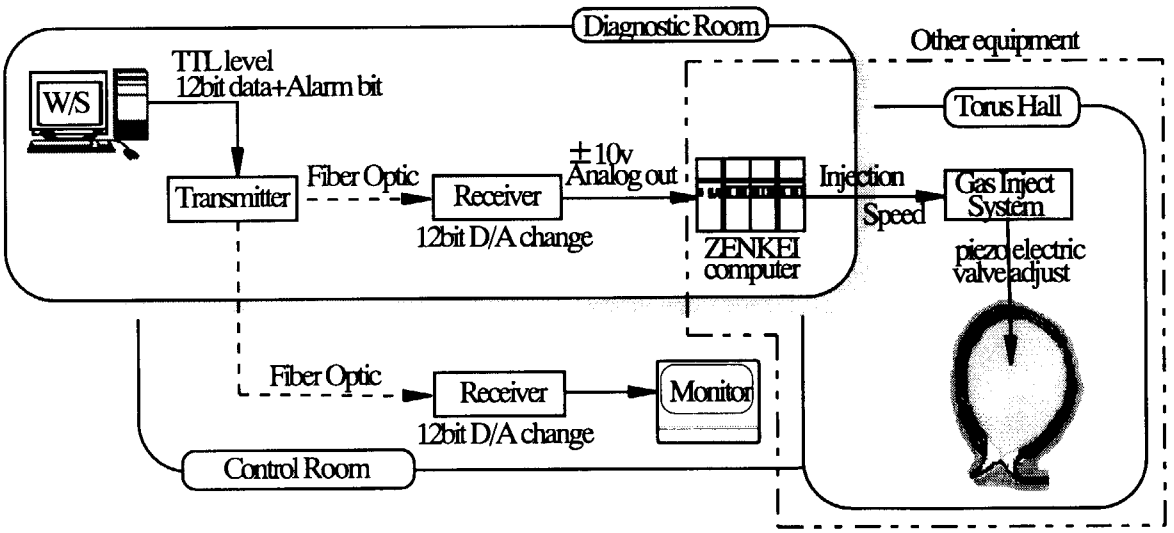

Fig.1. Schematic diagram of realtime processing system for density feedback using CO_2 laser interferometer signal. The analog output voltage of +10V corresponds to the line electron density of 2×10^{21} [m^{-2}]. The output data resolution should be 9.8×10^{17} [m^{-2}] because the system is designed to have 12-bit signal resolution.

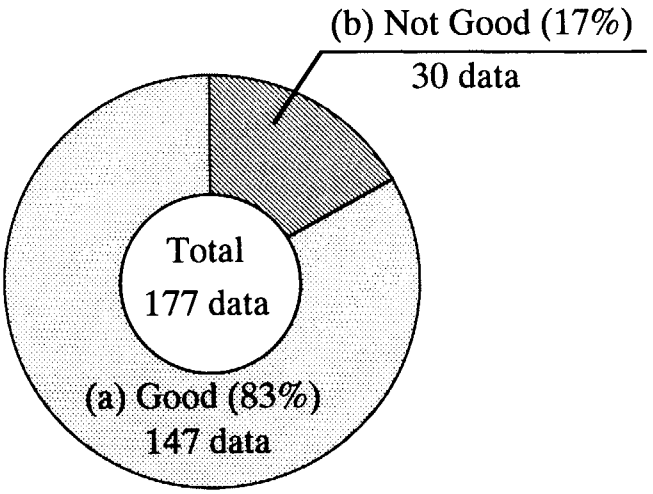

Fig.2. Statistical analysis of realtime density data.
(a) good enough for feedback control.
(b) not good for feedback due to electrical noises.

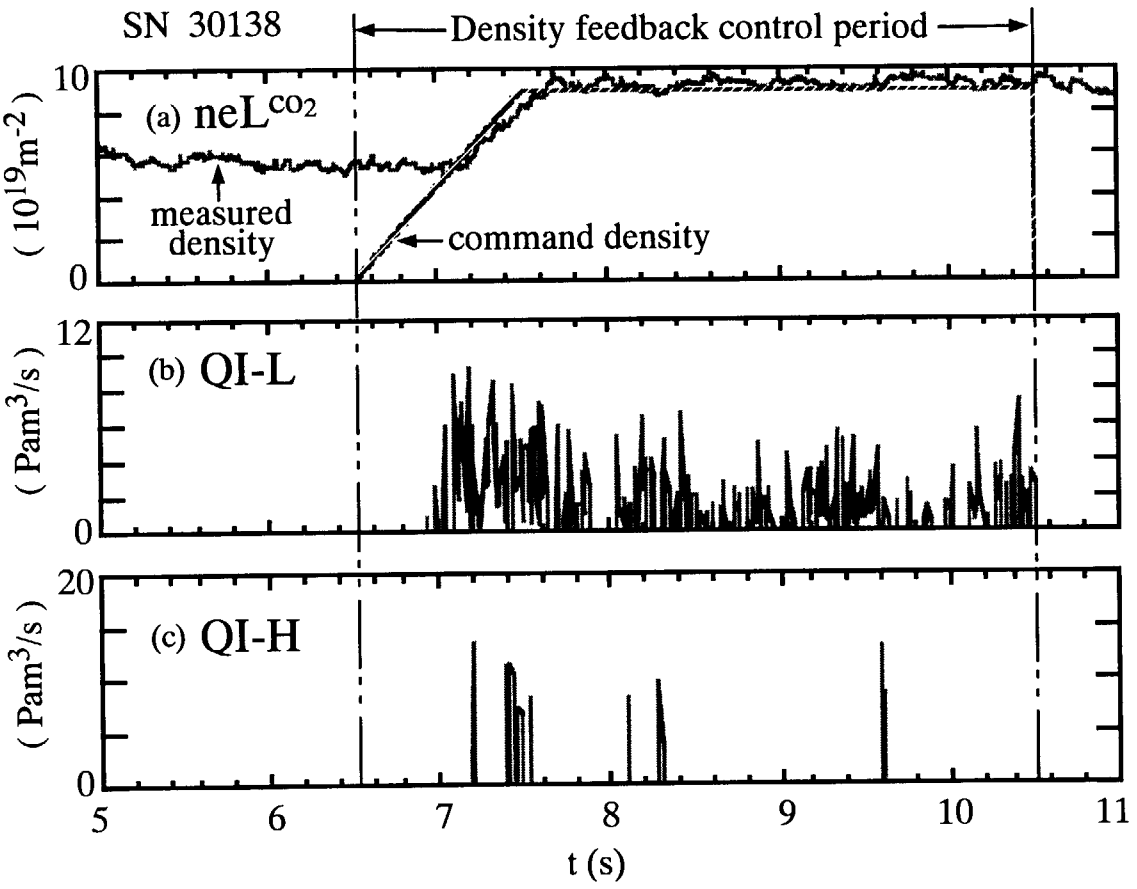

Fig.3. Typical waveforms of density feedback control using CO_2 laser interferometer signal f or a OH hydrogen discharge. The plasma current Ip and the toroidal magnetic field Bt are 2.0MA and 3.5T. (a) Electron density measured by the CO_2 laser interferometer and density command. (b) Gas puffing rate through gas valves I (low rate valves). (c) Gas puffing rate through gas valves I (high rate valves).

2.3 Feedback control of divertor neutral pressure

H. Tamai, N.Hosogane, S. Konoshima, T. Fukuda, S. Sakata, H. Akasaka, and K. Kurihara

2.3.1. Introduction

Since the intense gas puff is fed to divertor for achieving a dense and cold divertor plasma, the back flow of the divertor neutral into the main chamber should be suppressed for sustaining the high performance core plasma. In addition, excessive gas puff into the divertor should also be avoided for the stability of the divertor plasma. In order to adjust the proper divertor gas puff, feedback control system is conducted as an actuator of the divertor neutral pressure.

2.3.2. Feedback control system

Figure 2.3.1 illustrates the block diagram of the feedback control system of the divertor neutral pressure, which is very much similar to that for the divertor radiation power[1), 2)]. Measured signal of the fast response ionisation gauge, described in Chapter 8.4, on the inside divertor plate is fed to the real-time processor composed of the high speed digital computer.

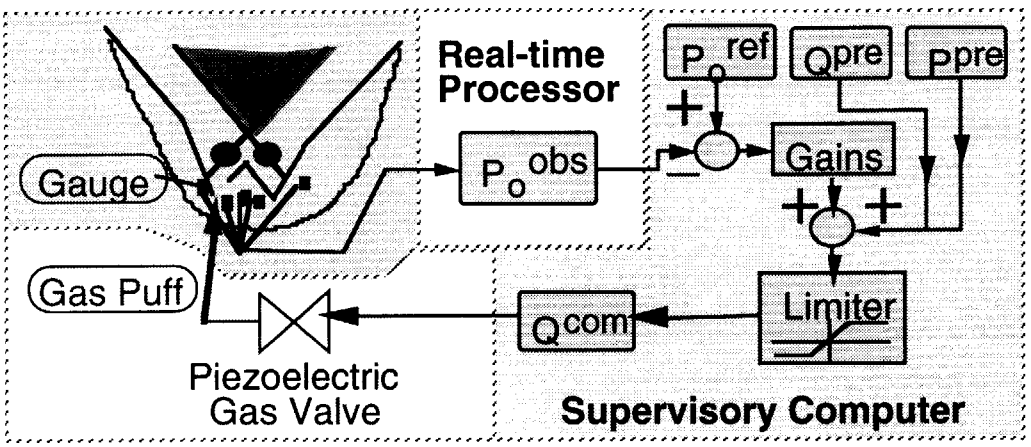

Fig.2.3.1 Block diagram of the feedback control system of the divertor neutral pressure.

Divertor neutral pressure, P_o^{obs}, is calculated as

$$P_o^{obs} = (1 / \alpha) * I_i / (I_e - I_i), \qquad \text{Eq. 2.3.1}$$

where, I_e, I_i, and α are the emission current, the ion current, and the sensitivity of the gauge, respectively. The calculated divertor neutral pressure is fed to the supervisory computer for the plasma control with the time delay of less than 1 millisecond, which is negligibly small compared to the delay of the gas feed system of about 100 milliseconds. A command signal of the gas puffing rate, Q^{com} is determined so that P_o^{obs} traces the pre-determined reference of the divertor neutral pressure, P_o^{ref}, in every 10 milliseconds with an equation as

$$Q^{com} = Q^{pre} + G_P[P_o^{ref} - P_o^{obs}] + G_D[d(P_o^{ref} - P_o^{obs})/dt], \qquad \text{Eq. 2.3.2}$$

where Q^{pre}, G_P, and G_D are pre-programmed signal of the gas puffing rate, proportional gain,

and differential gain, respectively.

The command signal of the calculated gas puffing rate, Q^{com}, is sent to the piezoelectric gas valve. The hydrogen gas flow into the divertor region is changed in 100 milliseconds, which is the delay of the gas feed system.

2.3.3. Determination of gas puffing rate

In order to estimate a gas puffing rate, Q^{com}, corresponding to a desired divertor neutral pressure in the real time control, proportional gain, and the differential gain, are determined beforehand. Experimental shots are referred to pick up the response of the neutral pressure to the divertor gas puffing of a constant rate with step-wise increase.

Figure 2.3.2 shows the the hydrogen gas puffing rate plotted against the divertor neutral pressure in the case of hydrogen ohmic discharge with the X-point height of 8cm from the dome top. In the range of the gas puffing rate from 5 to 15 Pa m^3/s, the divertor neutral pressure has certain scatters due to the time delay of the response. The proportional gain, G_P, is deduced from the linear fitting of those plots as $Gp=73m^3/s$ with the accuracy of 94%. Whereas, the differential gain, G_D, is empirically deduced by the shot-to-shot adjustment in order to suppress the oscillation of the command signal induced by the time delay between command signal and the observed divertor neutral pressure.

The proportional gain tends to increase with increase of the X-point height. For example, at the X-point height of 16cm, the proportional gain is deduced as $Gp=130m^3/s$ in the same procedure of linear fitting. This tendency indicates that more intense puff is required for higher X-point height to maintain the divertor neutral pressure, and suggests the effective compression of divertor neutral would be brought by the adjustment of the plasma position.

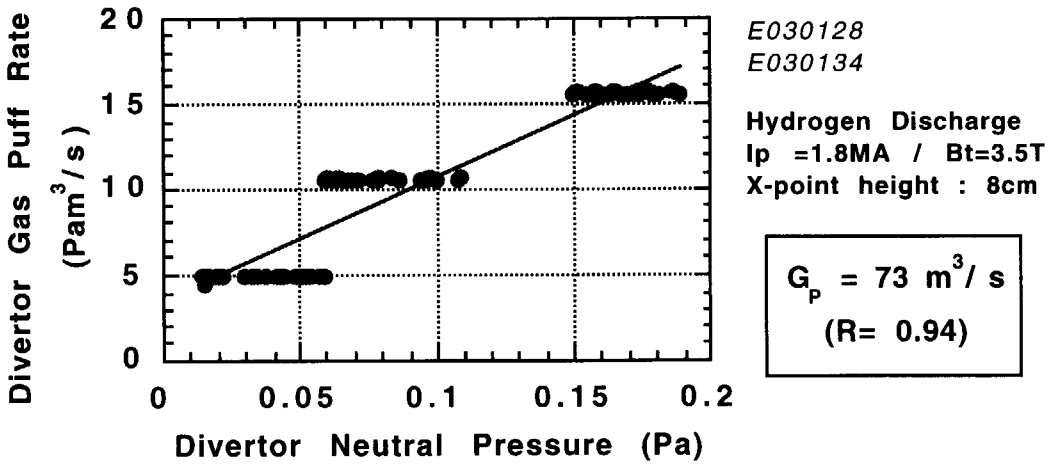

Fig.2.3.2 Hydrogen gas puffing rate versus divertor neutral pressure.

2.3.4. Successful example of feedback control

The feedback control of the divertor neutral pressure is performed by the hydrogen puffing

under the following operational conditions; OH discharge with plasma current of 1.2 MA, toroidal magnetic field of 3.5 Tesla, height of X-point from the dome top of 7.3 cm.

Figure 2.3.3 shows the example of successful feedback control of the divertor neutral pressure. Temporal traces are (top) measured divertor neutral pressure, and reference pressure, (second) gas puffing rate at the divertor, (third) averaged electron density, and H_α emission through the inside divertor chord. The divertor neutral pressure is pre-programmed at 0.1 Pa with a flat top duration of 3 seconds.

An increase of gas pulse at around 10.5 seconds indicates that the gas injection is performed so as to compensate the difference between the measured pressure and the reference pressure. The gas pulses become small as the measured pressure grows to the reference pressure. Therefore, the divertor neutral pressure is successfully controlled at the reference value for about 2 seconds. Averaged electron density gradually increases during the feedback control of the divertor neutral pressure. Since the gas feed from the top puff is shut off during this phase, increase of the density is contributed by the divertor puff.

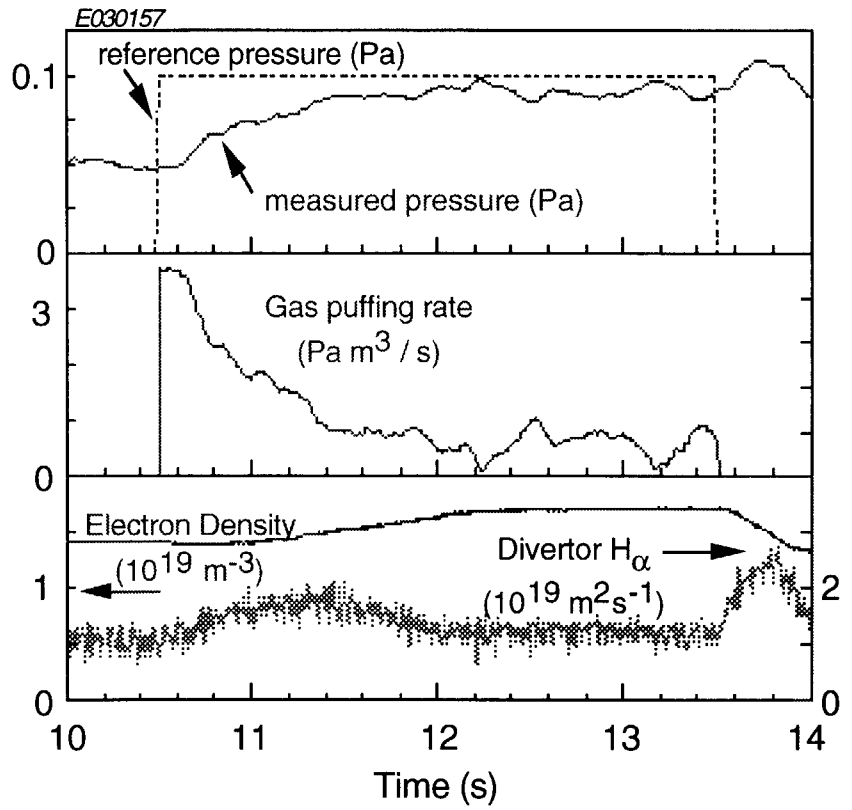

Fig.2.3.3 Typical example of the feedback control of divertor neutral pressure. Parameters are the reference and observed divertor neutral pressure(top), gas puffing rate(second), averaged electron density, and the divertor H_a emission (bottom).

References

1) S.Konoshima *et al.*, JAERI-Research, *96-018* (1996).

2) H.Tamai *et al.*, 4th International Symposium on Fusion Nuclear Technology, Tokyo 1997.

2.4 A New Function Parametrization Formula for the JT-60U X-Point Position Control

Y.M. Miura, Y. Kawamata, T. Fukuda and K. Kurihara

1. Introduction

A function parametrization (FP) method[1] has been adopted for the real-time control of JT-60U plasma position and shape, where sets of linear coefficients in the FP formulas for plasma geometrical center (R_p, Z_p), X-point position Z_x, and triangularity δ, are determined through regression analyses based on the numerically-prepared equilibrium database. According to modification of the divertor structure (to a W-shape) in 1997, the number of the linear coefficients was simply increased from 7 to 33 to improve the control accuracy. Although the numerical examination using the database had shown a good accuracy (standard deviation $\sigma \leq 2$ cm), the experimental comparison of the FP method and the equilibrium analysis resulted in considerably large discrepancy for X-point position solely (offset bias and standard deviation) as in Fig. 1. In the following subsections, we discuss the causes of the problems, compose a new FP formula for more precise X-point detection, and describe results in its application to the experiment.

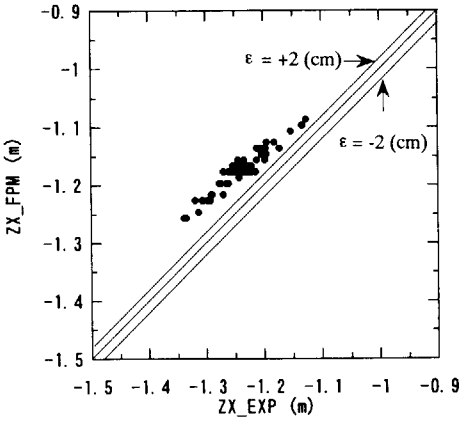

Fig. 1 Correlation of X-point vertical positions of Z_{X_FPM} and Z_{X_EXP}. (Z_{X_FPM}: Results from the FP formula on experimental data. Z_{X_EXP}: Results from the equilibrium analysis. Three lines indicate −2, 0, +2 cm errors (ε).)

2. Cause Analysis and Results by Taking Measures

Corresponding to two problems of large offset bias and large standard deviation, we came to consider the following items could be the causes.

(1) Ill-posed problem

The formula of the FP method for detection of the plasma parameter X^{RG} has been commonly expressed as

$$X^{RG} = C_0 + \sum_{i=1}^{N_\omega} \left(C_{\omega i} + D_{\omega i} \cdot \frac{I_D}{I_P} \right) \frac{B_{\omega i}}{I_P} + \sum_{i=1}^{N_\rho} \left(C_{\rho i} + D_{\rho i} \cdot \frac{I_D}{I_P} \right) \frac{B_{\rho i}}{I_P}, \quad (1)$$

where I_P and I_D are a plasma and a divertor coil currents, $B_{\omega i}$ and $B_{\rho i}$ are tangential and normal components of magnetic fields at the i-th probe positions, and N_ω and N_ρ are the numbers of probes. In previous years, only 7 coefficients had been used on the basis of the design principle of parsimony. However, improvement of accuracy requires all of the 33 coefficients C_0, $C_{\omega i}$, $D_{\omega i}$, $C_{\rho i}$, and $D_{\rho i}$ in the FP formula to be calculated using the method of

least squares (LS) on the equilibrium database. In general, if strongly correlated sensors or very insensitive sensors are involved in the LS analysis, their coefficients tend to be large numbers. This is an ill-posed problem that small amount of actual sensor noise or error could make large difference from the numerical results on the ideal database.

To put it concretely in our case, (a) tangential component probes (T-probe) of #1 and #16, which show similar sensitivity to X-point displacement, were involved in Eq. (1) as independent valuables, and (b) the #8 normal component probe (N-probe), which is insensitive to X-point vertical displacement, was mingled in the equation (the probe locations are shown in Fig. 2, and the probes available for control are circled). Consequently, we have excluded #1 T-probe and #8 N-probe from the coefficient calculations, and the results using a new coefficients set are shown in Fig. 3, which indicates that the offset bias was completely suppressed.

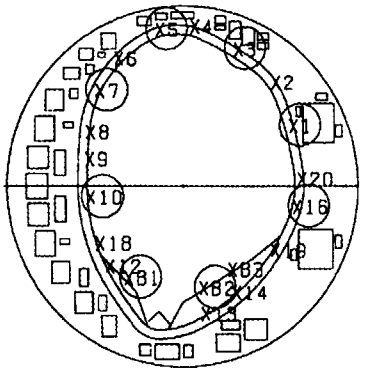

T-probes

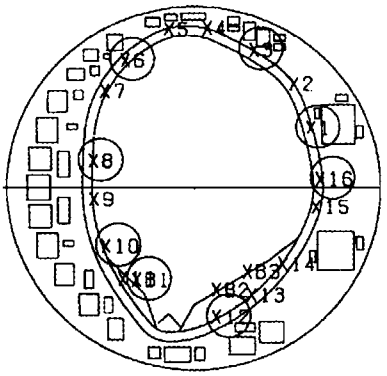

N-probes

Fig. 2 Locations of T-probes and N-probes (The probes available for control are circled.)

(2) Effects of OH-coil field

Since there exists a systematic error in Fig. 3, and an essential problem is still surely remaining in the method. The following results suggested that the effect of ohmic-heating coil (forcing (F-) coil) field has strong influence on the error.

(a) The F-coil in JT-60U produces magnetic field in the plasma column as a consequence of the initial design for poloidal field coils.

(b) The large errors had been observed when F-coil current is driven in the opposite direction to the plasma current.

(c) In the equilibrium analysis, it was found divertor configurations could be formed by large negative F-coil currents without a divertor coil (D-coil) excitation (Fig. 4).

From the above point of view, we have developed a new FP formula that takes the effects of the F-coil current as well as the D-coil current. This formula

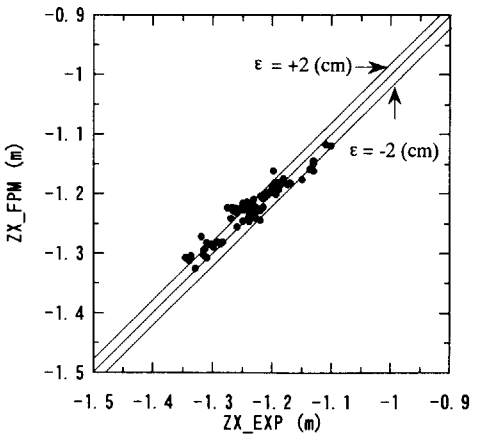

Fig. 3 Correlation of X-point vertical positions of Z_{X_FPM} and Z_{X_EXP}. (Z_{X_FPM}: Results from the FP formula on experimental data. Z_{X_EXP}: Results from equilibrium analysis.)

was first composed from the assumption that X-point be located on the segment of the plasma and D/F coil currents centroids (Fig. 5). The new FP formula including the term of F-coil current I_F is

$$X^{RG} = C_0 + C_1\frac{I_D}{I_P} + C_2\frac{I_F}{I_P} + \sum_{i=1}^{N_\omega}\left(C_{\omega i} + D_{\omega i}\frac{I_D}{I_P} + E_{\omega i}\frac{I_F}{I_P} + F_{\omega i}\frac{I_D I_F}{I_P^2} + G_{\omega i}\frac{I_D^2}{I_P^2}\right)\frac{B_{\omega i}}{I_P} + \sum_{i=1}^{N_\rho}\left(C_{\rho i} + D_{\rho i}\frac{I_D}{I_P} + E_{\rho i}\frac{I_F}{I_P} + F_{\rho i}\frac{I_D I_F}{I_P^2} + G_{\rho i}\frac{I_D^2}{I_P^2}\right)\frac{B_{\rho i}}{I_P}, \quad (2)$$

where the C_1, C_2, $E_{\omega i}$, $F_{\omega i}$, $G_{\omega i}$, $E_{\rho i}$, $F_{\rho i}$ and $G_{\rho i}$ are the coefficients determined by the method of LS.

For installation of the new FP formula to the JT-60U real-time feedback computer, a computation time should be minimized as far as the accuracy exceeds the allowable limit. In this sense, 22 coefficients are properly chosen. We have calculated this FP formula coefficients using the data with and without D-coil excitation. The determined terms are listed in Table 1. The test calculations with the old and new FP formulas on the numerical plasma equilibrium database are shown in Figs. 6 and 7. In spite of the smaller number of terms with the new formula, the standard deviation is decreased. The accuracy has been improved especially for a plasma, of which X-point is located in the neighborhood of the divertor dome (Z_x ~ -1.36 m). The application of the new FP formula to the actual experiments are shown in Fig. 8, where X-point positions are surely detected within 2 cm, as expected in the numerical analysis.

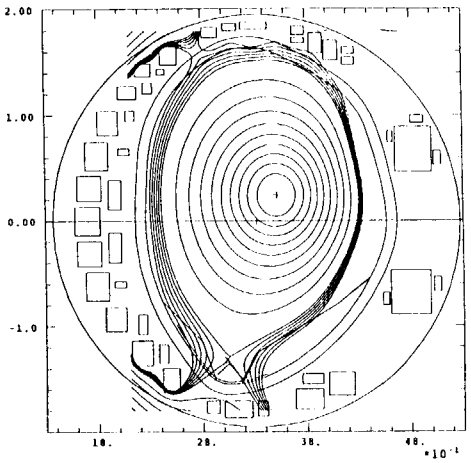

Fig. 4 Divertor configuration without D-coil excitation (I_P: 750 kA, I_F: -50 kA, I_D: 0 kA, I_V: 9.1 kA, I_H: -4.4 kA)

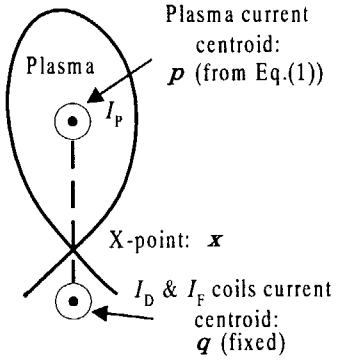

Fig. .5 Basic intuitive concept for the FP formula (The X-point x is assumed on the segment of the plasma current p and the D/F coil current centroid q: $x = t\,p + (1\text{-}t)\,q$, $t \sim I_F/I_P$ & I_D/I_P.)

3. Conclusions

The accuracy deterioration of X-point position detection with the FP method was caused by both the ill-posed problem of the FP formula coefficients and the effects of F-coil field. By avoiding of ill-posed conditions and employment of the newly proposed FP formula, the X-point position detection was successfully improved in the JT-60U highly-elongated plasma experiment.

Table 1 The terms in the new FP formula

Co	$B_{\omega B2} I_D^2/I_P^3$
$B_{\omega 7}/I_P$	$B_{\rho 3}/I_P$
$B_{\omega B1}/I_P$	$B_{\rho 12}/I_P$
$B_{\omega B2}/I_P$	$B_{\rho 3} I_D/I_P^2$
$B_{\omega 5} I_D/I_P^2$	$B_{\rho 16} I_D/I_P^2$
$B_{\omega 7} I_D/I_P^2$	$B_{\rho 12} I_D/I_P^2$
$B_{\omega B2} I_D/I_P^2$	$B_{\rho 16} I_F/I_P^2$
$B_{\omega 5} I_F/I_P^2$	$B_{\rho 12} I_F/I_P^2$
$B_{\omega 10} I_F/I_P^2$	$B_{\rho 12} I_D I_F/I_P^3$
$B_{\omega 7} I_D^2/I_P^3$	$B_{\rho 3} I_D^2/I_P^3$
$B_{\omega 10} I_D^2/I_P^3$	$B_{\rho 12} I_D^2/I_P^3$

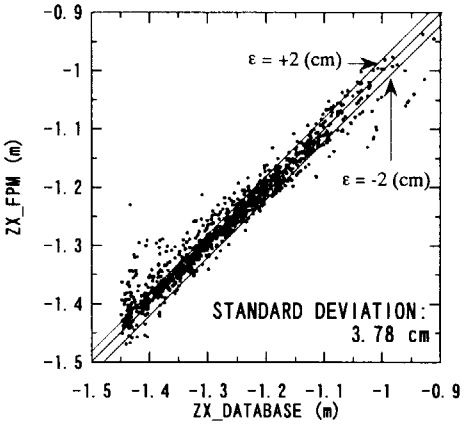

Fig. 6 Correlation of X-point vertical positions of Z_{X_FPM} and $Z_{X\_DATABASE}$. (Z_{X_FPM}: Results from the old FP formula on numerical equilibrium database. $Z_{X\_DATABASE}$: Given para-meter from the database.)

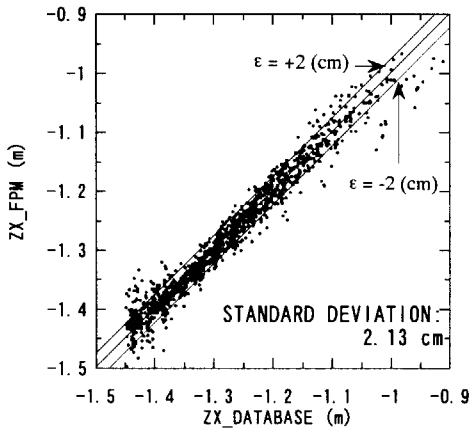

Fig. 7 Correlation of X-point vertical positions of Z_{X_FPM} and $Z_{X\_DATABASE}$. (Z_{X_FPM}: Results from the new FP formula on numerical equilibrium database. $Z_{X\_DATABASE}$: Given parameter from the database.)

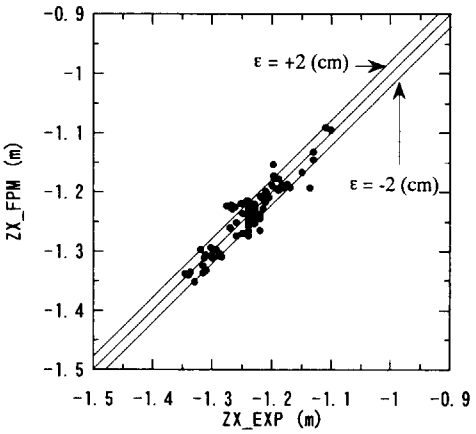

Fig. 8 Correlation of X-point vertical positions of Z_{X_FPM} and Z_{X_EXP}. (Z_{X_FPM}: Results from the FP formula on experimental data. Z_{X_EXP}: Results from the equilibrium analysis.)

References

1) N. Hosogane, H. Ninomiya and S. Seki, Nucl. Fusion, **26**, 657 (1986).

3. Confinement and Stability

3.1 Long Pulse H-mode toward Steady-State High Performance

Y. Kamada, A.Isayama, T.Oikawa, N. Hosogane, Y.Kusama, T.Fujita, S.Takeji, T.Ozeki, K. Ushigusa, O. Naito, S.Ishida, Y. Koide, T. Fukuda, T. Takizuka, H.Shirai and T. Hatae

This paper treats recent development of quasi-steady ELMing discharges with enhanced confinement, high-β stability and current drive capabilities, where increase in absolute values of fusion performance and sustainment time are emphasized. After modification to the new W-shaped pumped divertor, a long heating time (9sec) of high power NB (20 -25MW) became possible without harmful increase in impurity and particle recycling. The total energy input reached 203MJ. In addition to it, optimization of the pressure profile and selection of appropriate electron density enabled us to extend pulse length with high performances; DT equivalent fusion gain Q_{DT}~0.1 was sustained for 9 sec (triangularity δ =0.16), and Q_{DT} ~0.16 for 4.5 sec (δ =0.30) at I_p=1.5MA. In the latter case, H-factor ($=\tau_E/\tau_E^{ITER89PL}$)~2.3, β_N~2 and β_p~1.6 were sustained with 60-70% of noninductive current drive (NB driven and bootstrap). The new extension of pulse length accelerates understanding of roles of parameters with long time constants such as the current profile and particle recycling. Concerning the former, appearance of low-n resistive modes is the issue, because sustainable β_N in a long pulse is lower (~ 2 for 5- 9sec) than that achievable transiently (~3.2 ~ ideal limit) due to these modes. To improve the stability, high δ and high density are beneficial. On the other hand, at the edge, the confinement and steadiness of the H-mode are affected by giant ELMs and depth of the edge pedestal Δ_{ped}. The depth Δ_{ped} in the ELMing phase is 2-3 times larger than that in the ELM-free phase and reaches ~10-15cm with a roughly constant pressure gradient. With increasing recycling, the pedestal layer moves inward and ELM frequency increases, which cause the gradual confinement degradation in a long pulse.

1. Sustainment of High Integrated Performance and High Fusion Gain

Toward the *simultaneous* achievement of i) high confinement , ii) high β limit, iii) high bootstrap fraction and iv) high efficiency of heat and particle exhaust in the *steady-state*, discharges have been optimized in JT-60U mainly based on the high-β_p H-mode with q(0)>1.

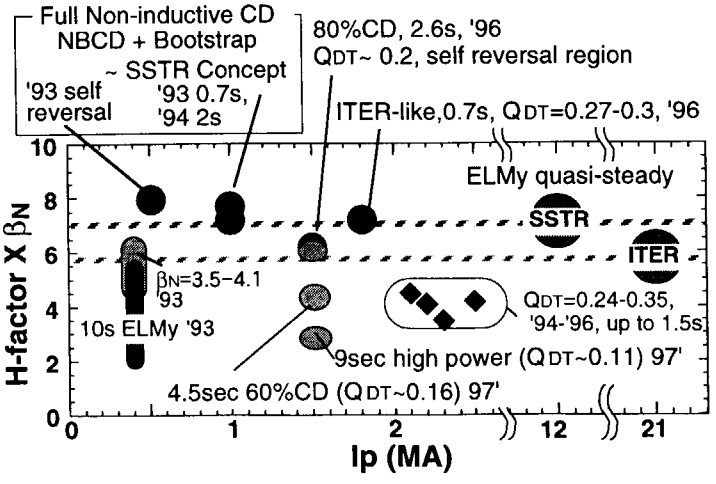

Figure 1.
Discharge regions of ELMing quasi-steady discharges with high integrated performances in JT-60U

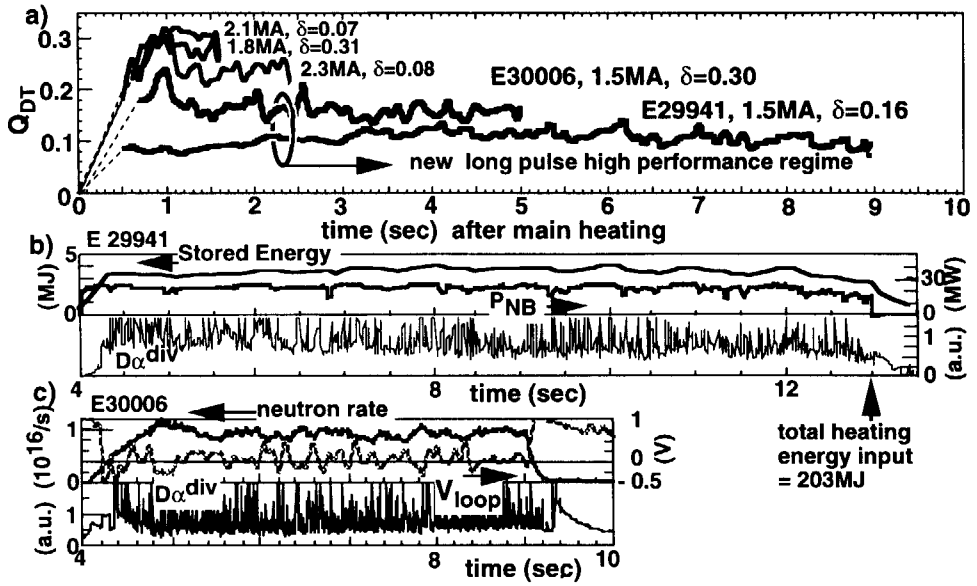

Figure 2.

(a):Sustainment of high Q_{DT} for long duration. (b): low-δ (0.16): Stored energy ~4MJ and Ti(0)~ 10 keV with P_{NB}=20-25MW were sustained for ~9 sec (~50 τ_E). The total energy input reached 203MJ. (c): high-δ (0.3): D-D neutron rate ~1x10 ^{16}/s, β_N~2 and H-factor ~2.3 under 60-70% of non-inductive current drive sustained for ~ 4.5 sec.

The discharge regions are summarized in Fig.1. Up to I_p=1MA, an optimized pressure profile with high triangularity δ (=0.35) enabled the favorable integrated performance with H-factor~ 2.5 and β_N~3 under full non-inductive current drive (bootstrap ~60%) sustained for 2s (~10τ_E)[1,2]. In a 1.5MA/3.6T discharge with δ=0.35, a favorable integrated performance was sustained for ~2.6s (~8 τ_E) with Q_{DT}~0.2, β_N~2.5 and H-factor~2.5, bootstrap current~ 50%, beam driven current ~25% (~75% non-inductive). In this discharge regime, a current profile with natural shear reversal close to the steady-state solution was observed because of sustainment of high values of β_p. At a higher I_p =1.8MA (B_t=3.6T) with an ITER-like configuration (q_{95}= 3.4, δ= 0.3, κ =1.5), Q_{DT}= 0.27-0.3, β_N= 2.7-2.9, H~2.5, H/q_{95}= 0.74 was sustained for 0.7s (2xτ_E). With the new W-shaped pumped divertor [3], a long heating time with high power became possible. We obtained an ELMy H-mode with Q_{DT}~0.11, H-factor ~1.7, T_i(0)~10keV and β_N~1.8 sustained for 9 sec (~50τ_E) under a high NB power of 20-25MW (I_p=1.5MA, B_t=3.6T, δ=0.16) (Fig.2 a) and b)). Even with the high total energy input up to 203MJ, no increase in impurity (carbon) and particle recycling was observed. Before the divertor modification, increase in carbon and recycling degraded performance at ~3 sec of high power (20-30MW) heating. In case of high δ (=0.3), the better performance with Q_{DT}~0.16, H-factor~2.3, β_N~2 and β_p~1.6 was sustained for 4.5 sec with 60-70% of non-inductive driven current at a relatively high density of ~45% of the Greenwald limit (Fig.2 a) and c)). Duration of the high δ equilibrium is limited (< 5sec) by heat capacity of the shaping coils. Without the divertor pumping, gradual increase in recycling degraded energy confinement.

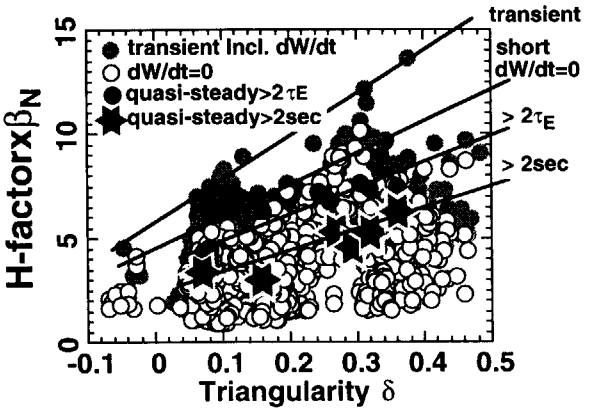

Figure 3. *H-factor x β_N increases with triangularity δ. Sustainable values of Hβ_N for > 2sec is ~60% of that achievable in a short duration.*

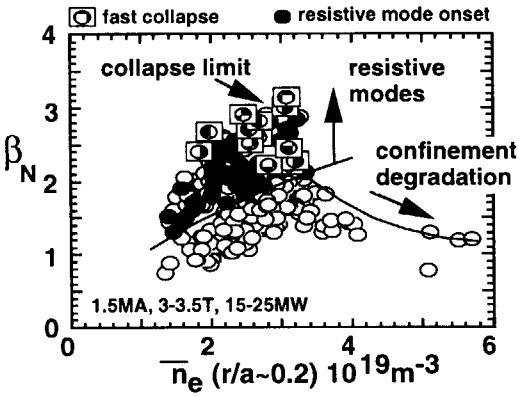

Figure 4. *Regions of fast collapses, onset of resistive modes and degradation in confinement on the density - β_N plane (I_p=1.5 MA, B_t=3-3.5T, P_{NB}=15-25MW).*

2. β-limits in Long Pulses

In these long pulse discharges, we controlled the heating profile to produce the optimum peakedness of pressure profile p(r) for maximizing β_N [2]. At a larger peakedness, the β_N-limit is lower due to the βp-collapse which is consistent with the ideal kink-ballooning limit. At a smaller peakedness, β_N is limited by giant ELMs which is consistent with the high-n ballooning limit. The ELM-limit increases with δ [2]. Figure 3 shows Hβ_N increases with δ in any duration from 'transient' to 'long pulse'. However, the level of Hβ_N decreases with extending sustainment time. Among discharges with dW/dt=0 (W: stored energy), Hβ_N decreases by ~40% from a short duration (upper envelope of open circles) to quasi-steady>2sec (closed stars). This is due to slowly (~100ms) growing resistive instabilities with mode numbers of (m/n)=(3/2), (2/1), (3/1) etc. The island width estimated from the T_e profile is 5 - 10 cm. So far, even with the optimum p(r), sustainable β_N is ~2.5 for 2.6sec and ~2 for 5-9sec at I_p=1.5MA, B_t=3.6T , q_{95}~4 and l_i~1 with collisionality similar to ITER (transiently $\beta_N{}^{max}$ =3.2; Fig.4). The threshold β_N for onset of the resistive modes (closed circles) increases with increasing electron density and with broadening of p(r). The neoclassical tearing mode is a candidate. When q(0)<1, β_N is lower (~1.5) due to (m/n) =(1/1) mode and sawteeth. In Fig.4, at a density higher than ~3.4x$10^{19}$$m^{-3}$ (~50% of Greenwald limit), β_N decreases because of confinement degradation at high recycling. For sustainment of long pulse discharges, we kept the optimum set of density and β_N to avoid both the resistive modes and confinement degradation. (For example, the shot E30006 shown in Fig.1 has β_N =2 with n_e=3.2x$10^{19}$$m^{-3}$.)

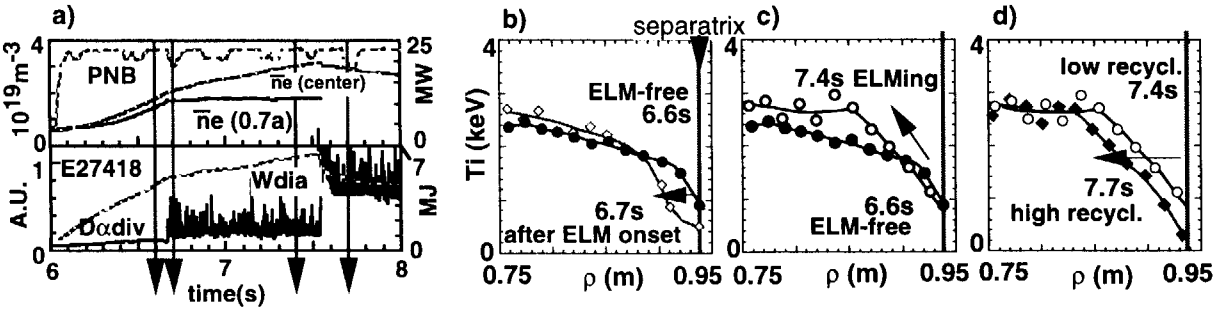

Figure. 5. *Change of edge ion temperature profile. Depth of pedestal is changing due to ELMs and recycling.*

3. Giant ELMs and Deepening of Edge Pedestal

To sustain high confinement, control of ELM effects is essential. In JT-60U ELM-free H-mode, the edge pedestal Δ_{ped} is 3-5cm at I_p~2MA and scales roughly with the ion poloidal gyro radius [4]. On the other hand, in the giant-ELMy phase, Δ_{ped} can be 10-15cm (r/a~85 %). Figure 5 shows onset of giant ELMs makes Δ_{ped} large (b)) and the pedestal temperature in the ELMy phase can be higher than that in the ELM-free phase (c)). Figure 4d) shows that the pedestal layer shifts inward after increase in particle recycling. Such shrink of the edge pedestal degrades the confinement at a high recycling. In this case, the ELM frequency f_{ELM} was also increased from 140Hz (7.4s) to 260Hz (7.7s). We found f_{ELM} increases linearly with increasing density (or particle recycling) in case of gas puffing in addition to the known dependence on heating power and the ballooning parameter [1]. By these results, it can be explained that the energy confinement slowly decreases with increasing particle recycling in long pulse H-mode plasmas without divertor pumping. On the other hand, the maximum edge pressure gradient was almost unchanged in all cases (Fig.5b)-d)).

REFERENCES

[1] Kamada, Y., et al., Plasma Phys. Cont. Nucl. Fusion Res. Proc.15th Int. Conf. (Seville, 1994) Vol 1, p651.
[2] Kamada, Y., et al., Fusion Energy Proc. 16th Int. Conf. (Montreal, 1996) Vol 1, p247.
[3] Hosogane, N., et al., Fusion Energy Proc. 16th Int. Conf. (Montreal, 1996) GP-11.
[4] T. Hatae et al., to appear in Plasma Phys. Control. Fusion

3.2 MHD Activities in Steady State High Performance Discharges

A. Isayama, Y. Kamada, S. Ishida and N. Isei

1. Introduction

In order to realize an economical tokamak reactor, most of the plasma current must be driven by bootstrap current. In JT-60U, an experiment aiming at a steady state high performances was performed and ELMy H-mode state with β_N~1.8–2.0, H-factor~2.0–2.3 was sustained for about 5 seconds[1]. Although MHD instabilities are suppressed for low β_N(<2) discharges, in higher β_N(>2) discharges low-n resistive instabilities, such as m/n=3/2 and/or 2/1 modes are destabilized and degrade the plasma performance. It is probable that these modes are neoclassical tearing modes[2], which are regarded as important in ITER EDA[3].

In this section, characteristics of low-n resistive instabilities in the steady state high performance, mainly focusing on the relationship between the neoclassical tearing mode, is described.

2. Characteristics of MHD activities

Plasma parameters used for analysts are as follows: I_p=1.2–2.0[MA], B_t=3.0–4.2[T], R_p=3.1–3.4[m], a_p=0.74–0.96[m], V_p=49–78[m^3], q_{eff}=4.0–7.1, q_{95}=3.3–5.2, triangularity δ=0.07–0.28, $P_{NB}\leq$25[MW], $\bar{n}_e$=1.2–2.0[$10^{19}m^{-3}$], $W_{dia}\leq$6.4[MJ] and $S_n\leq 2.4\times10^{16}$[s^{-1}]. Typical waveforms in the steady state high performance discharges are shown in Fig. 1. After the NB injection at t=4.8 s, stored energy W_{dia} increases and soon the plasma transits to the ELMy H-mode state. At t~6.5 s, n=2 mode glows and W_{dia} slightly decreases. At t~6.7 s, n=1 mode glows and W_{dia} decreases down to 50% of its maximum value. This kind of mode seems to be triggered by ELM as shown in Fig. 2, where 3/2 mode glows from t~5.65[s]. These modes are stabilized at several hundred milliseconds after NB turn off. Note that, in these discharges, the central safety factor is kept larger than unity to avoid sawtooth oscillations by injecting NB early in the discharges.

The dependence of onset β_N on averaged electron density is shown in Fig. 3. Averaged electron density $\bar{n}_e$ used here is the one measured by FIR interferometer with tangent radius of r/a~0.4. Open square and open circle correspond to m/n=3/2 mode for li>1.0 and li<1.0, respectively. Closed square and closed circle correspond to m/n=2/1 mode for li>1.0 and li<1.0, respectively. Beta limit for these modes have positive dependence on $\bar{n}_e$, which is similar to neoclassical tearing modes in DIII-D[4]. The onset β_N for 2/1 mode seems is smaller than that for 3/2 mode, and in each mode the onset β_N for lower li case seems smaller than that for higher li case.

It is shown that onset β_N for the neoclassical tearing mode has positive dependence on collisionality[5]. In Fig. 4, dependence of onset β_N on collisionality is shown, where data are plotted on the figure shown in Ref. 5. Open circle is the data points from the steady state high performance experiment in 1997. In Fig. 4, only the onset β_N for m/n=3/2 mode is plotted. Collisionality in Fig. 4 is defined as follows: $\nu_e*=0.012 n_e[10^{20}m^{-3}]qR[m]/\varepsilon^{3/2}T_e^2$ [keV], where electron density and electron temperature is the ones at r/a=0.5 measured by YAG Thomson scattering and ECE, respectively. Although the ν_e* dependence is not clear because of the smallness of the data points, they lie on the line of the ITER database. In order to clarify the collisoinarity dependence, more data set is needed.

It is known that, for neoclassical tearing modes, β_N when the mode appears is higher than that when the mode is stabilized. In the experiments in 1997, such hysteresis in β_N is observed and β_N for the mode destabilization is higher than that for the mode stabilization by a factor three. This tendency is also observed in other tokamaks such as ASDEX-U[5, 6].

3. Estimation of island width

When a tearing mode is destabilized, magnetic islands are formed. In order to observe the electron temperature fluctuation and estimate the island width, heterodyne radiometer(HR) is used. The space and time resolution of HR are 2cm and 20μs, respectively. In Fig. 5, a contour plot of electron temperature fluctuation $\delta T_e/T_e$ during m/n=3/2 mode is shown. The measurement range of HR is shown in Fig. 6. The horizontal and the vertical axis correspond to time and major radius, respectively. White region indicates $\delta T_e>0$, and black region indicates $\delta T_e<0$. The amplitude of the fluctuation at R~3.65[m] is about 5%. The frequency of the fluctuation is 5.5 kHz, which is identical to that of the magnetic fluctuation. The phase of the fluctuation is inverted across R~3.6[m], where the amplitude of the fluctuation is nearly zero during the mode. According to the MSE polarimeter, safety factor at R~3.6[m] is about 1.5. Electron temperature profile at t=6.50208[s] is shown in Fig. 7. The solid line is the fitting curve of the data of the Fourier transform spectrometer(FTS). Closed circle is electron temperature measured by HR, which is relatively calibrated by using FTS. In an ELMy phase, FTS is usually unavailable because nonthermal heat pulses enter the intefergram. Electron temperature shown in Fig. 7 is deduced by removing the heat pulse and restoring the interferogram[7]. As shown in Fig. 7, fluctuation shown in Fig. 6 is sufficient to form the flat region in electron temperature profile. The width of the flat region, which suggests the existence of magnetic islands, is about 5 centimeters. It is clear from Fig. 7 that HR is a powerful tool to observe the tearing mode and measure the island width.

4. Summary and future plan

Characteristics of MHD activities in the steady state high performance experiment is discussed. The behavior of the instability shows same as the neoclassical tearing mode

observed in other tokamaks and results and no contradictory data was found. In order to conclude the mode in JT-60U as the neoclassical tearing mode, further investigation should be done. A numerical calculation code to solve the Rutherford equation which describes evolution of the island width is under development. Another approach is to evaluate Δ', which is defined as $\Delta'=(1/Br)(\partial Br/\partial r)|_{r_s+w/2}-(1/Br)(\partial Br/\partial r)|_{r_s-w/2}$. Br, rs and w are radial magnetic field, minor radius at a resonant surface and island width, respectively. The neoclassical tearing mode can be destabilized even when Δ' is negative, while Δ' needs to be positive for a classical tearing mode to be destabilized. A method to evaluate Δ' using ECE data[8] is to be applied.

References

1) Y. Kamada et al., in this review. Section 3.1.
2) Z. Chang et al., Phys. Rev. Lett. **74** (1995) 4663.
3) N. Fujisawa et al., Journal of Plasma and Fusion Plasma Research **73** supplement (1997) (in Japanese).
4) H. Wilson et al., Plasma Phys. Control. Fusion **38** (1996) A149.
5) O. Sauter et al., Phys.Plasmas **4** (1997) 1654.
6) H.Zorm et al., Plasma Phys. Control. Fusion **39** (1997) B237.
7) A. Isayama et al., in "Reviews of JT-60U Experimental Results from February to November, 1996", JAERI research 97-047
8) C. Ren et al., Phys.Plasmas **5** (1998) 450.

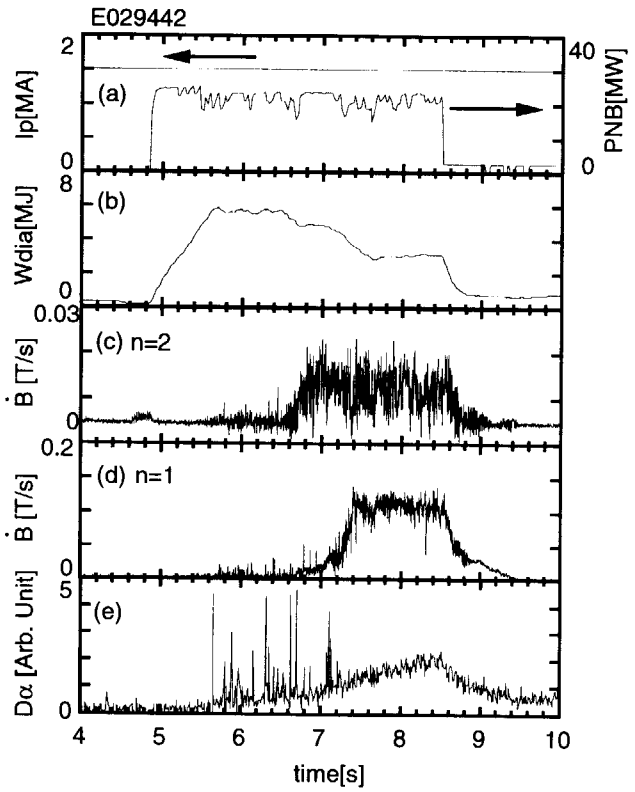

Fig. 1: Time evolution of (a) plasma current and NB injection power, (b) stored energy, (c) magnetic field fluctuation with toloidal mode number n=2, (d) magnetic field fluctuation with n=1 and (e) Dα signal.

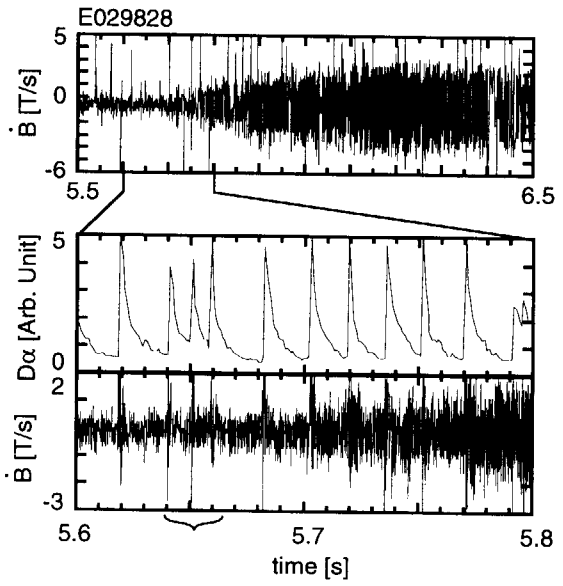

Fig. 2: Time evolution of magnetic fluctuation and Dα signal near the onset of 3/2 mode. Amplitude of Ḃ increases at t~5.65[s]

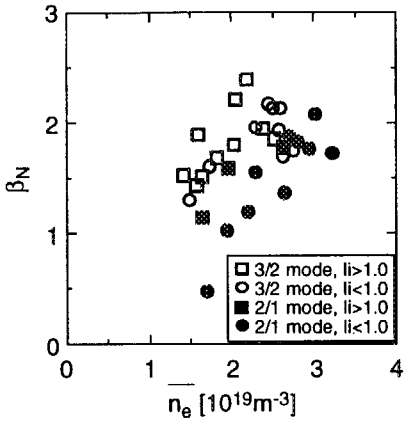

Fig. 3: Dependence of β_N for onset of 3/2 and 2/1 modes on averaged electron density. (I_p=1.5[MA], B_t=3.5–3.7[T], q_{95}=3.6–4.4, l_i=0.90–1.18 for 3/2 mode and 0.74–1.13 for 2/1 mode)

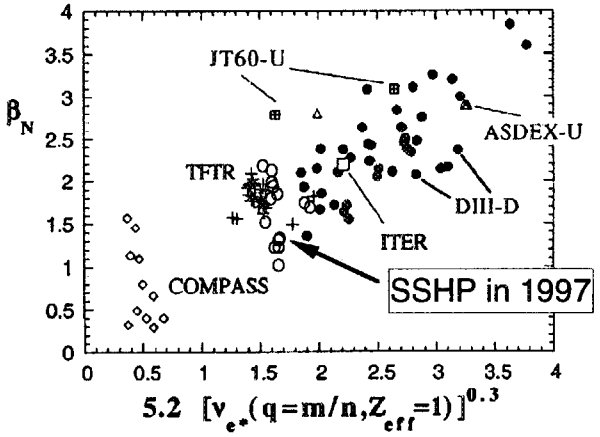

Fig. 4: Dependence of β_N for onset of neoclassical tearing modes on collisionality. Open circle corresponds to the onset of 3/2 mode in the steady state high performance experiment in 1997.

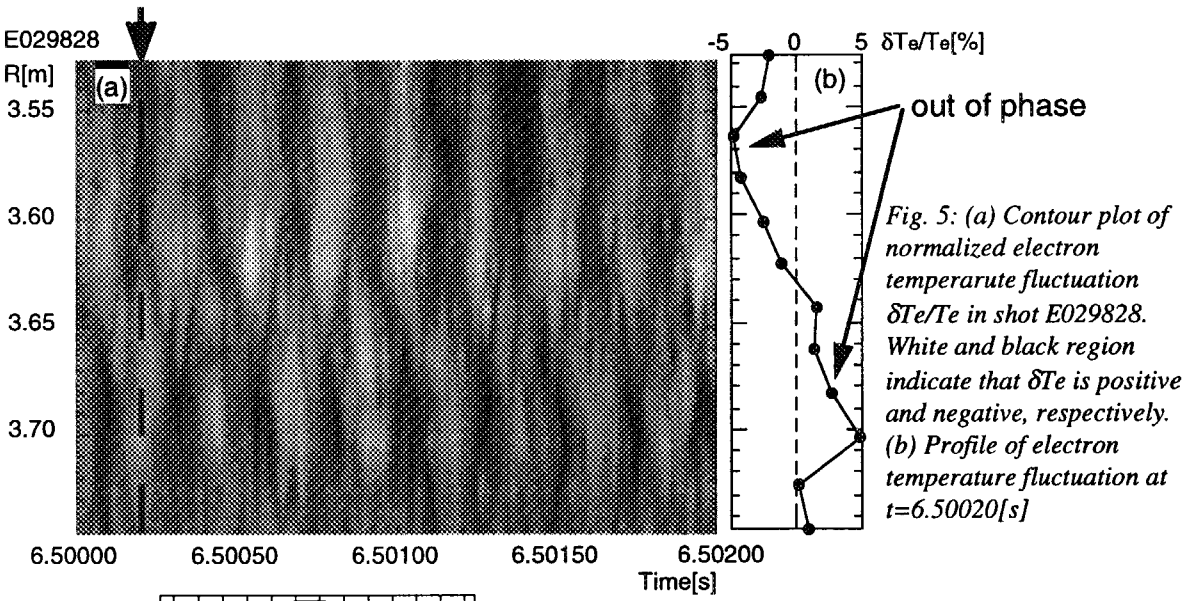

Fig. 5: (a) Contour plot of normalized electron temperarute fluctuation δTe/Te in shot E029828. White and black region indicate that δTe is positive and negative, respectively. (b) Profile of electron temperature fluctuation at t=6.50020[s]

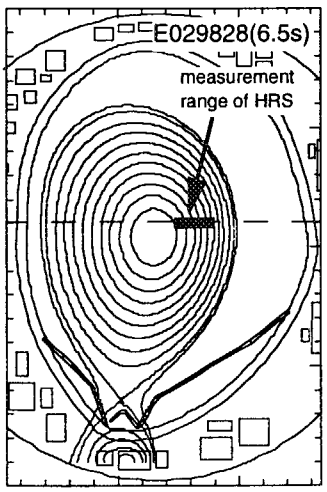

Fig. 6: Equiliblium configuration and measurement range of heterodyne radiometer in shot E029828.

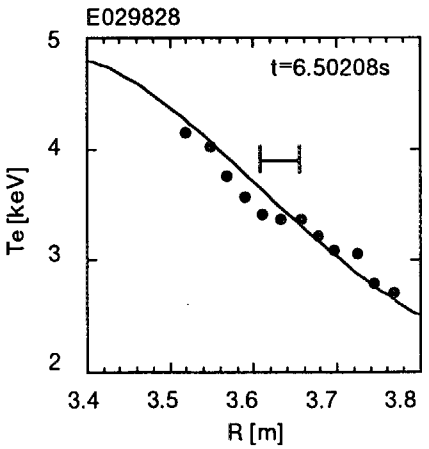

Fig. 7: Electron temperature profile at t=6.50208[s] in shot E029828.

3.3 Stability Improvement and Sustainment of Improved Confinement in Reversed Shear Plasmas with an ELMy H-mode edge

T. Fujita, Y. Kamada, Y. Neyatani, S. Ishida, S. Ide, T. Oikawa, H. Shirai, S. Takeji

1. Introduction

In JT-60U reversed shear discharges, high performance was obtained by formation of an internal transport barrier (ITB) with a large radius [1] and a deuterium-tritium-equivalent fusion power gain of 1.05 was achieved [2]. However, these discharges encountered a beta collapse when q_{min} decreased to 2, which restricted the fusion performance and the duration of high confinement. The beta limit was β_N~2 (β_N is the normalized beta) at q_{min}~2, and a low-q_{min} region below q_{min} = 1.7 could not be reached [1]. It was observed that fluctuations of electron temperature grew explosively from the ITB region with a very fast growth time of order ~10 μs at collapses [3]. These observations on the beta limit and instability growth time agree with calculated values for low-n kink-ballooning modes as predicted by the ERATO-J code [4]. Since this mode is destabilized by a large pressure gradient in the ITB region, broadening of the pressure profile by combining an H-mode with an ITB was attempted for the improvement of stability and sustainment of improved confinement. High triangularity configurations were also aimed at to increase an edge pressure gradient in an H-mode.

2. Operation for obtaining an H-mode

In the original plan, combining an H-mode was to be attempted in plasmas with an ITB with a large radius, which would be created in a similar way that was used in high performance reversed shear plasmas with an L-mode edge; i.e. formation of an ITB by injecting a relatively high power (~ 15 MW) beam into a low current (~ 1 MA) plasma followed by current ramp-up. However, this scenario was given up since the reproducibility of the ITB formation in this method was not good. The reason of the poor reproducibility is not well understood; the difference was a weaker toroidal field (3.5 T against 4.3 T) and injection of tangential beams before high power heating. Consequently, the method to obtain an H-mode was to reduce the beam power during the current ramp to prevent the development of a strong ITB, since strong ITBs appeared to make the H-mode transition difficult due to the small power flow across it [3]. High power heating at an later period or at the current flat-top triggered the H-mode transition.

The edge pedestal in an H-mode in a low trianglarity (δ) configuration appeared to be insufficient to make a broad pressure profile which had a high stability. To enhance the edge pedestal, increasing the triangularity was attempted. Increasing δ from 0.1 to 0.3 in a short period (~ 0.2 s) resulted in decrease in internal inductance and in a collapse. Slow δ ramp in a long period (~ 1.5 s) and keeping q_{eff} larger than 5 leaded to realization of high δ reversed shear discharges. An example of discharge is shown in Fig. 1. The triangularity was gradually

increased from 0.1 to 0.3 during t = 4.0-5.5 s. The plasma volume was also increased to keep q_{eff} larger than 5. The ELM started at 5.0 s. The ITB also started to form at around 5.0 s and continued to develop as shown in the increase of stored energy, neutron emission rate and central density, which resulted in a beta collapse at 6.8 s. Hence, the edge pedestal in high δ ELMy H-mode could not avoid steeping the pressure gradient at the ITB or the resultant collapse at least when the beam power was kept constant.

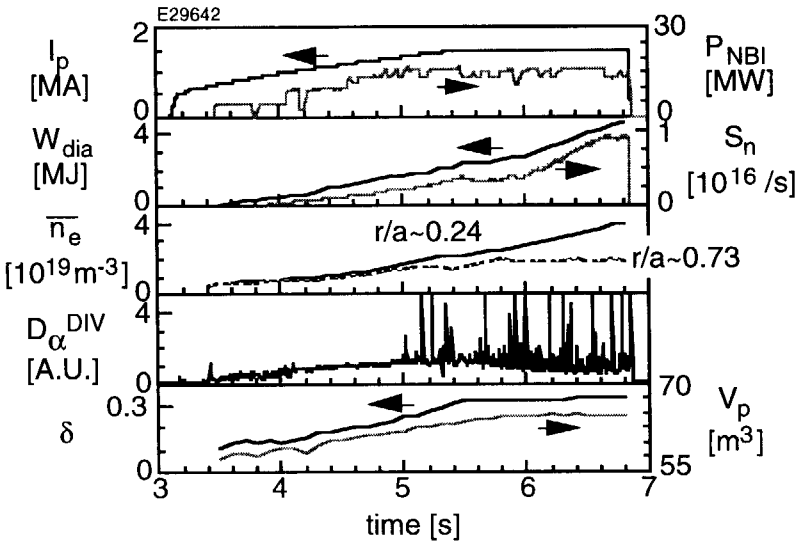

Fig. 1. Waveforms of a reversed shear discharge with an ELMy H-mode edge in a high triangularity (δ~0.3) configuration.

3. Stability and confinement in reversed shear plasmas with an H-mode edge

In Fig. 2, beta limits in H-mode edge discharges and those in L-mode edge discharges are compared. The stability in the low-q_{min} region was successfully improved in the H-mode edge discharges, and a lower-q_{min} region of $q_{min} < 1.7$ became accessible. As a result, a high β_N value of 2.3 has been achieved at $q_{min} = 1.5$. On the other hand, the confinement in H-mode

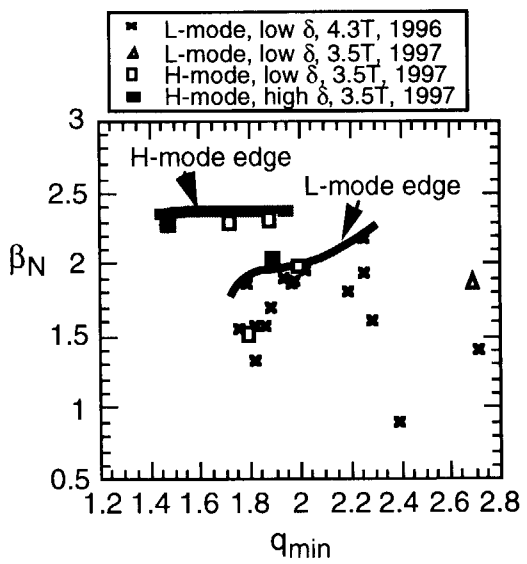

Fig. 2. Normalized beta β_N at a collapse against q_{min}. The operational beta limits for H-mode edge and L-mode edge discharges are shown by solid curves.

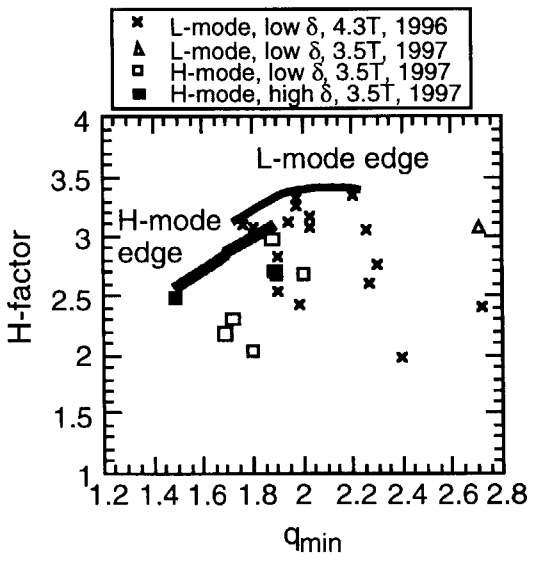

Fig. 3. H-factors against q_{min}. The H-factors in H-mode edge plasmas are not higher than those in L-mode edge plasmas.

edge plasmas was not better than that in L-mode edge plasmas as shown in Fig. 3. This is due to smaller ITB radius in H-mode edge plasmas. The ion temperature profile in an H-mode edge plasma is shown in Fig. 4. The radius of ITB is about 0.5a (a is the plasma minor radius). In L-mode edge plasmas, the ITB radius of up to 0.7a was obtained and higher confinement was achieved with a larger ITB radius [1]. The smaller ITB radius cancels the benefits of H-mode. The smaller ITB radius in H-mode edge plasmas is related to smaller negative shear region in these plasmas, which appeared to be caused by lower beam power during current ramp-up. In Fig. 5, trajectories of (ρ_{qmin}, q_{min}) are shown. In L-mode edge plasmas, high beam power was injected during current ramp, which kept the radius of q_{min} around 0.7 while q_{min} continued to decrease, and large ρ_{qmin} of 0.7 was achieved in a low-q_{min} region of q_{min}~2. In H-mode edge plasmas, the beam power during current ramp was reduced as mentioned in section 2, which resulted in lower electron temperatures and faster current penetration. Though the radius of q_{min} was nearly equal to that in L-mode edge plasmas when q_{min} was around 4, ρ_{qmin} continued to decrease during the current ramp-up and reached about 0.5a when q_{min} became 2. High heating power during the current ramp appears to be necessary to create a large negative shear region.

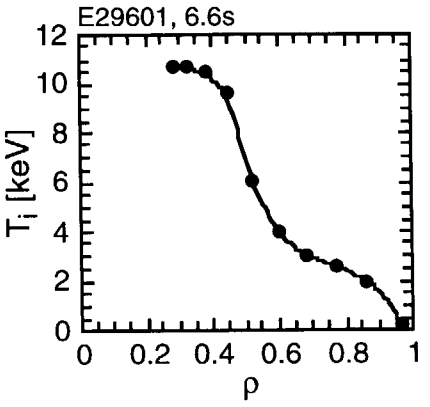

Fig. 4. T_i profile in an H-mode edge reversed shear discharge (δ = 0.3).

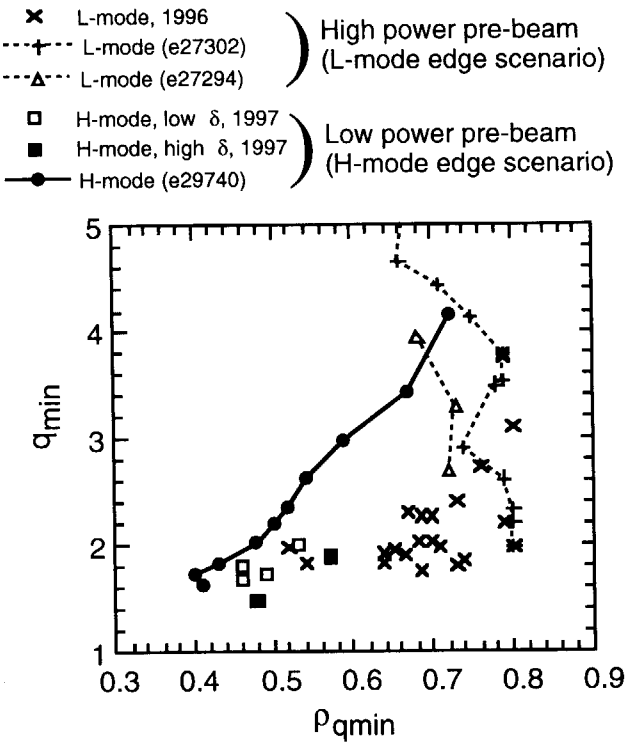

Fig. 5. (r_{qmin}, q_{min}) for high power pre-beam (crosses, plus sign and open triangles) and for low power pre-beam (open rectangular, closed rectangular and closed circles).

4. Sustainment of improved confinement

Avoidance of beta collapse and quasi-steady sustainment of improved confinement were attained in reversed shear discharges with an ELMy H-mode edge by using power step-down. An example is shown in Fig. 6. An H-factor of 1.8-2.5 and β_N of 1.5-1.8 were sustained for 1.5 s (4-5 times τ_E) in a discharge with high triangularity (B_t = 3.5 T, I_p = 1.5 MA, q_{95} = 4.5, δ ~ 0.28). The ITB was established and developed sufficiently by the high power heating before 6 s, as indicated by the rise of density along the central (r/a ~ 0.17) chord, and the beam

power was stepped down. As a result, the stored energy remained constant while q_{min} continued to decrease. The reversed shear configuration and the ITB were sustained until the end of beam heating. Long sustainment, reaching 4.3 s, of improved confinement with an H-factor ~ 1.7 and β_N ~ 1.5 was also demonstrated using feedback control of the beam power to maintain a fixed neutron emission rate.

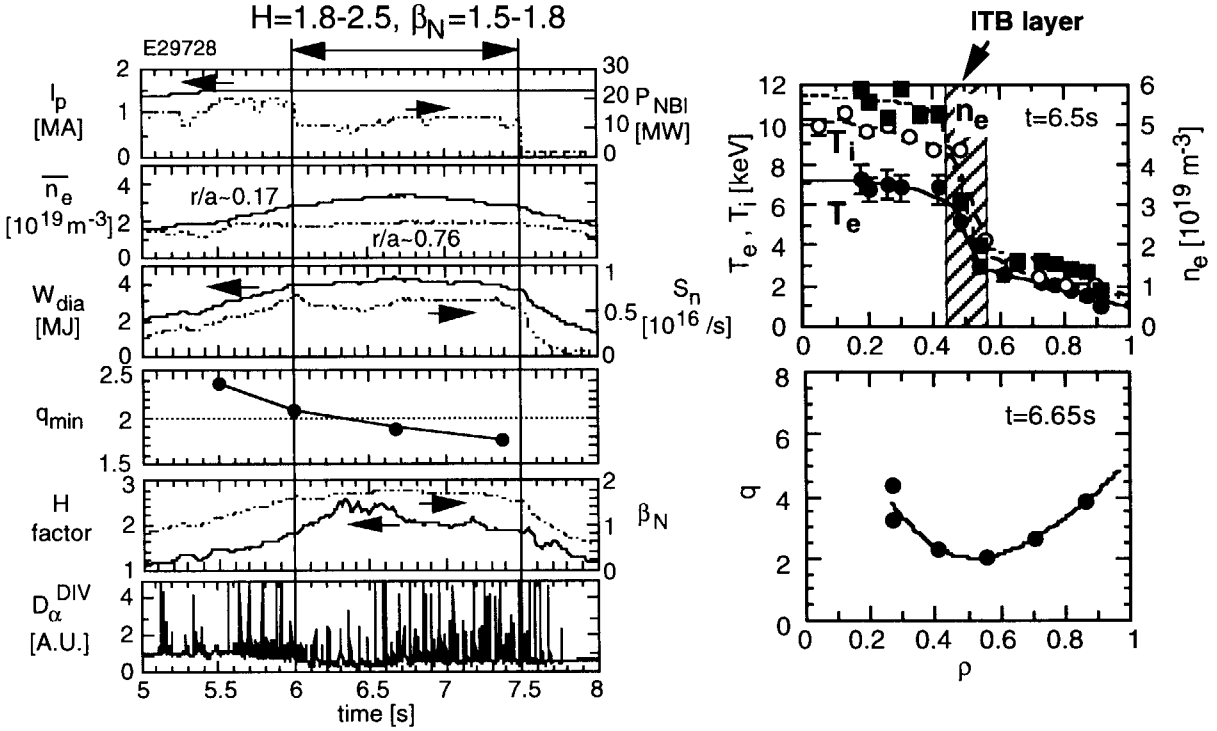

Fig. 6. Waveforms and profiles of a reversed shear discharge with an ELMy H-mode edge where an H-factor of 1.8-2.5 and β_N of 1.5-1.8 were sustained for 1.5 s.

References

1) Fujita, T., et al., Nucl. Fusion **38** (1998) 207.

2) Ishida, S., et al., Phys. Rev. Lett. **79** (1997) 3917.

3) Ishida, S., et al., in Proc. 24th Eur. Conf. on CFPP, Berchtesgaden, 1997, Vol. 21A, Part II, 489.

4) Ozeki, T., et al., Plasma Phys. Control. Fusion **39** (1997) A371.

3.4 Study of Internal Transport Barriers by Comparison of Reversed Shear and High-β_p Discharges in JT-60U

Y. Koide, M. Mori, T. Fujita, H. Shirai, T. Hatae, T. Takizuka, H. Kimura, T. Oikawa, N. Isei, A. Isayama, S. Takeji, Y. Kawano, A. Sakasai, Y. Kamada, T. Fukuda and S. Ishida

1. Introduction

One of the candidates for advanced tokamak scenario is reversed shear operation[1, 2]. This regime is characterized by a region where the magnetic shear, s=(r/q)dq/dr, is negative in the core region. Here, q is the safety factor and r is the minor radius. The improved core confinement with good bootstrap-current alignment and high β is believed to be promising for achievement of steady-state reactor conditions[3]. Equivalent Q_{DT} of 1.05 has been transiently achieved in JT-60U in reversed shear plasmas[4]. The large effective confinement volume with the reduction in the electron thermal diffusivity χ_e [5] suggests that the reversed shear operation is promising for burning plasmas.

The present approach to address the physical reason for the χ_e reduction is to compare results with those in high-β_p mode[6], where no clear ∇T_e with spatial localization was observed.

The present paper deals with the comparison of internal transport barrier (ITB) between reversed shear and high-β_p discharges. The effect of safety factor profile on the χ_e reduction, and radial location of ITB are discussed. Reversed shear plasmas in electron heating regime is also discussed.

2. ITB location and effect of q profile

Profiles are compared between reversed shear (Figs. 1(a-c)) and high β_p (Figs. 1(d-f) discharges. These discharges had similar conditions of I_p=2.3-2.2MA, B_t =4.3-4.4T, R/a=3.1/0.74-3.1/0.72 and q_{95}=3.7-3.3. Heating power and line average electron density were different between them: P_{NB}=13MW and $\bar{n}_e(0.5a)=3\times10^{19}$ m^{-3} for the reversed shear case; P_{NB}=30MW and $\bar{n}_e(0.5a)=1\times10^{19}$ m^{-3} for the high β_p case. Reversed shear (Fig. 1(c)) was produced using an early neutral beam injection in the initial current ramp[7]; scenario of high β_p discharge is to apply high heating power into sawtooth-free target plasmas with low n_e and relatively high internal inductance (l_i ~1.1),[8] which leads to monotonic q(r)[9] (Fig. 1(e)) or positive magnetic shear (Fig. 1(f)).

One of the most dramatic differences is the steep and localized ∇T_e observed in the reversed shear case, where power balance analysis for a similar discharge showed a reduction in χ_e by a factor of 20.[5] Since such clear χ_e reduction is only observed in strong negative shear discharges in JT-60U to date, we consider that s<0 may be one of important factors for the reduced χ_e. It should be pointed out that negative shear is not a sufficient condition for the electron thermal barrier formation. This is because there is a heating power below which the χ_e reduction is not observed. The threshold power for the ITB formation will be discussed in a separate paper. If we consider the reduced transport rates in terms of the turbulence suppression, responsible turbulence should be considered separately for ion and electron systems. This is because the reduction in χ_e is not so clear while χ_i is reduced significantly in high β_p mode.[10]

The location of ITB is important from the viewpoint of confinement improvement because it provides the boundary of the effective confinement volume. Vertical thick lines in Fig. 1 show locations of "ITB foot" from T_i profile ($\equiv \rho_{Ti}$), which is defined as radial location of d^2T/dr^2 maximum. Magnetic shear at the positions for these particular discharges is s~-1 (reversed shear case) and s~1 (high β_p case), respectively.

Figure 1(g) shows evolution of ρ_{Ti} in the reversed shear discharge, together with the positions of q_{min} ($\equiv \rho_{q_{min}}$; a thin solid line) and integer-q rational surfaces (dotted lines). Here q_{min} was decreased in time monotonically from 5 (t=4 s) to 2 (t=7 s).[11] An outward propagation of ρ_{Ti}=0.5 →0.8 (t=4-5.2 s) and the subsequent localization of $\rho_{Ti} \leq \rho_{q_{min}}$ ($t \geq$ 5.2 s) were observed. The profiles shown in Fig. 1(a)-(c) are at t=6.6 s i.e. in the stagnation phase. ρ_{Te}(triangles) and ρ_{ne} (a closed circle), which are defined in the same way from profiles of T_e and n_e, respectively, were found to be at the similar location to ρ_{Ti}.

The ρ_{Te} in high β_p mode, even without $\rho_{q_{min}}$ except on axis, also sometimes propagates outwards[12] and, however, stagnates at regions of s>0 as shown in Fig. 1(d)-(f). We consider that the propagation and the stagnation are governed by a kind of balance between driving and suppression factors for the ITB formation as has been discussed in Ref. 13. We first investigated the threshold heating power P_{th} for the ITB formation in the high β_p case in order to understand the balance. We found that higher heating power into the central region (with no net external momentum input) triggered the ITB formation, while no ITB was observed with lower central power deposition with a fixed total heating power;[14] P_{th} increased faster than linearly with n_e.[12] These results qualitatively supports the hypothesis of turbulence suppression by $E \times B$ shear as discussed in Ref. 15, considering that radial electric field E_r, which increases with pressure gradient, contributes to $E \times B$ shear and that E_r decreases with n_e. Study of P_{th} for the reversed shear case is now in progress, preliminary results of which suggest no strong n_e dependence of P_{th}, which is in contrast to the high β_p case.

On suppression factors for ITB, s≤0 seems to have effect to stagnate the ITB location in JT-60U reversed shear discharges. However, the stagnation of ρ_{Ti} suggests the existence of other suppression factors than s≤0 because s at ρ_{Ti} is positive in typical high β_p discharges (This feature is similar to TFTR discharges, where ρ_{Ti} extends beyond the reversed shear radius in TFTR reversed shear discharges.[1]).

3. Reversed shear discharges in electron heating regime

ITB discussed in the previous sections was produced by neutral beam injection (80keV beams into plasmas of T_e=8keV), where ion heating was predominant (~80%). We have just started to investigate ITB characteristics in electron heating regime without central particle fueling by using ICRF.[16] Information of this type is essential to predict ITB performance in burning plasmas, which is mainly heated by α particles.

Evolution of the discharge is shown in Fig. 2(a) (I_p=2MA, B_t=3.3T, q_{95}=3.8, H beams into H-He plasmas). NB power was reduced from 8.5MW to 1.5MW at t=5.8 s, which was followed by an ICRF injection (4.5MW) during t=6-7.5 s. Passive charge exchange analyzer detected particle flux with high energy tail, the fraction of which monotonically increased up to ~1 MeV through the IC injection. This is one of items of evidence of the production of electron heating source.

It should be noted that T_e(0.2) rapidly increased after the start of ICRF injection

while $T_e(0.4)$ decreased, suggesting the reduction of χ_e at $\rho \leq 0.4$; and that the slight increase in ∇T_e at $\rho \sim 0.35$ (a vertical thick line in Fig. 2(b)) was sustained even after the reversed shear profile was relaxing with time ($s=-0.8 \rightarrow -0.3$) (Fig. 2(c)).

In a reference discharge, where the IC power was replaced by the same amount of beam power, ∇n_e was locally increased inside the ITB at $\rho=0.4$ (closed circles in Fig. 2(d)). In contrast to this, n_e profile during ICRF, where there was little particle source in the core (only from diagnostic beams), showed gentle ∇n_e (open circles in Fig. 2(d)). This result suggests that steep ∇n_e seems not to be essential for the ITB formation.

4. Summary

ITB in reversed shear and high β_p discharges were compared, and data has been accumulated for the understanding the ITB formation with χ_e reduction. Reduction in χ_e was significant in strongly reversed shear discharges. Radial location of ITB propagated outwards and then localized near or just inside the $\rho_{q_{min}}$ both for the ion and electron channels. Reduction in χ_e was also observed when electron heating by ICRF was applied, where steep ∇n_e seems not to be essential for the ITB formation.

References

1) F.M. Levinton et al., Phys. Rev. Lett. **75**, 4417 (1995).
2) E.J. Strait et al., Phys. Rev. Lett. **75**, 4421 (1995).
3) T. Ozeki et al., Plasma Phys. and Control. Nucl. Fusion Research 1992 (IAEA, Vienna, 1993), Vol. 2, 187.
4) S. Ishida et al., to appear in Phys. Rev. Lett..
5) T. Fujita et al., Phys. Rev. Lett. **78**, 2377 (1997).
6) Y. Koide et al., Phys. Rev. Lett. **72**, 3662 (1994).
7) T. Fujita et al., Proc. 16th IAEA Fusion Energy Conference, Montreal, 1996, IAEA-CN-64/A1-4 (IAEA, Vienna).
8) S. Ishida et al., Plasma Phys. and Control. Nucl. Fusion Research 1992 (IAEA, Vienna, 1993), Vol. 1, 219.
9) Y. Koide and JT-60 Team, Phys. Plasmas **4**, 1623 (1997).
10) H. Shirai et al., Plasma Phys. and Control. Nucl. Fusion Research 1994 (IAEA, Vienna, 1995), Vol. 1, 355.
11) T. Fujita et al., submitted to Nucl. Fusion.
12) Y. Koide et al., Plasma Phys. Control. Fusion **38**, 1011 (1996).
13) P.H. Diamond et al., Phys. Rev. Lett. **78**, 1472 (1997).
14) Y. Koide et al., Plasma Phys. and Control. Nucl. Fusion Research 1994 (IAEA, Vienna, 1995), Vol. 1, 199.
15) K.H. Burrell, Phys. Plasmas **4**, 1499 (1997).
16) K. Ushigusa et al., Proc. 12th topical conf. on RF Power in Plasmas, Savannah (1997).

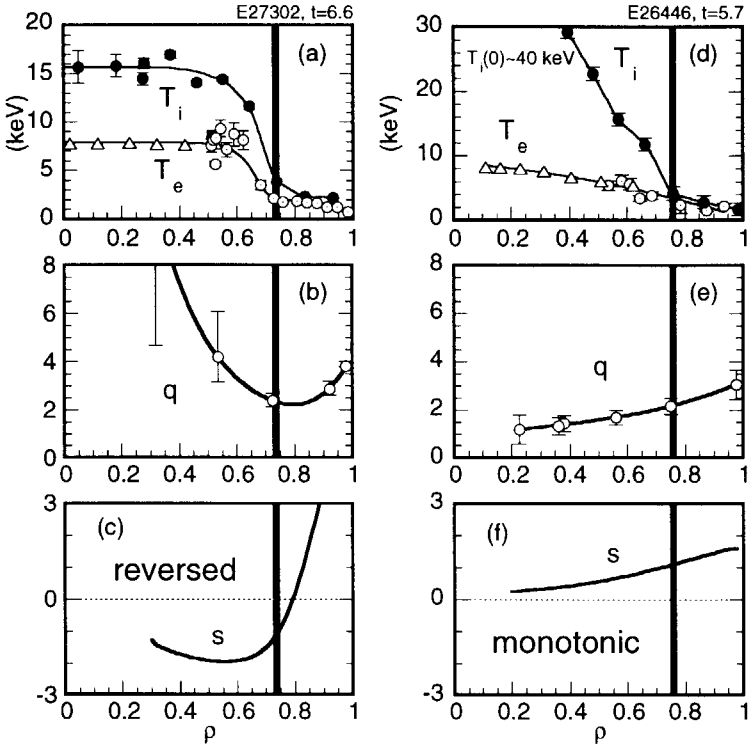

Fig. 1 Profiles of reversed shear discharge and high β_p discharge. (a, d) Ion and electron temperatures, (b, e) safety factor and (c, f) magnetic shear. These plasmas have similar I_p, B_t, R, a and q_{95} while they have different n_e and P_{NB}. (g) Evolution of locations of q_{min} (a thin solid line), integer-q (dotted lines) for the reversed shear discharge. Characteristic ITB radius deduced from $T_i(r)$ is shown with a thick solid line; open triangles from $T_e(r)$; and a closed circle from $n_e(r)$.

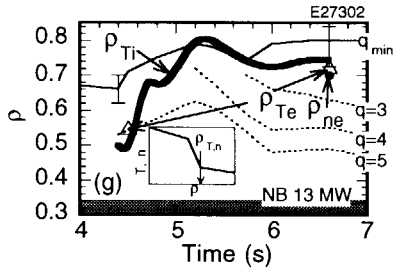

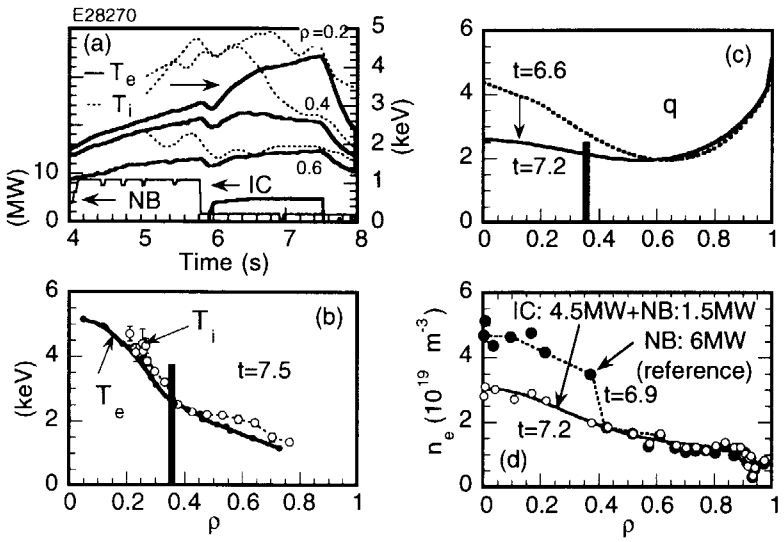

Fig. 2 (a) Evolution of T_e (solid lines) and T_i (dotted lines), together with the heating powers from NBI and ICRF. (b) Temperature profiles at t=7.5 s. (c) q profile at t=6.6 and 7.2 s. (d) Electron density profiles, where reference profile with NB only is shown with closed circles.

3.5 Particle transport analysis of ICRF heated plasmas during reversed shear experiments in JT-60U

M. Iwase, Y. Koide, K. Tobita, S. Moriyama, Y. Kusama, H. Takenaga, H. Shirai, M. Nemoto, A. Morioka, T. Fujita, Y. Kamada, T. Oikawa, G. J. Kramer

1 Introduction

Plasma performance has been progressively enhanced with the reversed magnetic shear (RS) configuration in JT-60U, reaching Q_{DT}^{eq}=1.05. To verify the validity of RS operations in a future tokamak reactor where particle fueling into the central region is difficult and α particle heating is dominant, ICRF minority heating which fuels no particles was applied to RS plasmas[1]. In order to study the behaviors of RS plasmas on the reduced particle fueling, NBI heating power (P_{NB}) was scanned. The particle confinement time (τ_p) and the effective particle diffusivity (D_{eff}) at an ITB were derived from global particle balance inside the ITB.

2 Method of analysis

The particle transport analysis is done only for the inside of ITB. The definitions of variables in the analysis are illustrated in Fig.1. In this situation, only the particle source (S_{NB}) by NBI heating is taken into account because the particle source by the recycling from the first wall is negligible. The total number of electrons and the volume integrated particle source inside the ITB are denoted by N_e and S, respectively. These values are expressed as follows;

$$N_e = \int n_e dV, \qquad S = \int S_{NB} dV, \tag{1}$$

where V is the plasma volume inside the ITB. The equation of global particle confinement is described with N_e, S and τ_p as follows;

$$\frac{\partial N_e}{\partial t} = -\frac{N_e}{\tau_p} + S. \tag{2}$$

From this equation, τ_p is written as follows;

$$\tau_{\rm p} = \frac{N_{\rm e}}{S - \frac{\partial N_{\rm e}}{\partial t}}. \tag{3}$$

Neglecting the convective term, we can obtain the following equation.

$$S - \frac{\partial N_{\rm e}}{\partial t} = A\Gamma = -AD_{\rm eff}\nabla n_{\rm e} \tag{4}$$

$$D_{\rm eff} = \frac{S - \frac{\partial N_{\rm e}}{\partial t}}{-A\nabla n_{\rm e}}. \tag{5}$$

Here, Γ and $D_{\rm eff}$ are the particle flux and the effective particle diffusivity at the ITB. The surface area at the ITB is denoted as A.

3 Analyzed results

The second harmonic ICRF minority heating was applied to the RS plasmas consist of hydrogen and helium 4. The power scan of NBI heating is done shot by shot as showin in Fig.2. $I_{\rm p}$ and $B_{\rm t}$ are 2.0 MA and 3.5 T, respectively.

The typical profiles of the electron density ($n_{\rm e}$) analyzed here are shown in Fig.3. For the integration in eq.(1), the measured $n_{\rm e}$ profile is fitted with a continuous function. The open circles show the case of NBI heating only at 6.0 MW. The circles show the case where $P_{\rm NB}$ of 2.0 MW and $P_{\rm IC}$ of 4.0 MW are injected. In both cases, the configuration of the plasmas are almost the same. The radial profile of $S_{\rm NB}$ calculated with an OFMC code is shown in Fig.4.

Fig.5 shows $\tau_{\rm p}$ at the ITB as a function of $S_{\rm NB}$. Even in the case where $S_{\rm NB}$ is considerably small, no degradation of $\tau_{\rm p}$ is seen. The dependence of $D_{\rm eff}$ on $S_{\rm NB}$ at the ITB is depicted in Fig.6. It seems that $D_{\rm eff}$ is independent of $S_{\rm NB}$.

4 Summary

The particle transport analysis was done for ICRF heating experiments with the view of studying the particle fueling effect on the sustainment of ITB in RS plasmas. The central particle source by NBI heating was scanned from $7\times10^{19}{\rm s}^{-1}$ to $22\times10^{19}{\rm s}^{-1}$. The analyzed values of $\tau_{\rm p}$ at the ITB were of the order of 1 s, and there is no degradation

of τ_p during the particle source scan. D_{eff} at the ITB, neglecting the convective term, was calculated. The value of D_{eff} was of the order of 0.01∼0.1 m^2/s. Due to the limited amount of data we were not able to study the dependence of D_{eff} on the central particle fueling.

The duration and the power of ICRF heating in the present situation is limited to 4∼5 MW. In order to verify the sustainment of the ITB with only ICRF heating, the high power ICRF experiment is essential to understand the detailed relation between the central particle fueling and the sustainment of ITB in a steady-state tokamak reactor.

References

1) Kimura H. et al., Plasma Phys. Contrl. Nucl. Fusion Research (Proc. 16th IAEA Fusion Energy Conf., Montréal, 1996), paper F1-CN-64/E-6.

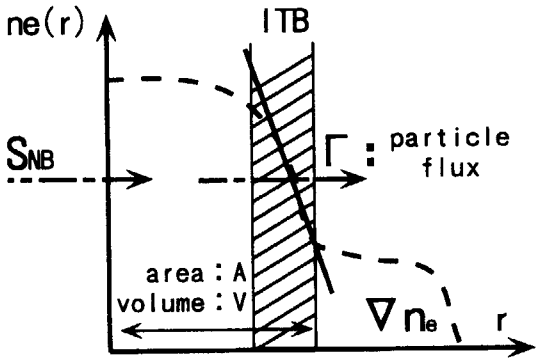

Fig.1 Method of analysis. The dashed curve shows the fitted n_e profile. ∇n_e at ITB isderived from experimental data to deduce D_{eff}.

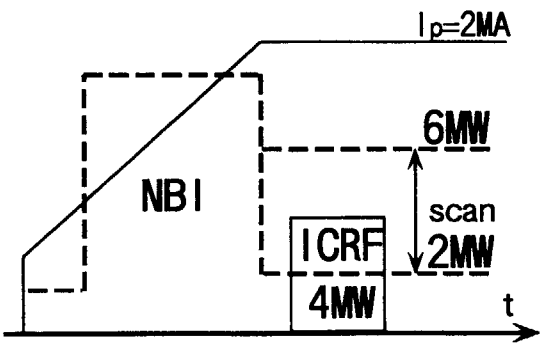

Fig.2 Schematic drawing of P_{NB} scan experiment. P_{NB} during ICRF heating is changed shot by shot.

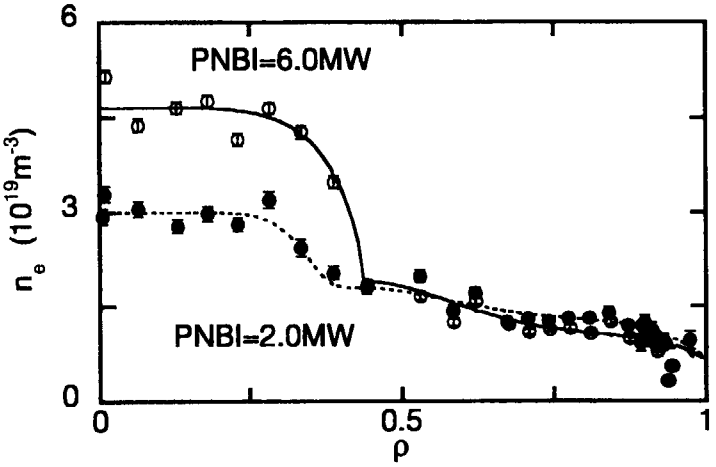

Fig.3 Electron density profile used in the analysis. The solid curve with open circles show the case where only P_{NB} of 6.0MW is injected. The dashed curve with closed circles show the case where P_{NB} of 2.0MW and P_{IC} of 4.0MW are injected. In both case, the configurations of the plasmas are almost the same.

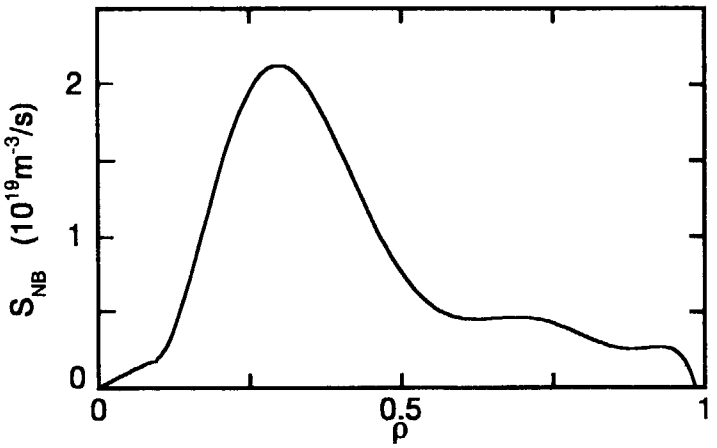

Fig.4 Radial profile of particle source by NBI heating.

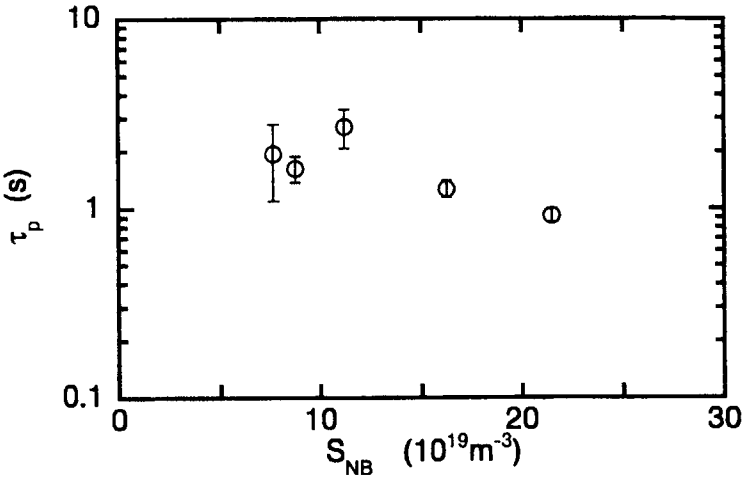

Fig.5 Particle confinement time τ_p at ITB. The error bars reflect miscalculations in the time derivative of n_e.

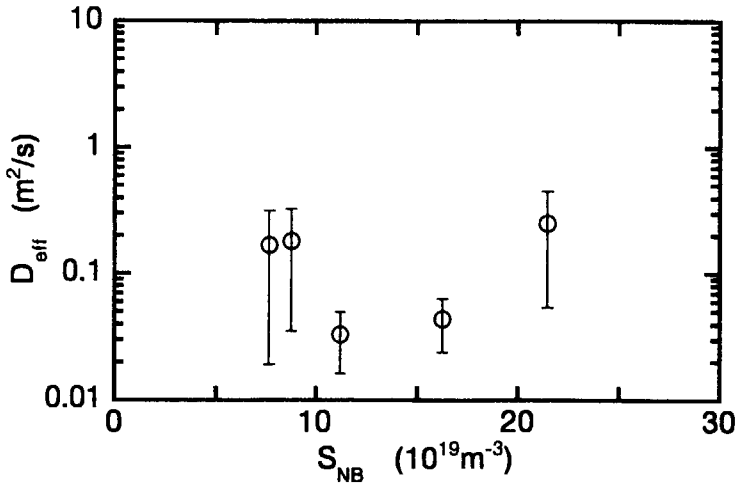

Fig.6 Effective particle diffusivity D_{eff} at ITB. The error bars reflect miscalculation in the calculation of ∇n_e.

3.6 Effect of Impurity on Neoclassical Ion Thermal Diffusivity

M. Kikuchi, H. Shirai, H. Itakura*, M. Azumi

1 Introduction

Recent progress of reversed shear experiments shows significant reduction in ion thermal diffusivity close to the neoclassical value in the negative shear region.

Although the neoclassical transport theories are well-developed [1, 2],we do not have an accurate formula for ion thermal diffusivity valid for arbitrary shape, aspect ratio and impurity content. So far, approximate ion thermal diffusivity given by Chang-Hinton [4] has been used. But, their formula was constructed empirically to match the Hinton-Hazeltine formula valid at high aspect ratio without impurity [1] and Hazeltine-Hinton-Rosenbluth result at unit aspect ratio without impurity [6]. The impurity effect was incorporated similarly based on Hirshman's result [5] at high aspect ratio and inclusion of impurity effect on energy scattering at unit aspect ratio.

In this paper, we have applied the so called **Matrix Inversion Method (MI method** developed for the bootstrap current [7, 8, 3] to calculate the neoclassical ion thermal diffusivity. And this value was compared with Chang-Hinton value for typical JT-60U experiments. Details of the theoretical background will be described elsewhere.

2 Chang-Hinton Neoclassical Ion Thermal Diffusivity

The ion thermal diffusivity by Chang-Hinton [4] is expressed as,

$$\chi_i^{CH} = \sqrt{\epsilon}\hat{\rho}_{pi}^2 \nu_{ii}^{CH} \hat{K}_{2CH}, \hat{K}_{2CH} = \hat{K}_{2CH}^{PS} + \hat{K}_{2CH}^{BP} \tag{1}$$

$$\nu_{ii}^{CH} = \frac{4\sqrt{\pi} n_i e_i^4 \ln\Lambda}{3\sqrt{m_i} T_i^{1.5}}, \hat{K}_{2CH}^{PS} = \frac{1.169\mu_{*i}\epsilon^{1.5} H_p F}{(1+0.74\mu_{*i}\epsilon^{1.5})}, \hat{K}_{2CH}^{BP} = \frac{\overline{K}_2}{(1+1.03\mu_{*i}^{0.5}+0.31\mu_{*i})} \tag{2}$$

$$\epsilon = r/R, \hat{\rho}_{pi} = \frac{m_i V_{Ti}}{e_i B_{p1}}, V_{Ti} = \sqrt{\frac{2T_i}{m_i}}, B_{p1}^2 = \frac{B_0^2 < R^2 B_p^2 >}{I^2}, F = \frac{1}{2\sqrt{\epsilon}} (< \frac{B_0^2}{B^2} > - \frac{B_0^2}{< B^2 >}) \tag{3}$$

$$H_p = \frac{1+1.33\alpha(1+0.6\alpha)}{1+1.79\alpha}, \overline{K}_2 = (0.66(1+1.54\alpha) + (1.88\sqrt{\epsilon} - 1.54\epsilon)(1+3.75\alpha)) < \frac{B_0^2}{B^2} > \tag{4}$$

$$\mu_{*i} = \nu_{*i}(1+1.54\alpha), \alpha = \frac{Z_I^2 n_I}{Z_i^2 n_i}, < A >= \oint \frac{A dl_p}{B_p} / \oint \frac{dl_p}{B_p} \tag{5}$$

3 Neoclassical Ion Thermal Diffusivity by MI Method

An exact expression of the thermal diffusivity for plasma species a can be obtained using the normalized parallel friction coefficient $\hat{l}_{ij}^{ab}$ and the normalized viscosity coefficient $\hat{\mu}_{ia}$ as follows,

$$\chi_a^{NC} = \sqrt{\epsilon}\hat{\rho}_{pa}^2 \nu_{aa} \hat{K}_{2a}, \hat{K}_{2a} = \hat{K}_{2a}^{CPS} + \hat{K}_{2a}^{BP} \tag{6}$$

where CPS and BP are abbreviations for classical+Pfirsh-Schlüter and Banana-Plateau transport coefficients, respectively.

$$\hat{K}_{2a}^{CPS} = \frac{B_0^2(\hat{l}_{21}^{aa} - \hat{l}_{22}^{aa})}{2\sqrt{\epsilon} < B^2 >}(\frac{< R^2 >< B^2 >}{I^2} - 1) \tag{7}$$

$$\hat{K}_{2a}^{BP} = \frac{B_0^2(\hat{\mu}_{3a}(1 - \alpha_{a+3,a} + \alpha_{a+3,a+3}) - \hat{\mu}_{2a}(1 + \alpha_{aa} - \alpha_{a,a+3}))}{2\sqrt{\epsilon} < B^2 >} \tag{8}$$

$$\alpha_{ij} = [(\hat{L} - \hat{M})^{-1}\hat{M}]_{ij}, \nu_{aa} = \frac{4\sqrt{2\pi}n_a e_a^4 \ln\Lambda}{3\sqrt{m_a}T_a^{1.5}} \tag{9}$$

where $\hat{L}$ and $\hat{M}$ are normalized friction and viscous matrixes, respectively.

$$\hat{L} = \begin{bmatrix} \hat{l}_{11}^{ee} & \hat{l}_{11}^{ei} & \hat{l}_{11}^{eI} & \hat{l}_{12}^{ee} & \hat{l}_{12}^{ei} & \hat{l}_{12}^{eI} \\ \hat{l}_{11}^{ie} & \hat{l}_{11}^{ii} & \hat{l}_{11}^{iI} & \hat{l}_{12}^{ie} & \hat{l}_{12}^{ii} & \hat{l}_{12}^{iI} \\ \hat{l}_{11}^{Ie} & \hat{l}_{11}^{Ii} & \hat{l}_{11}^{II} & \hat{l}_{12}^{Ie} & \hat{l}_{12}^{Ii} & \hat{l}_{12}^{II} \\ \hat{l}_{21}^{ee} & \hat{l}_{21}^{ei} & \hat{l}_{21}^{eI} & \hat{l}_{22}^{ee} & \hat{l}_{22}^{ei} & \hat{l}_{22}^{eI} \\ \hat{l}_{21}^{ie} & \hat{l}_{21}^{ii} & \hat{l}_{21}^{iI} & \hat{l}_{22}^{ie} & \hat{l}_{22}^{ii} & \hat{l}_{22}^{iI} \\ \hat{l}_{21}^{Ie} & \hat{l}_{21}^{Ii} & \hat{l}_{21}^{II} & \hat{l}_{22}^{Ie} & \hat{l}_{22}^{Ii} & \hat{l}_{22}^{II} \end{bmatrix}, \hat{M} = \begin{bmatrix} \hat{\mu}_{1e} & 0 & 0 & \hat{\mu}_{2e} & 0 & 0 \\ 0 & \hat{\mu}_{1i} & 0 & 0 & \hat{\mu}_{2i} & 0 \\ 0 & 0 & \hat{\mu}_{1I} & 0 & 0 & \hat{\mu}_{2I} \\ \hat{\mu}_{2e} & 0 & 0 & \hat{\mu}_{3e} & 0 & 0 \\ 0 & \hat{\mu}_{2i} & 0 & 0 & \hat{\mu}_{3i} & 0 \\ 0 & 0 & \hat{\mu}_{2I} & 0 & 0 & \hat{\mu}_{3I} \end{bmatrix} \tag{10}$$

where,

$$\hat{\mu}_{1a} = \frac{f_t}{f_c}\{\nu_a^{tot}(v)\tau_{aa}\}, \hat{\mu}_{2a} = \frac{f_t}{f_c}\{(2.5 - x_a^2)\nu_a^{tot}(v)\tau_{aa}\}, \hat{\mu}_{3a} = \frac{f_t}{f_c}\{(x_a^4 - 5x_a^2 + 6.25)\nu_a^{tot}(v)\tau_{aa}\} \tag{11}$$

$$f_c = \frac{3 < B^2 >}{4}\int_0^{1/Bmax} \frac{\lambda d\lambda}{< \sqrt{1 - \lambda B} >}, f_t = 1 - f_c, \{A\} = \frac{8}{3\sqrt{\pi}}\int_0^{\infty} e^{-x^2}x^4 A(xv_{Ta})dx \tag{12}$$

$$\nu_{tot}^a(v)\tau_{aa} = \frac{\nu_D^a \tau_{aa}}{(1 + 2.48\nu_a^* \nu_D^a \tau_{aa}/x_a)(1 + 5\pi\nu_T^a(v)/8x_a\omega_{Ta})} \tag{13}$$

$$\nu_D^a(v)\tau_{aa} = \sum_b \frac{3\sqrt{\pi}}{4}\frac{n_b Z_b^2}{n_a Z_a^2}\frac{\Phi(x_b) - G(x_b)}{x_a^3} \tag{14}$$

$$\Phi(x_b) = \frac{2}{\sqrt{\pi}}\int_0^{xb} e^{-t^2}dt, G(x_b) = \frac{\Phi(x_b) - x_b\Phi'(x_b)}{2x_b^2} \tag{15}$$

$$\hat{l}_{ij}^{ab} = \sum_k \frac{n_k Z_k^2}{n_a Z_a^2}M_{ak}^{i-1,j-1}\delta_{ab} + \frac{n_b Z_b^2}{n_a Z_a^2}N_{ab}^{i-1,j-1} \tag{16}$$

where $M_{ab}^{i,j}$ and $N_{ab}^{i,j}$ are given in Eq. (4.11-17) of reference [2]. And δ_{ab} is Cronecker's delta function.

When the $T_i = T_I$, the total ion thermal diffusivity is defined as,

$$\begin{aligned} \chi_i^{tot} &= \frac{< (\vec{q}_i + \vec{q}_I)\nabla\rho >}{-(n_i + n_I) < \mid \nabla\rho \mid^2 > \partial T_i/\partial\rho} \\ &= \frac{n_i}{(n_i + n_I)}\chi_i^{NC} + \frac{n_I}{(n_i + n_I)}\chi_I^{NC} \\ &= \sqrt{\epsilon}\hat{\rho}_{pi}^2\nu_{ii}[f_i\hat{K}_{2i} + (1 - f_i)\alpha\sqrt{\frac{A_I}{A_I}}\hat{K}_{2I}] \end{aligned} \tag{17}$$

Heat flux through impurity channel $\vec{q}_I$ can be larger than that of ion channel by a factor of $\alpha\sqrt{A_I/A_i}$ which can be 5-10 for $Z_{eff} = 2 - 3$ if both ion and impurity are deeply collisionless. However, impurity collisionality ν_{*I} is O(1) while ion is deeply collisionless ($\nu_{*i} \ll 1$) for typical high β_p and reversed shear regime in JT-60U. Therefore we can neglect ion thermal conduction through impurity channel.

4 Comparison of MI Method against other theories

Comparison of MI method with other theories are made. Figure 1 shows ϵ dependence of $\hat{K}_{2CH}$, $\sqrt{2}\hat{K}_{2i}$ and $\sqrt{2}\hat{K}_{2i}^{HS}$ derived from eq.(7.53) of [2] for electron-ion plasma in collisionless regime. Three formula agrees each other at $\epsilon = 0$ limit ($K_2 = 0.66$ as given by Hinton-Hazeltine [1]). But MI method gives slightly higher value at $\epsilon = 1$ limit, similar to Bolton-Ware results given in [9]. This is due to the finite contribution of electron-ion collision term (M_{ie}^{11}) to the normalized friction coefficient $\hat{l}_{22}^{ii}$. This term is usually neglected in [6, 9].

Effect of impurity on ion thermal diffusivity is analyzed with MI method and compared with Chang-Hinton formula. Figure 2 shows the ϵ dependence of $\hat{K}_{2CH}$ and $\sqrt{2}\hat{K}_{2i}$ for collisionless plasma $\nu_{*i} = 10^{-4}(\nu_{I*} = \dfrac{Z_{eff} - Z_i}{Z_I - Z_{eff}} \dfrac{Z_I^3}{Z_i^3}\nu_{*i})$ with $Z_{eff} = 3.0$ (impurity species is assumed to be Carbon). Two results agree at infinite aspect ratio end ($\epsilon = 0$). But they have a large difference at other aspect ratio. The reason for this difference is the simpler treatment of the impurity effect in [4]. For $\epsilon = 1$ plasma, for example, neoclassical ion thermal diffusivity is dominated by the Pfirsh-Schlüter transport (whole particles are trapped and there is no Banana-Plateau transport). The Pfirsh-Schlüter transport consists of ion-electron collsion, ion-ion collision and ion-impurity collision, as given in eq. (16). Although the ion-impurity pitch-angle scattering plays a dominant role in effect of impurity on ion thermal diffusivity as discussed by Chang [4], there are significant contribution from other terms (including correction to large impurity mass limit).

Finally neoclassical ion thermal diffusivity is calculated for typical JT-60 plasma parameter of SN=E29854 as shown in Fig.3. The neoclassical ion termal diffisivity from Chang-Hinton formula is two times larger than that from MI method as expected from above discussion.

References

[1] F.L.Hinton and R.D. Hazeltine, Reviews of Modern Physics Vol.48 (1976)239.

[2] S.P. Hirshman, D.J. Sigmar, Nuclear Fusion 21(1981)1079.

[3] M. Kikuchi, M. Azumi, Plasma Physics and Controlled Fusion 37(1995)1215.

[4] C.S. Chang, F.L.Hinton, Physics of Fluids 29(1986)3314.

[5] S.P. Hirshman, Physics of Fluids 19(1976)155.

[6] R.D. Hazeltine, F.L. Hinton, M.N. Rosenbluth, Physics of Fluids 16(1973)1645.

[7] M. Kikuchi, M. Azumi, et al., Nuclear Fusion 30(1990)343.

[8] K. Tani, M. Azumi, R.S. Devoto, Journal of Computational Physics 98(1992)332.

[9] C.S. Chang, F.L.Hinton, Physics of Fluids 25(1982)1494.

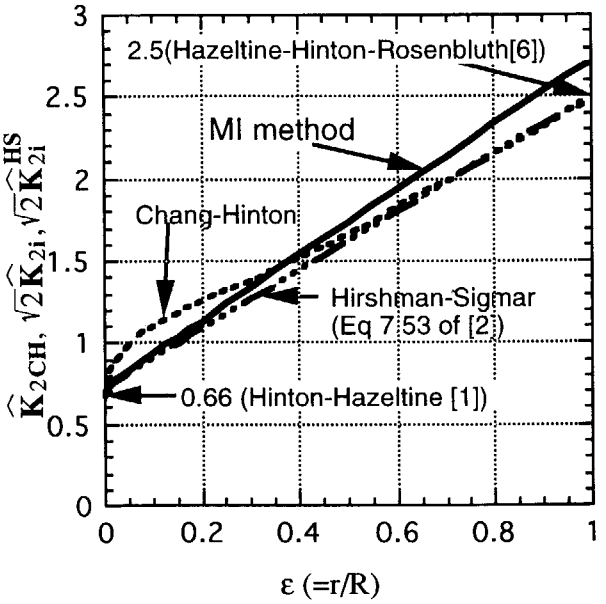

Fig. 1 Aspect ratio dependence of ion thermal diffusivity coefficient for various theories. Comparison was made for circular plasma $<B_0^2/B^2>=1+1.5\varepsilon^2$, $B_0^2/<B^2>=(1-\varepsilon^2)^{0.5}$. HHR result at $\varepsilon=1$ underestimates K_2 due to finite contribution from e-ion collision.

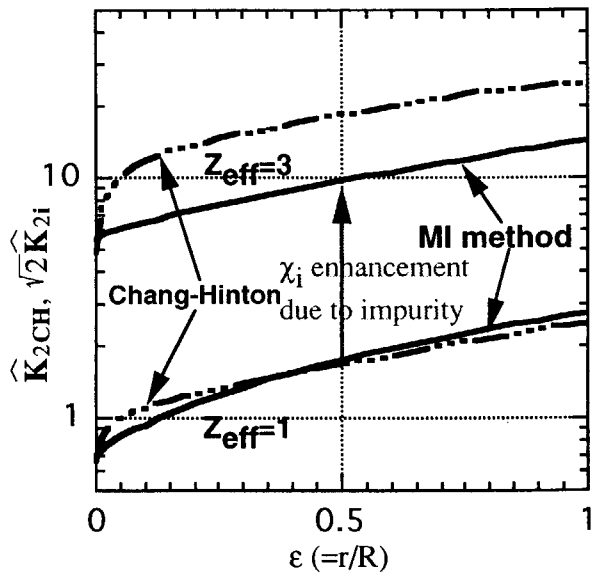

Fig. 2 Aspect ratio dependence of ion thermal diffusivity coefficient for Chang-Hinton and MI method for $Z_{eff}=1$ and 3 for a circular plasma. Chang-Hinton formula gives higher enhancement factor than MI method due to simpler impurity treatment.

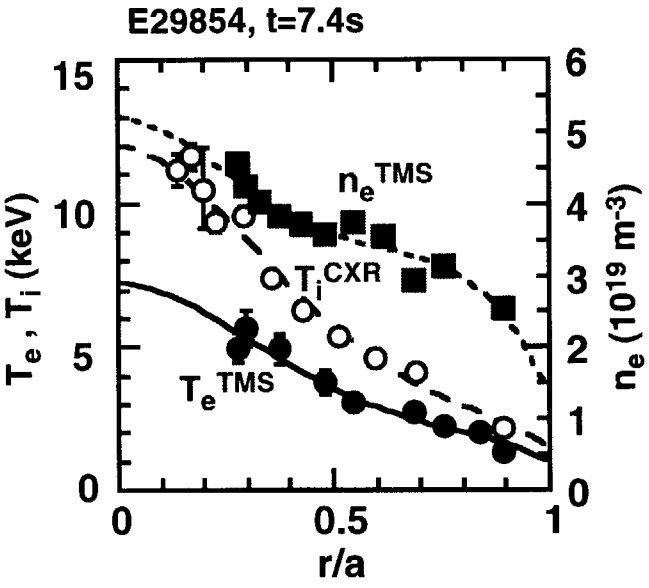

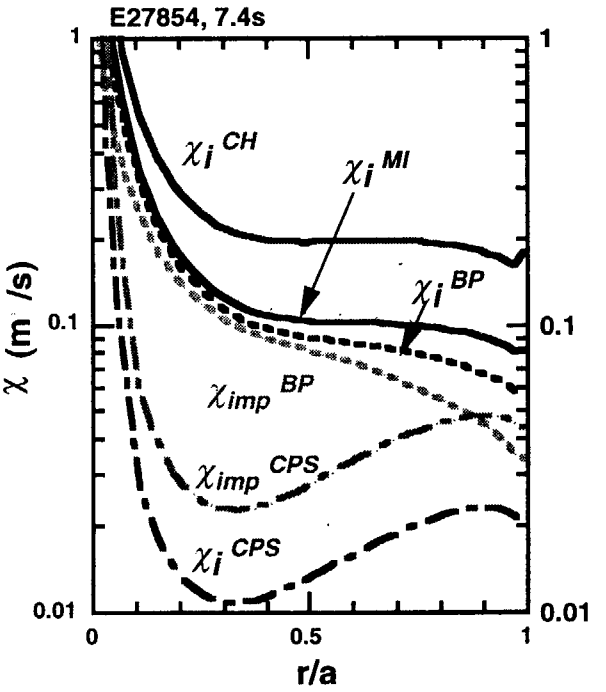

Fig. 3 Radial profiles of ne, Te and Ti for typical hot ion H-mode and neoclassical ion thermal diffusivity given by Chang-Hinton and MI method. Ion thermal diffusivity is decomposed to BP, CPS for ion and impurity. Total ion thermal diffusivity χ_i^{tot} is close to χ_i^{MI}.

3.7 Violation of the Mercier Criterion in Reversed Shear Confinement Configurations [1]

T Ozeki, M Azumi, S Ishida and T Fujita

It is found that the Mercier criterion can be violated in a reversed shear plasma of a tokamak. A reversed shear plasma has negative magnetic shear and negative pressure gradient in the inner region of a plasma. In the negative shear region, stabilizing terms due to the parallel current and the magnetic well produced by the poloidal current change to destabilizing ones.As $(q0\text{-}qmin) / qmin$ increases, the destabilizing effects increase and the Mercier criterion can be violated. Here, $q0$ and $qmin$ are the safety factor on the plasma axis and the minimum value along the minor radius, respectively.

In JT-60U reversed shear plasmas, the value of $(q0\text{-}qmin) / qmin$ becomes large. The Mercier criterion is evaluated for the JT-60 reversed shear plasma where the discharge attained high performance [2]. Figure 1(a) shows the q profile and pressure profile for the equilibrium at around 4.8sec of E27969. As shown in Fig.1(b), the Mercier criterion is violated ($DM<0$) near the region of the large pressure gradient and near the plasma center. In this calculation, the value of $q0$ is assumed to be 18, but the stability result does not change very much with the variation of $q0$ from 12 to 18. During the ramp-up phase of E27969, the reversed shear plasma experiences a stagnation in the increase of the stored energy and occurrences of MHD activity localized near the ITB around 4.8-5.2sec. The observed MHD activity includes a small collapse with a fast growth rate (~100μs) and no precursor. During the stagnation, the Mercier criterion is violated near the region of the ITB, although the measurement of $q0$ has a large error.

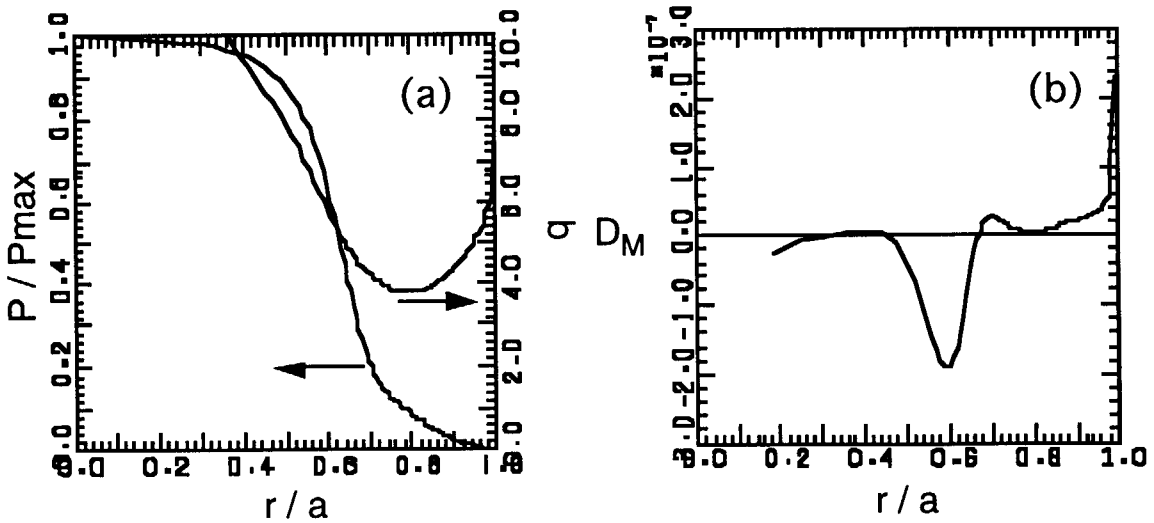

Fig.1 Profiles of the pressure and the safety factor at around 4.8sec of E27969. q0 is assumed to be 18 in the calculation. and (b) the Mercier criterion, DM.

[1] Ozeki, T., Azumi, M.,, Ishida, S., Fujita, T., to appear in Plasma Phys. Control. Fusion.
[2] Ishida S., *et al.*, Phys. Rev. Lett. **79** (1997) 3917.

3.8 "Hidden" variables affecting the L-H transition [1)]

T Fukuda

Since the discovery of H-mode in 1982, significant progress has been made especially in the theoretical field of investigations. Accordingly, theoretical picture of the L-H transition has consequently converged. However, it still remains in part as elusive as before in terms of the quantitative treatment, being deficient in the predictive capabilities. In order to elucidate the cause of scatters in the threshold power scaling for ITER, parametric dependencies of the L-H threshold power on global quantities observed in various tokamaks, such as n_e, B_T and q_{95}, were first reviewed, and it was then suggested that an atomic process may provide significant contributions as a "hidden" variable. Theoretical predictions of the neutrals effects can be both negative and positive through the L-H transition dynamics. It was found in JT-60U by DEGAS that n_o^{95}/n_e^{95} evaluated by DEGAS modifies ν_i^{*95} at the L-H transition, and suggested that ν_{cx}^{95}/ν_b may elucidate the n_e dependence of the threshold power. Here, ν_i^{*95} is the edge ion collisionality defined as $\nu_i^{*95} = \nu_{ii} R q_{95} / \varepsilon^{3/2} v_{th}^{95} (n_e/n_i)(Z_{eff}/Z_i^2)$, and ν_b is the bounce frequency ($= \varepsilon^{1/2} x v_{th}^{95} / R p q_{95}$) of trapped ions. The so called "wall effect" on the threshold power was also resolved in terms of n_o^{95}/n_e^{95}. On the other hand, DIII-D emphasized that the SOL pressure is not necessarily a relevant quantity to discuss the neutrals effect, based on the B2.5 analysis, and introduced the ratio of $\nu_{cx}^{95} (= n_o^{95} \langle \sigma v \rangle_{cx})$ and the neoclassical damping rate (ν_{cx}/μ_{neo}). However, the DIII-D results in part ostensibly contradict with the JT-60U results and observations in PDX and various tokamaks, and extended efforts on the neutrals analysis are thereby required for the comprehensive descriptions.

Among many controversies, investigations of the edge temperatures and ion collisionality have been the most vigorous issues. However, the edge plasma quantities observed in various tokamaks are diversified, and their relation to the global scaling is obscure. Therefore, we would first have to convince ourselves that the H-mode transitions in different tokamaks may not necessarily be described by identical theoretical models, on which the edge parameters are determined. The effort in JT-60U to describe the global threshold scaling with the conventional edge nondimensional quantities does not provide consistent results with C-Mod. Therefore, the development of a comprehensive model which not only quantitatively predicts conditions for the L-H transitions to occur but also considers the core transport is indeed urged to improve the extrapolative capability of our knowledge on the L-H transition.

1) T. Fukuda, to be published in Plasma Phys. Contr. Fusion

3.9 Nondimensional threshold scaling of edge plasma quantities in JT-60U [1)]

T. Fukuda, T. Takizuka, Y. Kamada, K. Tsuchiya, M. Mori and the JT-60 Team

In order to correlate the edge quantities with the H-mode power threshold, exploratory work of scaling the H-mode power threshold with the edge nondimensional quantities was first undertaken in JT-60U. We have employed the well established nondimensional treatment, and thereby described the conventional nondimensional quantities in terms of the relevant edge variables, namely $\rho^{*95}(=[T_i{}^{95}]^{0.5}/RB)$, $\beta^{95}(=n_e{}^{95}T_i{}^{95}/B^2)$ and $\nu^{*95}(=Rn_e{}^{95}/[T_i{}^{95}]^2)$. The nondimensional formulae for the threshold power (P_{th}) are also transformed to

$$P_{th} = (\rho^{*95})^{\alpha_\rho{}^{95}}(\beta^{95})^{\alpha_\beta{}^{95}}(\nu^{*95})^{\alpha_\gamma{}^{95}}R^2n_e{}^{95}[T_i{}^{95}]^{3/2}, \quad (1)$$

$$\alpha_\rho{}^{95}/2 - 2\alpha_\gamma{}^{95} + \alpha_\beta{}^{95} + 3/2 = 0. \quad (2)$$

A postulated hypothesis regarding the significance of the ρ^{*95} dependence, based on the ion orbit loss theory, is as follows. For a given width of the edge layer determined by the magnetic shear or pressure profile, it is necessary for ions to have an adequate orbit width to link the inside and outside of the layer, in order to produce the radial electric field (E_r). Therefore, in the small ρ^{*95} case which applies to high-field large tokamaks, the necessary condition for E_r formation is more stringent, and bulk ion contribution is more predominant. On the other hand, for low-field small tokamaks with a large ρ^{*95}, H-mode is more accessible and sensitive to the fast ions. The contribution of β^{95} is directly relevant to the edge threshold pressure, and ν^{*95} is regarded as a determinant in the ion orbit loss theory. The result of scaling is written as

$$[\rho^{*95}]^{1.2}[\beta^{95}]^{-1.1}[\nu^{*95}]^{0.45}R^2n_e{}^{95}[T_i{}^{95}]^{3/2}. \quad (3)$$

The obtained scaling satisfies the constraint written in equation (2), with its value being 0.1. In addition, it yields the exponents of 0.4, 1.0 and 1.3 respectively for $n_e{}^{95}$, B and R, which is quite consistent with our global scaling result of $P_{th} = n_e{}^{0.5}B^{1.0}R^{1.5}$. As indicated in equation (3), ρ^{*95} has a positive contribution to the threshold power against our hypothesis. It is somewhat amazing, since ρ^{*95} increases with β^{95} for a fixed value of ν^{*95}. However, the global scaling also provides 1, -1 and 0.5 for the exponents of α_ρ, α_β and α_γ parameters, respectively. As to the β^{95} contribution, the threshold decreases with β^{95}, as we expected. It is also clear that an increase of ν^{*95} results in higher threshold power. A speculated reason for the apparent inconsistency on ρ^{*95} is that the above procedure does not separate the bulk plasma transport from the transition physics. Therefore, it would be necessary to take the contribution of nondimensional confinement scaling into account. Another consideration is that additional nondimensional edge parameters e.g., atomic processes may have to be introduced.

1) T. Fukuda *et al.*, to be published in Plasma Phys. Contr. Fusion

3.10 Comparison of edge neutral effect on the condition of H-mode transition before and after the modification of the divertor geometry in JT-60U [1)]

K. Tsuchiya, T. Fukuda, Y. Kamada, H. Takenaga, T. Takizuka, M. Mori, T. Fujita
and the JT-60 Team

The influence of the edge neutrals on the L-H transition condition was investigated in the W-shaped pumped divertor in JT-60U, which is an extension of the previous work published in Ref. 2, where negative contribution of the neutrals effect on the L-H threshold power scaling was documented by the DEGAS analysis. Related subject is treated in PDX and DIII in 1984, where it was speculated that the reduction of molecular deuterium flow back from the divertor to main plasma region can improve the H-mode accessibility.

In the dedicated experiment, the density was scanned in the range $(1.5\text{-}4.0)\times10^{19}\mathrm{m}^{-3}$. It was found, however, that the amount of reduction in the H-mode threshold power in the modified divertor geometry was subtle, in comparison with the open divertor. The density exponent also remained in the range 0.5 to 0.75, whilst it was 0.5 for the previous open divertor case. In addition, the effect of pumping was very small, although it actually reduced the threshold power by a noticeable amount. The signs of presumed geometry effect was found in the detailed analysis, where the slight reduction of threshold power was observed as the compression ratio was increased i.e., the distance between the inner separatrix and the mouth of pumping duct was reduced. Here, the compression factor was defined by the ratio of the line-integrated D_α signal in the main plasma region and divertor region.

As to the edge neutrals density, it was found that ν_i^{*95} stays around unity even under the condition that n_o^{95}/n_e^{95} is considerably large in the modified divertor geometry, although the remarkable reduction of ν_i^{*95} was documented at a high n_o^{95}/n_e^{95} in the open divertor. Here, n_o^{95} was evaluated as a poloidally averaged quantity in the both cases. However, it was also found that the consideration of the wall source at the outer buffle plate is necessary, whereas it was negligible in the open divertor geometry. The DEGAS calculation indicates that the neutral flux from the outer baffle plate is 5% of that from the divertor plates. However, the amount of neutral penetration is 1% of the outflux from the divertor plates, whilst 20% of the outflux from the outer baffle plate penetrate into plasma edge. Therefore, the contributions of each source regions can be comparable, which means that the poloidal averaging may possibly produce misleading results, as we have not resolved where in the edge poloidal section of the plasma being the most influential on the L-H transition.

1) K. Tsuchiya *et al.*, to be published in Plasma Phys. Contr. Fusion
2) T. Fukuda *et al.*, Nucl. Fusion **37** (1997) 1199.

4. High Energy Particles

4.1 Enhancement in the ionization cross-section of a 350 keV hydrogen beam on JT-60U plasmas[1)]

M. Nemoto, K. Tobita, K.Ushigusa, Y. Kusama, M. Kuriyama, K. Kodama, K. Masaki, A. Sakasai and Y. Kamada

Enhancement of the effective ionization cross-section has been investigated by shine-through measurements of a 350 keV hydrogen Negative ion based Neutral Beam (NNB) on the JT-60U tokamak. The NNB was injected into hydrogen plasmas, which were a fixed configuration, with an electron density range of $(1.0\text{-}4.1)\times10^{19}$ m^{-3} and an effective ionic charge of 1.3-2.2. As a fraction of beam power not absorbed by the plasma, the experimental shine-through was measured by thermo-couple arrays which were installed crosswise on the armor tiles where were irradiated by penetrated NNBs.

The experimental shine-through was compared with theoretically predicted shine-through which were based on single-step ionization processes and multi-step ionization processes. Except for the low density region near 1×10^{19} m^{-3}, the experimental shine-through was remarkably smaller than predictions based on single-step ionization processes, suggesting that the effective ionization cross-section of the NNB was enhanced by multi-step ionization.

For evaluation of the cross-section enhancement, the enhancement factor of the cross-section was defined as $(\sigma_S - \sigma_S^{(0)}) / \sigma_S^{(0)}$, where σ_S was the effective ionization cross-section of the NNB and $\sigma_S^{(0)}$ was the cross-section for the conventional single-step processes. The enhancement factor increased with electron density in the range of $(1.0\text{-}2.8)\times10^{19}$ m^{-3} up to a maximum of 80%. It was shown that the experimental enhancement in the range of $(2.8\text{-}4.0)\times10^{19}$ m^{-3} , where was in the operational range on ITER, agreed with the theoretical predictions of Janev et al. in Ref. 2.

References

1) M. Nemoto et al., J. Plasma and Fusion Res. **73**, 1374 (1997).

2) R. K. Janev et al., Nuclear Fusion **29**, 2125 (1989).

4.2 Excitation of Toroidicity-induced Alfvén Eigenmodes with NNB

Y. Kusama, R. Nazikian[1], G.J. Kramer[2], K. Tobita, A. Morioka, T. Ozeki, T. Oikawa, F.V. Tchernychev[3], M. Nemoto, C.Z. Cheng[1], K.W. Hill[1], M. Kuriyama and H. Kimura

The Toroidicity-induced Alfvén Eigenmodes (TAE modes) were excited with the Negative-ion-based Neutral Beam (NNB). Both burst and continuous modes with low toroidal mode numbers were observed in a low β_h regime of $<\beta_h>\leq 0.1$-0.2%. The amplitude of magnetic fluctuations of the burst modes is about ten times as large as that of the continuous modes. Accompanying these bursting activities were a few percent drops in the neutron emission rate. This small drop indicates that the loss of co-injected NNB ions is small.

Continuous TAEs were observed with H^0-NNB injection (360 keV, 1.5-2 MW) into helium plasmas (1.7 T) for the first time as beam-ion-driven TAE modes. The NNB was injected during a ramp-up phase of the plasma current, where a weak central magnetic shear was formed. As shown in Fig. 1, TAE modes continued for 0.35 s, in contrast to burst TAEs lasting a few milliseconds excited with tangential NBI in TFTR [1] and DIII-D [2]. The mode frequency is in a range of 120-210 kHz and the toroidal mode number is n=1-2. The TAE mode frequency calculated from the relation $f_{TAE} = V_A/4\pi qR$ is shown in Fig. 1. Here, V_A is the Alfvén velocity ($\propto B/\sqrt{\rho_i}$, B is the magnetic field, ρ_i is the ion mass density), q is the local safety factor and R is the major radius, respectively. In the calculation, V_A was evaluated using the line-averaged electron density $\overline{n_e}$ and the toroidal magnetic on axis B_{t0}. The time evolution of measured mode frequency is well explained by assuming q=1.5 (m=1) for n=1 mode and q=1.75 (m=3) for n=2 mode. The TAE modes are excited for $v_{b//}/v_A$~0.4-0.7 ($v_{b//}$: parallel velocity of beam ions, v_A: Alfvén velocity). The volume-averaged beam beta at 4.8 s is calculated to be

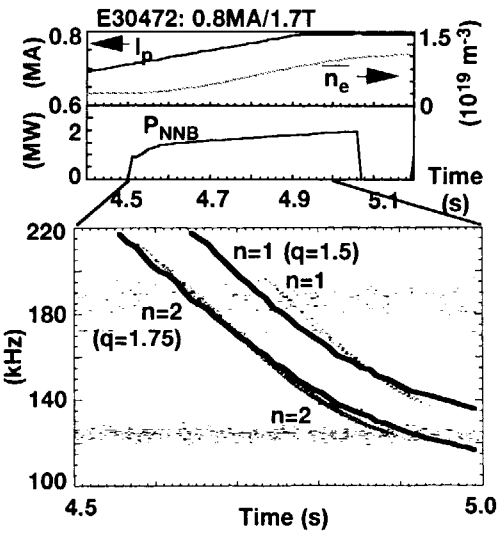

Fig. 1: TAE modes driven by NNB. Top figure; time traces of plasma current I_p, line-averaged electron density $\overline{n_e}$, NNB power P_{NNB}. Bottom figure; temporal evolution of measured frequency and calculated TAE mode frequency. B_{t0}=1.7 T and Ip=0.8 MA at the flat top.

---

present address; [1]Princeton Plasma Physics Laboratory, USA, [2]JAERI Research Fellow, [3]Ioffe Physical-Technical Institute, Russia.

$<\beta_h>$~0.09% (~100 kJ) from a steady-state analysis with the OFMC code [3]. The TAEs were detected only during a ramp-up phase of the plasma current and no TAE was observed at a higher electron-density after reaching a flat-top. A magnetic shear effect and damping by electrons are considered to be the stabilizing mechanism there.

Figure 2 shows the Alfvén continuum spectra calculated with the NOVA-K code [4] for continuous modes at 4.8 s in Fig. 1. A q-profile having q_0=1.4 was assumed as presented in Fig. 2. The TAE gaps are well aligned for both n=1 and n=2 modes. Measured mode frequencies shown in broken lines in Fig. 2 are above the lower Alfvén continuum, which is consistent with the TAE mode excitation. The OFMC calculation shows a steep pressure profile around r/a~0.6 consistent with the gap location of n=2 mode. For q_0=1.2, the measured TAE mode frequency of the n=2 mode crosses the Alfvén continuum and the TAE gap is not aligned well since a TAE gap with a narrow gap width is aligned at q=1.25 near the center. This suggests that the TAE mode is stable for such a low q_0. This consideration should be confirmed by measuring a q-profile from the MSE spectroscopy.

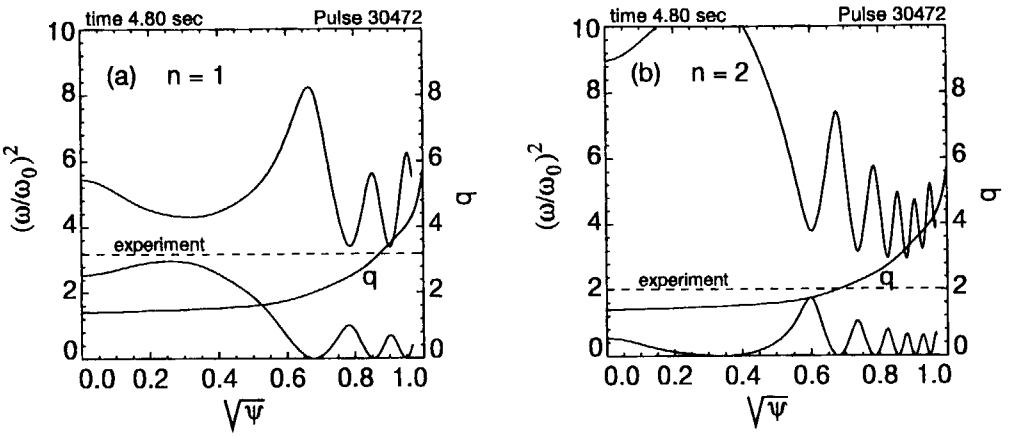

Fig. 2: Alfvén continuum spectra of continuous modes at 4.8 s in Fig. 1; (a) for n=1 mode and (b) for n=2 mode. Measured mode frequencies are shown with broken lines. A safety factor profile with q_0=1.4 was assumed as shown in the figure. The frequency is normalized to $\omega_0=v_{A0}/2q_aR_p$, here, v_{A0} is the Alfvén velocity on the magnetic axis, q_a is the safety factor at the plasma surface and R_p is the major radius.

Burst modes with n=1 (40-70 kHz) and n=2 (70-110 kHz) were also observed when D^0-NNB (350 keV, 2.6-3 MW) was injected into a D^+ plasma, where $v_{b//}/v_A$~0.5-0.6 and $<\beta_h>$~0.2%. Time evolution of plasma parameters and frequency spectrum of observed modes are shown in Fig. 3. The calculated TAE frequencies are also shown in the frequency spectrum. The frequency of the n=2 mode is sharp as similar to that of continuous modes shown in Fig. 1. However, the frequency of the n=1 mode is broad. A mode burst starts with the n=2 mode, and this mode seems to trigger the n=1 mode, which causes the mode burst to terminate. Figure 3 shows the Alfvén continuum spectra for these burst modes at 4.8 s. The measured modes frequency of the n=1 mode crosses deeply the Alfvén continuum and it means that the n=1 burst mode is not the TAE mode. On the other hand, the observed

frequency of the n=2 mode is just above the Alfvén continuum, but very close to the continuum. The n=2 mode seems to be consistent with the TAE mode. The amplitude of magnetic fluctuations of the burst modes shown in Fig. 3 is about ten times as large as that of the continuous modes in Fig. 1. Accompanying these bursting activities were a few percent drops in the neutron emission rate [5]. This small drop indicates that the loss of co-injected NNB ions is small.

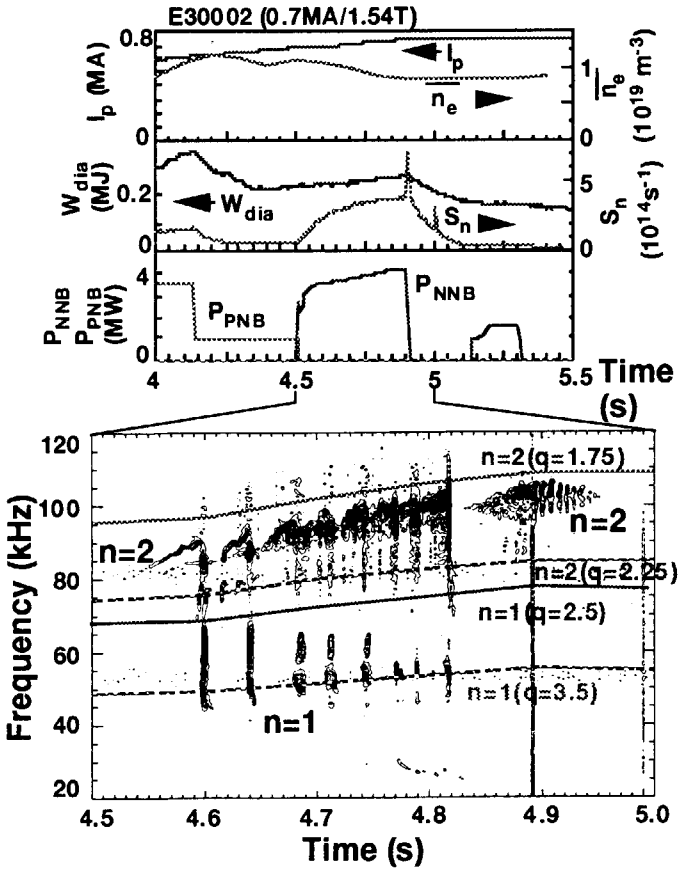

Fig. 3: NNB-excited burst modes. Temporal evolution of plasma parameters (top) and frequency spectrum (bottom) are shown. Solid and broken lines in the bottom figure shows the TAE mode frequencies calculated by assuming safety factor presented. B_{t0}=1.54 T and I_p=0.7 MA at the flat top.

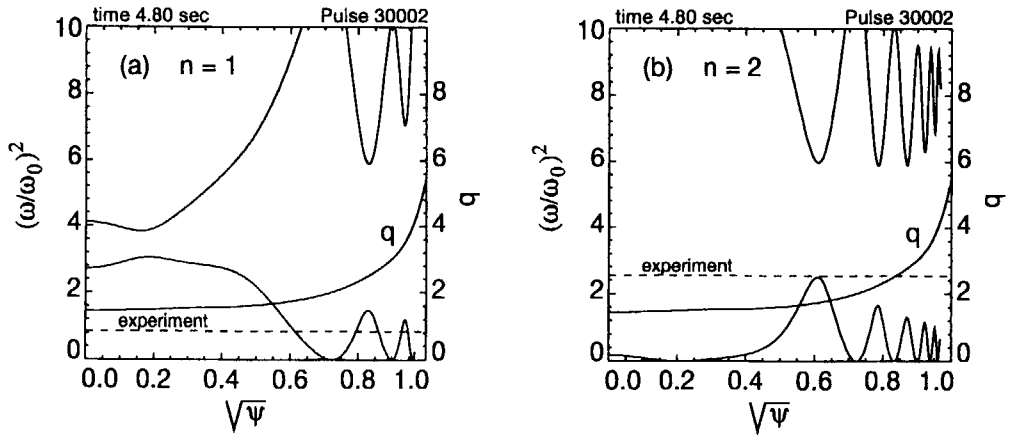

Fig. 4: Alfvén continuum spectra of burst modes (a) for n=1 mode and (b) for n=2 mode at 4.8 s shown in Fig. 3. Measured mode frequencies are shown with broken lines. A safety factor profile was assumed as shown in the figure. Frequency is normalized to ω_0 as the same as Fig. 2.

The excitation regime of continuous mode and burst modes in $<\beta_h>$ and $v_{b//}/v_A$ space is shown in Fig. 5 together with a domain of the TAE mode excitation in TFTR [1] and DIII-D [2]. The beta value of the continuous mode excitation shown in Fig. 1 is about one-fifth to one-tenth the threshold value for excitation of TAEs in TFTR and DIII-D. Table 1 summarizes the excitation conditions and characteristics of continuous modes and burst modes.

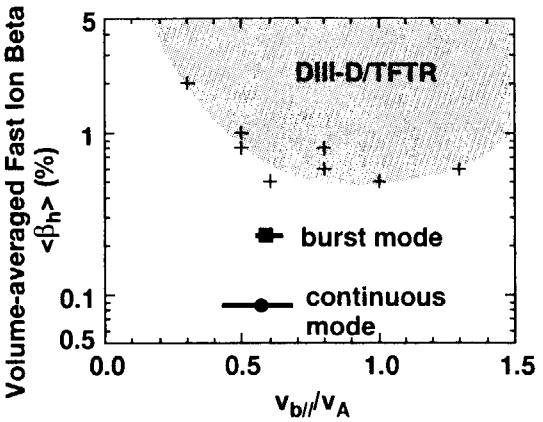

Fig. 5: Excitation condition of continuous modes and burst modes is compared with a domain of the TAE mode excitation in TFTR and DIII-D.

	NNB/Plasma	$v_{b//}/v_A$	$<\beta_h>$	f (kHz)	n	TAE?
Cont. modes	H^0/He^{2+}	0.4-0.7	~0.1%	120-210	1&2	Yes
Burst modes	D^0/D^+	0.5-0.6	~0.2%	40-70	1	No
				70-110	2	Yes

Table 1: Excitation conditions and characteristics of continuous modes and burst modes.

References

[1] K.L. Wong, et al., Phys. Rev. Lett. **66** (1991) 1874.

[2] E.J. Strait, et al., Nucl. Fusion **33** (1993) 1849, W.W. Heidbrink, Plasma Phys. Control. Fusion **37** (1995) 937.

[3] K. Tani, et al., J. Phys. Soc. Jpn. **50** (1981) 1726.

[4] C.Z. Cheng, Phys. Report **211** (1992) 1.

[5] A. Morioka, et al., Paper 4.3 in this Review.

4.3 Correlation between neutron yield drop and magnetic fluctuation during N-NBI driven TAE

A. Morioka, G. J. Kramer, Y. Kusama, K. Tobita,
T. Nishitani, Y. Neyatani and H. Kimura

4.3.1 Introduction

When the plasma current is driven by Negative ion source injector (N-NBI) , it is possible that the current drive efficiency is reduce because of fast particle losses and pitch angle scattering by Toroidicity-induced Alfvén Eigenmodes (TAE modes). In JT-60U, TAE modes excited by ICRF heating have been studied[1], and the degradation of the energetic particle confinement due to TAE modes has been investigated[2]. Positive ion source injector (P-NBI) driven TAE have been observed in TFTR[3] and DIII-D[4].

Recently, in JT-60U TAE modes have been observed when N-NBI beams were injected. We have studied the correlation between the TAE modes and the drop in neutron yield. In eight shots, N-NBI driven TAE modes were observed in 1997.

In this paper, we report on the results of the correlation between magnetic fluctuations and the drop in neutron yield for shot E030002.

4.3.2 Experiment

For this shot the plasma parameters were : toroidal magnetic field, 1.5 T, plasma current, 0.7 MA, averaged electron density, (0.8-1.1)x10^{19} m^{-3}, major radius, 3.3 m and minor radius, 1.0 m. A deuterium neutral beam was injected. The energy of the injected deuterium was 350 keV and the maximum beam power was 3 MW.

Under these conditions, the beam deuteron velocity (v_d) was

$$v_d = \sqrt{\frac{2E_d}{m_d}} \cong 5.9 \times 10^6 \, m\, s^{-1}$$

and the Alfvén velocity (v_A) was

$$v_A \cong \frac{B}{\sqrt{\mu_0 \rho_i}} = 8.1 \times 10^6 \, m\, s^{-1}$$

where B is the magnetic field, μ_0(=4π 10^{-7}) is the magnetic permeability of vacuum and ρ_i is the mass density. The beam parallel velocity of deuteron was more than $v_A/3$. So in this experiment beam particles fulfill the resonance condition for TAE mode excitation after they have reduced their speed due to slowing down processes[5].

TAE modes were observed with an array of 8 Mirnov coils. The Mirnov coil diagnostic had a maximum sampling rate of 1 MHz. The neutron diagnostic had a sampling time of 1 msec[6].

4.3.3 Results

The time history of the power of N-NBI, electron temperature at the plasma center, the averaged electron density and total neutron yield for shot 30002 is shown in Fig.1. The change of beam slowing down time ($\tau_s \propto (T_e)^{3/2}/n_e$ where T_e is electron temperature and n_e is electron density) during N-NBI inejection is small. The time history of the magnetic fluctuations is shown in Fig.2. The bursts observed below 70 kHz have a toroidal mode number of one. The activity between 70 kHz and 110 kHz has a n = 2 toroidal mode number, The n = 2 frequency scales with $1/(n_e)^{1/2}$, which is expected for TAE modes. In sec.4.2 of this review, it was shown that the n = 2 activity is likely a TAE mode whereas the n = 1 activity is not a TAE mode[7]. The correlation between the neutron signal and the Mirnov signal is shown in Fig.3(a) for the n = 1 activity and in Fig.3(b) for the n = 2 activity. The total neutron emission was seen to drop during each burst in Mirnov signal. Fig.4 shows the total neutron drop rate plotted against the averaged magnetic activity between 70 kHz and 120 kHz in the n = 2 TAE mode. There is no correlation between the magnetic fluctuations and the drop in neutron yield during N-NBI driven TAE. The neutron diagnostics has 3.7% of uncertainly in total neutron yield. In such a circumstance, a neutron drop during N-NBI driven TAE was undetected so far.

References

1) Kimura H. et al., Proc. 16th IAEA Fusion Energy Conf., Montréal, F1-CN-64/E-6 (1996)
2) Saigusa M. et al., Plasma Phys. Control. Fusion, 37, 295 (1995)
3) K. L. Wong, R. Durst, R. J. Fonck, et al., Phys. Fluids,B ,4 , 7, 2122 (1992)
4) W. W. Heidbrink, E. J. Strait, E. Doyle, et al., Nucl. Fusion, 31, 9, 1635 (1991)
5) W. Kerner, D. Borba, et al., Plasma Phys. Control. Fusion, 36, 911 (1994)
6) Nishitani T. et al., Rev. Sci. Instrum., 63, 5270 (1992)
7) Kusama Y. et al., Section 4.2 in this review.

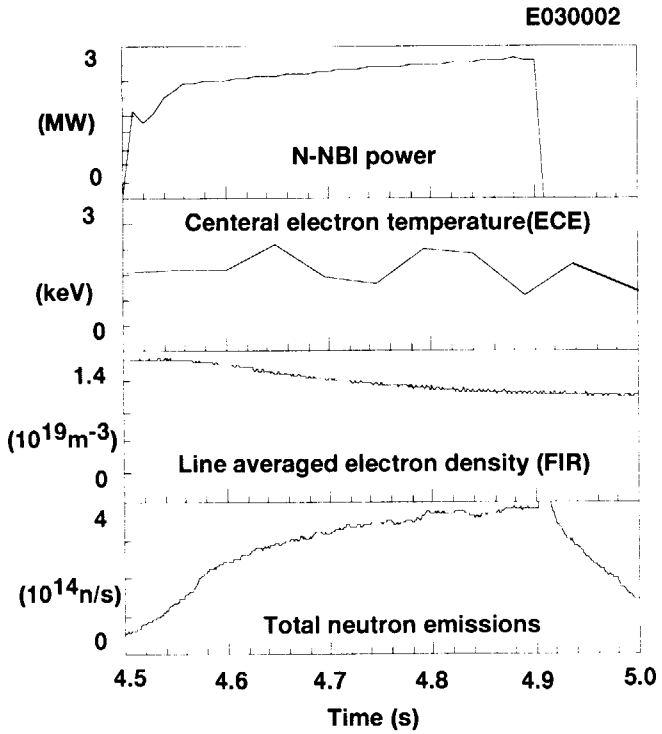

Fig.1 The time history of the power of Negative ion source injector, electron temperature at the plasma center, line averaged electron density and total neutron yield for a plasma in which a TAE mode was driven by 350keV deutrons from the negative ion source injector system of JT-60U.

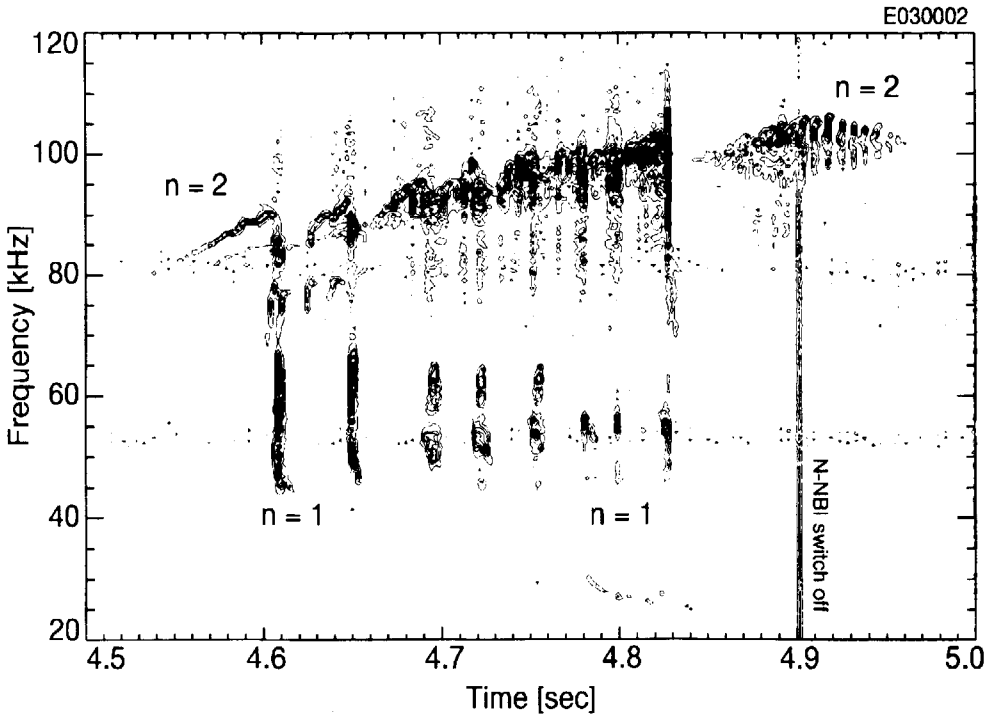

Fig.2 Time history of the magnetic fluctuations

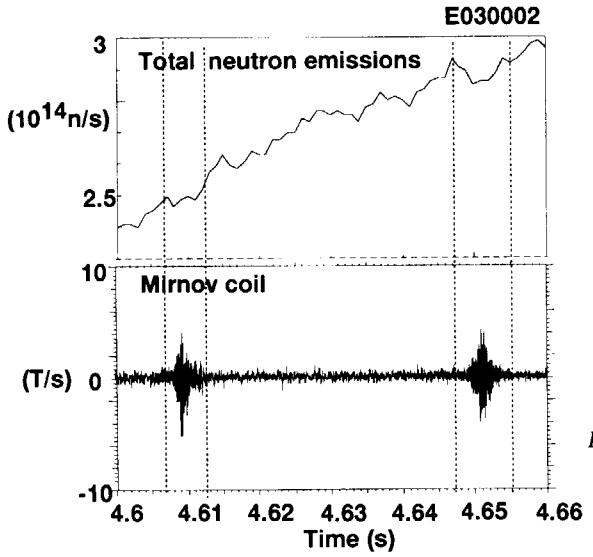

Fig.3(a) Time history of the total neutron yield and the Mirnov coil signal.

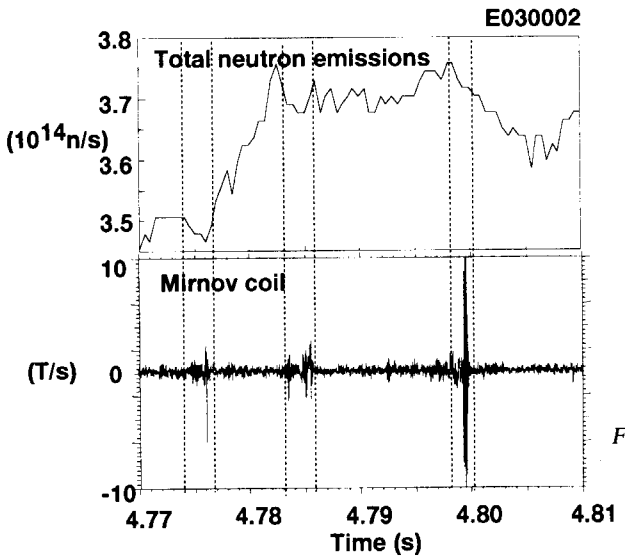

Fig.3(b) Time history of the total neutron yield and the Mirnov coil signal.

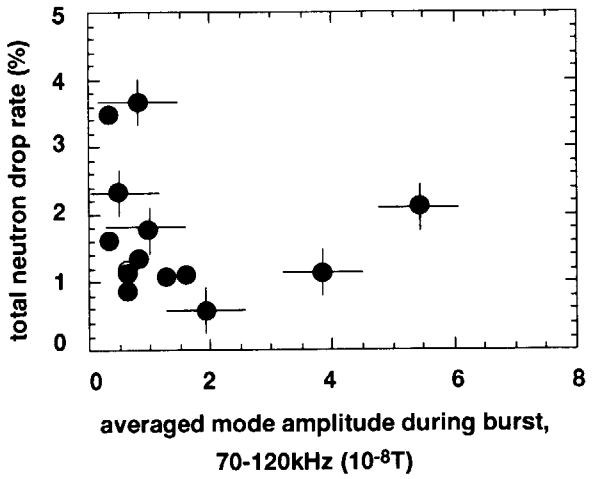

Fig.4 The total neutron drop rate plotted against the averaged magnetic fluctuations during bursts between 70kHz and 120kHz. (The N-NBI driven n = 2 TAE mode.)

4.4 The correlation between sawteeth and TAE, EAE, and NAE modes.

G.J. KRAMER, K. TOBITA, Y. KUSAMA, T. FUJITA, T. OIKAWA, T. OZEKI,
C.Z. CHENG†, G. FU†.

†*PPPL, Princeton University, Princeton, New Jersey 08543, U.S.A.*

4.4.1 Introduction.

During sawtooth stabilization experiments Torodicity induced Alfvén Eigenmodes (TAE modes) often observed before Giant Sawtooth Crashes (GST) (see fig. 1 and ref. 1). These TAE modes can lead to fast particle losses and thereby degrading the fusion performance of the plasma as can be seen from fig. 1 where the neutron signal decreases when the TAE modes are present. After the GST the TAE modes have disappeared completely. Recently, we have also observed strong magnetic fluctuations after the GST in the frequency range between 450 and 600 kHz. These fluctuations also correlate with a drop in the neutron signal (see fig. 1) so they too reduce the plasma performance. We have identified these fluctuations as Elipticity induced Alfvén Eigenmodes (EAE). As can bee seen in fig. 1, the mode frequency is changing rapidly in time. In this paper we will investigate the correlation between this TAE and EAE mode-frequency chirping and the magnetic safety factor or q-profile.

4.4.2 Experiment.

In this paper we have studied pulse 28401 extensively. For this shot there are good q-profiles available that were measured with the Motional Stark Effect (MSE) diagnostic. The main plasma parameters for this shots were: toroidal magnetic field, $B_T = 3.5$ T, plasma current, $I_p = 2.6$ MA, major radius, $R = 3.47$ m, minor radius, $a = 1.03$ m, ellipticity, $\kappa = 1.37$, triangularity, $\delta = 0.21$, a line integrated electron density of $n_{el} = 1.9\ 10^{19}$ m^{-3}. In this shot 3.8 MW of ICRF power was injected together with 1.8 MW of NBI power for ion-temperature and plasma rotation measurements. For this pulse good experimentally measured q-profiles are available, obtained with the Motional Stark (MSE) diagnostic. Furthermore, the density profiles are also well known from the two Thomson scattering diagnostics here at JT-60U. For the theoretical analysis the q- and density profiles are very important because the (local) Alfvén speed depends on the mass density and the location of the Alfvén Eigenmodes depends on the local q-value[2].

From fig. 1 we see that before the two GST a number of TAE modes are excited that are well separated from each other in frequency. The modes are labeled with their toroidal mode number. After the first GST a number of modes appear at around 535 kHz. Here modes with different toroidal numbers appear at almost the same frequency. We have identified these modes as Elipticity induced Alfvén Eigenmodes. At 550 kHz and around 9.85 sec. we also observe two modes with a rather different frequency behavior then the TAE and EAE modes. In the following we will present evidence that these modes might be Noncircular triangularity induced Alfvén Eigenmodes (NAE) which are localized near the edge of the plasma.

4.4.3 Theoretical analysis and discussion.

For this pulse we have performed a large number of calculations with the NOVA-k code[2] in order to obtain the mode structure of the TAE, EAE, and NAE modes as observed in this shot. First we have simulated the TAE modes at 9.50 sec. The result for the n=5 TAE mode is shown in fig. 2. In the left panel the Alfvén continuum is depicted with the experimentally observed frequency. In the right panel the displacement of the mode is shown. From this figure it can be seen that the main contribution to this TAE mode comes from the m=4 and m=5 poloidal harmonics which are located in the gap at the

core of the plasma. This gap is inside the $q = 1$ surface that is present at $r/a = 0.42$. There are other small contributions of higher poloidal harmonics towards the edge region which contribute to this wave function as well. Similar results were obtained for the other TAE modes. So the TAE modes here are excited inside the $q = 1$ surface. The succession of TAE modes and the chirping down in frequency can be attributed to the decrease of q in the center of the plasma before the GST.

For the EAE modes after the GST we have performed similar calculations at 9.70 and 9.80 sec. Results of these calculations for the n=5, 6, and 7 EAE modes at 9.80 sec. are presented in fig. 3. It can be seen that these EAE modes peak all at the $q = 1$ surface. These EAE modes are formed by coupling poloidal modes with $m_1 = n - 1$ and $m_2 = n + 1$. From the simple relation: $\omega_{EAE} = V_A/(Rq_{EAE})$, with $q_{EAE} = (m_1 + m_2)/2n$, it can be seen that EAE modes with different toroidal mode numbers appear at the same frequency, More extensive calculations with the NOVA-k code have shown that there are very small frequency differences for the different EAE modes as observed experimentally. The rapid frequency chirping of the modes could also be simulated with the NOVA-k code. During the time that the EAE modes are active the $q = 1$ surface is expanding rapidly from $r/a = 0.19$ at 9.7 sec. to $r/a = 0.37$ at 9.8 sec. This expantion is the reason that those modes chirp down in frequency.

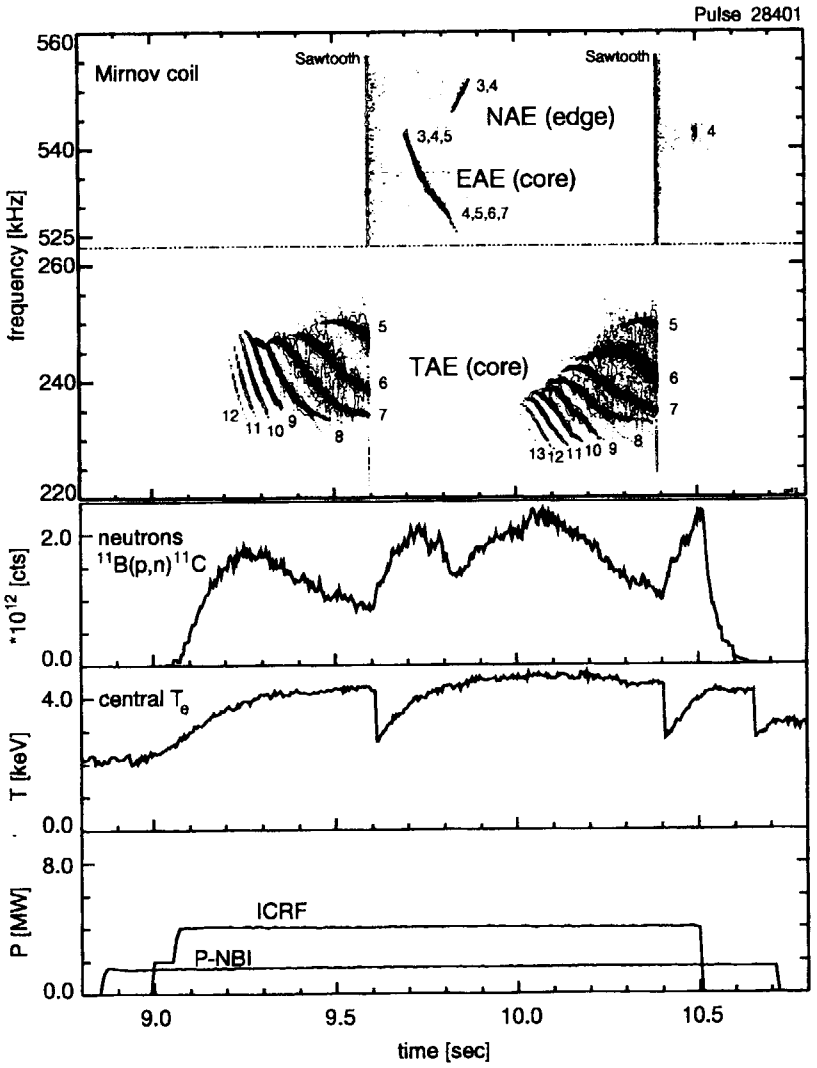

FIGURE 1: The observed AE modes from the Mirnov coil measurements (top trace), the neutron signal from the reaction ^{11}B(p,n)^{11}C (second trace) the central electron temperature, showing two Giant Sawtooth crashes (third trace), and the applied heating (bottom trace) for the shot studied in this paper. The different AE modes are indicated with their respective toroidal mode numbers.

There is a delay of about 0.1 sec. between the GST crash and the onset of the EAE modes. This delay can be explained if the q in the center relaxes back to one. After the GST the $q = 1$ surface starts growing again from the center and after 0.1 sec. it moves into the region where the fast particle drive is large enough to drive the EAE modes unstable.

As mentioned before, we have some indication that the two modes at 550 kHz are edge localized modes. From the NOVA-k simulations we could only find an edge localized $n = 3$ mode with the correct frequency. During this time the line averaged density in the edge region, as observed with the U1 interferometer, is decreasing. This explains the increase of the frequency during the time that the modes are visible. These modes can be driven by the fast particles that are lost due to the EAE activity.

4.4.4 Conclusions.

In this paper we have shown that the chirping of the TAE and EAE mode frequency which has been observed before and after giant sawteeth crashes carries detailed information on the development of the q-profile. We have been able to simulate these modes and the frequency chirping accurately with the NOVA-k code in which we have used the experimentally observed q-, density and pressure profiles. In fusion reactors these core localized modes are not wanted because they suppress the plasma performance. However, because these modes are very sensitive to the q-profile in the center of the plasma, we can use them to obtain information on the q-profile there which is often difficult to obtain otherwise.

1. M. Saigusa *et al.* Plasma Phys. and Contr. Fusion, **37** (1995) 295.

2. C.Z. Cheng, Phys. Rep. **211** (1992) 1.

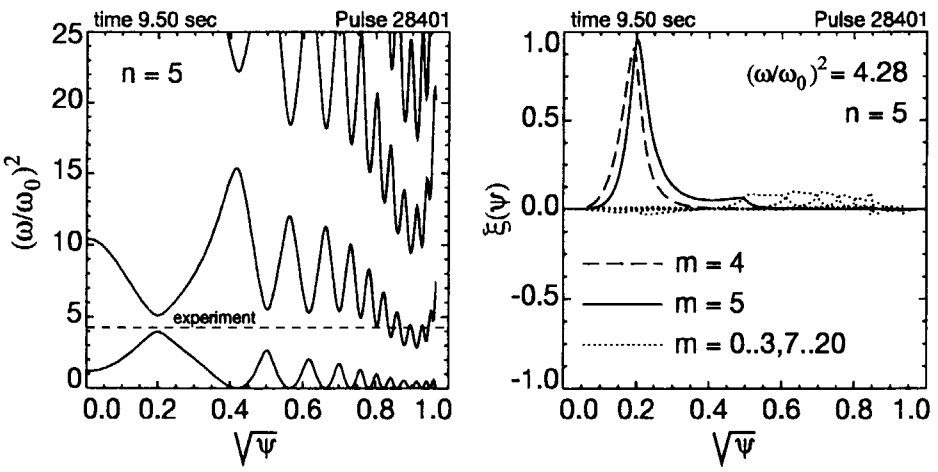

FIGURE 2: The Alfvén continuum for the toroidal mode number five at 9.50 sec (left panel). The mode structure as calculated with the NOVA-k code for the n=5 TAE mode is shown in the right panel. For this mode the poloidal harmonics with $m = 4$ and $m = 5$ are the dominant harmonics here. The frequencies are normalized to $\omega_A = v_A(n_e(\rho = 0))/(R * q(\rho = 1))$. And the horizontal axis is the normalized minor radius ($\sqrt{\Psi} \simeq r/a$). The $q = 1$ surface is at $r/a = 0.42$.

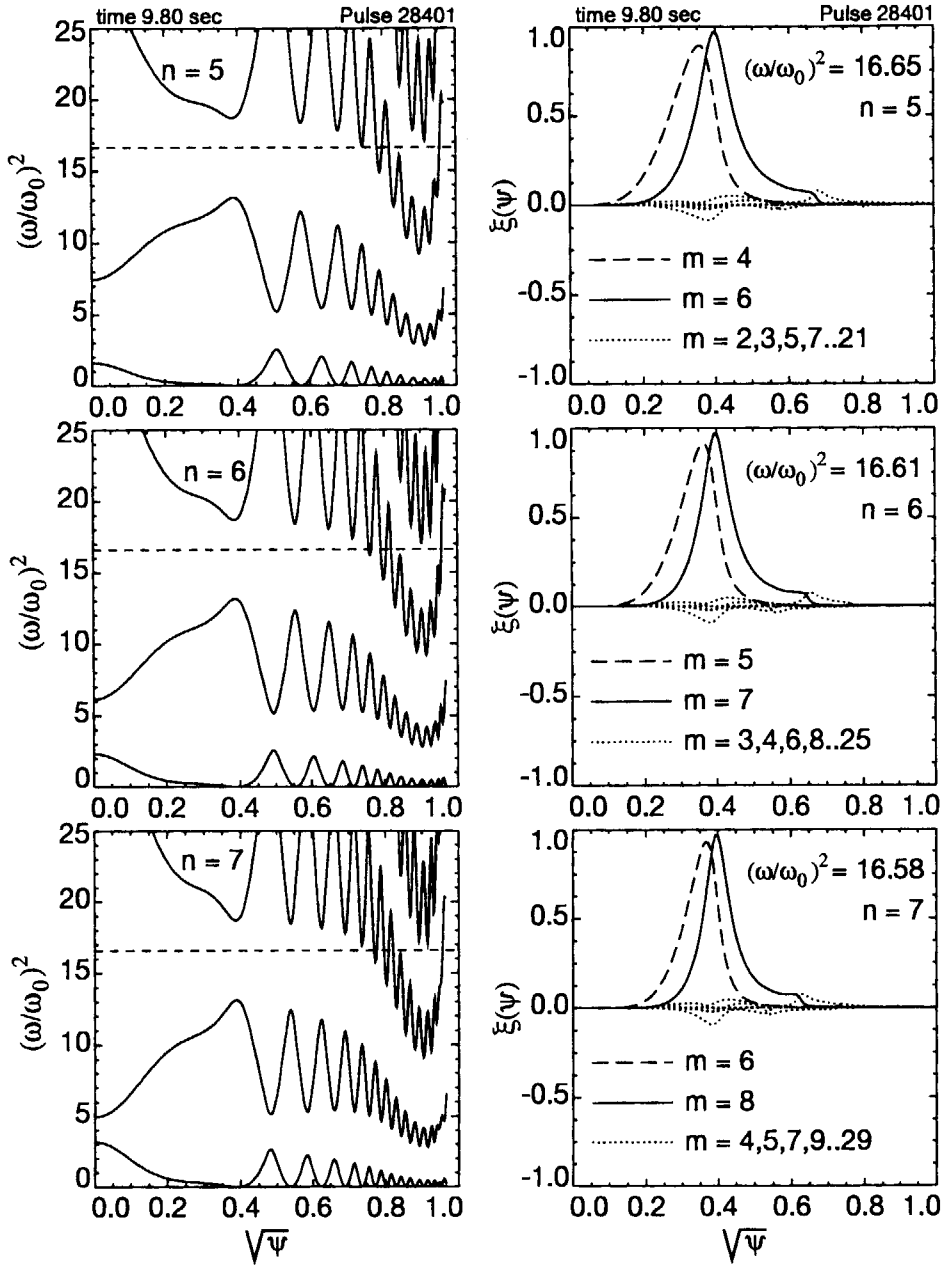

FIGURE 3: The Alfvén continuum for the toroidal mode number five, six, and seven at 9.80 sec (left panel). The mode structure as calculated with the NOVA-k code for the n=5,6, and 6 EAE modes are shown in the right panel. It can be seen that all the three EAE modes peak a the same location where the $q = 1$ surface is located (at $r/a = 0.37$). For these EAE modes the poloidal harmonics with $m_1 = n - 1$ and $m_2 = n + 1$ are the dominant poloidal harmonics here. The frequencies are normalized to $\omega_A = v_A(n_e(\rho = 0))/(R * q(\rho = 1))$. And the horizontal axis is the normalized minor radius ($\sqrt{\Psi} \simeq r/a$).

4.5 The determination of the q-profile in the plasma core from Alfvén Eigenmodes[1)].

G.J. KRAMER, T. OIKAWA, T. FUJITA, Y. KAMADA, Y. KUSAMA, K. TOBITA, T. OZEKI, C.Z. CHENG†, R. NAZIKIAN†.

†*PPPL, Princeton University, Prinston, New Jersey 08543, U.S.A.*

Torodicity induced Alfvén Eigenmodes (TAE modes) can exist at well defined q-surfaces. We have used core-localized TAE modes to study the q-profile inside the $q = 1$ surface. The magnetic field safety factor $q(r)$ is essential in the theoretical modeling of plasma equilibria and stability. Presently, the q-profile can be obtained from the Motional Stark Effect (MSE)[2)].

In experiments it is often found that the TAE mode frequency is chirping (i.e. the frequency is changing rapidly in time[3)]. This chirping can be attributed to the dynamical development of the plasma parameters where the TAE modes are excited. From the parameters that affect the TAE mode frequency, the mass-density, the toroidal magnetic field, and the toroidal rotation velocity of the plasma, are well diagnosed whereas the q-profile is in general less well known. The radial position of the TAE modes depends strongly on the q-profile.

We have been able to relate the TAE frequencies (after corrections for the mass-density and toroidal rotation) to the radial location in the plasma. Because TAE modes are related to rational q-surfaces via the relation: $q_{\mathrm{TAE}} = 1 - 1/2n$ (n the toroidal mode number) for modes inside the $q = 1$ surface, we could reconstruct the q-profile in the center of the plasma from the measured TAE frequencies and mode numbers and the density profile. The result is shown in fig. 1 where the MSE q-profile contour plot has been overlaid with the q-contours as determined from the TAE modes. From this figure it can be seen that the agreement with the two q-profile as measurements is very good.

If in future fusion devices (core localized) TAE modes are driven unstable, it is possible to obtain information of the q-profile in the region where these modes are unstable.

1. G.J. Kramer *et al.* Accepted for publication in Plasma Phys. and Contr. Fusion.
2. F.M. Levinton, Rev. Sci. Instrum. **63)** (1992) 5157.
3. M. Saigusa *et al.* Plasma Phys. and Contr. Fusion, **37** (1995) 295.

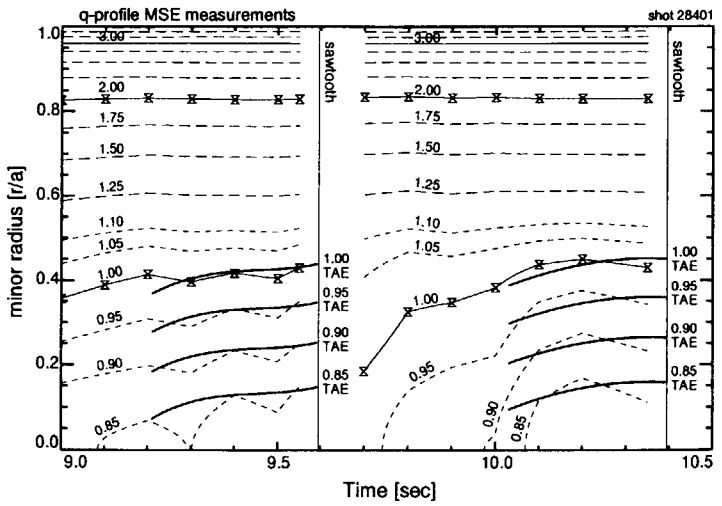

FIG. 1 The contour plot of the q-profile as a function of time (horizontal) and minor radius (vertical). The q-profile as determined from the TAE modes are indicated by the solid lines before the two sawtooth crashes. The MSE contours are shown with dashes and solid lines for the at $q = 1$, 2, and 3 contours. At the $q = 1$ and 2 contours the double triangles indicate the times where the MSE q-profiles were evaluated.

4.6 Interaction of NNB-injected ions with ICRF-excited TAE modes and EAE modes

Y. Kusama, G.Y. Fu[1], G.J. Kramer[2], T. Ozeki, T. Oikawa, K. Tobita,
F.V. Tchernychev[3], M. Saigusa[4] and C.Z. Cheng[1]

Interaction of NNB-injected hydrogen ions with Alfvén eigenmodes (AE modes) exited by ICRF heating was investigated as an simulation of interaction between alpha-particle-driven AEs and beam-injected energetic ions for heating and current drive. Ellipticity-induced Alfvén eigenmodes (EAEs) disappeared by the NNB injection, where $v_{b//}/v_A$~0.55. The damping mechanism was shown to be the beam ion Landau damping from a stability analysis using the NOVA-K code.

Figure 1 shows time traces of frequency spectra and plasma parameters in a typical discharge heated with ICRF waves (102 MHz, $2\omega_{CH}$) in the latter part (l_i=1.24) of the discharge (I_p=2.6 MA, B_{t0}=3.3 T, q_{eff}=3.5). The bulk ion is He^{2+} and H^0-beams are injected. Multiple TAE modes with medium to high toroidal mode numbers (n=5-13) were observed before sawtooth crashes [1]. A decrease in the neutron emission rate due to the appearance of TAE modes indicates a loss of energetic protons over 3 MeV. The stored energy and electron temperature saturates or decreases simultaneously with the energetic ion loss. The NOVA-K [2] calculation shows that these TAE modes are driven inside the q=1 surface. High frequency modes of 525-550 kHz with n=3-7 were detected for 0.2 s after the first sawtooth crash at 9.6 s as shown in Fig. 1. The neutron emission rate decreases again due to the appearance of high frequency modes.

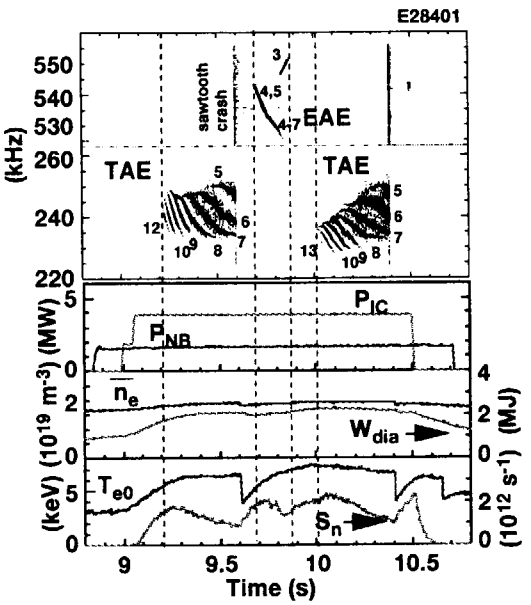

Fig. 1: Time traces of frequency spectra in two frequency bands, ICRF power P_{IC}, NBI power P_{NB}, line-averaged electron density $\bar{n}_e$, diamagnetic stored energy W_{dia}, central electron temperature T_{e0} and rate of neutron emission S_n from $^{11}B(p, n)^{11}C$ reaction. Toroidal mode numbers of TAEs and EAEs are shown in the frequency spectrum.

---

present address; [1]Princeton Plasma Physics Laboratory, USA, [2]JAERI Research Fellow, [3]Ioffe Physical-Technical Institute, Russia, [4]Ibaraki University, Japan.

Figure 2 shows the density and the safety factor profiles before and after the first sawtooth crash in the discharge shown in Fig. 1. The density profiles are similar. The safety factor near the center jumps up due to the sawtooth crash and decreases gradually in the reheat phase. At the 9.8 s, the electron temperature and the stored energy recovers to the value before sawtooth crash. It means that the profile of ICRF-accelerated energetic protons almost returns to that before the sawtooth crash. The Alfvén continuum spectrum is modified by a change in q profile after sawtooth crash. Therefore, the change in q-profile considered to be essential for excitation of EAE modes. The NOVA-K analysis shows that these high frequency modes are EAE modes excited at the q=1 surface [3].

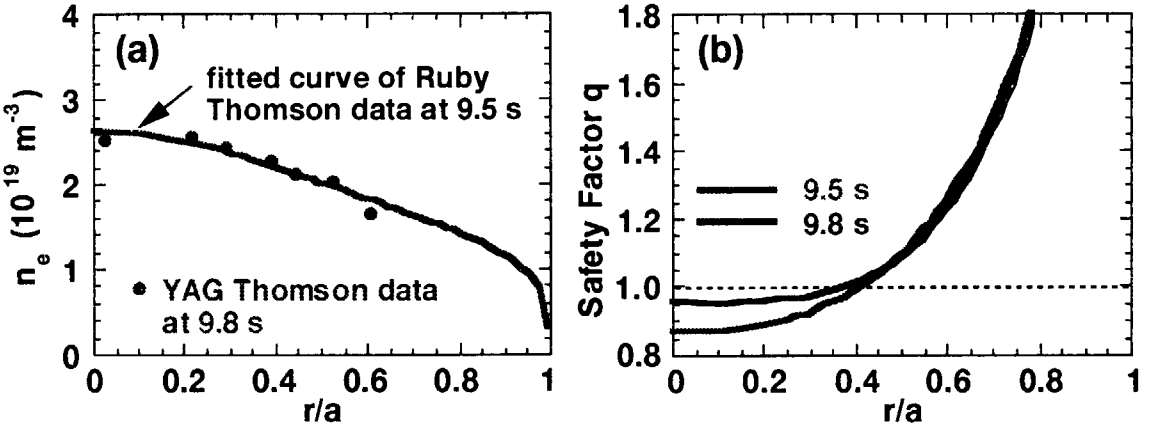

Fig. 2: Profiles of the density (a) and the safety factor (b) before (9.5 s) and after (9.8 s) the first sawtooth crash at 9.6 s in the discharge shown in Fig. 1.

The NNB(H^0/350 keV/1.6 MW) was injected into the similar discharge shown in Fig. 1 and the interaction of NNB ions with TAE and EAE modes was investigated. As shown in Fig. 3, similar TAE modes were excited also in the case of NNB injection and no significant change was observed in TAE modes comparing with the case without NNB. On the other hand, EAE modes observed in the discharge without NNB almost disappeared. The pressure profile of NNB-injected ions was calculated using the orbit-following Monte Carlo (OFMC) code [4]. Figure 4 shows the pressure profile at 9.9 s in Fig. 3. The total stored energy of NNB ions is ~160 kJ and the volume-averaged

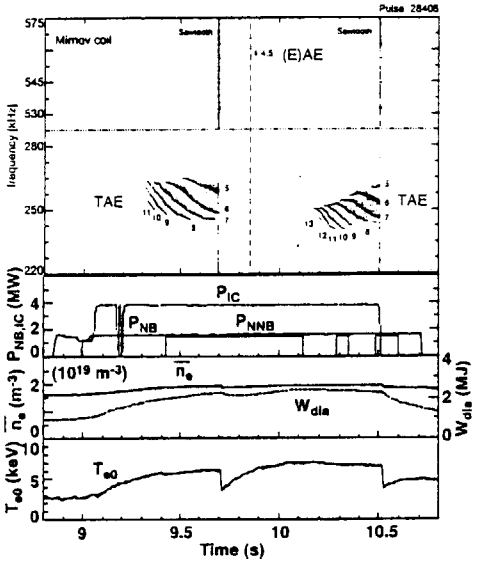

Fig. 3: Discharge with NNB injection. The NNB wave form (P_{NNB}) shows only the injection timing and power of the first pulse is 1.6 MW at 350 keV. This discharge is similar to that shown in Fig. 1 except for the NNB injection.

beta of NNB ions is $<\beta_h>\sim 0.03\%$ (B_{t0} = 3.3 T, V_p=93 m^3). A ratio of velocity of hydrogen beam of 350 keV in a toroidal field direction $v_{b//}$ to Alfvén velocity v_A is $v_{//}/v_A \sim 0.6$, which is slightly higher than $v_{//}/v_A$=0.5 of the EAE mode resonance [5]. It means that NNB-injected ions can resonate with EAE modes and beam ion Landau damping can play an effective role for the mode stability. Concerning the effect of TAE modes on confinement of NNB-injected ions, no clear degradation of the confinement was observed from the charge-exchange measurements [6] in a range of 130-500 keV.

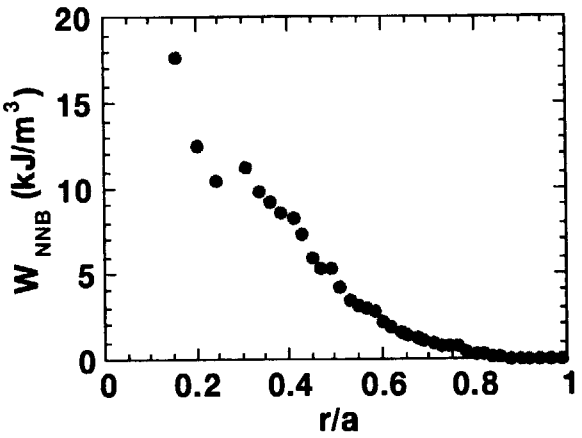

Fig. 4: Pressure profile of NNB-injected ions at 9.9 s of E28408.

Stability analysis using the NOVA-K code was made for discharges without and with the NNB injection shown in Fig. 1 and Fig. 3 to understand the excitation of EAE modes after the sawtooth crash and stabilization of EAE modes by the NNB injection. The radiative damping is not treated for EAE modes in the present NOVA-K code. In the analysis, the density and safety factor profiles presented in Fig. 2 were used, the plasma species and main impurity was assumed to be He^{+2} and C^{+12}, respectively. For parameters of ICRF-accelerated energetic protons, tail temperature of 220 keV measured (may be underestimated because of the CX target effect) with the CX neutral particle analyzer installed vertically, the tail ion stored energy of 200 kJ and profile scale length of 15 cm were used for both before (9.5 s) and after (9.8 s) the sawtooth crash in the discharge shown in Fig. 1.

	9.5 s of E28401	9.8 s of E28401	9.9 s of E28408
f_{EAE}	554 kHz	559 kHz	
γ_{tail}/ω	0.5×10^{-4}	1.7×10^{-4}	
γ_{ELD}/ω	-3.4×10^{-4}	-2.8×10^{-4}	
γ_{NNB}/ω			-4.0×10^{-4}

Table 1: The results of stability analysis for the n=4 EAE mode in the discharges without (E28401) and with (E28408) NNB injection. Calculated EAE mode frequency f_{EAE}, growth rate by ICRF tail ions γ_{tail}, electron Landau damping γ_{ELD}, NNB beam Landau damping γ_{NNB} are shown. All growth rate and damping rates are normalized by the mode frequency.

Table 1 shows the results of the stability analysis for the n=4 EAE mode. The ICRF tail ion drive at 9.8 s is increased by a factor of 3.4 from that of 9.5 s because the safety factor is increased and the mode is closer to the center. Therefore, the EAE modes is considered to appear only after sawtooth crash even though the driving rate does not exceed the damping rate. A damping rate of EAE modes by NNB ions through beam ion Landau damping was also evaluated using the pressure profile shown in Fig. 4. As shown in Table 1, the contribution of NNB beam Landau damping to stabilization of EAE modes is large and a ratio of growth rate to damping rate ($\gamma_{ELD}+\gamma_{NNB}$) decreases down to 25%. The NOVA-K code analysis shows qualitatively that the stabilization mechanism of EAE modes is beam ion Landau damping by NNB injected ions. As mentioned above, tail temperature is possibly underestimated because of the CX target effect [7] and would be about 300 keV. The driving term should be considered again using the corrected tail temperature. The corrected tail temperature will increase the driving rate.

References

[1] G.J. Kramer et al., paper 4.4 in this Review.
[2] C.Z. Cheng, Phys. Report **211** (1992) 1.
[3] Y. Kusama, et al., 24th European Physical Society Conference on Controlled Fusion and Plasma Physics, Berchtesgaden, 9th-13th June 1997, Vol. 21A Part II, p513-p516.
[4] K. Tani, et al., J. Phys. Soc. Jpn. **50** (1981) 1726.
[5] W. Kerner, et al., Plasma Phys. Control. Fusion **36** (1994) 911.
[6] Y. Kusama, et al., Fusion Eng. Design **34-35** (1997) 531.
[7] Afanassiev V I et al., Plasma Phys. Control. Fusion **39** (1997) 1509.

4.7 Chirping modes in ICRF-heated weak shear plasmas

Y. Kusama, H. Kimura, T. Ozeki, M. Saigusa [1], G. J. Kramer [2], G.Y. Fu [3], R. Nazikian [3], T. Oikawa, S. Moriyama, M. Nemoto, T. Fujita, K. Tobita and C.Z. Cheng [3]

In central magnetic shear plasmas produced by decreasing the main-heating beam power of the negative-shear operation the discharge, modes with very rapid chnage in the frequency (frequency chirping) were observed during the ICRF heating[1,2]. The frequencies of these TAE modes rapidly increased from ~30 kHz up to ~110 kHz in a period of ~150 ms as shown in Fig. 1. The sequential appearance of many modes with different toroidal mode numbers can be well explained with the ACG map of TAE modes [3]. A very flat q profile was measured over a minor radius of $0.35 \leq r/a \leq 0.75$ and a weak ITB was found in the electron density profile at r/a~0.35.

The TAE mode theory shows that the TAE mode frequency can change when the magnetic shear, the plasma beta, the plasma density and the safety factor change. However, the observed change in the mode frequencies is so large that the present TAE mode theory cannot explain the frequency chirping from the change in plasma parameters and profiles. Although the final chirped-up frequency is consistent with the TAE mode frequency, the initial frequency of the chirping is well below the TAE mode frequency and is close to the frequency of energetic-particle continuum mode [4]. The chirping modes in Fig. 1 seem to have characteristics of both fluid TAE modes and energetic-particle modes.

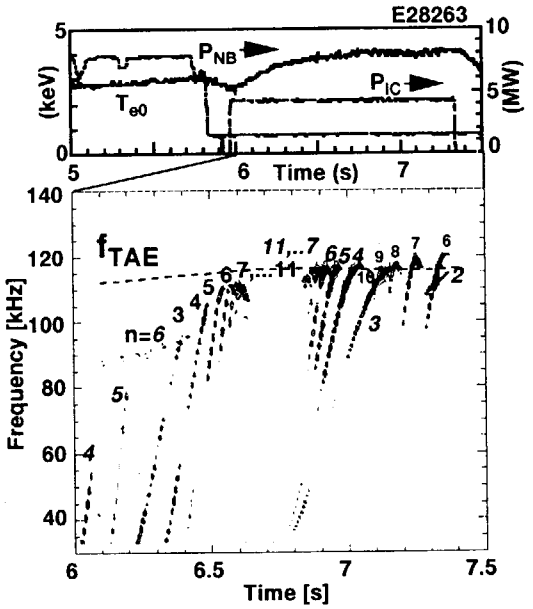

Fig. 1: Chirping modes observed in a weak negative-shear discharge. Four series of modes are distinguished with different styles of numbers showing toroidal mode numbers. Theoretically predicted TAE mode frequency f_{TAE} is shown with a broken line.

References

[1] H. Kimura, et al., accepted for publication in Nucl. Fusion.

[2] Y. Kusama, et al., submitted to Nucl. Fusion.

[3] M. Saigusa, et al., Plasma Phys. Control. Fusion **37** (1995) 295.

[4] S.T. Tsai, and L. Chen, , Phys. Fluids B **5** (1993) 3284.

---

present address; [1] Ibaraki University, Hitachi-city, Ibaraki-ken, 316 Japan.

[2] JAERI Research Fellow, [3] Princeton Plasma Physics Laboratory, Princeton University.

4.8 Amplitude of TAE modes

K. Tobita, G.J. Kramer, Y. Kusama

1. Introduction

Study of the growth rate of TAE modes is of great importance for validating theory on the drive and damping of the modes. Furthermore, the nonlinear evolution of the modes provides a key to understanding why TAE modes saturate. For ICRF-driven TAE modes on TFTR, a comparison between experimental results and nonlinear theory was made [1], which concluded that the nonlinear theory based on wave-particle trapping explained the evolution of the amplitude of a single TAE mode near the instability threshold. As a matter of fact, since TAEs and their impact on the plasma have a wide variety, this kind of work should be proceeded to clarify the nonlinear behavior of TAEs.

As far as the observations on JT-60U go, TAE modes always evolve slowly (of the order of 0.1 s) , which suggests that the mode amplitude follows slow changes in plasma parameters such as q(r). For this situation, we focus on the mode amplitude rather than the growth.

2. ICRF-driven TAE

One of the most interesting results on TAE is multiple modes observed in plasmas heated by ICRF fast waves at the 2nd harmonic cyclotron frequency of the hydrogen minority ions. When the modes were unstable at $q > 1$, low n (= 3 and 4) TAE modes appeared and the n number increased with time as shown in Fig. 1 (a). In contrast, when the modes were destabilized at $q < 1$, higher n (= 11 to 5) modes emerged and disappeared by turns; in addition, four modes (multiple modes) with different n numbers appeared at the same time. In these two shots with $P_{IC} = 4$ MW and $P_{NBI} = 2.5$ MW, the difference in q comes from I_p rather than r, and the location where the TAE modes are unstable is the plasma core region. As pointed out before [2], the multiple modes accompanied a definite loss of 3 MeV protons which is seen in neutron drops during the appearance of the modes in Fig. 1. Mode amplitude in Fig. 1, which is defined by

$$B = \int_{f_{\min}}^{f_{\max}} \frac{v(f)}{2\pi f N_{turn} A}\, df \;/\; \int_{f_{\min}}^{f_{\max}} df$$

with the number of Mirnov coil turns, N_{turn}, and the measuring area of a Mirnov coil, A, indicates that decreasing n raises the mode amplitude. This result denies a previous claim [3] that the mode amplitude increases with n. It should be noted that the different modes does not necessarily reflect the relative amplitude between the modes. Because the amplitude of higher n modes internally localized is difficult to detect with Mirnov coils equipped on the first wall. Considering this point, the amplitudes of the TAE modes in Fig. 1 (a) and (b) are almost the same.

Neutron emission, S_n, which is believed to reflect the number of protons with energies above 3 MeV, is suppressed by n = 3, 4 modes in Fig. 1 (a), while a large drop in S_n is observed in Fig.1 (b) showing multiple modes (n = 5 to 11) excitation. Such a large loss of the energetic protons is probably not due to 'mode overlap', but probably due to the superposition of fast ion response (chaotic orbit) in a single TAE mode. Because, theoretically, when mode overlap takes place, the mode amplitude should explosively grow up, leading to the pulsation of TAE modes. The observations that the modes saturate on a level comparable with a single mode (n =3) as seen in Fig.1 (a) and that the energetic particle loss increases gradually in the time scale of 0.1 s, does not match to the anticipated consequences of 'mode overlap'.

3. NNB-driven TAE

By 360 keV NNB injection at 2 MW into He plasmas, low n TAE modes were observed [4] . The amplitude of the TAE modes changes slowly with a typical time scale of ~0.1 s. The observed mode amplitude is much smaller than ICRF-induced TAE modes. Build-up of NNB ions is not responsible for the slow growth of the modes. Because calculation using an orbit following Monte Carlo indicates that the volume-averaged beta of the fast ions, $<\beta_h>$, already reaches a steady state at the onset of the n = 2 TAE mode (Fig. 2). As pointed out in Section 4.2, the threshold value of $<\beta_h>$ for mode excitation seems considerably small compared with DIII-D and TFTR experiments. Because of a small beam width of NNB, the radial profile of NNB fast ion beta has steep gradients which may be a cause for the onset at comparatively low $<\beta_h>$ (Fig. 3).

4. Summary

Systematic study of the mode amplitude has not yet carried out. We do not understand well how TAE modes evolve and saturate, nor what determines the toroidal mode numbers of TAE modes, nor how dangerous high n TAE modes (which will be unstable in ITER) are in the point of view of fast ion confinement. The study presented here is only the initial work, but aims to answer these questions eventually. For the purpose, the expansion of the parameter space for NNB-driven TAE modes is required.

References

[1] K.L. Wong et al., Phys. Plasmas **4** (1997) 393.
[2] M. Saigusa et al., to be published.
[3] H. Kimura et al., Phys. Lett. A **199** (1995) 86.
[4] Y. Kusama et al, in this Report, Section 4.2.

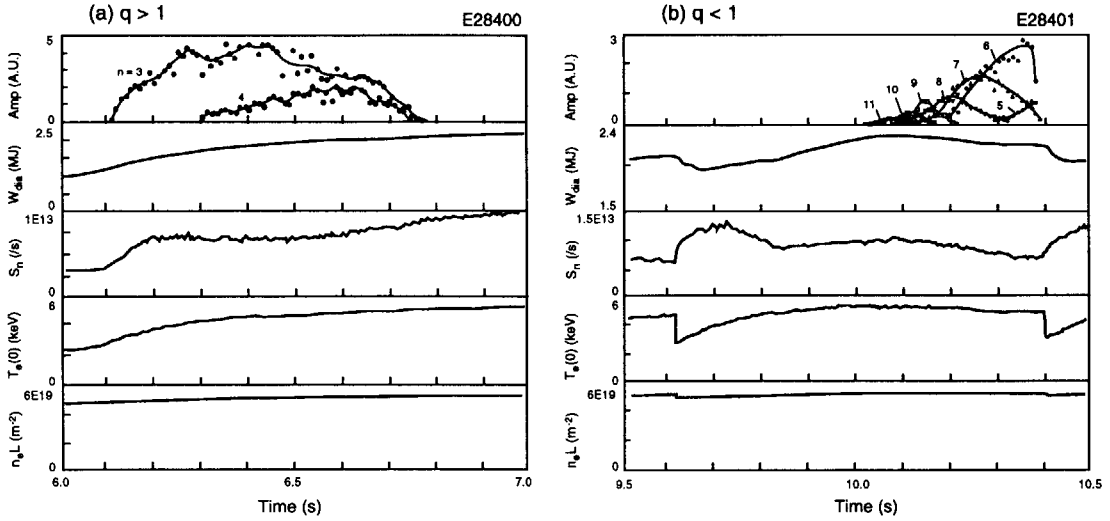

Fig.1 Evolution of ICRF-induced TAE modes excited in (a) q > 1 and (b) q < 1.

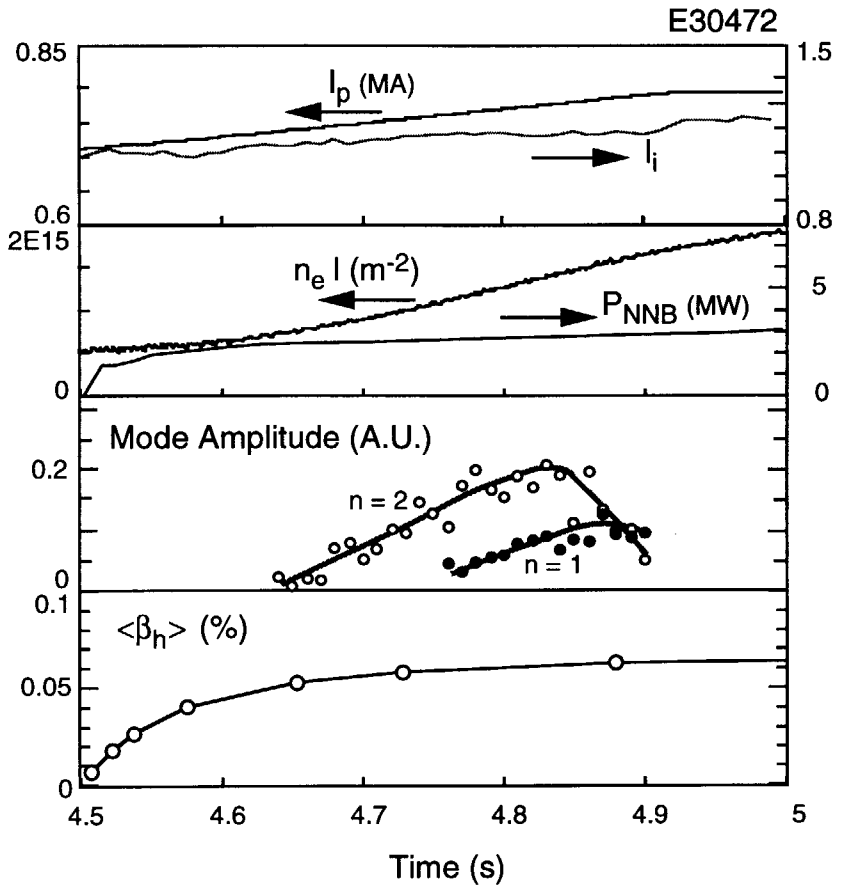

Fig.2 Evolution of the amplitude for n = 1 and 2 TAE modes appearing in N-NBI heating.

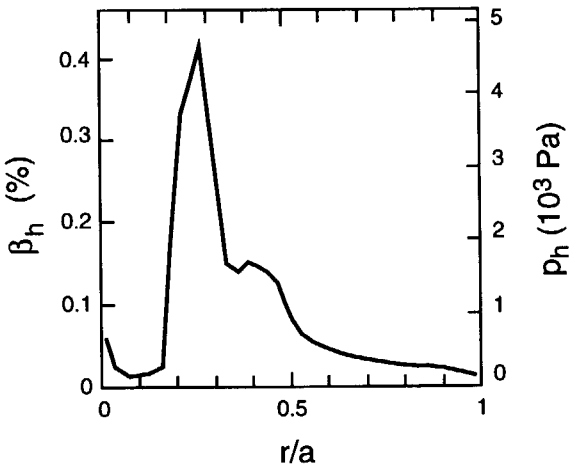

Fig.3 Calculated fast ion beta (or fast ion pressure) for NNBI in Shot E30472 in the steady state as a function of the radius.

4.9 ICRF coupling in W-shaped divertor configuration

S. Moriyama and N. Asakura

4.9.1 Optimization of the shape of the plasma for ICRF coupling

Shape of the plasma was optimized for ICRF coupling. The gap between the antenna and separatrix was tried to kept constant in front of the antenna, and kept around 6 cm - 15 cm. We paid attention to keep at least 3 cm of the gap at the outer baffle plate of W-shaped divertor under the antenna in order to reduce plasma wall interaction there, by means of adjusting the height of the X-point. Typical parameters for ICRF coupling experiments were plasma current = 1.7 MA, toroidal magnetic field on the axis = 3.34T, triangularity = 0.28, and plasma volume = 80 m^3.

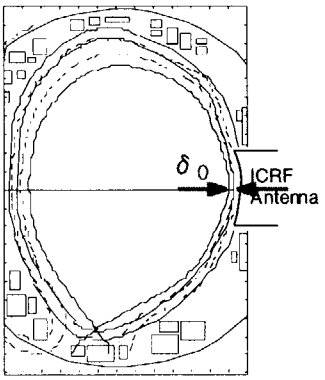

Fig. 1 Configuration with open divertor for ICRF coupling

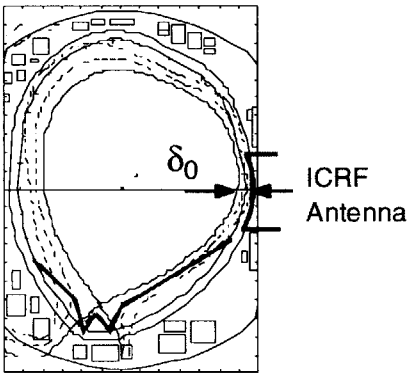

Fig. 2 Configuration with W-shaped divertor for ICRF coupling

4.9.2 Antenna coupling resistance

To evaluate the antenna - plasma coupling, coupling resistance (R_C) is often used. R_C is defined as $R_C = 2PZ^2V_{max}^{-2}$, where P is the input power to the antenna, Z the characteristic impedance of the coaxial line in the antenna, and V_{max} the maximum RF voltage of the standing wave on the coaxial line in the antenna. When high R_C is obtained, high power can be coupled to the plasma with low RF voltage at the antenna. As a result of optimization of the plasma shape, reasonably high R_C was obtained with W-shaped divertor[1]. The R_C is not so different from that of open divertor case as shown in Fig. 3. About 2.5 Ω of R_C was obtained with around 10 cm of first wall - separatrix gap at the antenna (δ_0). When the breakdown voltage of the antenna is 40 kV which was obtained in the antenna conditioning in vacuum, 6.4 MW will be coupled to the plasma with 10 cm of δ_0.

4.9.3 Scrape off layer (SOL) density distribution

SOL measurement by a reciprocating probe[2] shows that the gradient of the SOL density of closed divertor plasma optimized for ICRH was close to that of open divertor plasma as shown in Fig.4. Unfortunately the density just in front of the antenna (2nd SOL) was not measured because of fluctuation of the ion saturation current of the probe, however it may have the same tendency with the open divertor case because the measured coupling resistance was similar.

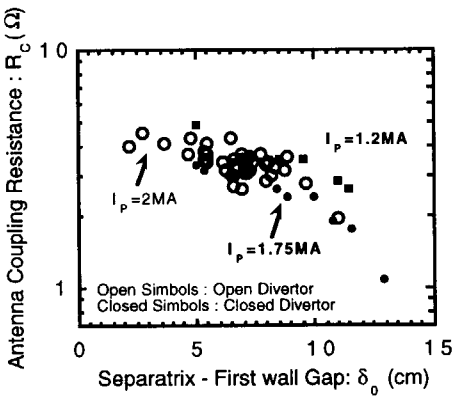

Fig. 3 Coupling resistance with W-shaped divertor was similar to that with open divertor.

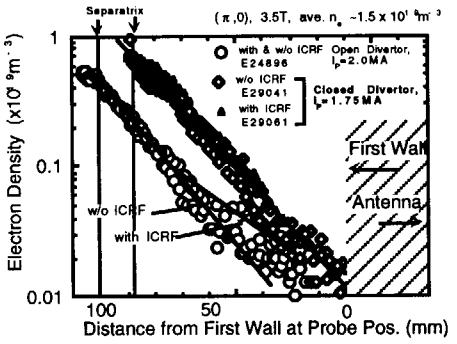

Fig. 4 SOL density gradient with W-shaped divertor was similar to that with open divertor.

4.9.4 Antenna aging with W-shaped divertor plasma

Coupled power of 1 MW for 1.5 sec and 5.1 MW for 50 ms were obtained after only 6 days' antenna aging after divertor modification. In September, 4 MW for 1.5 sec and 4.3 MW for 1 sec were achieved, and 4 MW of ICRF power was routinely coupled to the plasma for the experiments on ICRF heating of reversed shear plasma[3].

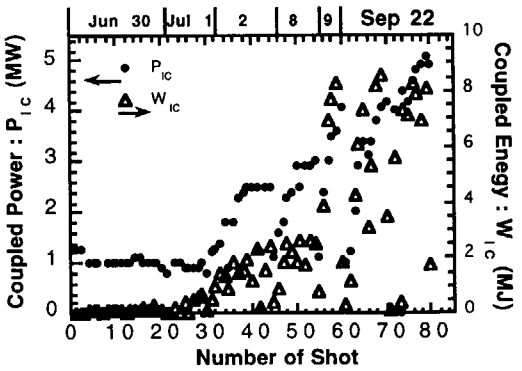

Fig. 5 Progress of the coupled ICRF power and energy with W-shaped divertor.

4.9.5 Summary

After a optimization of the plasma shape suitable for ICRF coupling, reasonably high coupling resistance (R_C) was obtained with W-shaped divertor. The Rc is not so different from that of open divertor case. It is consistent to the result of the reciprocating probe measurement which shows that the gradient of the scrape off plasma density in W-shaped divertor case is similar to that in open divertor case. About 2.5 Ω of R_C was obtained with around 10 cm of first wall - separatrix gap at the antenna. As a consequence of obtained relatively high R_C, 4 MW of ICRF power was routinely coupled to the plasma for the experiments on ICRF heating of reversed shear plasma

References

1) S.Ide, S. Moriyama, et al., "RF Experiments on JT-60U", Contributed paper of 2nd Europhysics Topical Conference on Heating and Current Drive in Fusion Devises, Brussels, January. 1998.

2) N. Asakura, S. Tsuji-Iio, Y. Ikeda, Y. Neyatani, M. Seki, "Fast reciprocating probe system for local scrape-off layer measurements in front of the lower hybrid launcher on JT-60U", Rev. Sci. Instrum.

3) M. Iwase et al, "ICRF heating of reversed shear plasma ", 4.11 of this report.

4.10 Application of ICRF to reversed shear after divertor modification

Y. Koide, K. Tobita, M. Iwase, S. Moriyama, M. Nemoto, Y. Kusama and H. Kimura

1. Introduction

This paper describes application of ICRF heating to reversed shear configuration after divertor modification to W-shaped one (Section 3.5 and 4.11 deal with experiments before the modification.). One of advantages of ICRF heating is its core electron heating which can make it easy to detect χ_e reduction. Unfortunately results are not satisfactory to date, which is mainly due to severe impurity radiation: ITB is produced in discharges with higher heating power, however, such discharges are disruptive; lower heating power results in no clear ITB. Status of the experiments are described in the following.

2. Electron heating by ICRF

Heating scheme of ICRF is 2nd harmonic minority heating. In typical discharges with ICRF pulse, acceleration of high energy ions up to 500 keV was detected by neutral particle analyzer. We consider that the origin of the fast ions is neutral beams for heating, the original energy of which is ~80 keV. This idea is based on numerical calculation by Fokker-Planck code combined with wave equation[1], where 90% of ICRF power is directly absorbed by beam ions. Energy of these fast ions is transferred to electrons as follows. Fraction of the initial fast ion energy (E_0~500 keV) which goes to electrons (F_e) is expressed as

$$F_e \equiv \frac{1}{E_0}\int P_e dt = 1 - \int_0^{E_0/E_c} \frac{E_c d(E_0/E_c)}{1+(E_0/E_c)^{3/2}}$$

where E_c is critical energy

$$E_c \equiv 14.8 Z_b^{4/3} A_b T_e [\mathrm{keV}] \left(\sum_i \frac{Z_i^2 n_i}{A_i n_e} \right)^{2/3}.$$

E_c is estimated to be 24 keV for typical target plasmas (T_e=3.5 keV, $n_e = 3.6\times10^{19}\,\mathrm{m}^{-3}$, $n_H \sim n_{He}$ from balance of H-beam fueling and He-gas fueling). The relatively low E_c is ascribed to the presence of He ions, which enhances electron heating compared with pure hydrogen case.

3. Experimental results

Reversed shear configuration was produced using early neutral beam injection (H^0 beam into H^+ and He^{2+} mixture) in the initial current ramp (t < 5.3 s). Beam power was stepped down during current flattop (t > 5.3 s), when ICRF of 4 MW was injected for 1 to 1.5 s (Fig. 1). When we injected much more pre-heating NB power (t < 5.3 s) than that in the figure, clear ITB was formed during the pre-heating phase, however, such plasmas were very disruptive

and had poor reproducibility; NB power level in the current flattop phase was fixed at just below 10 MW, above which collapse in T_e occurred without ICRF injection (E30443). Plasma configuration is shown in Fig. 2 (solid line: I_p=1.6 MA, B_t=3.5 T, q_{eff}=4.6). The B_t was determined from central resonance condition for ICRF frequency (102 MHz); I_p was limited in order to keep moderate q_{eff}, below which discharges became unstable due to unexpected change in q_{eff} close to 4.0.

We observed, during ICRF pulse, that central T_e increased, while T_e in the outer region slightly decreased (Fig. 1(b)). This feature is a temporal criterion for ITB formation because it suggests an interruption of heat flow. After that, however, we found it difficult to conclude that decrease in T_e(0.5) and T_e(0.74) by ≤0.1 keV during ICRF is due to ITB formation. This is because they naturally decreased independently of ITB formation by ~0.1 keV (Fig. 3). We speculate that the relaxation of $T_e(\rho)$ was due to change in ohmic heating profile from hollow to centrally peaked one, which idea is supported by increasing internal inductance (l_i) with time (Fig. 1(c)). Therefore we must estimate all of the deposition profiles of OH, NB and ICRF in order to discuss transport reduction, which will be future study.

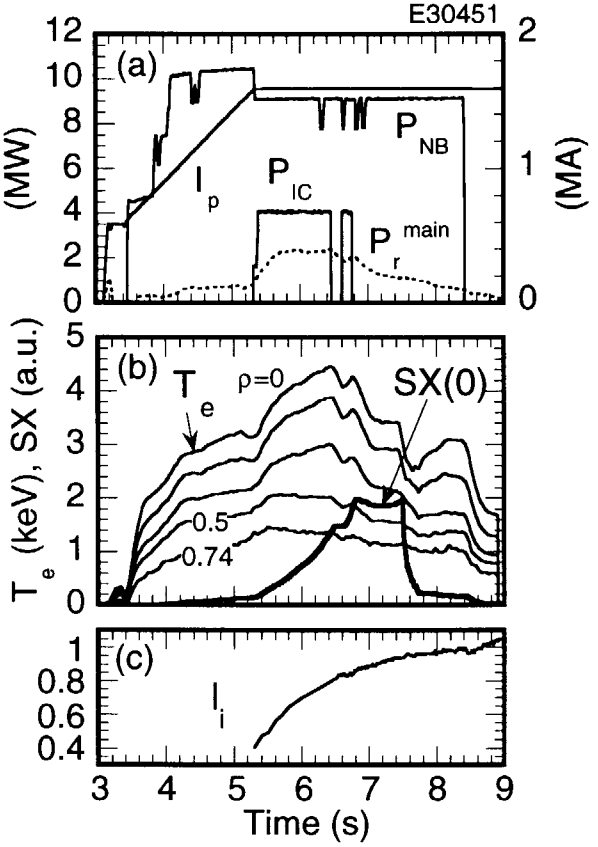

Fig. 1 Evolution, (a) plasma current, NB and ICRF power, total radiation power, (b) electron temperature and central soft X-ray intensity, (c) internal inductance.

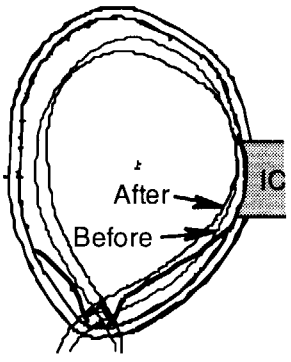

Fig. 2 Plasma configurations before and after divertor modification.

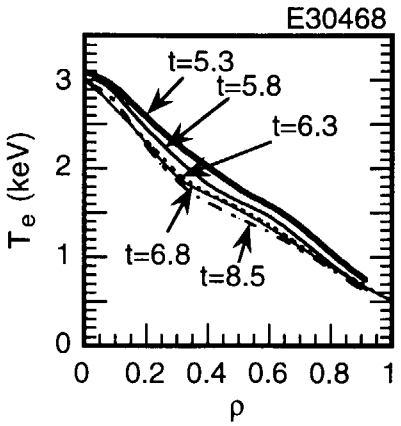

Fig. 3 Natural relaxation of electron temperature profile without ICRF.

Next we carried out a scan of start timing of ICRF pulse by a time step of 0.5 s (t_s=5.3, 5.8 and 6.3 s) in order to change q(ρ) at the onset of ICRF pulse, where l_i at t_s for the three is 0.4 (hollow j(ρ)), 0.7 and 0.84 (peaked j(ρ)), respectively. In order to highlight the effect of ICRF, incremental portion ($\Delta T_e(\rho) \equiv T_e(\rho)^{IC+NB} - T_e(\rho)^{NB}$) was analyzed, where $T_e(\rho)^{NB}$ is base T_e shown in Fig. 3, by which uncertainty due to the above-mentioned natural change in $T_e(\rho)$ may be removed. In Fig. 4, evolution of central ΔT_e of three discharges is compared, where horizontal axis is shifted accordihng to the difference in t_s. Earlier ICRF injection (t_s =5.3 s) lead to lower rate of rise in ΔT_e, which may be due to lower confinement of fast ions due to lower B_p. It should be noted that decay time of ΔT_e after ICRF pulse for the three cases is almost identical between them, suggesting that central confinement does not depend on l_i i.e. q-profile.

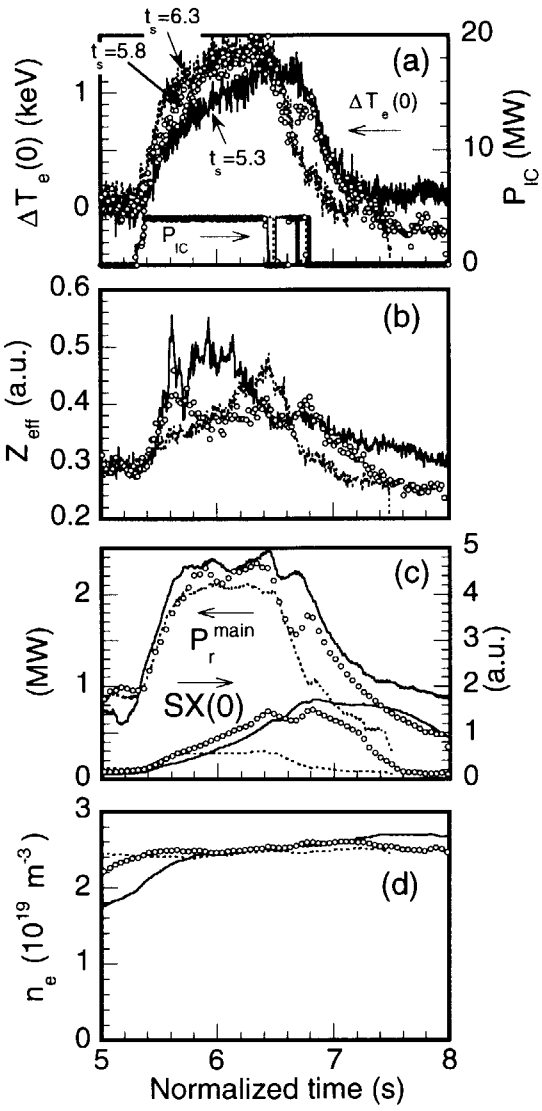

Fig. 4 Comparison of three discharges with different timing of ICRF injection. (a) incremental central electron temperature and ICRF power, (b) effective ionic charge, (c) total radiation power and central soft X-ray intensity, (d) line-average electron density.

4. Severe impurity radiation

Total radiation power (P_r^{main}) increased during ICRF pulse (Fig. 4(c)). As seen from Fig. 1(a), 50% of ICRF power is lost through radiation power. Central soft X-ray emission (SX(0)) also increased during ICRF (Fig. 4(c)), which seems to be due to Cu radiation (Fig. 5). We speculate that accelerated ions bombarded Cu material of ICRF launcher, leading to enhanced Cu radiation in the central region; the higher SX level with lower l_i may be attributed to poor confinement of fast ions in lower B_p. The contamination level of Cu seemed to be high enough to induce thermal collapse (see sudden decrease in T_e at t=7.5 s in Fig. 1(b)). This impurity contamination leads to different heating and cooling power fractions between the three cases, which made it complicated to discuss q(ρ) dependence on ITB formation. Figure 4(b) shows evolution of Z_{eff}, which is simply defined as

$I_{brems}(0)\sqrt{T_e(0)}/\left(\int n_e dl\right)^2$. In the case of the lowest l_i (solid lines), higher Z_{eff} was sustained in the post ICRF period of t > 7.2 s, which is consistent with sustainment of higher P_r^{main} and SX(0). The higher Z_{eff} with similar n_e (Fig. 4(d)) leads to higher heating power, which is likely explanation of higher $\Delta T_e(0)$ in the period (a solid line in Fig. 4(a)).

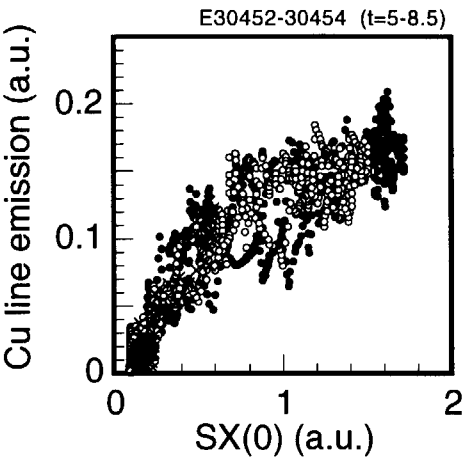

Fig. 5 Correlation of Cu line emission and central soft X-ray intensity.

5. Summary

We tried to investigate ITB formation under electron heating by ICRF after divertor modification, however, clear results were not obtained to date, which is partly due to severe impurity radiation and is partly due to poor confinement of fast ions due to low B_p. One of effective way to increase B_p with keeping reversed shear is to increase I_p, however, it is limited by q_{eff}. Increase in B_t together with ICRF frequency is another option, which leads to less machine time. Negative NB (~350 keV) with long pulse may improve this situation.

References

1) K. Hamamatsu et al., Nucl. Fusion **29**, 147 (1989).

4.11 ICRF heating of revsersed shear plasmas in JT-60U

M. Iwase, Y. Koide, K. Tobita, S. Moriyama, Y. Kusama, H. Takenaga, H. Shirai, M. Nemoto, A. Morioka, T. Fujita, Y. Kamada, T. Oikawa, G. J. Kramer

1 Introduction

High performance plasmas with an internal transport barrier (ITB) have been produced in reversed magnetic shear (RS) configuration. These plasmas were produced and sustained by NBI heating which supplied particles into the central region and transferred the energy mainly to ions. The sustainment of ITB by the ICRF minority heating is an important subject for the investigation of a future tokamak reactor where particle fueling in the central region is difficult and electron heating by α particles is dominant.

In JT-60U, ITB was maintained even in the case where the input power of ICRF heating is larger than that of NBI heating. It was shown that the particle fueling is essential for the sustainment of the large gradient in the profile of the electron density (n_e).

2 Experiment

The second harmonic ICRF minority heating was applied to RS plasmas[1] consisting of hydrogen and helium 4. The frequency of ICRF corresponds to the second cyclotron harmonic of a hydrogen ion. The target RS plasmas were produced by hydrogen beams in the ramp-up phase of the plasma current (I_p).

Fig.1(a)-(d) show typical waveforms of a RS discharge with the toroidal magnetic field on the axis (B_t)=3.5 T, I_p=2.0 MA. While I_p reaches a flat top value, P_{NB} is reduced. ICRF wave is injected 0.2s after the reduction of P_{NB}.

The solid lines in Fig.1(a)-(c) show the low particle fueling case where ICRF power (P_{IC})=4.0 MW and NBI power (P_{NB})=2.0 MW are injected into the plasma. Owing to the decrease of P_{NB}, the line integrated electron density ($n_e l$) of the central code drops. On the other hand, the electron temperature (T_e) and the ion temperature (T_i) at the center increase during ICRF heating.

P_{NB} is scanned shot by shot as shown in Fig.1(d). The dashed lines in Fig.1(a)-(c) correspond to the shot of P_{NB}=5.0 MW with ICRF heating at 4.0 MW. In this case, $n_e l$

keeps constant value during ICRF heating. However, the disruption occurs because the pressure gradient increases.

3 Effect of central particle fueling on n_e profile

In order to study the relation between the reduction of central n_e and the amount of central particle fueling, the number of NBI beam is scanned. Fig.2(a)-(d) give profiles of T_e, T_i, n_e and the safety factor (q), respectively. The open circles show the case where P_{IC} is larger than P_{NB} (ICRF heating at 4.0 MW with NBI heating at 2.0 MW), and the closed circles show the case of NBI heating only at 6.0 MW is applied to the plasma. In both cases, the configuration of the plasmas and other experimental conditions are almost the same. The amount of particle source inside the ITB ($\rho \sim 0.4$) for each case are $7\times10^{19}s^{-1}$ (for NBI at 2.0 MW) and $22\times10^{19}s^{-1}$ (for NBI at 6.0 MW) from the calculation with an OFMC code.

The large gradients in T_e and T_i profiles clearly indicate the existence of ITB during ICRF heating. In spite of that, the gradient in n_e profile diminishes. These figures lead to the conclusion that large gradients in T_e and T_i profiles can be maintained even in the low fueling condition. The apparent degradation of central n_e during ICRF heating is attributed to the decrease of the central particle fueling.

4 Summary

It was confirmed that ITB created by the NBI heating can be sustained even in the case where P_{IC} is larger than P_{NB}. The central particle fueling is essential to maintain the large gradient in n_e profile. Further data analysis of high power experiments is required for the detailed investigation of particle fueling effects on the plasma with ITB. It is necessary to verify whether the particle fueling can reproduce the steep gradient in n_e profile.

References

1) Kimura H. et al., Plasma Phys. Contrl. Nucl. Fusion Research (Proc. 16th IAEA Fusion Energy Conf., Montréal, 1996), paper F1-CN-64/E-6.

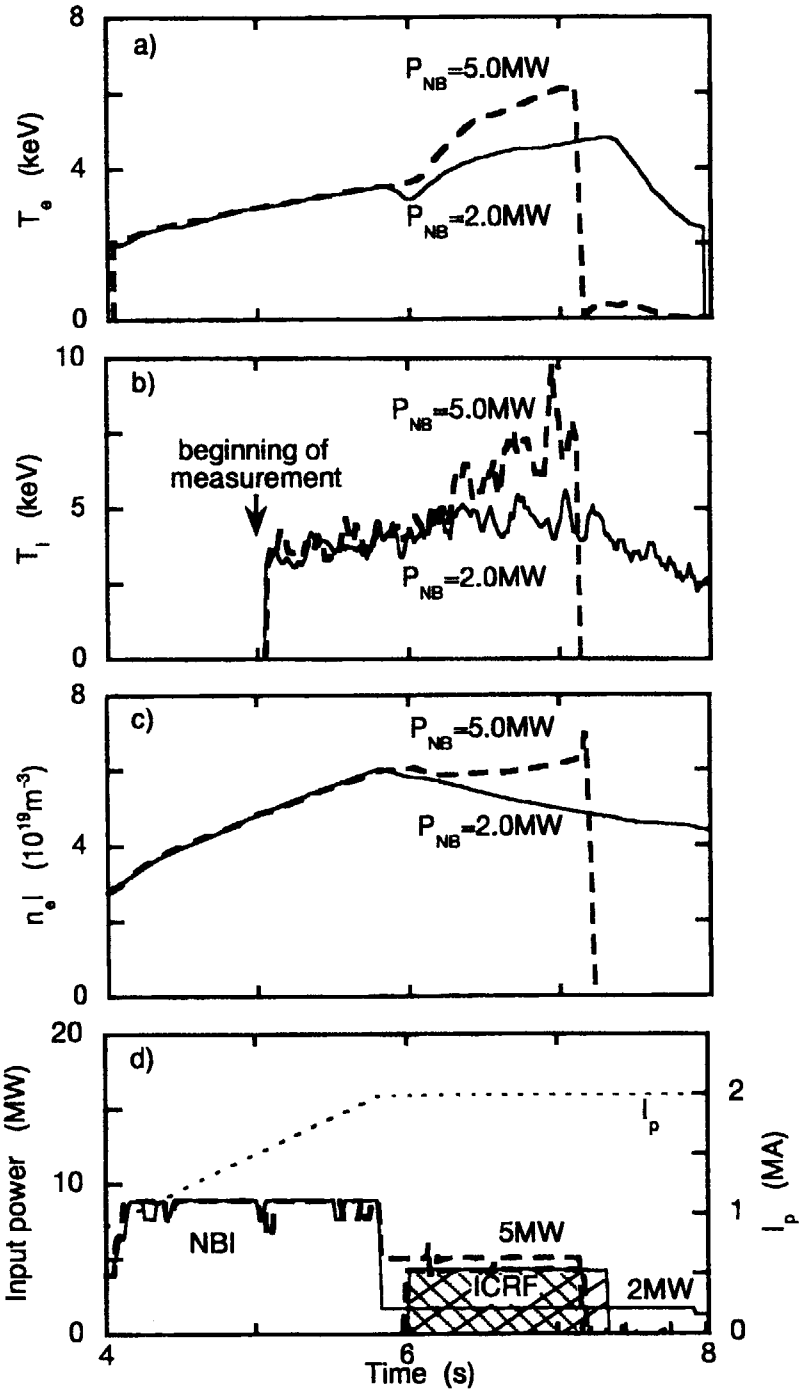

Fig.1 Time evolutions of plasma parameters during ICRF heating at 4.0MW. The solid lines show the case with NBI heating at 2.0MW, and the dashed lines give the case with NBI heating at 5.0MW. a) Time evolution of the central T_e. b) Time evolution of the central T_i. c) Temporal change in $n_e l$ of the central code. d) The heating power of NBI and ICRF for two cases are shown. The thin dotted line shows I_p. T_e and T_i increase durig ICRF heating in both cases. $n_e l$ during ICRF heating in the case of 2.0 MW NBI heating decreases from the lack of the central particle fueling. In the case of NBI heating at 5.0 MW, $n_e l$ is kept constant value successfully.

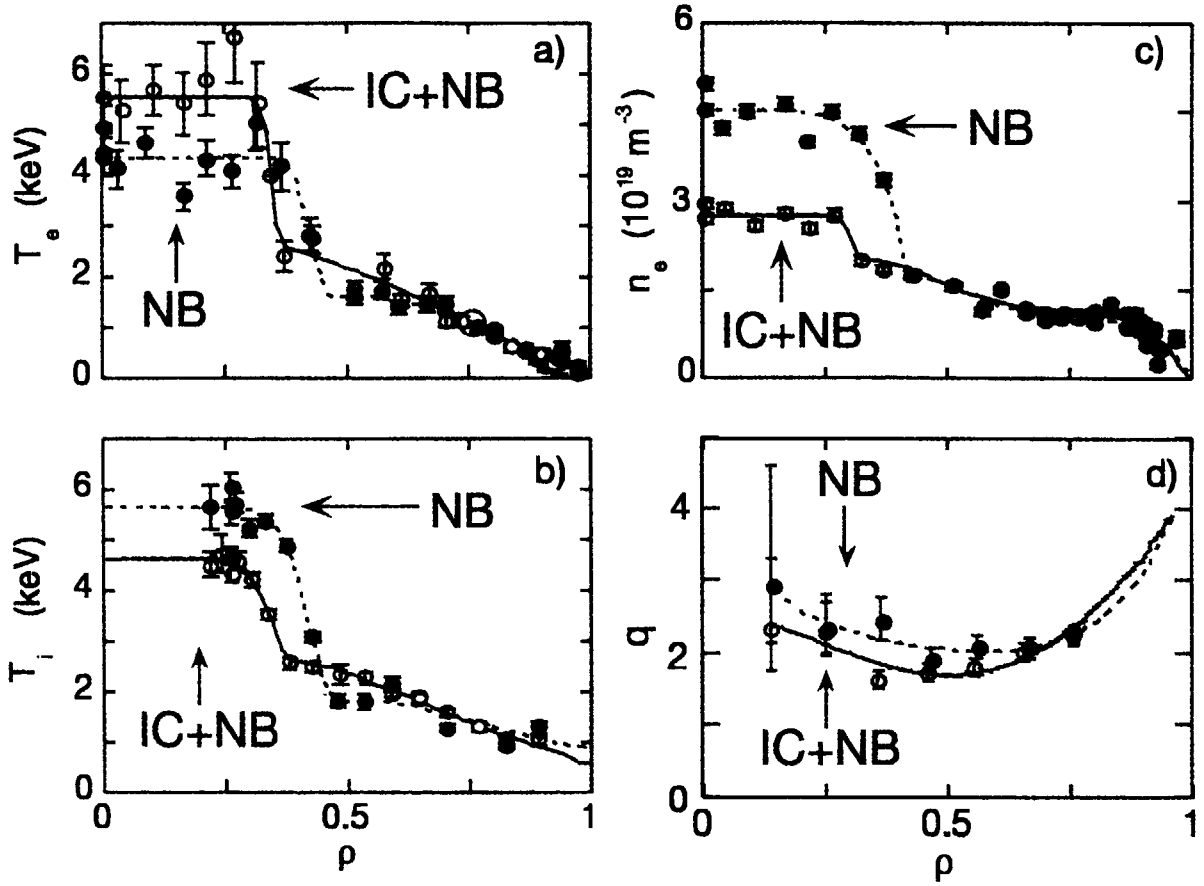

Fig.2 Radial profiles of plasma parameters. The closed circles show the case of the NBI heating only at 6.0 MW. The open circles give the case where the NBI heating at 2.0 MW and the ICRF heating at 4.0 MW are injected into the plasma. The total input power is the same for both cases, but the amount of the central particle fueling is different. a) Radial profile of T_e. b) Radial profile of T_i. c) Radial profile of n_e. d) Radial profile of q. Although the profile of q is almost the same, the value of n_e inside of the ITB is small in the case of the ICRF heating.

4.12 Magnetic shear effect on ICRF-produced fast ions

K. Tobita, M. Iwase, Y. Koide, S. Moriyama, T. Oikawa, Y. Kusama

1. Fast ions in revesed shear

In reversed magnetic shear plasmas, enhanced ripple transport is anticipated due to comparatively high safety factor q in the central region [1]. High q leads to the expansion of banana orbits and an effective rise in TF ripple amplitude along magnetic field lines, eventually enhancing ripple transport. In ITER advanced operational scenario based on reversed shear, neutral beam ions deposited and alpha particles created in the peripheral plasma can be lost from the plasma. In comparison, for ICRF-produced fast ions, the revesed shear effects seem to be less important because the fast ions are produced in the core where TF ripple is low enough.

In recent experiments on JT-60U, we investigated magnetic shear effects on ICRF heating. This note describes the result, pointing out the importance of magnetic shear on fast ion density profile.

2. Experiment and results

2.1 Experimental conditions

The target plasma was produced by a standard reversed shear set-up, i.e. fast I_p ramp-up with early NBI heating. Just after I_p reached a flat-top, NBI power was stepped down from 10.5 MW to 9 MW to avoid a collapse and then ICRF was turned on with a certain time delayed. By the delay of ICRF heating, we intended to change the magnetic shear of the target plasma. As a matter of fact, the magnetic shear changes from strongly reversed shear to monotonic revesed shear as time evolves in the I_p flat-top. ICRF waves of 4 MWheat hydrogen minority ions in He plasma at 102 MHz ($2\omega_{cH}$) .

2.2 Experimental results

Figure 1 is the time evolution of T_e at different radii for no delayed heating, which corresponds to a strongly reversed shear target. The figure shows T_e rise in the central region (r = 0.02a and 0.16a) by ICRF-produced fast ions whereas small T_e rise is observed in the peripheral plasma (r = 0.63a and 0.86a). At r = 0.43a, Te increases just after ICRF turns on, and T_e ceases to increase 0.3 s after the ICRF onset. These time evolution of T_e suggests that electron heating profile by ICRF-produced fast ions varies as the magnetic shear changes with time. In fact, T_e profiles during ICRF heating shows a distinctive difference: Te profile peaks more in normal monotonic shear than in strongly reversed shear, as shown in Fig. 2.

Figure 3 shows the temporal evolution of T_e at r = 0 and 0.6a during ICRF heating. In normal monotonic shear, $T_e(0)$ increases rapidly, following which it saturates

in 0.4 s after the onset of ICRF heating. In contrast, $T_e(0)$ gradually rises during ICRF heating. The gradual increace in $T_e(0)$ in the strongly reversed shear is understood with the evolution of magnatic shear: The magnetic shear changes from strongly reversed to weakly reversed during ICRF heating as time evolves. In the normal shear case, ICRF heating is carried out well after the plasma current penetrates in the plasma and thus the magnetic shear unchanged during ICRF heating. As to $T_e(0.6a)$, the temporal evolution is basically the same in both magnetic shears. A slight decrease in $T_e(0.6a)$ in the normal shear probably comes from thermal transport like the equipartition between electrons and ions, which is out of interest in this research.

Representing the quantities soon after the onset of ICRF (the time interval, Δt) with prime ($T_e' = T_e^0 + \Delta T_e$, $P_{f\text{-}e}' = P_{f\text{-}e}^0 + \Delta P_{f\text{-}e}$, $P_{rad}' = P_{rad}^0 + \Delta P_{rad}$, where $P_{f\text{-}e}$ and P_{rad} stand for the power transferred from fast ions to electrons and the power lost by radiation, respectively, and the suffix '0' means quantities just before ICRF heating), $\Delta T_e/\Delta t$ is approximated as follows.

$$\frac{\Delta T_e}{\Delta t} \simeq \frac{2}{3n_e}\left[\Delta P_{f-e} - \Delta P_{rad} - \frac{1}{r}\frac{\partial}{\partial r}\left(r n_e \chi_e \frac{\partial \Delta T_e}{\partial r}\right)\right] .$$

In the equation, ΔP_{rad} is negligibly small in the early time of ICRF heating. Thus, the energy transfer from fast ions to electrons, which is originally from fast ion density, and the electron heat conduction are responsible for ΔT_e. Experimental $\partial T_e/\partial t$ profiles for various shears are shown in Fig. 4. Compared with reversed shears, the normal shear indicates an efficient T_e rise. As the magnetic shear reverses strongly, ΔT_e declines and the profile becomes hollow. Such T_e heating characteristics connected with magnetic shear seems to be attributed to the distribution of ICRF-generated fast ions. In strongly reversed shear with high q in the core, low poloidal magnetic field expands the banana width of fast ions, effectively reducing fast ion population in the core. There is a possibility that the hollow heating profile is partly due to enhanced ripple transport in the high q region. To identify the reason for the observation, a modified orbit following Monte Carlo code [2] would be useful, which has been developed to treat fast ion transport in a ripple magnetic field with the inclusion of ICRF wave-particle interaction [3].

3. Conclusions

In the ICRF $2\omega_{CH}$ minority heating experiments, we observed magnetic shear effect in T_e which is heated up by ICRF-produced fast ions. This suggests that, in strongly reversed shear, an expansion of banana orbits and/or enhanced ripple transport reduces fast ion population in the core, resulting in a hollow heating profile. The effect will be less important in a fusion reactor like ITER where the banana width of fast ions is much smaller than the minor radius. But, in order to predict the stability for descrete

Alfvén eigenmodes such as TAE modes, fast ion pressure profile must be delived with the inclusion of the shear effect. For the purpose, the observation should be compared with calculations to conclude if the experimental results can be simply explained with existing theory.

Refercences

[1] K. Tobita et al., Nucl. Fusion **37** (1997) 1583.

[2] K. Tani et al., J. Phys. Soc. Jpn. **50** (1981) 1726.

[3] K. Hamamatsu, private communication (Japan Atomic Energy Research Institute).

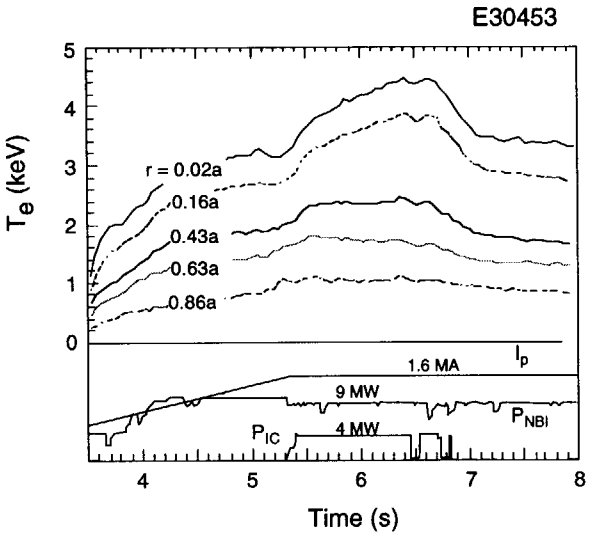

Fig.1 Time evolution of electron temperature in ICRF 2nd harmonic hydrogen heating.

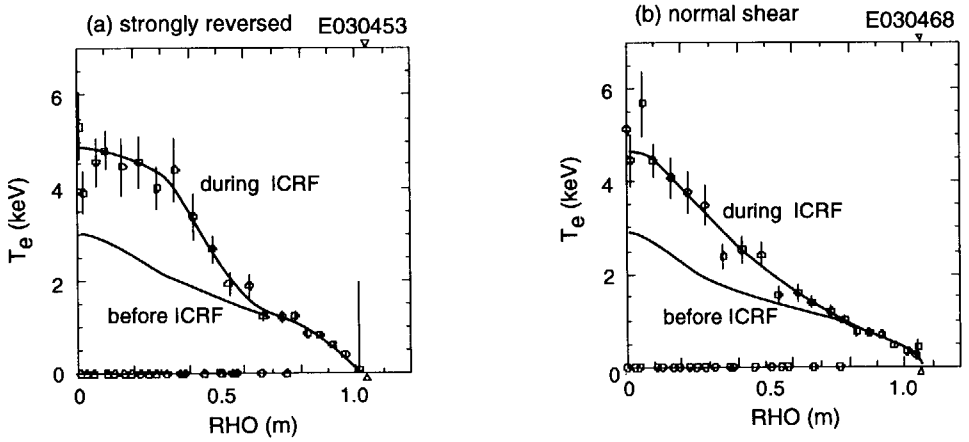

Fig. 2 Electorn temperature profiles before and during ICRF heating in (a) strongly revesed and (b) monotonic normal shear discharges.

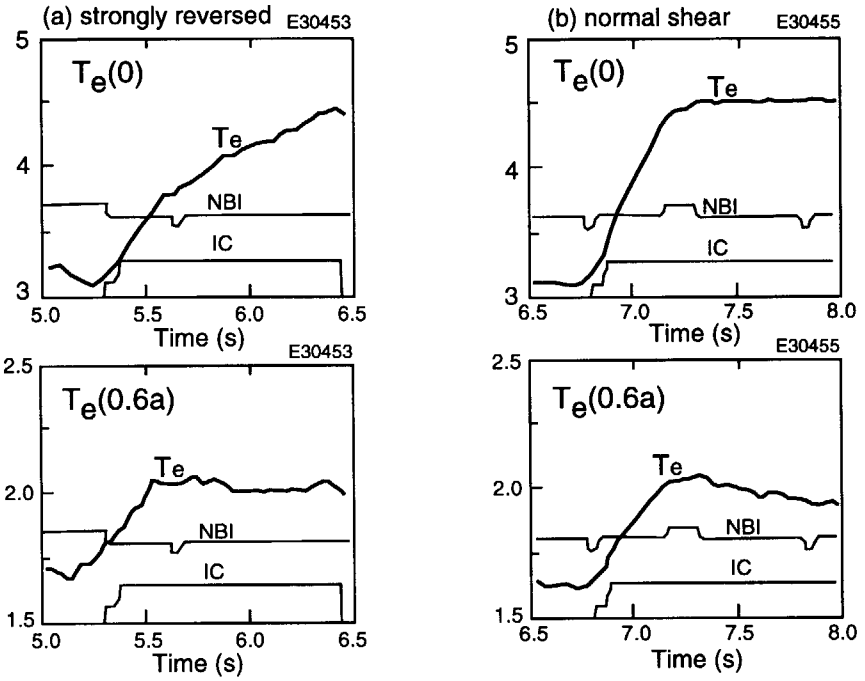

Fig. 3 Electron temperature rises at r = 0 and 0.6a during ICRF heating in (a) strongly revesed and (b) monotonic normal shear discharges.

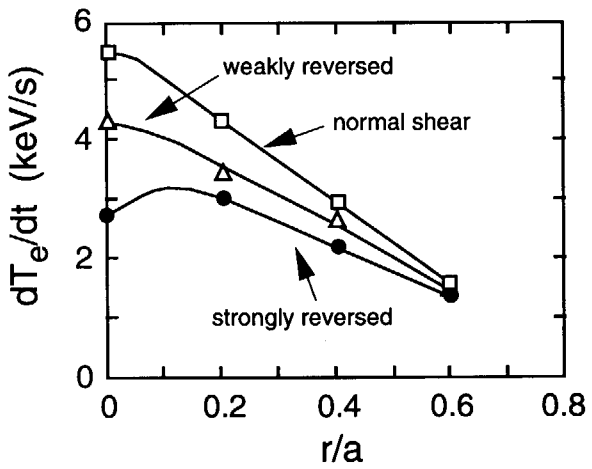

Fig. 4 Electron heating profiles by ICRF-produced fast ions just after ICRF turns on.

4.13 Experimental Scaling for Fast Ion Temperature during ICRF Heating

F.V. Tchernychev*, V.I. Afanassiev*, Y. Kusama, A.R. Polevoi•, M. Nemoto, A. Morioka, H. Kimura and S. Moriyama
*A.F.Ioffe Physical-Technical Institute, St. Petersburg, Russia
•RRC "Kurchatov Institute", Moscow, Russia

1. Introduction

Ion Cyclotron Range of Frequency (ICRF) heating is one of the methods to achieve burning conditions in thermonuclear plasmas. Therefore, the study of ICRF heating is important for the application to the tokamak reactors.

In JT-60U the study of energy distributions of ICRF-driven fast ions in the MeV energy range has begun in 1994 after the installation of the high energy Neutral Particle Analyzer (NPA) [1]. The measurements of fast particles were performed in various plasmas. Several dependencies of effective temperature of tail minority ions on plasma parameters were observed [2-4]. However, a general theoretical explanation of these dependencies was not found. In this paper we present the scaling for minority ion temperature based on a diffusive model of particle losses and we compare it with the ion temperature observed with the NPA.

2. Fast ion power balance

The power balance of minority ions during ICRF heating in a steady-state can be described by

$$3/2\ n_f T_f / \tau_{Tse} + 3/2\ n_f T_f / \tau_L = P_{IC} \qquad (1)$$

where n_f is fast particle density, τ_{Tse} is energy slowing down time on electrons, τ_L is fast ion confinement time and P_{IC} is IC power absorbed by fast ions per unit volume. The first term on the left hand side of equation (1) corresponds to the energy transfer from ions to electrons and the second term describes the particle losses.

2.1. Ideal case. Let us consider the ideal case, when all IC power is transferred from the ions to the electrons. In other words the slowing down dominates and $\tau_{Tse} << \tau_L$. Then, neglecting the second term in equation (1) we have the expression for the minority ion tail temperature obtained by Stix [5]

$$T_{stix} = 2/3\ P_{IC}\ \tau_{Tse} / n_f$$

Taking into account that τ_{Tse} is proportional to $T_e^{3/2}/n_e$ and assuming that $n_f = \alpha n_e$, we can evaluate the scaling for the fast ion temperature

$$T_f \propto P_{IC}\ T_e^{3/2}/n_e^2, \qquad (2)$$

where T_e and n_e are the electron temperature and density respectively. It is generally assumed that the fast ion temperature can be described by this scaling [5,6]. However, such a dependence was not observed experimentally in JT-60U. Figure 1 presents the temperature of fast ions measured by the NPA versus the Stix's parameter $P_{IC}\ T_e^{3/2}/n_e^2$. The data shown in

Fig. 1 was obtained during second harmonic ICRF heating experiments in D(H) and He(H) plasmas in which the plasma parameters (such as P_{IC} ,T_e, n_e and I_p) were varied. To exclude the difference between charge-exchange target for fast protons in He and D plasmas the ion tail temperature was estimated over the energy range where the carbon impurity target dominated [3]. As it is seen from the picture, there is no correlation between the experimental data and the temperature predicted by scaling (2). At the same time, the fast ion temperature seems to be dependent on *plasma current* I_p. As one can see, the high experimental values of temperature were observed with high plasma current and the low temperature values were observed with low current.

2.2. Low confinement case. To take into account this correlation between T_f and I_p let us examine another extreme case, when the temperature of minority ions is determined by particle losses rather than slowing down on electrons (i.e. $\tau_L << \tau_{Tse}$). Neglecting the first term in equation (1) we obtain

$$T_f = 2/3\, P_{IC}\, \tau_L / (\alpha n_e).$$

Assuming that a diffusive model of the particle losses is valid, we can describe the particle confinement time as $\tau_L = a^2 / D$, where a is plasma minor radius and D is coefficient of particle diffusion. For the present purposes it is not necessary to specify the mechanism of particle diffusion. It can be, for example, the diffusion due to stochastic ripple losses. An important fact is that the diffusion of ICRF-driven banana particles can be expressed as

$$D = \Delta^2 / \tau_d,$$

where Δ is banana orbit width and τ_d is diffusion time. Taking into account that $\Delta = r_c\, q\, /\varepsilon^{1/2}$ (r_c is giroradius, q is safety factor and ε is reversed aspect ratio), it can be shown that

$$\tau_L \propto \tau_d\, (I_p\, Z_f / k)^2\, (A_f T_f \varepsilon)^{-1},$$

where Z_f is fast ion charge, k is plasma elongation and A_f is fast ion mass. Adopting for simplicity that diffusion time is energy independent, we obtain

$$T_f \propto (2 / 3)^{1/2}\, Z_f / k\, (\tau_d / A_f \varepsilon)^{1/2}\, (P_{IC} / \alpha n_e)^{1/2}\, I_p.$$

And hence we have a following scaling for the fast ion temperature

$$T_f \propto I_p\, (P_{IC} / n_e)^{1/2}. \qquad (3)$$

In Fig. 2 the experimental values of the fast ion temperature are plotted against parameter $I_p\, (P_{IC} / n_e)^{1/2}$. This picture presents the same data as shown in Fig. 1 together with recently obtained data in normal shear plasma and also in reversed shear plasma. As can be seen from the Fig. 2, the normal shear data correlates well with the scaling (3). For the reversed shear case the model predicts enhanced losses of fast ions due to the increased safety factor in the plasma core ($D \propto q^2$). The measurements in reversed shear plasma give relatively lower values of fast ion temperatures predicted by the new scaling.

2.3. Heating efficiency. Even in the case of bad confinement when the losses dominate, some IC power is transferred from the fast ions to the electrons. Defining this part of IC power as the power which heats the Maxwellian plasma P_h, we can write

$$P_h = P_{i,e} = P_{IC} / (1 + \tau_{Tse} / \tau_L), \quad (4)$$

where $P_{i,e}$ is power transferred from ions to electrons per unit volume. Then the efficiency of heating η can be expressed by

$$\eta = Ph / P_{IC} = (1 + \tau_{Tse} / \tau_L)^{-1}. \quad (5)$$

In the case of low confinement we can write

$$\eta \approx \tau_L / \tau_{Tse}.$$

Which can be interpreted as follows: the heating efficiency is determined by the competition between the particle losses and the energy slowing down through the electron drag. Taking into account the expressions for τ_L and τ_{Tse}, we obtain

$$\eta \propto I_p (n_e / T_e)^{3/2} (P_{IC})^{-1/2}. \quad (6)$$

Thus we have a dependence of the heating efficiency on plasma parameters in the case of low confinement.

3. Numerical estimations

The efficiency of ICRF heating can be estimated independently from experimental results. The power transferred from the ions to the electrons can be obtained using measurements of electron density and electron temperature profiles:

$$P_{i,e} = 3/2\ \delta(\partial n_e T_e / \partial t),$$

where $\delta(\partial n_e T_e / \partial t)$ is the change of derivative $\partial n_e T_e / \partial t$ after switching-on of IC power. Then the total heating power is equal to the integral

$$Q_h = \int P_{i,e}(r) dV = 2/3 \int \delta(\partial n_e T_e / \partial t)(r)\, dV, \quad (7)$$

and the volume averaged efficiency of heating can be estimated as

$$<\eta> = Q_h / Q_{IC},$$

where Q_{IC} is the total ICRF input power. This estimation was performed for shot #23101 with highest tail temperature (see Fig. 2). The derivative $\partial n_e T_e / \partial t$ was evaluated during the linear phase after the sawtooth crash and the integral (7) was taken over the volume inside the inversion radius, assuming that all the IC power is absorbed there. From the Table 1 it can be seen that the heating power absorbed by the electrons in the central region of the plasma is about (25 - 35)% of the input IC power. (The range given here is the result of the uncertainty in profiles).

Table 1.

$n_e(0)$	$T_e(0)$	$T_{f\,(exp.)}$	τ_{Tse}	Q_{IC}	Q_h	$<\eta>$
$3.5 \cdot 10^{19}$ m^{-3}	4.2 keV	423 keV	0.15 s	4.66 MW	(1.16-1.38) MW	0.25-0.35

From expression (5), we can estimate also the averaged confinement time:

$$<\tau_L> \approx \tau_{Tse} / (<\eta>^{-1} - 1) \approx (50 - 80) \text{ ms}.$$

This indicates that the condition of low confinement ($\tau_L << \tau_{Tse}$), which was assumed to obtain scaling (3), is supported by the experiment.

The estimation of the heating efficiency presented above is for the plasma parameters at the center. The total amount of transferred heating power could be significantly lager than the estimated local value. The slowing down time τ_{Tse} decreases toward the plasma edge and the power transported from the center by fast ions can be absorbed by thermal electrons in the outer regions. Thus, the enhanced fast ion transport can cause a redistribution of the heating power initially absorbed at the center as well as an increase of power losses from plasma volume.

4. Summary

A scaling for the temperature of ICRF-heated ions based on a diffusive model for fast particle losses was obtained. The experimentally found dependence of fast ion temperature on plasma current is described well with this scaling.

The applicability of this approach was examined using measurements of electron density and temperature. It was shown that the power balance of ICRF-driven ions in JT-60U is close to the low confinement case, which was used in the evaluation of the scaling.

References

[1] Kusama, Y., et al., Rev. Sci. Instrum. 66 (1995) 339.
[2] Afanassiev, V.I., et al., 22nd EPS Conference on Plasma Phys. Control. Fusion (Bournemouth, 1995) vol. 19 C(II), 57.
[3] Afanassiev, V.I., et al., Plasma Phys. Control. Fusion 39 (1997) 1509.
[4] Nemoto, M., et al., Plasma Phys. Control. Fusion 39 (1997) 1599.
[5] Stix, T.H., et al., Nuclear Fusion 15 (1975) 737.
[6] Heidbrink, W.W., et al., Nuclear Fusion 34 (1994) 535.

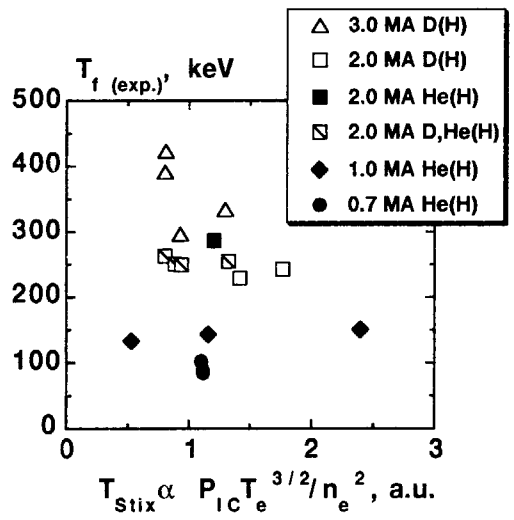

Fig.1
The temperature of fast minority ions measured with the MeV energy range NPA versus the Stix's parameter $P_{IC}T_e^{3/2}/n_e^2$ for normal shear plasma.

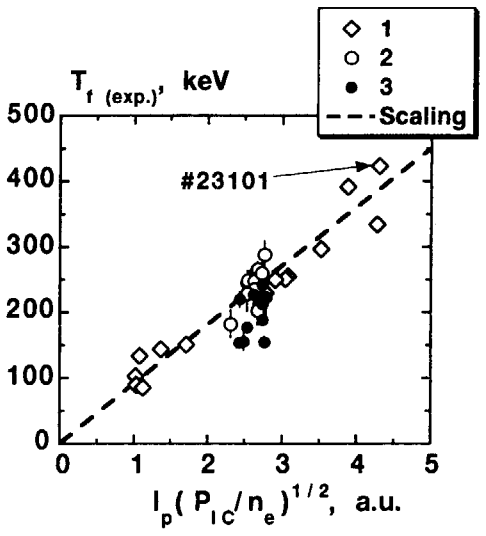

Fig.2
The temperature of fast minority ions versus the parameter $I_p(P_{IC}/n_e)^{1/2}$.
1 - the same data as in Fig. 1.
Newly obtained data:
2 - in normal shear plasma,
3 - in reversed shear plasma.
The dashed line is the scaling prediction.

4.14 CX Measurements of d-d Triton Distribution Function in High Power NB Heating[1)]

F.V. Tchernychev*, Y. Kusama, M. Nemoto, A. Morioka, K. Tobita, S. Ishida
*A.F.Ioffe Physical-Technical Institute, St. Petersburg, Russia

Measurements. We present the first results of d-d triton measurements in JT-60U using Neutral Particle Analyzer (NPA) of MeV energy range [2)]. The measurements were performed during experiments of high power Neutral Beam Injection (NBI). The plasma created in these experiments had significant d-d reactivity due to beam-plasma and plasma-plasma interactions. Because of a high level of neutron background, the experimental conditions were unfavorable for the triton observation during NBI. The energy distribution of tritons was measured after the decay of neutron background (from 0.5 to 1.0 s after termination of NBI).

Modeling. The time evolution of triton energy distribution after NBI termination was modeled by analytical solution of simplified zero-dimensional Fokker-Planck equation [3)]

$$f_t(t,v) = S_t(t,v)\ \tau_{se}\ (v^3 + v_c^3)^{-1}, \qquad (1)$$

where $S_t(t,v)$ is triton birth function, τ_{se} is slowing down time on electrons, and v_c is critical velocity (velocity at which the electron friction balances the ion friction). The variations in triton birth velocity due to thermal particle motion and due to geometry of experiment were taken into account in birth function. A qualitative comparison of experimental spectrum with solution (1) was performed. To obtain the agreement of experiment with model various possibilities of triton neutralization were examined. Triton neutralization in the plasma has been determined as a charge-exchange with mixed target, consisting of residual neutral deuterium d^0 and hydrogen-like impurity carbon C^{5+} [4)].

Summary. The passive signal of neutralized d-d tritons was reliably detected in the experiments of NBI in JT-60U. The energy spectrum of tritons was measured by MeV energy range NPA in (0.5-1.0) s after termination of NB heating. The agreement of experimental spectra with model based on the simplified Fokker-Planck equation was obtained in assumption of mixed neutralization target.

References

1) F.V. Tchernychev, et al., to be submitted to Plasma Phys. Control. Fusion.
2) Y. Kusama, et al., Fusion Engineering and Design 34-35 (1997) 531.
3) D.J. Sigmar, in Proceedings of the Varenna Course on Physics of Plasmas Close to Thermonuclear Conditions, Vol.1, Commission of the European Communities, Brussels (1980) 271.
4) V.I. Afanassiev, et al., Plasma Phys. Control. Fusion 39 (1997) 1509.

4.15 Confinement of Super-Thermal Ions in The Q_{DT} = 1.05 Discharge

K. Tobita, S. Higashijima, A. Isayama

1. Q_{DT} = 1.05 Shot

For the estimation of the equivalent fusion multiplication factor, Q_{DT}^{eq}, for the assumed D:T = 1:1 plasma, kinetic analysis is done to interpret consistently the measured D-D neutron emission, S_{DD}, and the stored energy, W_{dia}, using the measured plasma profile data. One of the most important quantities in the process to reach the consistent understanding of the experimental data is Z_{eff}. But Z_{eff} usually has no accuracy enough to determine the deuterium content. Therefore, the measured Z_{eff} is used to check a value of Z_{eff} inferred from reasonably matching of the kinetic analysis of S_{DD} to the measured value.

For the Q_{DT}^{eq} = 1 shot (E27969), Z_{eff} is estimated to be 3.49 from the kinetic analysis [1] which contradicts with Z_{eff} from bremstrahlung measurement (3.2). The disagreement in Z_{eff} should be examined well because the overestimation in Z_{eff} may reduce the estimated value of Q_{DT}^{eq}. Unfortunately, the reason why bremstrahlung indicates a smaller value than the kinetic analysis is uncertain. But there is a possible interpretation [2]: If super-thermal ions are lost from the plasma due to TF ripple transport and distort the ion velocity distribution, S_{DD} can be reduced. This idea can lead to reasonable agreement of the kinetic S_{DD} with the measurement even with adopting Z_{eff} from bremstrahlung. S_{DD} can be scaled as $S_{DD} \propto n_D^2 \propto (1 - Z_{eff}/q_z)^2 \sim 1 - 2Z_{eff}/q_z$ with the charge number of impurity ions, q_z. Assuming carbon impurity, $S_{DD}(Z_{eff}=3.49)/S_{DD}(Z_{eff}=3.2) \approx 0.9$. This suggests that if 10% of super-thermal ions are lost due to ripple loss, we can explain the measured S_{DD} using the value of Z_{eff} from bremstrahlung.

In this note, we examine the possibility of the above interpretation by computer analysis, indicating that this does not explain the contradiction on Z_{eff}.

2. Ripple Loss of Super-Thermal Ions

Figure 1 is the D-D fusion reactivity for T_i = 15 keV corresponding to the ion temperature inside an internal transport barrier formed in E27969 (Fig. 2). At this temperature, the confinement of fast ions with super-thermal energies of 30-100 keV predominantly determines S_{DD}. The reactivity peaks at 50 keV, indicating that the confinement of super-thermal ions with ~50 keV can affect the reactivity the most. Like beam ions, does these energetic ions constituting a Maxwell distribution escape the plasma due to ripple transport and apparently reduce S_{DD}? In order to answer the question, we calculated ripple loss of super-thermal ions using an orbit following Monte Carlo code (OFMC) [3]

In the calculation, test particles with a certain energy are launched on a magnetic surface of r/a = 0.5. The reason for launching at r/a = 0.5 is that the radius corresponds to the shoulder of n_e and thus it contributes the most to the volume-integrated the D-D neutron emission. The other initial conditions of each test particle such as the toroidal and poloidal phases, the pitch angle are simulated with the Monte Carlo method. After launching, the OFMC code simulates slowing

down and pitch angle scattering while following the guiding-center orbit of each test particle in a rippled magnetic field reasonably modeled until its thermalization (the assumed thermalization energy is 30 keV) or loss from the plasma. Taking an ensemble of 8,000 particles, the ripple loss was estimated.

The calculated ripple loss is shown in Fig. 3. The loss increases with the initial energy and the total ripple is only 1.6% for 80 keV. With such a low fraction of loss, it is impossible to explain the measured S_{DD} using the value of Z_{eff} from bremstrahlung. Therefore, the ripple loss is low enough to rule out the possibility of super-thermal ion ripple loss. The calculation ignored the radial electric field E_r produced by the steep pressure gradient at the ITB. The **E×B** points in the poloidal direction and displaces the turning points of toroidally trapped particles, in principle, affecting ripple transport. But the TF ripple at r/a = 0.5 seems to be too low ($\sim 5\times10^{-4}$) to enhance ripple transport even with the inclusion of E_r.

3. Conclusions

With the OFMC code, the ripple loss of super-thermal ions in the equilibrium of the $Q_{DT}^{eq} = 1$ shot (E27969) was calculated. For the shot with reversed magnetic shear, the ripple loss of super-thermal ions (~80 keV) launched at r/a = 0.5 (shoulder of the ITB) is as low as 1.6%, which is small enough to neglect in the estimation of Q_{DT}^{eq}.

References

[1] S. Ishida et al., Phys. Rev. Lett. **79** (1997) 3917.

[2] R.V. Budny, private communication (Princeton Plasma Physics Laboratory).

[3] K. Tani, et al., J. Phys. Soc. Jpn. **50** (1981) 1726.

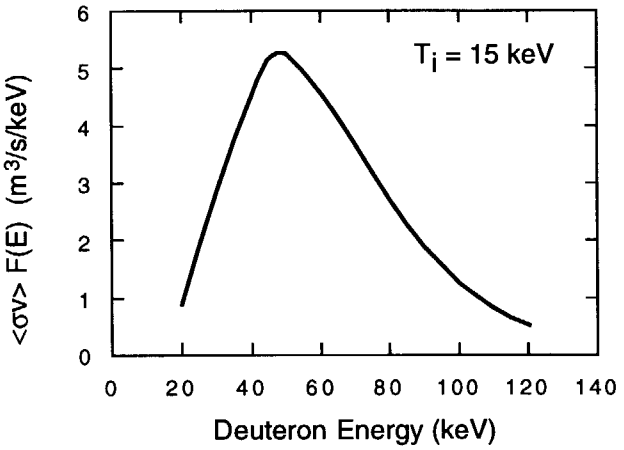

Fig. 1 D-D fusion reaction rate for a thermal plasma with T_i = 15 keV.

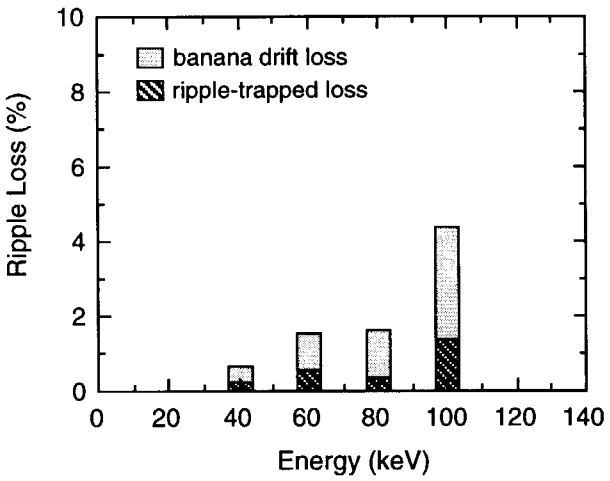

Fig. 3 Calculated ripple losses of fast particles launched at r/a = 0.5 in E27969.

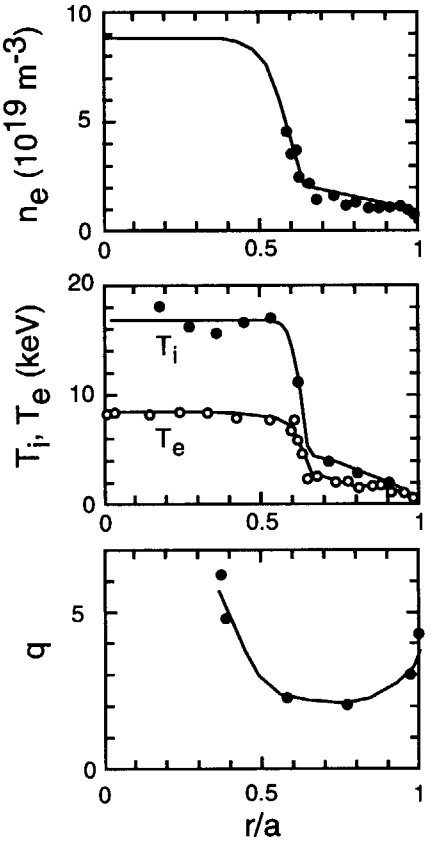

Fig. 2 Density, temperature and safety factor profiles in E27969.

5. Current Drive

5.1 Non-inductive current drive by N-NB

T. Oikawa, K. Ushigusa, O. Naito, Y. Kusama, T. Fujita, Y. Kamada,
C. B. Forest* and the JT-60 Team
*University of Wisconsin-Madison

5.1.1 Introduction

Since first injection of N-NB in Mar. 1996, N-NBI experiments in JT-60U to study current drive capability has been being performed. As reported in Ref. 1), total current non-inductively driven by N-NB has been estimated using the ACCOME code and it has been demonstrated that N-NB has higher current drive efficiency than P-NB. This result proves effectiveness of N-NB as a current drive method. In order to study N-NB current drive in detail and use N-NB effectively for current drive and current profile shaping, information of N-NB driven current profile is useful and necessary. N-NB driven current profile is experimentally determined for the first time using the new analysis technique[2] and time-evolution of equilibrium reconstructed accurately with MSE(Motional Stark Effect) polarimeter.

5.1.2 Analysis Method

A technique for determining the non-inductive current profile[2] is described in this section. Key points for this technique are the determination of the current density profile from internal MSE and external magnetic measurements and a method for determining the parallel electric-field profile. The non-inductive portion of current is the difference between the total current density $j(\rho)$ and the inductive current density $j_{oh}(\rho)$. $j(\rho)$ is determined from equilibrium reconstruction. $j_{oh}(\rho)$ can be calculated by determining the parallel electric-field profile $E_{//}(\rho)$ and the conductivity profile calculated from measured $T_e(\rho)$, $n_e(\rho)$ and $Z_{eff}(\rho)$ assuming conductivity model, where $E_{//}(\rho)$ is calculated from time-evolution of poloidal flux profile $\Psi(\rho)$.

Current density is related to the electric field in the following equation,

$$\langle j \cdot B \rangle = \sigma_{//} \langle E \cdot B \rangle + \langle j_{NI} \cdot B \rangle,$$

where <...> denotes the flux surface average, $\sigma_{//}$ is the parallel conductivity, and j_{NI} represents non-inductive portion of current including both auxiliary driven currents and bootstrap current. Parallel electric field term in the above equation $< \mathbf{E} \cdot \mathbf{B} >$ can be shown to be

$$\langle E \cdot B \rangle = \frac{\langle B_t^2 \rangle}{F} \frac{\partial \Psi}{\partial t}\bigg|_{\Phi},$$

where $F = RB_t$ and the derivatives of poloidal flux are taken on surfaces of constant toroidal flux Φ. $< \mathbf{j} \cdot \mathbf{B} >$ and $< \mathbf{E} \cdot \mathbf{B} >$ are determined by equilibrium reconstruction, and $\sigma_{//}$ is calculated

from $T_e(\rho)$, $n_e(\rho)$ measured by Thomson scattering and $Z_{eff}(\rho)$ determined by CXRS and Bremsstrahlung measurements with assumption of neoclassical conductivity. Neo-classical conductivity was confirmed in JT-60[3].

MSE measurements and equilibrium reconstruction code EFIT[4], which was introduced in collaboration with General Atomics, enables accurate reconstruction for this analysis technique.

5.1.3 Determination of N-NB driven current profile

N-NBI experiments have been performed for heating and curret drive study with the following parameters : E_B=360keV, P_{INJ}=2.1MW, I_p=0.6MA, n_e=0.7×10^{19}/m^3 and $T_e(0)$~2.5keV, as shown in Fig.1. In this discharge, only lower unit of N-NB is injected. MSE beam #7 is injected from I_p ramp-up phase for reconstructing time evolution of current density profile. Current driven by this counter-directional beam #7 is cancelled by co-directional beam #9 for accurate analysis of N-NB current drive. Injection of CXRS beam #14 for T_i and impurity density profile starts 0.2s before N-NB injection because pulse-duration of perpendicular beam is restricted by shinethrough for low density plasma. Plasma configuration, beam trajectories and measured

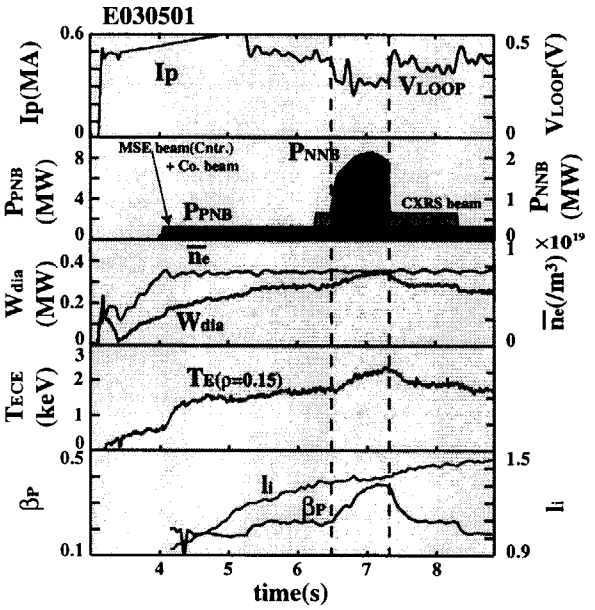

Fig. 1 : Discharge waveforms of N-NB current drive experiments

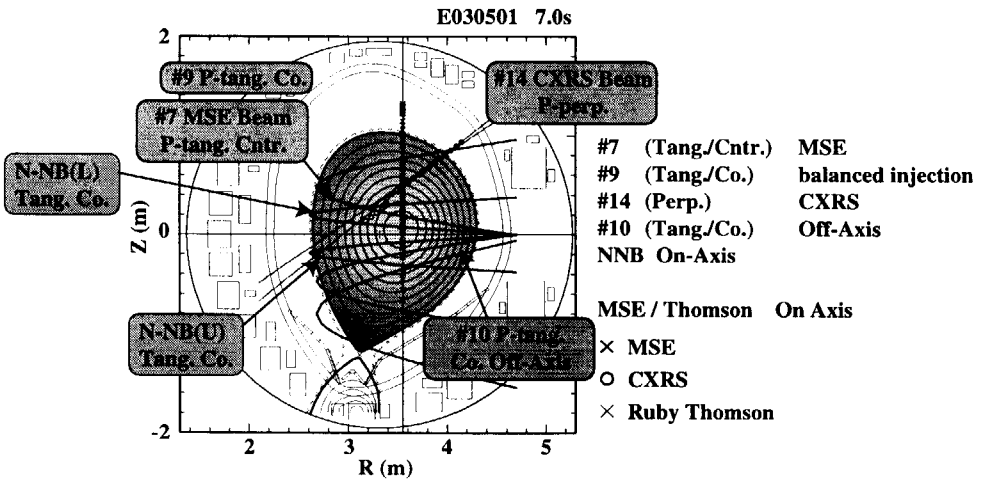

Fig. 2 : Plasma configuration and NB trajectories. Configuration is adjusted as diagnostic beams(#7 for MSE, #14 for CXRS) and Thomson scattering laser path cover from magnetic axis to surface for accurate equilibrium reconstruction and determination of conductivity profile.

points of critical diagnostics for determining non-inductively driven current profile are shown in Fig.2. Plasma configuration is adjusted so that MSE and CXRS beams and Thomson scattering laser path cover from near magnetic-axis to plasma surface for accurate equilibrium reconstruction and determination of conductivity profile. As for heating by N-NBI, increases in stored energy, β_p and T_e in the central region are observed during N-NB injection and the decay-times after the turn-off of N-NBI pulse are longer than those for P-NBI because high energy ions of N-NBI have longer slowing-down time than P-NBI ions. Loop voltage profile during N-NB injection is shown in Fig.3(a). A hollow of loop voltage in the central region(ρ<0.4) suggests center current drive by N-NBI. Neo-classical conductivity profile calculated on the basis of T_e, n_e and Z_{eff} measurements is shown in Fig.3(b). Non-inductive driven current profile $j_{NI}(\rho)$ is the difference between total current profilej(ρ) (Fig.4(a)) and inductive current profile $j_{OH}(\rho)$ (Fig.4.(b)). $j_{NI}(\rho)$ consists of N-NBdriven current $j_{NNB}(\rho)$ and bootstrap current $j_{BS}(\rho)$ (P-NB driven current can be considered to be almost zero because of balanced injection of tangential P-NB). Thus, $j_{BS}(\rho)$ has to be evaluated in order to determine $j_{NNB}(\rho)$. $j_{BS}(\rho)$ is calculated by ACCOME code using measured T_e, T_i, n_e andZ_{eff}. By subtracting $j_{BS}(\rho)$ from $j_{NI}(\rho)$, non-inductive current profile by N-NBI is determined as shown in Fig.5. Centrally-peaked profile is confirmed experimen-

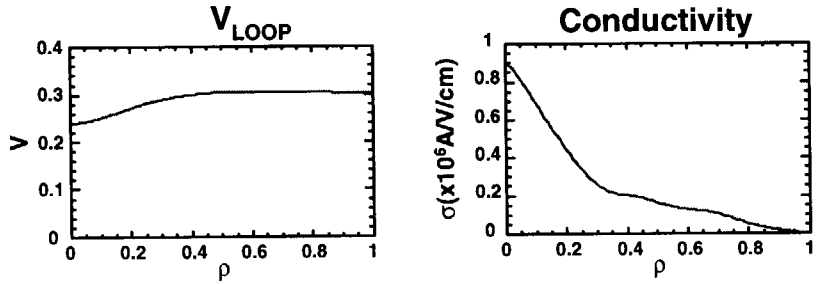

Fig. 3 : (a) Loop voltage profile calculated from the time-derivatives of reconstructed poloidal flux during N-NB injection, and (b) Neo-classical conductivity profile calculated from reconstructed equilibrium and measured T_e, T_i, n_e and Z_{eff}.

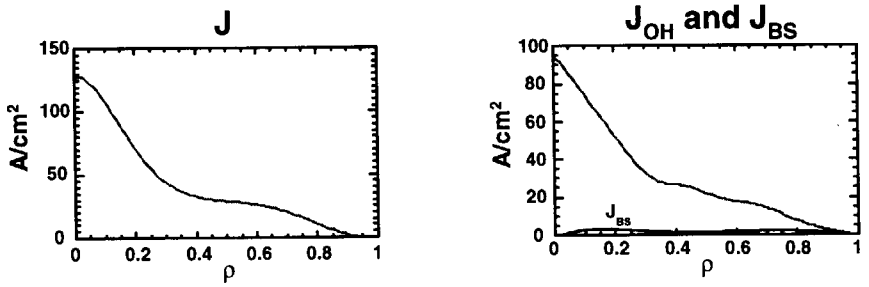

Fig. 4 : (a) Total current density profile reconstructed by equilibrium code using MSE and magnetic measurements, and (b) profiles of the inductive current density j_{OH} and the bootstrap current density j_{BS}, j_{OH} is calculated from V_{LOOP} and conductivity shown in Fig.3. j_{BS} is calculated by ACCOME code using measured T_e, T_i, n_e and Z_{eff}

tally as expected from on-axis trajectory of N-NB. Total non-inductive driven current is 102kA and the current-drive efficiency is 0.29×10^{19}A/W/m^2. Theoretically calculated result using current-drive code ACCOME is also shown. ACCOME code solves equilibrium, bootstrap current and beam-driven current consistently. Experimental and calculated results agree well within the experimental error, which means that the heating deposition and current drive performance of N-NBI can be predicted based on the theory and the design of N-NBI on ITER is reliable. Using this technique and various NBI in JT-60U(N-NBI, co-/counter-directional and on-/off-axis tangential P-NBI), we can study current profile control with NB in detail, which helps to optimize and maintain steady-state current profile for high performance in JT-60U plasmas.

1) K. Ushigusa, *et al.*, Proc. of 16th IAEA Fusion Energy Conference(IAEA, Vienna) 1996.
2) C. B. Forest, *et al.*, Phys. Rev. Lett. **73**, 2444(1994).
3) M. Kikuchi, *et al.*, Nuclear Fusion **29**, 343(1990).
4) L. L. Lao, *et al.*, Nuclear Fusion **20**, 1025(1990).

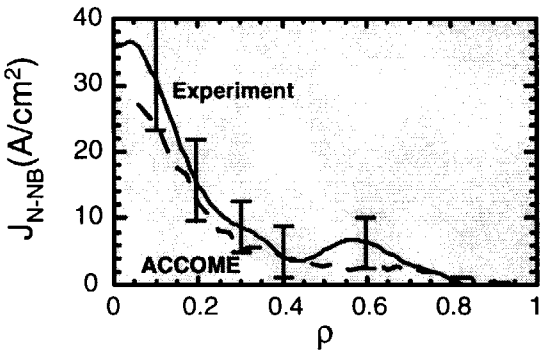

Fig. 5 : N-NB driven current profile. Experimental result agrees well with the theoretical calculation.

5.2 Sustainment of ITB by LHCD

S. Ide, O.Naito, K. Ushigusa, T. Oikawa, T. Kondoh and M. Seki

1. Introduction

Achievement of high confinement in recent reversed magnetic shear (R/S) experiments[1-4], such as achievement of break even in the JT-60U tokamak, has emphasized the importance of plasma current profile control. Non inductive current drive experiments by means of lower hybrid waves (LHCD by LHW) on JT-60U have been oriented toward well established current profile control and confinement improvement. In previous LHCD experiments on R/S plasmas, quasi-steady sustainment of R/S configuration by means of LHCD and control of the internal transport barrier (ITB) by LHCD current profile control have been demonstrated on JT-60U[5,6]. Furthermore, it was shown experimentally that R/S could be formed in a plasma start-up phase by LHCD only. Following these results, the next step toward steady state operation of improved confinement plasma is to optimize an LH driven current profile together with bootstrap current profile for sustainment of ITB keeping R/S and avoidance of fatal MHD modes. Approach to this step has been carried out. For the time being, sustainment of the ITB for about 2 s during R/S was kept by LHCD with small but continuous neutral beam injection (NBI) heating was observed.

2. Experimental Results

The experiments was performed on a plasma with the plasma current of I_P = 1 MA and the toroidal magnetic field of B_T = 3 T. The working gas and the NBI beam species were hydrogen. Firstly at the I_P ramp up phase, the NBI heating power P_{NB} was applied in order to form a R/S configuration by delaying the current penetration. The NBI power was raised to about 12 to 13 MW as I_P increased and kept high for 1 s to form a clear ITB. After that P_{NB} was reduced to 4 MW, and the LH power P_{LH} of about 1.8 MW was injected at the same time. In Fig. 1 plotted are the temporal evolutions of I_P, the loop voltage

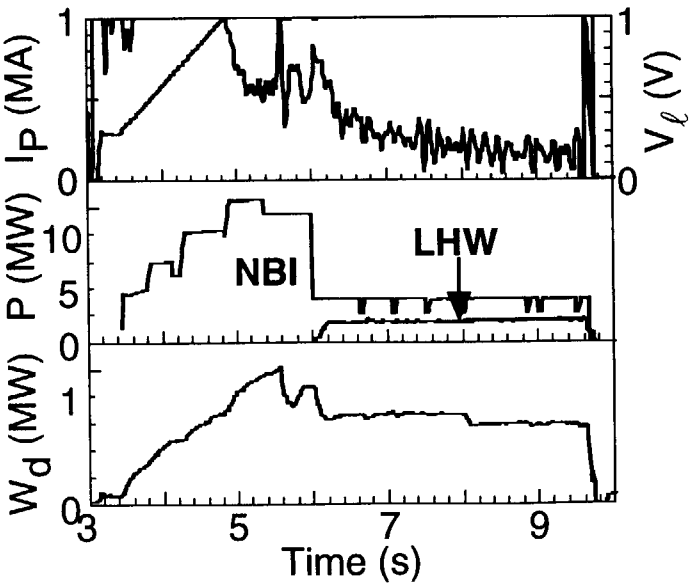

Fig. 1. The temporal evolutions of I_P, V_l, P_{NB}, P_{LH} and W_d.

V_ℓ, P_{NB}, P_{LH} and the diamagnetic stored energy W_d.

The internal transport barrier was found to evolve well during the higher P_{NB} phase. In the shot shown in Fig. 1, a mini collapse occurred, a rapid drop in W_d corresponds to this. The steep gradients of plasma profiles became weaker at the mini collapse, but were recovering until P_{NB} was lowered as shown in Fig. 1.

In the experiments, an LHW launcher which was located in a horizontal port and another LHW launcher which was located in a inclined port about 45° above the equatorial plane were used. The injected spectra of the pararell refractive index of the LHW were chosen so as to drive non-inductive current as hollow as possible in order to keep the R/S configuration. The spatial profile of the line averaged hard X-ray (HX) emission intensity is shown in Fig. 2. Although it is not a very hollow profile, the profile is flat and suggests that the waves drive a current in the outer region.

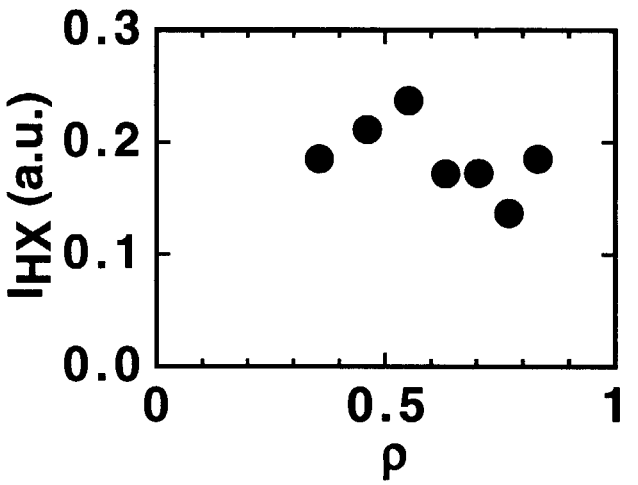

Fig. 2. The spatial profile of the line averaged HX intensity integrated during from 7 s to 8 s.

In the temporal evolution of W_d shown in Fig. 1, a small drop can been seen at around 8 s. Although the change was small, the ITB was found to survive until this point. In Fig. 3 shown is a temporal evolution of the soft X-ray (SX) intensity profile. The SX intensity is roughly proportional to the square of the product of the electron density n_e and the electron temperature T_e. Although the profile is not shown in spatial position but in the channel number of the detector fan array, it would be closely related to the spatial profile. As is seen in the figure, a very steep gradient is observed until about 8 s suggesting the existence of the ITB. The radial profile of n_e measured by Thomson scattering at 7.5 s is plotted in Fig. 4 (a). A large change of the density gradient is fond around mid radius. Similarly, a steep gradient was confirmed both in the

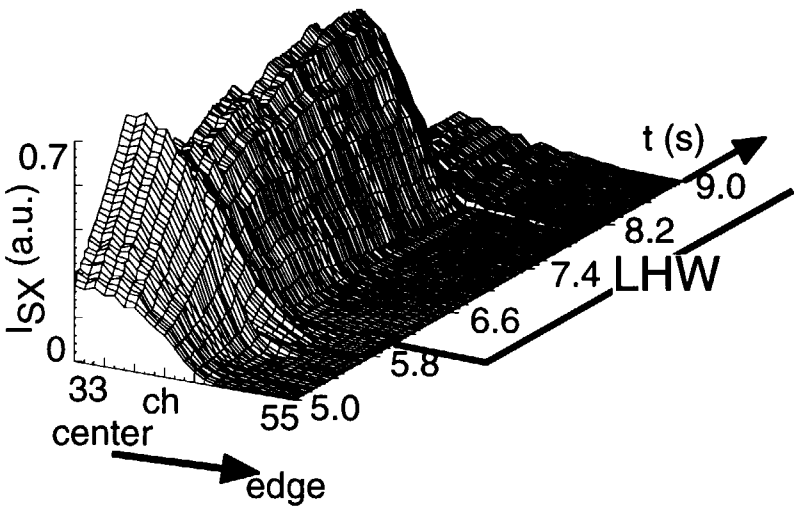

Fig. 3. Temporal evolution of I_{SX} profile.

T_e and the ion temperature T_i profiles.

The safety factor q profiles at three time, deduced from the motional Stark effect (MSE) measurement, are shown in Fig. 4 (b). In the q profile measured at 6.05 s, just after the P_{NB} step down, from about 55% of the minor radius q increases toward the plasma center indicating that the magnetic shear is reversed. This R/S configuration was formed by delaying current penetration by the NBI heating at the current ramp-up. As time goes, q gradually decreases but q at the center is still larger than the minimum as is seen in the profile at 7.9 s. That is, the R/S configuration is supposed to be maintained during the ITB was kept. The reason why q continued decreasing might be attributed to that the LHCD driven current profile was not hollow enough. The driven current in the central region helped to lower q in the central region. To compare with the result, different LHW spectra were injected so as to drive more peaked LHCD current profile. In this case, the q profile was found to decrease more quickly and the R/S region disappeared simultaneously. The ITB seemed to be lost quickly as well.

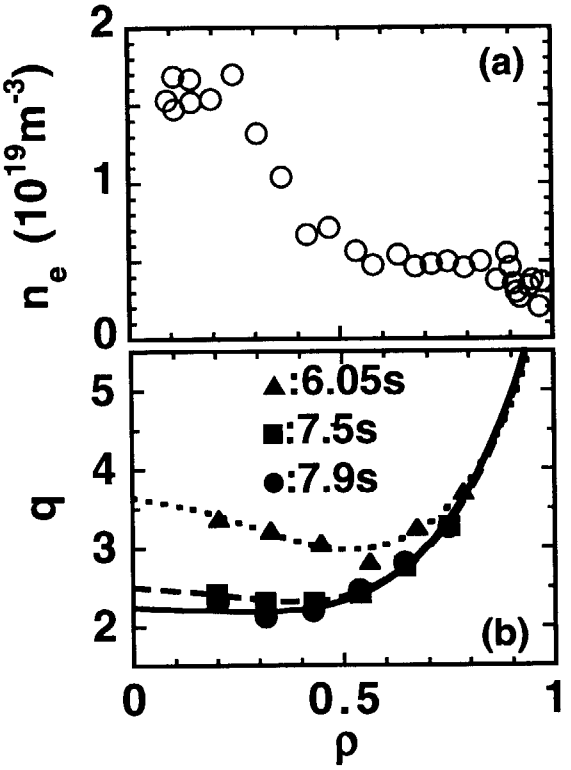

Fig. 4. (a) The radial profile of the electron density. (b) The safety factor profiles at three time.

3. Conclusions

Sustainment of an ITB in a R/S configuration has been investigated by means of LHCD. For the time being the ITB was sustained for 2 s while the R/S was maintained by LHCD. Further optimization of the LHW spectra would be necessary to maintain the R/S configuration longer. When more current was tried to drive in the central region, the R/S configuration and the ITB were found to disappear quickly. More detailed investigation is necessary whether the disappearance of the ITB is related to the R/S or the stability condition against the MHD modes. Strategy in the next step is to ; 1) optimize further LHCD for more peripheral current drive and 2) raise P_{NB} to increase bootstrap current and 3) optimize both the non-inductive current so as to maintain ITB.

Acknowledgments

The Authors would like to express their appreciation to the members of the JT-60 team for the continuous support.

References

1) S. Ishida, *et al.*, Phys. Rev. Lett., **79**, 3917 (1997).
2) T. Fujita, S. Ide, H. Shirai, M. Kikuchi, O. Naito, *et al.*, Phys. Rev. Lett., **78**, 2377 (1997).
3) F. M. Levinton, *et al.*, Phys. Rev. Lett., **75**, 4417 (1995).
4) E. J. Strait,*et al.*, Phys. Rev. Lett., **75**, 4421 (1997).
5) S. Ide, T. Fujita, O. Naito and M. Seki, Plasma Phys. Controlled Fusion, **38**, 1645 (1996).
6) S. Ide, O. Naito, T. Fujita, T. Oikawa, M. Seki and the JT-60 team, in Fusion Energy 1996 (Proc. 16th Int. Conf. Montreal, 1996), IAEA Vienna, Vol. 3, 253 (1997)

5.3 Coupling of Lower Hybrid Waves to Semi-Closed Divertor Configuration

O. Naito, M. Seki, S. Ide, T. Kondoh, K. Ushigusa

After the modification of the divertor to a semi-closed W-shaped-type, it was anticipated that the coupling of lower hybrid wave (LHW) to the plasma became worse because the average plasma-launcher distance would be larger and the outer scrape-off layer plasma would be limited by the baffle plates. To examine the applicability of LH to new plasma configuration, coupling of LHW to the plasma was tested.

JT-60U has two lower hybrid wave (LHW) launchers, one of which locates on a horizontal port (Unit A: lower half, Unit B: upper half) and the other on an inclined port (Unit C). After the divertor modification, the basic configuration for RF coupling is high triangularity plasma (δ = 0.27-0.36). Since Unit C is less affected by this modification, hereafter the results are only described on Units A and B.

Figure 1 shows the reflection coefficient R of Units A and B as a function of plasma-wall distance d_0 on the mid plane before and after the divertor modification. Before the modification, good coupling (R < 10%) can be established even for a large plasma-wall distance of d_0 > 15 cm. After the modification, however, it is necessary to make the plasma closer to the wall, typically about 5 cm. The operation of LH is of course possible for larger distance of d_0 ~ 14 cm at the cost of higher reflection (R < 20%). Possible side effects such as reduction in current drive efficiency and current profile controllability are to be clarified by systematic scan, but the reduction seems to be not so large.

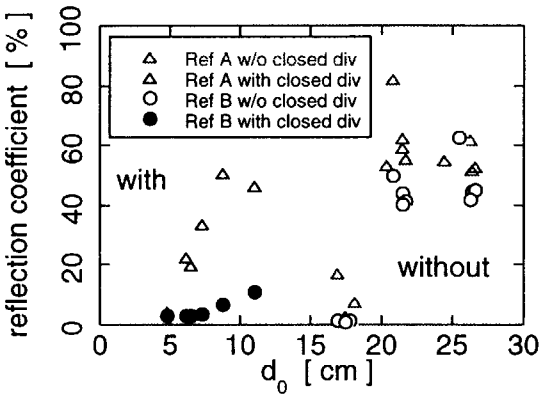

Fig. 1: Reflection coefficient versus plasma-wall distance before and after the divertor modification.

As for a technical aspect, Units A and B have been equipped with a protection system against arcing at ceramic windows: that is RF is switched off immediately on detection of arc. The protection of launcher grill mouth against breakdown has been, however, depending on human monitoring. In order to realize reliable fast switching off of RF, a new protection system which monitors breakdown at the grill mouth and switch off RF has been installed and proved to work well in the routine operation. This should be useful in avoiding metal impurities when breakdown occurs.

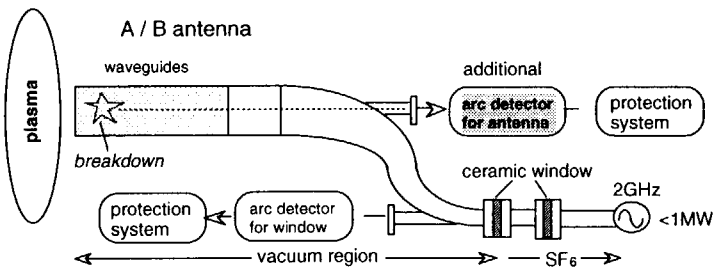

Fig.2: Schematic of new protection system.

5.4 Current profile measurement during lower hybrid current drive

O. Naito, S. Ide, T. Oikawa, T. Kondoh, M. Seki, K. Ushigusa

JT-60U has demonstrated the effectiveness of current profile control by lower hybrid waves (LHW) for getting better confinement and stability in ohmic and beam-heated plasmas. The current profile during lower hybrid current drive (LHCD) has been, however, only inferred from hard X-ray intensity profile or global equilibrium quantities such as internal plasma inductance. Recently, a more direct measurement of current profile using the motional Stark effect (MSE) is available in JT-60U. In this section, preliminary result of current profile measurement during LHCD is described. Details including the effect of safety factor on the driven current profile will soon be published elsewhere by one of the authors (S. I.).

The current profiles were measured in discharges with I_p = 1.2 MA, B_t = 3.5 T, and $n_e = 0.7\times10^{19}$ m^{-3} using the upper half of the horizontal launcher (Unit B) operated at the frequency of f = 2 GHz. To compare the influence of phase velocity on the driven current profile, two different phasing were examined, namely 0 deg ($N_{//}$ = 1.6) and 180 deg ($N_{//}$ = 2) where $N_{//}$ is wave refractive index parallel to the magnetic field.

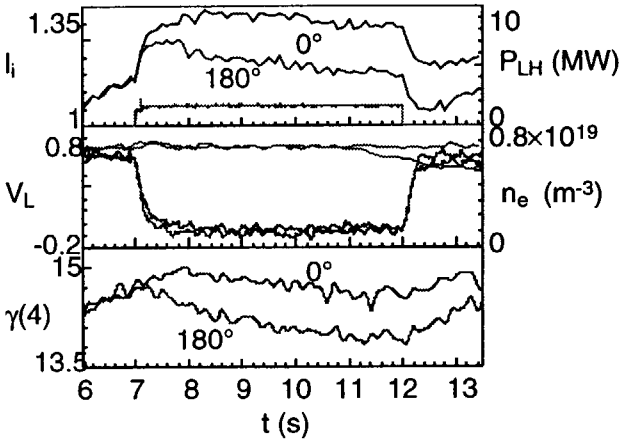

Fig 1: Time evolutions of internal inductance, lower hybrid power, loop voltage, line average density, and polarization angle at 50% of minor radius for small $N_{//}$ case (0 deg) and large $N_{//}$ case (180 deg).

The time evolutions of internal inductance l_i, lower hybrid power P_{LH}, loop voltage V_L, line average density n_e, and the polarization angle at 50% of minor radius $\gamma(4)$ are shown in Fig. 1. Consistent with the previous results, the internal inductance for larger $N_{//}$ case (180 deg) was lower than that for smaller $N_{//}$ case (0 deg). Accordingly, the observed hard X-ray intensity profile was broader for the case with larger $N_{//}$ indicating that broader non-inductive current was driven by LHW (Fig. 2). Finally, the polarization angle at 50% of minor radius measured by MSE was smaller for the case with larger $N_{//}$, showing that the current within 50% of minor radius was smaller (i.e. broader current profile). The agreement of current profile inferred from internal inductance and/or hard X-ray profile and that directly measured by MSE shows the validity of previous conclusions related to LH driven current profile derived from the former method.

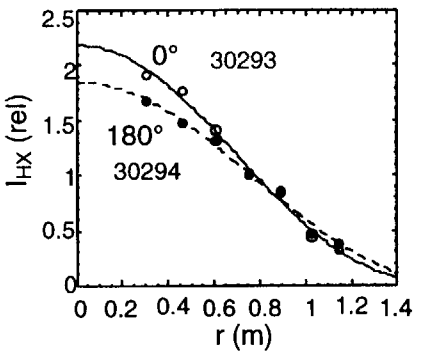

Fig. 2: Hard X-ray intensity profile during LHCD for small $N_{//}$ (0 deg) and large $N_{//}$ (180 deg) cases.

6. Particle Control

6.1 Particle balance and neutral behavior

H. Takenaga, A. Sakasai, H. Tamai, A. Kumagai, H. Kubo, N. Asakura,
K. Shimizu, N. Hosogane

1. Introduction

It is very important to estimate the capability of the divertor pumping system in W-shaped divertor of JT-60U, because it is closely related with density control, helium ash exhaust and SOL flow formation. Since particles are also pumped out by the divertor plates and the first wall (wall pumping), the divertor pumping rate considering wall pumping should be estimated. In this report, the experiments were performed with and without divertor pumping using the fast shutter valves installed to the pumping ports, and then the divertor pumping rate was estimated from the quantitative analyses of the particle balance in the vacuum vessel. Furthermore, in order to understand the divertor pumping characteristics, the neutral behavior was analyzed using the neutral particle transport code DEGAS. This report presents the experimental and simulation results on particle balance and neutral behavior.

2. Analysis method of particle balance

The particle balance is considered in the steady state phase with and without divertor pumping at the same NBI heating power and the same main plasma density sustained by gas-puffing. The particle balance equation with and without divertor pumping can be expressed as follows,

$$\Gamma_{NBI}+\Gamma_{GP}^{W}=\Gamma_{wall}+\Gamma_{div} \quad (1)$$

$$\Gamma_{NBI}+\Gamma_{GP}^{W/O}=\Gamma_{wall} \quad (2)$$

where Γ_{NBI} is the particle fuelling rate of NBI, and Γ_{GP}^{W} and $\Gamma_{GP}^{W/O}$ are the particle fuelling rate of gas-puffing with and without divertor pumping, respectively. Γ_{wall} and Γ_{div} are the particle pumping rate of wall pumping and divertor pumping, respectively. Here, the wall pumping rates with and without divertor pumping are assumed to be equal. By subtracting eq. (2) from eq. (1), the following equation is obtained.

$$\Gamma_{div}=\Gamma_{GP}^{W}-\Gamma_{GP}^{W/O} \quad (3)$$

The divertor pumping rate can be estimated from the comparison of gas-puffing rates, which are required for keeping constant density with and without divertor pumping.

3. Analysis results of particle balance

Figure 1 shows the time evolution of line averaged electron density ($\bar{n}_e$), NBI power (P_{NBI}), gas-puffing rate, Dα emission from the divertor region and neutral pressure under the divertor baffle for ELMy H-mode plasma with the plasma current (I_p) of 1.5 MA and the

toroidal magnetic filed (B_T) of 3.5 T. The solid and dotted lines show the data with and without divertor pumping, respectively. MARFE occurred at t=8.8 and 7.1 s in the cases with and without divertor pumping, respectively. The value of $\bar{n}_e$ is kept constant at 4.5×10^{19} m^{-3} during t=9-10 s by feedback control system. P_{NBI} almost equals in the two cases, therefore, the particle fuelling rate due to NBI equals in the two cases. The value of P_{NBI}=12 MW corresponds to the particle fuelling rate of 1×10^{21} /s. The gas-puffing rate to keep the constant $\bar{n}_e$ is evaluated to be 20.0 and 7.7 Pam^3/s, which correspond to 1×10^{22} and 3.9×10^{21} /s, in the case with and without divertor pumping, respectively. The base intensity of Dα emission and the neutral pressure become constant value. These results indicated that the steady state condition for the neutral density is satisfied.

In this case, the divertor and wall pumping rates are estimated to be 6.2×10^{21} and 4.9×10^{21} /s, respectively. The ratio of the divertor pumping rate to the particle flux onto the divertor plates is estimated to be about 2.4%, because the amount of recycling is evaluated to be about 2.5×10^{23} /s from the Dα emission intensity.

The dependence of the divertor pumping ratio to the particle flux onto the divertor plates on the electron density are shown in Fig. 2. The circles and squares show the data for the high q (I_p=1.0 MA and B_T=3.8 T) and low q (I_p=1.5 MA and B_T=3.5T) cases, respectively, with Gap_in=3.5 cm, which is a distance between the pumping duct and the inner strike point. The triangles show the data for the low q case with Gap_in=10 cm. The closed and open symbols show the data with and without MARFE. It can be seen from Fig. 2 that the pumping ratio

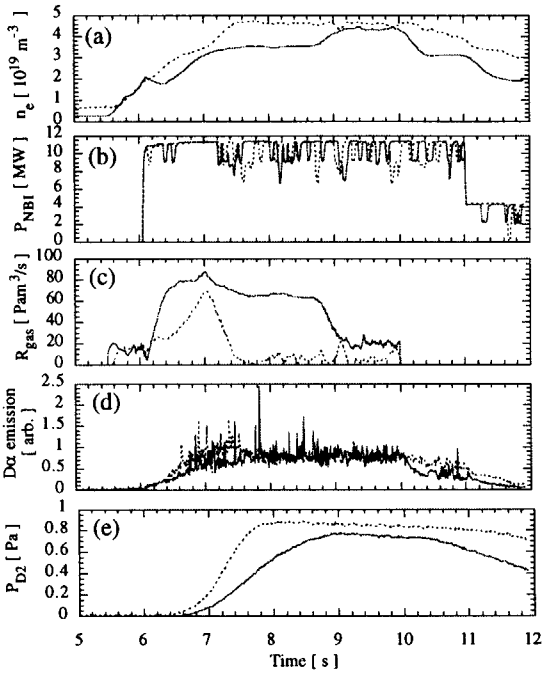

Fig. 1 Time evolution of (a)density, (b)NBI power, (c) gas-puffing rate, (d)Dα emission and (e)neutral pressure under the divertor baffle plate. Solid and dotted lines show the data with and without divertor pumping, respectively.

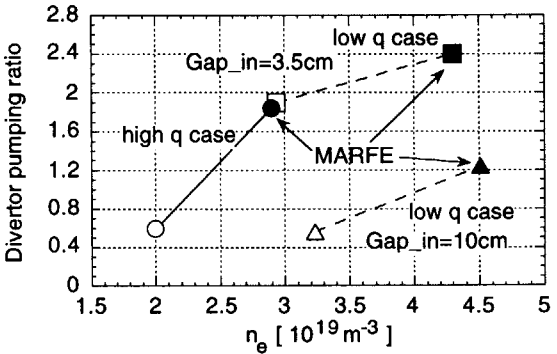

Fig. 2 Dependence of divertor pumping ratio on the electron density. Circles and squares show the data for the high and low q cases, respectively, with Gap_in=3.5 cm. Triangles show the data for the low q case with Gap_in=10 cm. The closed and open symbols show the data with and without MARFE.

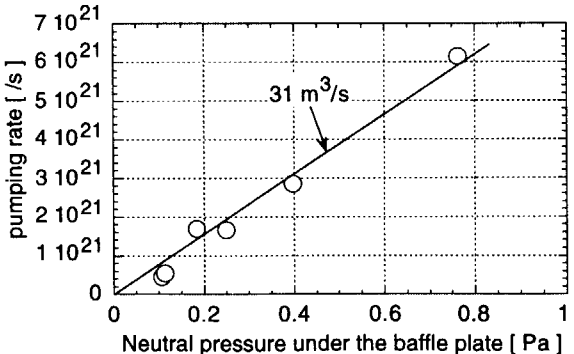

Fig. 3 Relationship between divertor pumping rate and neutral pressure under the baffle plate.

for Gap_in=10 cm is two or three times smaller than that for Gap_in=3.5 cm. The difference of the divertor pumping ratio between the high and low q cases and between the cases with and without MARFE is not obvious. In the high density region, the divertor pumping ratio with Gap_in=3.5 cm reaches up to 2% which is larger than the wall pumping ratio by about 20%.

The relationship between the divertor pumping rate and the neutral pressure under the baffle plate is shown in Fig. 3. The divertor pumping rate is proportional to the neutral pressure under the baffle plate. The pumping speed of the divertor pumping is estimated to be 31 m^3/s, because 1 Pam^3/s corresponds to 2.5×10^{20} /s at 300 degree centigrade.

4. Analysis results of neutral behavior

First, the effective pumping fraction (F^{eff}) was estimated at the pumping duct from the simulation of neutral behavior using the simple model under the divertor baffle plate in which the particles are released and escape from the pumping duct and are pumped out at the pumping port with pumping fraction of F_{pump} as shown in Fig. 4. Figure 5 (a) shows the dependence of F^{eff} on F_{pump}. Here, the neutral particles are released as atom with the energy of 1 eV and the cosine distribution. The value of F^{eff} increases with F_{pump} until F_{pump}=0.2, and saturates above this value. Since F_{pump} of the pumping system in JT-60U can be guessed to be 0.05 from the localization of the pumping port in the toroidal direction, F^{eff} is estimated to be about 0.3. Figures 5 (b) and (c) show the dependence of F^{eff} on the initial species, the initial energy and the initial angle. The effective pumping fraction has week dependence on the initial conditions, because the particle reflection at the wall is not dominant. From these results, F^{eff} at the divertor duct is estimated to be about 0.3.

Next, the neutral behavior is simulated for the L-mode plasma with I_p=2 MA, B_T=4 T, P_{NBI}=6 MW and $\bar{n}_e=2.5\times10^{19}$ m^{-3} with F^{eff} of 0.3. Figure 6 shows the comparison of Dα emission distribution between the simulation and measurement. The cross symbols show the measurement. The sight lines of the measurement are shown in the inset. The solid and dashed lines show the simulation with the particle source at the divertor and the outer baffle plate, respectively. The distribution of the divertor source and the outer baffle source are also shown in the inset. The thick line shows sum of the simulations for the divertor and outer baffle sources. It can be seen from this figure that the simulation with the divertor source agrees well with the measurement in the divertor and inner region. However, in the outer region, the measurement is one order of magnitude larger than the simulation with the divertor source. In order to fit the simulation to the measurement, the outer baffle source is needed. The divertor and outer baffle sources are estimated to be 2.6×10^{23} and 1.2×10^{22} /s, respectively. The outer baffle source is about 5% of the divertor source. However, since the penetration probability into the main plasma of the outer baffle source is larger than that of the divertor source, the particle source in the main plasma for the outer baffle source is only a

factor of three smaller than that for the divertor source. Touch of the second SOL plasma[1] which has the large decay length can be considered for the candidate of the outer baffle source. However, no definitive answer has yet emerged, and further work is to be made.

In this simulation, the pumping rate is calculated to be about 7.2×10^{21} /s which is 2.6% of the divertor flux. In this case, the neutral pressure under the baffle plate is measured to be 0.3 Pa, therefore, the pumping rate is estimated to be about 2.3×10^{21} /s. The simulation result is a factor of three larger than the experimental result. This difference might come form the effects of the structure under the baffle plate, the leak from the region under the baffle plate to the plasma region through the diagnostic ports and the wall pumping. These effects should be investigated in future work.

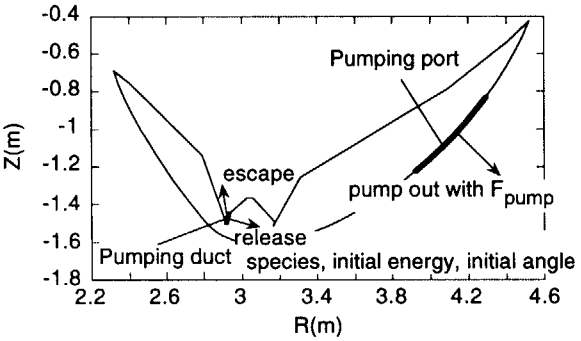

Fig. 4 Simulation model under the baffle plate. Particles are released and escape from the pumping duct and are pumped out at the pumping port with pumping fraction of Fpump.

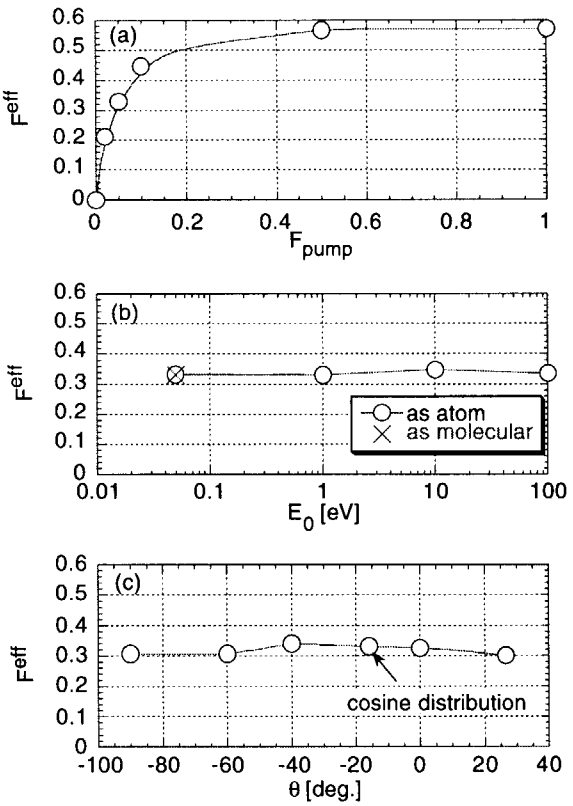

Fig. 5 Dependence of F^{eff} on (a) Fpump, (b) initial species and initial energy and (c) initial angle.

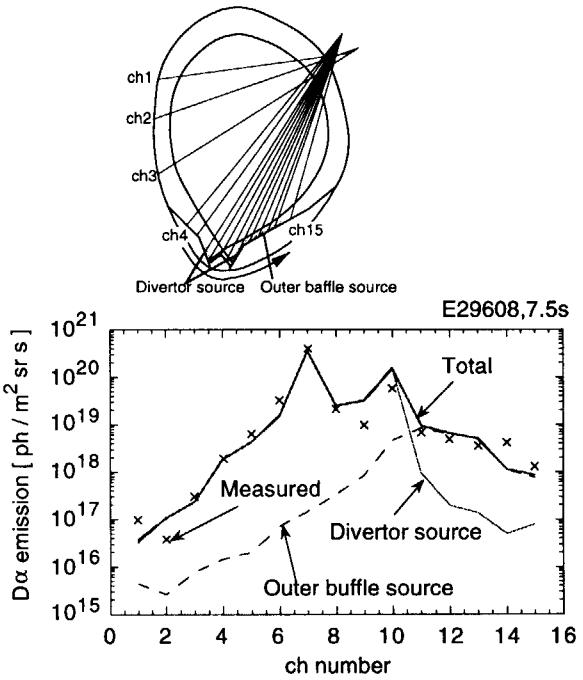

Fig. 6 Comparison of D_α emission distribution between the simulation and measurement. Cross symbols show the measurement. Solid and dashed lines show the simulation with the particle source at the divertor and the outer baffle plate. The thick line shows sum of simulations for the divertor and outer baffle sources. The sight lines of the measurement and the distribution of the divertor source and the outer baffle source are shown in the inset.

Reference

1) N. Asakura, et. al., J. Nucl. Mater. 241-243 (1997) 559.

6.2 Helium Exhaust and Transport in ELMy H-mode Plasmas

A. Sakasai, H. Takenaga, N. Hosogane, H. Kubo, S. Sakurai, N. Akino,
S. Higashijima, H. Tamai, N. Asakura, K. Itami

1. Introduction

The JT-60U divertor was modified from the open divertor to the W-shaped pumped divertor in Feb.-May, 1997. Helium exhaust was possible with wall pumping due to gettering by solid target boronization (STB) in low density H-mode plasmas and low recycling divertor so far[1, 2]. The divertor modification enabled helium exhaust in high density H-mode plasmas and high recycling divertor with the divertor pumping. Helium exhaust experiment was performed to investigate the effect of the W-shaped pumped divertor on helium exhaust.

2. Experimental Arrangement

The new divertor consists of inclined divertor plates (vertical divertor) and a dome arranged in a W-shaped configuration[3]. Three ports of NBI cryopumps with an argon (Ar) frost are used to exhaust helium (He) gas. The particle flux at the inner divertor is usually higher than that at the outer divertor in JT-60U. Helium neutral particles accumulated in the private region are exhausted through an inner exhaust slot. Three Ar frosted NBI cryopumps have a total pumping capacity of 2,250 Pa·m^3. The pumping speed for He was experimentally evaluated at 13 m^3/s. It is determined by the conductance of the slot and the throat under the dome.

To demonstrate steady-state helium exhaust, a long pulse NB heated discharge of ~5 s for He exhaust is possible for 30-40 shots using Ar frosted NBI cryopumps with a large pumping capacity in JT-60U. In DIII-D, helium exhaust experiment was carried out with He beam injection for 1.4 s and an in-vessel cryopump with an argon frost[4]. However, helium exhaust in a steady state was not achieved because of the limited He pumping capability.

3. Experimental Results

In the new divertor, effective He exhaust was demonstrated with He beam injection of 1.6×10^{20}/s (equivalent to 90 MW α heating) for 6 s into an ELMy H-mode discharge (I_p=1.4 MA, B_t=3.5 T, P_{NB}=13 MW) in Fig. 1. The line averaged electron density in the main plasma is $\overline{n_e}=3.4\times10^{19}$ m^{-3}, which is corresponding to 0.5 of Greenwald density limit, the central ion and electron temperatures are $T_i(0)$=3.2 keV and $T_e(0)$=3.1 keV in the ELMy H-mode plasma. Deuterium gas of about 30 Pa·m^3/s is puffing to keep the constant electron density by a density feed back control with pump. The He density with helium pumping measured by means of charge exchange spectroscopy (CXRS) reached a saturation level ($n_{He}=1.2\times10^{18}$ m^{-3} at r/a=0.24) at 1.2 s after the start of the He beam injection. The He concentration reached 4% of the electron density in the main plasma and was kept constant for 4 s. This indicates that the

He fueling rate (equivalent to 0.7 Pa·m^3/s) is balanced with the He pumping. In this discharge, τ^*_{He}=0.7 s and τ^*_{He}/τ_E=4 with H-factor($\equiv\tau_E/\tau_E^{ITER-89P}$)=1.3 were achieved, well within the range generally considered necessary for successful operation of future fusion reactor (i.e., $\tau^*_{He}/\tau_E \leq 10$), such as ITER. Here, τ^*_{He} is the global residence time of He within the plasma chamber and τ_E is the energy confinement time.

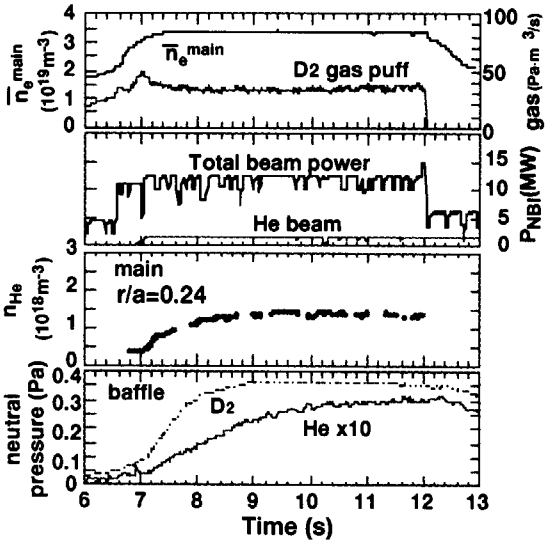

Fig. 1. The time evolution of steady-state He exhaust with He beam injection for 6 s into an ELMy H-mode discharge (I_P=1.4 MA, B_t=3.5 T, P_{NB}=12 MW).

The neutral pressure of He and D_2 below the outer baffle, which is corresponding to the neutral pressure in the divertor region linking with the exhaust ports , was measured by a Penning gauge. The D_2 neutral pressure below the outer baffle reached a saturation level of 0.4 Pa at t=9.0 s. The He neutral pressure gradually increased and reached a saturation level of 0.03 Pa at t=12.0 s.

The enrichment factor of He, $\eta=[P_{He}/2P_{D2}]_{div}/[n_{He}/n_e]_{main}$, was about 1.1, which is 5 times larger than the ITER requirement of η=0.2. The exhaust rate increased with the electron density in the main plasma[5].

Similar ELMy H-mode discharge was performed to close shutter valves in front of cryopumps. This condition of closed shutter valves is called as "without He pumping". Without He pumping, the He concentration linearly increased up to 10% at 5 s after the start of the He beam injection, which was 2.5 times as much as that with pump in Fig. 2. Without He pumping, τ^*_{He}=3.7 s and τ^*_{He}/τ_E=21 were obtained. However, a good enrichment factor of η=0.6 was obtained without He pumping.

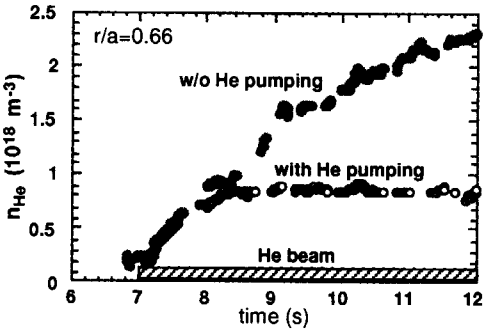

Fig. 2. Comparison of the time evolution of the He density with and without He pumping.

4. Conclusions

Injecting neutral beams of 60 keV helium atoms into ELMy H-mode plasmas for 6 s, efficient He exhaust was realized with He pumping using Ar frosted cryopumps in the new divertor. In a steady state, good He exhaust capabilities (τ^*_{He}/τ_E=4) were successfully demonstrated in ELMy H-mode plasmas. The enrichment factor of He was obtained about 1.1, which is 5 times larger than the ITER requirement of η=0.2.

References

[1] A.Sakasai, et al., Proc. 15th Int. Conf. on Plasma Physics and Controlled Nuclear Fusion Research (Seville, 1994), IAEA, Vienna, Vol. 2, 95 (1995) .

[2] A. Sakasai et al., Proc. of the 16th Int. Conf. on Fusion Energy (Montreal, 1996), IAEA, Vienna, Vol. 1, 789 (1997).

[3] N.Hosogane et al., Proc. of the 16th Int. Conf. on Fusion Energy (Montreal, 1996), IAEA, Vienna, Vol. 3, 555 (1997).

[4] M.R. Wade et al., Proc. of the 16th Int. Conf. on Fusion Energy (Montreal, 1996), IAEA, Vienna, Vol. 1, 801 (1997).

[5] A.Sakasai et al., to be published in Journal of Nuclear Materials.

6.3 Helium Exhaust in Reversed Shear plasmas

A. Sakasai, H. Takenaga, T. Fujita, N. Hosogane, S. Sakurai, H. Kubo,
S. Higashijima, H. Tamai, N. Asakura, K. Itami

1. Introduction

In reversed shear mode, the electron density in the central region is peaked and the confinement is remarkably enhanced inside the internal transport barrier (ITB), which is formed near the position of minimum q. The electron temperature and ion temperature profiles ($T_e(r)$, $T_i(r)$) inside the ITB are also peaked in JT-60U[1]. Then reversed shear mode is attractive because of its improvement of particle and energy confinement at the core region as a new operation scenario for ITER. Helium ash exhaust from the revered shear plasma is a matter of concern. It is very important to make clear He removal from reversed shear plasmas because of an enhancement of He particle confinement.

A previous study of He transport in reversed shear plasmas indicated that the improvement of the He particle confinement inside the ITB without He pumping[2]. After the divertor modification, helium exhaust in reversed shear plasmas has been investigated using He gas puff.

2. Experimental Results

Helium exhaust characteristics in the reversed shear plasma of hydrogen (I_P=1.2 MA and B_t=3.5 T) were investigated using a short pulsed He gas puff. The line averaged electron density in the main plasma is $\overline{n_e}=2.5\times10^{19}$ m^{-3}, the central ion and electron temperatures are $T_i(0)$=5.4 keV and $T_e(0)$=4.2 keV in the reversed shear plasma. Figure 1 shows the comparison of the time evolution of He II intensity at r/a=0.13 with and without He pump in the reversed shear plasmas. The He II intensity at r/a=0.13 inside the ITB (r/a=0.5) with He pump decreased with time. On the contrary, the He II intensity at r/a=0.13 without He pump did not decrease with time and it was almost constant. It was found that helium was removed from inside the ITB with He pump.

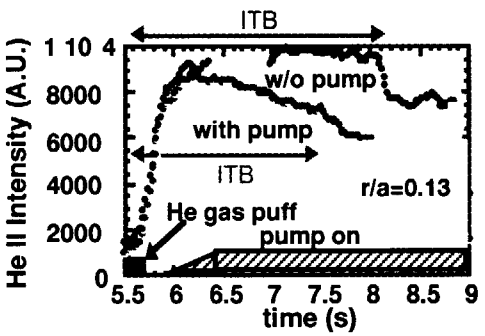

Fig. 1. Comparison of the time evolution of the He intensity at r/a=0.13 with He pump and without He pump.

Figure 2 shows the time evolution of the He density at r/a=0.13 and r/a=0.81 in the reversed shear mode. The decay time of the He density (equivalent to the local τ^*_{He}, the global residence time of He within the plasma chamber) at r/a=0.13 inside the ITB (r/a=0.5) is τ=5.5 s. While the decay time at r/a=0.81 outside the ITB is τ=1.9 s. The He residence time inside the ITB is three times as long as that outside the ITB[3]. This result indicates that it is fairly

difficult to remove helium particles inside the ITB as compared with those outside the ITB as predicted from the previous result. This is due to the improvement of He particle confinement inside the ITB.

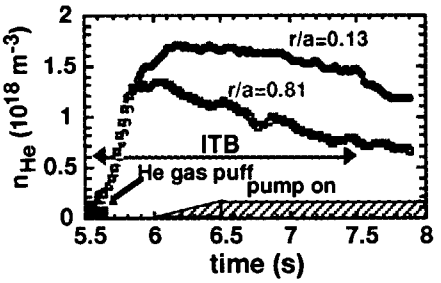

Fig. 2. Comparison of the time evolution of the He density at r/a=0.13 inside the ITB and r/a=0.81 outside the ITB in a reversed shear plasma.

This behavior of helium in reversed shear modes is clearly different from that in ELMy H-modes. The decay time is almost constant at the center and the peripheral region in ELMy H-modes. In general, τ^*_{He} is defined as the global residence time from the decay time of total helium particles . However, the He residence time in reversed shear plasmas should be newly expressed the local residence time. In a fusion reactor, the burning efficiency is large near the central core plasma due to high temperature and high density. Therefore, it is necessary to consider the local weight of the burning efficiency for a reversed shear operation.

The capability of helium exhaust depends on helium neutral pressure in the divertor region. It is possible to obtain better result of He removal in the high density deuterium operation of reversed shear modes.

3. Conclusions

After the divertor modification, helium exhaust in reversed shear plasmas has been investigated using He gas puff. Helium removal inside the ITB is about three times as difficult as that outside the ITB. The He residence time in reversed shear plasmas should be newly expressed the local residence time.

References

[1] T. Fujita et al., Phys. Rev. Lett. 78, 2377 (1997).

[2] A. Sakasai et al., Proc. of the 16th Int. Conf. on Fusion Energy (Montreal, 1996), IAEA, Vienna, Vol. 1, 789 (1997).

[3] A.Sakasai et al., to be submitted to Plasma Phys. Control. Fusion.

6.4 Active particle control for the average density and divertor pressure

H. Tamai, H. Takenaga, S. Sakurai, N. Asakura, A. Sakasai, and N. Hosogane

6.4.1. Introduction

One of the objectives of the modification to pumped W-shaped divertor is to realise the dense and cold divertor plasma with a reduced neutral back flow to the main plasma for aiming to simultaneously achieve the high performance core confinement. For the good isolation of main plasma region from the divertor, the divertor plasma parameters should be independently controlled from the main plasma paremeters. Multi feedback control by the dual gas puff into the divertor and the main plasma regions is performed in order to estimate the particle isolation between those regions.

6.4.2. Motivation

Figure 6.4.1 shows the dependence on the location of gas puff contributing to the increase of averaged density measured at U2-chord and that of divertor neutral pressure at the inside divertor. Diamonds and circles indicate the set of parameters in the cases of gas puff from only the top, and that from only the divertor, respectively. Those plots indicate the different trace by the gas puff location, that is, top puff has larger contribution to the density increase and divertor puff has larger contribution to the divertor neutral pressure. Therefore, the simultaneous control of averaged density and divertor neutral pressure by using each puff is expected.

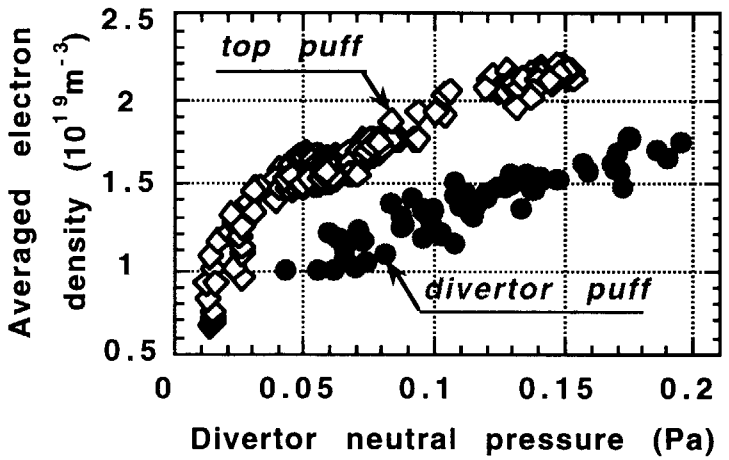

Fig.6.4.1 Dependence of neutral pressure and average density on the gas puff location. Diamonds and circles indicate the gas puff from the top, and from the divertor, respectively.

Figure 6.4.2 shows the temporal behaviour of the divertor neutral pressure and averaged density, as results of the simultaneous feedback control performed in L-mode plasma with divertor pumping. The first example indicates the waveform of relatively well controlled shot. Solid line in the boxes are reference waveform. Actual divertor neutral pressure and averaged

density well follow the reference by each corresponding gas puff. On the contrary, the second and the third examples are the shots inducing out-of-control. The second shows the over density from reference on contrary to well controlled divertor neutral pressure, and the third shows the over pressure from the reference on contrary to well controlled averaged density. During the out-of-control phase, the corresponding gas puff is not injected and the increase of the out-of-control parameter is contributed by the other gas puff.

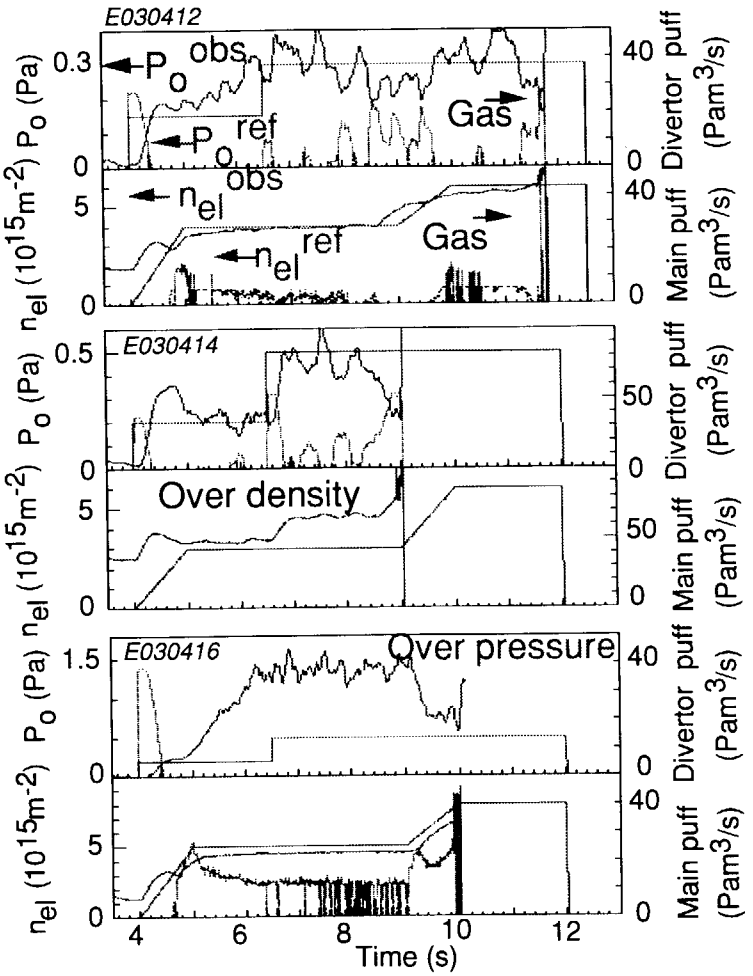

Fig.6.4.2 Temporal behaviours of the divertor neutral pressure, the averaged density and the gas puff during a simultaneous feedback control.

6.4.3. Contributions of each gas puff

From typical examples of simultaneous feedback control, existence of the coupling of each gas puff with averaged density and neutral pressure is found out. The coupling is described as

$$\begin{pmatrix} n_e \\ P_o \end{pmatrix} = \begin{bmatrix} f_1 & f_2 \\ g_1 & g_2 \end{bmatrix} \begin{pmatrix} V_1 \\ V_2 \end{pmatrix} \qquad \text{Eq. 6.4.1}$$

where f_i, g_i, and V_i (i=1, 2) are coupling coefficients for averaged density, that for neutral pressure, and the gas puff rate, while the suffix i denotes the gas puff of top (i=1) and that of

divertor (i=2). Coupling coefficients are the functions of divertor geometry and may be of SOL plasma parameters.

In order to estimate each coefficient, response to the single gas puff of pre-programmed pulse is referred. For each response to single gas puff of V_i, Eq.6.4.1 is reformed to

$$\begin{pmatrix} f_i \\ g_i \end{pmatrix} = \begin{pmatrix} n_e \\ P_o \end{pmatrix} \frac{1}{V_i} \qquad \text{Eq. 6.4.2}$$

In the ohmic discharge of I_p=1.7MA, B_t=3.5T, and the X-point height of 8cm without divertor pumping, the coupling coefficients are deduced to

$$\begin{bmatrix} f_1 = 5.7\times10^{18} & f_2 = 0.81\times10^{18} \\ g_1 = 0.65\times10^{-2} & g_2 = 1.0\times10^{-2} \end{bmatrix}$$

In this case the ratio of coupling $f_2 / f_1 = 0.14$, and $g_1 / g_2 = 0.65$, which indicates a higher contribution from top gas puff to divertor pressure than that from divertor gas puff to averaged density. Figure 6.4.3 shows the parameter plots of simultaneous feedback control in the ohmic discharge with the same configuration above. The cases of only single gas puff are also indicated by two lines (for V_1=0, and V_2=0). All plots are distributed between two border lines of V_1=0, and V_2=0, which supports the validity for the estimation of the coupling coefficients.

In order to reduce the coupling with each gas puff and to extend the operation window in n_e^{ave}-P_o^{div}, pellet injection deep into the plasma core would be one of the candidate

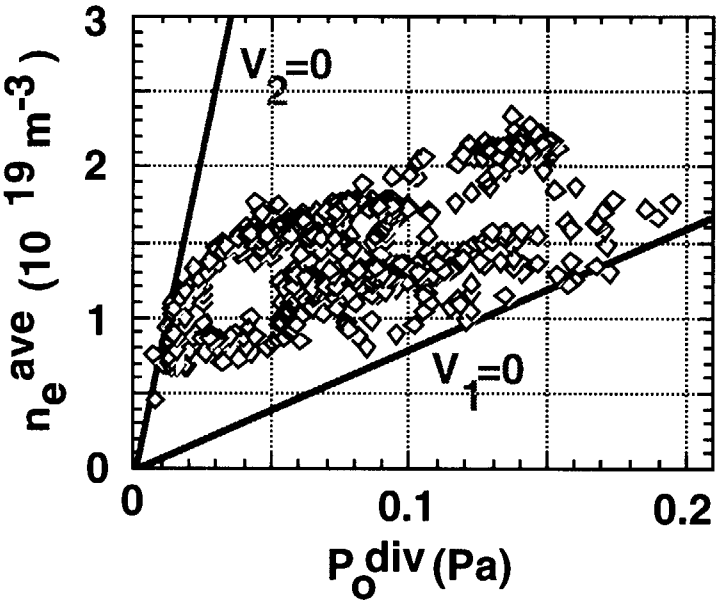

Fig.6.4.3 Parameter plots of simultaneous feedback control in the ohmic discharge of I_p=1.7MA, B_t=3.5T, and the X-point height of 8cm without divertor pumping. Two lines indicate the borders for V_1=0, and V_2=0.

6.5 Analysis of JT-60U Divertor Plasma Using a Five-Point Model

N. Hayashi*, T. Takizuka, K. Shimizu and N. Asakura
*Faculty of Science and Technology, Keio University, Yokohama, Japan

1. Introduction

The reduction of the heat load to the divertor plates is one of the most important issues for tokamak reactors. The radiative divertor is considered to be an effective method for the heat load reduction. The formation of a dense and cold divertor plasma is experimentally observed in accordance with the radiative divertor. It is important to understand the divertor physics and to control the radiative divertor for the fusion tokamak reactor.

Characteristics of divertor plasmas have been studied theoretically and numerically. Among these models of the divertor plasmas, a five-point model [1] is one of the simplest models. The five-point model is very simple and is not sufficient to study 1D or 2D structure of divertor plasmas. However, the model is very useful to understand the basic physics and the qualitative feature of divertor plasmas. In this study, we summarize characteristics of JT-60U divertor plasmas by using the five-point model.

2. Five-Point Model

Figure 1 shows the geometry used in the five-point model. The system of the model is divided into four regions. The size is measured along the magnetic field line. Two divertor regions are in the separatrix legs from the X-point to the divertor plate. The neutral recycling mainly occurs in divertor regions. Two SOL regions are separated at a stagnation point where the parallel ion flow velocity is zero. Fluids equations are integrated along a magnetic field line in each region and reduced to a set of nonlinear algebraic equations with physical variables at the five positions, as shown with closed circles in Fig. 1. The variables are those in a magnetic flux tube the nearest to the separatrix. Detailed explanation of the model is given in Ref. 1).

The model can describe the divertor asymmetry. In this study, however, we treat only the symmetric divertor plasmas ($l_{stag}=L_{SOL}/2$) where the SOL current dose not flow. Electron and ion temperatures are assumed to be the same, $T_e=T_i=T$. Recycling neutrals generated at the divertor plates have a fixed energy of 5 eV. The fraction of the recycling neutrals escaping radially from the divertor plasma is assumed to be constant ($\delta=0.05$). The parallel electron heat conductivity $\kappa_{e//}$ is a function of T and Z_{eff}, $\kappa_{e//} \propto T^{5/2}/Z_{eff}$. The impurity radiation is taken into account by enhancing the ionization energy ΔE (=13.6 eV) by a factor of 4 [2]. Geometrical parameters for JT-60U divertor plasmas are chosen as L_{SOL}=100 m, L_{div}=4 m (safety factor $q\approx5$). Radial particle and thermal diffusivities are $D_\perp$=1.0 m^2/s and $\chi_\perp$=2.0 m^2/s [2], respectively. The total particle flow Φ_{sep}, the heat flow Q_{sep} from the core plasma, and the

effective charge number Z_{eff} are given as input parameters.

3. Divertor plasma characteristics

We first consider the case Z_{eff}=1. Figure 2 shows contour plots of a calculated flux amplification factor R in a plane of Φ_{sep} and Q_{sep}. Here R is defined by the ratio of the plate particle flux to the throat particle flux of the divertor region, $R=\Gamma_p/\Gamma_u$. The maximum value of R is limited by $R_{max}=1/\delta=20$. Contour plots of a) T_{div} and b) n_{div} are also drawn in the figure with solid lines where T_{div} and n_{div} are values in front of the divertor plate.

Divertor plasmas have a transition between two equilibrium states near the region where R steeply changes (Q_{sep}>1 MW and 1×10^{22} s^{-1}<Φ_{sep}<3×10^{22} s^{-1}). One is the high recycling state with high n_{div} and low T_{div}, and the other is the low recycling state with low n_{div} and high T_{div}. These bi-stable solutions are caused to satisfy the particle balance of the divertor region through the interaction between divertor plasmas and neutral particles, which has been already found in 2D numerical simulation [3].

Figure 3 shows contour plots of a) T_{mid} and b) n_{mid} drawn with solid lines where T_{mid} and n_{mid} are values at the midplane of the SOL (stagnation point). In the low recycling region (R<2), T_{div} almost equals to T_{mid} and is larger than about 100 eV for Q_{sep}>1 MW and Φ_{sep}<3×10^{22} s^{-1}. Because the electron heat conductivity $\kappa_{e//}$ is large for high T, the temperature gradient is small. On the other hand, in the high recycling region (R>2), T_{div} is much lower than T_{mid} and decreases to 10 eV with increasing Φ_{sep}. In this case, the conductive heat flux is held by the large temperature gradient from the midplane to the plate. The decreasing in T_{div} is accompanied with the increasing in n_{div}. The dense and cold divertor plasma is maintained in a part of the high recycling region. Figure 4 shows contour plots of P_{rad}/Q_{sep} where P_{rad} denotes the total radiation power in the divertor regions. The divertor radiation is larger as divertor plasmas become denser and colder.

Finally, we analyze a dependence of the divertor plasma characteristics on Z_{eff}. Figure 5 shows contour plots of a) T_{mid} and b) n_{mid} with R for Z_{eff}=3. The other parameters T_{div}, n_{div} and P_{rad}/Q_{sep} as well as R are not much different from those for Z_{eff}=1, as shown in Fig. 2 and 4. In the low recycling region (R<2), T_{mid} and n_{mid} are also not much different from those for Z_{eff}=1. On the other hand, in the high recycling region (R>2), T_{mid} increases compared with that at the same Φ_{sep} and Q_{sep} for Z_{eff}=1 because $\kappa_{e//}$ decreases with increasing Z_{eff}. The midplane density n_{mid} decreases with increasing T_{mid} due to the pressure balance.

4. Discussion

In this study, we investigated characteristics of JT-60U divertor plasmas for the case that they are attached and symmetric between inside and outside divertors. When dense and cold divertor is formed, the following phenomena should be considered for more realistic study.

Plasma pressure, mnv^2+2nT, is assumed constant along the magnetic field line in the present study. In cases of detached divertor plasmas, however, the pressure drops towards the divertor plate through momentum losses by ion-neutral interactions. The SOL current due to the thermoelectric effect has been found to cause the divertor asymmetry at the onset of the thermoelectric instability [4,5]. The symmetric divertor plasmas become unstable due to the thermoelectric instability below a critical temperature T_{div}^{crit}, and stable asymmetric divertor plasmas are formed. As for Z_{eff}, we take into account of the relation $\kappa_{e//} \propto Z_{eff}^{-1}$, but we set the condition $n_e=n_i$ for simplicity. For high Z_{eff}, the ratio n_i/n_e becomes small. The dependence of n as well as P_{rad} on Z_{eff} should be considered for high Z_{eff} plasmas.

References

1) N. Hayashi, et al., J. Phys. Soc. Jpn. **66** (1997) 3815.
2) K. Shimizu, et al., J. Nucl. Mater. **196-198** (1992) 476.
3) M. Sugihara, et al., J. Nucl. Mater. **128-129** (1984) 114.
4) N. Hayashi, et al., to be submitted to J. Nucl. Mater.
5) N. Hayashi, et al., to be submitted to Nucl. Fusion.

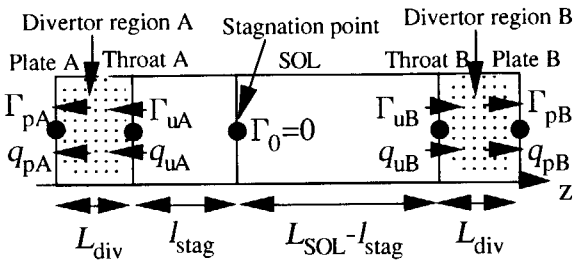

Fig. 1 Five-point model.

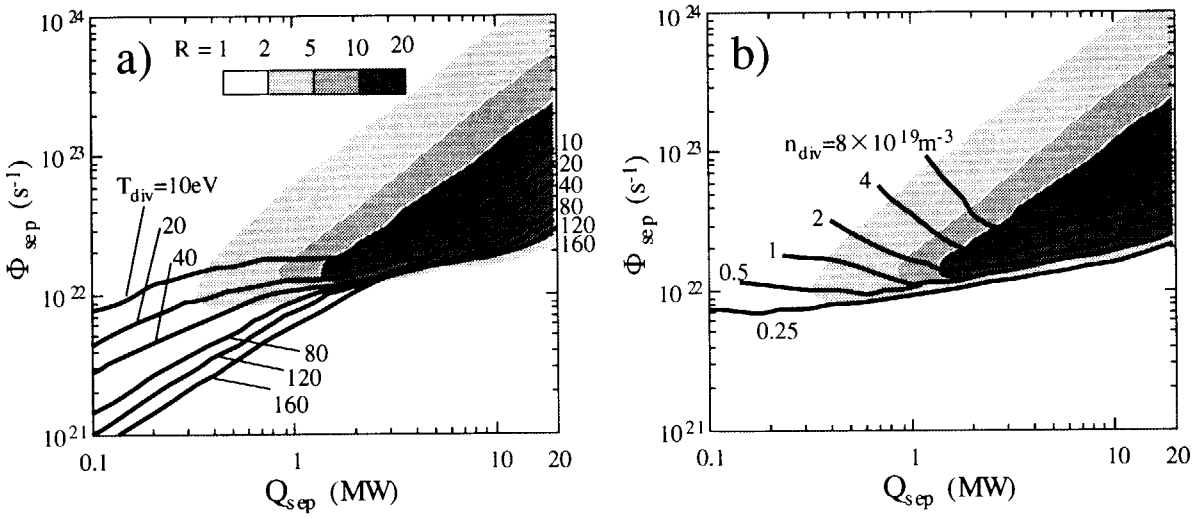

Fig. 2 Contour of a) T_{div} and b) n_{div} on contour of R.

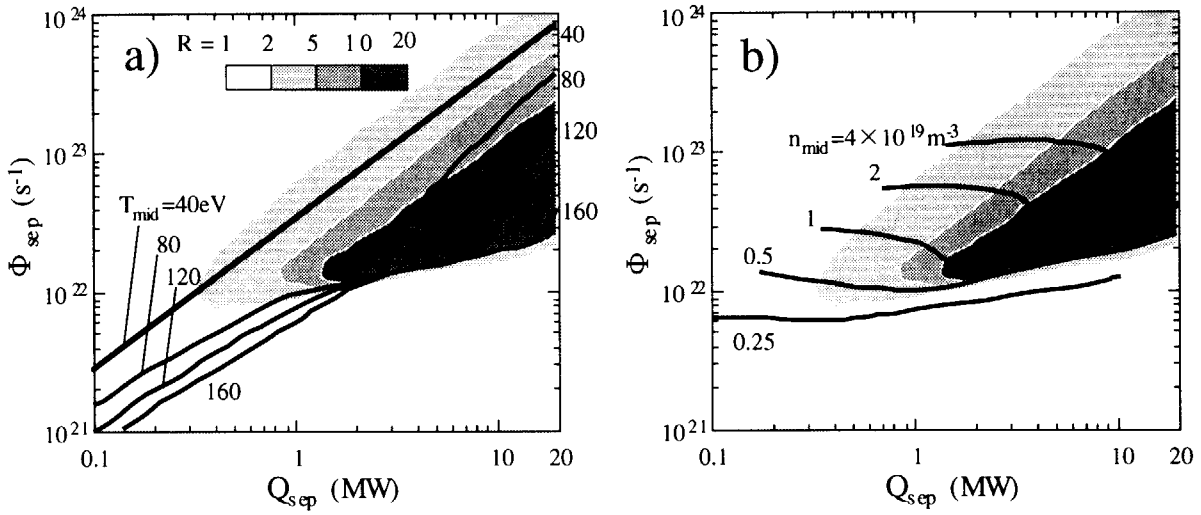

Fig. 3 Contour of a) T_{mid} and b) n_{mid}

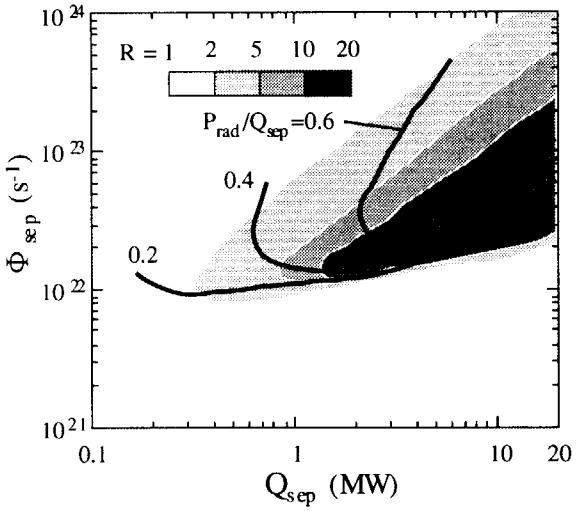

Fig. 4 Contour of P_{rad}/Q_{sep}

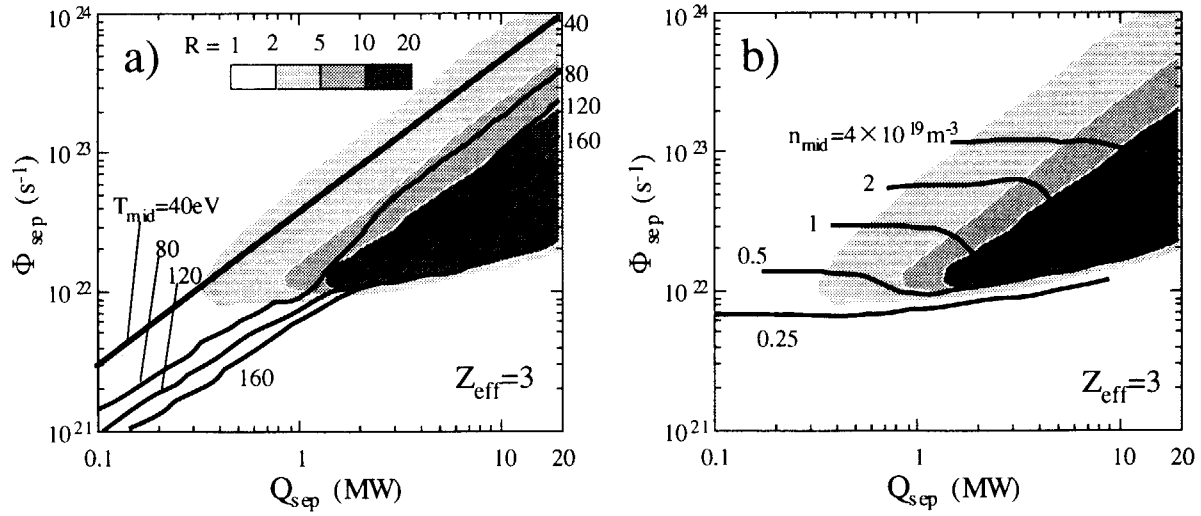

Fig. 5 Contour of a) T_{mid} and b) n_{mid} when Z_{eff}=3.

7. Radiative Divertor and SOL/Detachment Physics

7.1 Radiative divertor with seeded neon

K. Itami, S. Konoshima, N. Hosogane, N. Asakura and A. Sakasai

Noble gas, such as neon, has much larger radiation efficiency in the range of 20 eV < Te < 70 eV than carbon and oxygen. It has been found in ELMy H-mode discharges of JT-60U [1] that D_2 injection following Neon injection has such gains that 1) Increment of divertor particle recycling is fivefold large over simple D_2 injection and 2) Increment of radiation loss from the main and divertor plasma is twofold large over simple neon injection. These gains effectively promote dense and cold divertor plasma in which intrinsic carbon radiation is large enough to form x-point MARFE and divertor detachment. However there have been no ways to control neon content in the main plasma of JT-60U[2], since neon is recycling between the main plasma and the first wall. Neon content was kept constant in the main plasma once neon is introduced to the vacuum vessel.

In May 1997, the modification of the divertor to a W-shaped and the installation of divertor pump[3] was completed to address the advanced control of the divertor plasmas. Semi-closed structure is expected to have better neutral confinement in the divertor region and to facilitates high recycling in the divertor. Neutral particles are escaped through the pumping slot at the bottom of the inner divertor and then guided under the outer baffle to one of the three cryo-pump system. These cryo-pumps used to be a part of the NBI system before this divertor modification. Pumping speed from the three pumping ports is estimated to be as large as 14 m^3/s for deuterium gas. There are not pumping slot opened at the outer divertor.

The initial radiative divertor experiments with W-shaped divertor were carried out by applying a pulsed neon gas puff and intense D_2 puff to ELMy H-mode and reversed shear (RS) plasmas in JT-60U. Neon gas was injected from the inner slot in a pulse (typically 0.6 Pam^3/s x 0.4 s) into the divertor. D_2 gas puffing, as large as 40 Pam^3/s, was applied continuously from the two locations. The one is from the top of the vessel and the other is from the divertor slot. In this paper, we call the former "the main D_2 puff" and the latter "the divertor D_2 puff". It is estimated from the conductance to the divertor and that to the cryo-pumps that 30 % of D_2 puff is pumped out without entering the divertor in the divertor D_2 puff.

Figure 1 shows a typical wave form in this experiment. The neutral beam power of PNB = 25 MW was applied to the plasma with Ip = 1.2 MA and BT = 3.5 T in order to obtain target ELMy H-mode plasma. The divertor configuration is shown in Fig. 2(a) Radiation loss from the divertor, P_{rad}(div), started to increase just after neon injection as Ne^{9+} line intensity increased. However radiation loss from the main plasma, P_{rad}(main), was increasing after D_2 gas puff into the main plasma at t = 7.1 s. Additional boost of the radiation loss from the divertor P_{rad}(div) started at t = 7.8 s, the timing of the divertor detachment. Radiation loss from the divertor was increasing up to ~ 9 MW. This radiation loss is mainly from carbon ions radiating around the very narrow region around the X-point. [4]. This phenomenon is known as X-point MARFE. The total radiation loss reached to more then 70 % of the beam power. Divertor CII intensity has similar wave form with the radiation loss from the divertor.

It has been observed in JT-60U that CII intensity near the X-point starts to increase as the X-point MARFE is approaching to the X-point. Decay of Ne^{9+} intensity indicates that neon impurity was pumped out from the main plasma , effectively. Radiation loss from the main plasma was also decreasing, while Ne^{9+} was decreasing. Total radiation loss was kept constant, since decrease in the P_{rad}(main) is compensated by increase in P_{rad} (div) and the divertor MARFE was sustained.

Here the incremental radiation after neon injection was defined as

$\delta P_{rad}(main)\ (t) = P_{rad}\ (main)\ (t) - P_{rad}\ (main)\ (t_0)$.

Here t_0 is the timing at which Ne^{9+} line intensity started to grow up. Fig. 3 shows the relation between δP_{rad}(main) against the Ne^{9+} line intensity in the shot 29359, in which only neon gas was puffed, and the shot 29362, in which neon gas and main D_2 puff were puffed. As is shown in this figure, P_{rad}(main) was coupled with Ne^{9+} line intensity and P_{rad}(main) was enhanced by the main D_2 puff. No enhancement in P_{rad}(main) by the divertor D_2 puff was observed. Another important point in this figure is that P_{rad}(main) didn't decrease in the later phase, since neon was not pumped out in the shot 29359, the discharge without D_2 puff.

Pumping efficiency of neon is characterized by exponential decay time of neon content in the main plasma. Here we represent the neon content by the Ne^{9+} line intensity. D_2 gas puff rate and gas puff position were scanned in order to study the effects on neon pumping. It was observed that neon decay time was effectively reduced by additional D_2 puffing. Decay time constant, τ_{pump}, was reduced to as low as ~ 1 second in both the main and divertor D_2 puff, while the required D_2 puff rate was different. 20 Pam^3/s of gas puff rate was required for the main D_2 puff and 40 Pam^3/s, as shown in Fig. 4. τ_{pump} in the discharges with Ip = 1.5 MA and BT = 3.5 T is shown as a function of particle flux to the inner divertor. τ_{pump} was calculated for the period during the divertor attached. The total particle flux to the inner divertor was estimated by signal from Hα diodes viewing the divertor. This figure shows that main D_2 puff could reduced neon decay time more effectively than divertor D_2 puff as a function of divertor particle flux.

When the divertor detachment occurred, total particle flux to the inner divertor was reduced at the inner divertor side. However it was observed decay rate of neon was unchanged. In the shot 29362, in which the detached divertor phase was as long as 1.6 second, τ_{pump} was 1.2 second during the detached divertor phase. Therefore the decay time constant of neon during the detached divertor phase is as small as the smallest values during the attached divertor phase, regardless of the reduced particle flux to the inner divertor.

It has already been reported in the tokamaks with divertor pumping, such as ASDEX-U[5], DIII-D[6] and JET that pumping efficiency of impurity ions was enhanced by additional D_2 gas puffing. This is so called "puff and pump" effect. The following three effects are proposed to enhance the impurity pumping. 1) drag force to impurity ions by SOL flow. 2) Collisions with deuterium ions and neutrals 3) Ejection by ELM activity. However there are controversy about the major contributor for the enhancement. In DIII-D, they observe the most effective impurity pumping when the divertor separatrix is close enough to the pumping opening and D_2 puff is applied from the top of the plasma. However ASDEX-U pointed out that no significant difference by gas puff location and pointed out recycling particles are much more larger than flow particle flux. The result in JT-60U shows the difference between the divertor D_2 puff and the main D_2 puff, as is reported in DIII-D.

In most of the discharges during this experiment, separatrix at the inner divertor was located at the position where the slot-separatrix distance, d_{sep}, was 10 cm. From the point of the impurity exhaust, this divertor configuration might not be the optimum. Since escaping aperture for neutrals increases as the inner separatrix approaches to the pumping slot. The better pumping efficiency is expected at the smaller d_{sep}. Neon and D_2 puff was applied to the ELMy H-mode discharges in which d_{sep} = 2 cm and the other parameters are almost fixed. The divertor configuration is shown in Fig. 2(b). Smaller value of τ_{pump} was obtained in the discharge with d_{sep} = 2 cm, when no additional D_2 puff was applied. τ_{pump} was 2.3 second in the discharge, a factor of three to four improvement over the discharges with d_{sep} = 10 cm. However τ_{pump} was not so much improved as the discharges with d_{sep} = 10 cm,, when the main D_2 puff was applied. τ_{pump} = 1.6 s at 1.5 x 10^{23} s^{-1} of particle flux to the inner divertor was even worse than those with d_{sep} = 10 cm, very interestingly.

In addition, we found a difficulty in the discharges with d_{sep} = 2 cm to increase the radiation loss from the main and divertor plasmas. Figure 5 shows the discharges with d_{sep} = 2 cm have lower P_{rad}(div) fraction than those with d_{sep} = 10 cm. And δP_{rad}(main) , as a function of Ne^{9+} intensity, was found to be smaller by a factor of three than the discharges with d_{sep} = 10 cm. Therefore, it was impossible to increase the total radiation loss up to about 40 % of the input power to trigger the divertor detachment and X-point MARFE, even if neon gas injection was increased up to fivefold and the main D_2 injection was doubled.

Impurity seeding was also applied to the reversed shear discharges with Ip = 1.5 MA and BT = 3.5 T and PNB = 20 MW. Increase in the radiation loss in P_{rad}(div) during the improved core confinement with the internal transport barrier was obtained. Pump effect of neon in the main plasma was also observed.

In summary, modification of the divertor to a W-shaped pumped divertor and installation of pumping has enabled demonstration of puff and pump effect in injected neon during the detached divertor phase, albeit the pumping speed was modest (~ 14 m^3/s).

References

[1] K. Itami et al. Plasma Phys. controlled Fusion 36, Supplement 11A, A117 (1995).

[2] K. Itami et al. Plasma Phys. Contl. Nucl. Fusion Research (Proc. 16th IAEA Fusion Energy Conf. Montreal, 1996). IAEA-CN-64/GP-11., vol. 1, p. 385.

[3] N. Hosogane et al. in ref. [2] IAEA-CN-64/A4-2., vol 3, p. 555

[4] S. Konoshima, Private Communication.

[5] H.-S. Bosch et al Phys. Rev. Lett. 76 (1996) 2499.

[6] M. Wade et al., Bulletin of the APS Meeting, Pittsburgh, 1997.

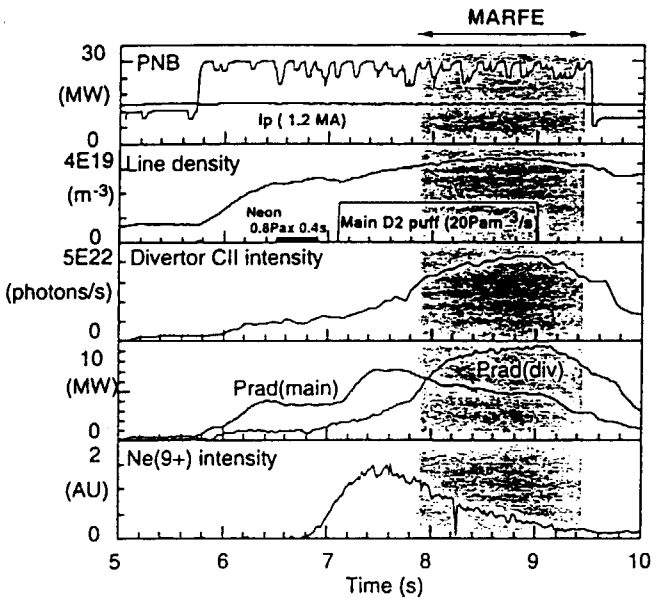

Fig. 1
A typical waveforms in the radiative divertor experiment with neon seeding.

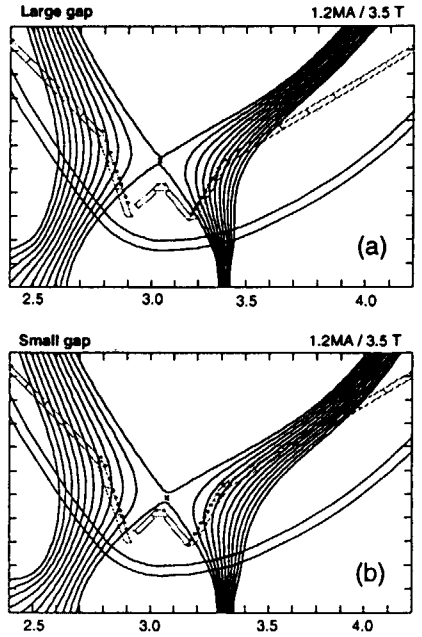

Fig. 2
Divertor configuration in this experiment.
(a) with large gap distance
(b) with small gap distance

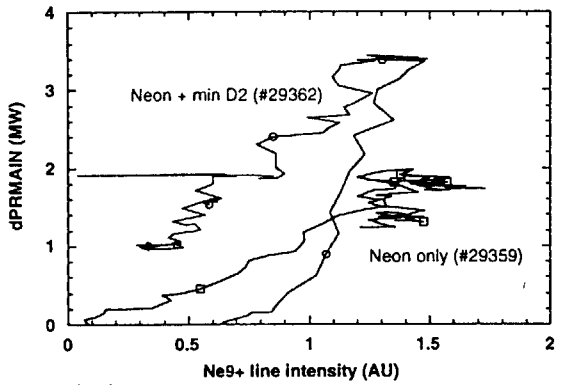

Fig. 3
Incremental radiation loss in the main plasam after neon injection is plotted as a function of Ne9+ line intensity.

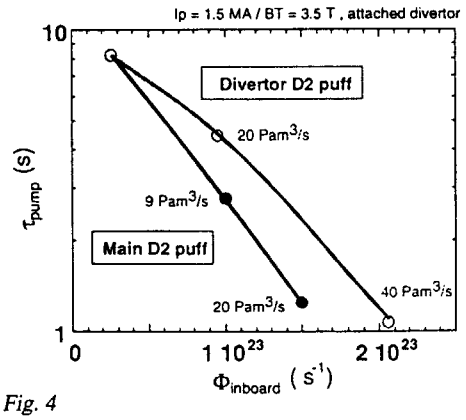

Fig. 4
Time constant for neon content, represented by exponential decay time of Ne9+ line intensity, plotted against paricle flux to the inner divertor .

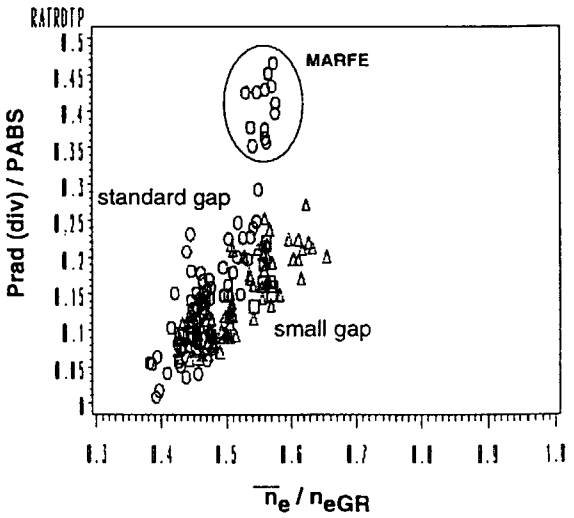

Fig. 5
Divertor radiation loss fraction against the beam imput power is plotted as a function of Greenwald normalized parameter.

7.2 SOL/divertor plasma study in high density discharges

N. Asakura and S. Sakurai

7.2.1 Introduction

Transport of particle and heat across and along the magnetic field line was investigated in the scrape-off layer (SOL). Radial profiles of electron density, n_e, and electron temperature, T_e, were measured with Langmuir probes, simultaneously at the four poloidal locations in the SOL and divertor: at outer midplane, near divertor x-point, on the inner and outer divertor plates as shown in Fig. 1. Two fast reciprocating Langmuir probe systems were installed at midplane[1] and near x-point[2]. In particular, up-stream divertor plasma profile was, for the first time in large tokamaks, measured from outer target plate to the private region near x-point. Mach probe was used to evaluate the plasma flow direction at the outer divertor throat. Systematic database of plasma profiles were obtained with density and x-point scans in OH discharges, and the results of high density SOL plasma and divertor plasma detachment are summarized.

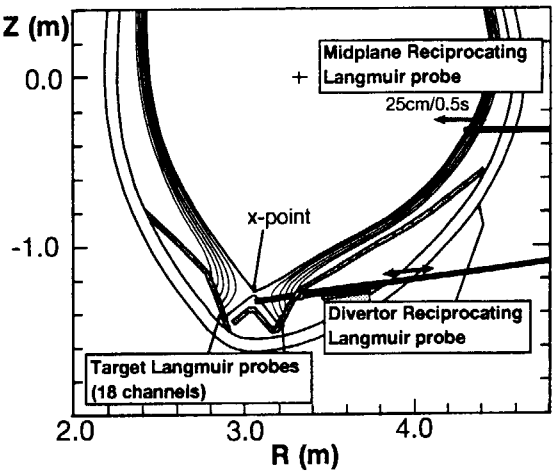

Fig.1 Plasma poloidal cross-section and arrangement of reciprocating Langmuir probes, and divertor target probes.

7.2.2 High density SOL

Electron plasma density near x-point is evaluated by ion saturation current, I_s^{up}, and electron temperature, T_e^{up}, at the upstream side: $n_e^{up} = 2I_s^{up}/(eA_\perp c_s)$, where $A_\perp$ is the effective collection area of the probe (assuming the area projected to the local field line and neglecting SOL plasma flow), and $c_s = [k(T_i + T_e)/m_i]^{1/2}$ is the ion acoustic speed (assuming that $T_i = T_e$).

Figure 2 shows that the time evolution of n_e^{up} and T_e^{up} profiles with increasing $\bar{n}_e$, where distance from separatrix is mapped on the midplane radius. A peak of n_e^{up} profile appeared near the separatrix and is enhanced extremely up to 1×10^{20} m^{-3} at high density. At the same time, the peak position shifts to the outer SOL region with increasing $\bar{n}_e$. Here, 2 mm at the midplane radius corresponds to 10 mm at the x-point. Appearence of large n_e peak was reported at the outer target probe in Alcator C-mod "death ray"[3] and in JET "high recycling peak"[4], and the density peak is for the first time observed at up-stream divertor. Since Mach number of the plasm flow could not be estimated due to the relatively large difference of electron temperatures at up- and down-streams, absolute value of the peak n_e^{up} is under investigation.. With an increase in n_e^{up}, the local T_e^{up} decreases, in particular, near the separatrix from 60 to 20 eV.

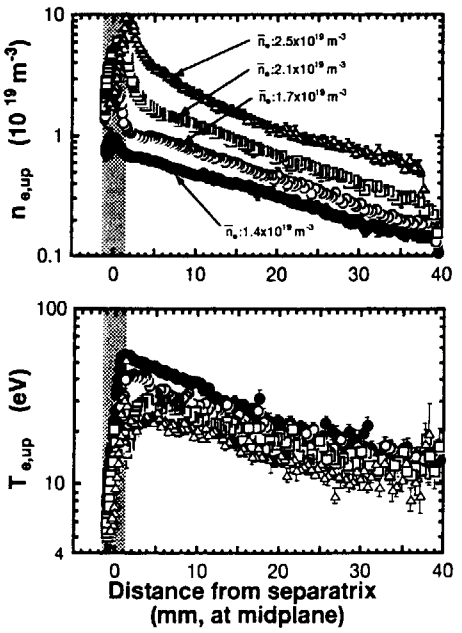

Fig. 2 Time evolution of electron density and temperature profiles measured with x-point reciprocating probe. Distance from separatrix is mapped on the midplane radius.

Figure 3 shows SOL and divertor plasma distributions at the relatively high $\bar{n}_e$ of 2.1×10^{19} m^{-3}, and the profiles are mapped on the midplane radius. Plasma profile at the divertor target is obtained by sweeping x-point height of 8−13 cm from the dome-top. Density, n_e, peaks are observed in profiles measured at the x-point and outer divertor target. The profiles can not be described by an exponential decay model. T_e at the separatrix decreases from 60 eV (at misplane) to 19 eV (near x-point) on the same magnetic flux surface, which shows that the gradient of T_e along the field line increases at the main plasma edge.
Electron pressure at the upstream divertor, p_e^{up}, defined by $n_e^{up} \times T_e^{up}$ assuming zero SOL flow velocity, is comparable to that at the outer radius of the midplane. However, the peak p_e^{up} near the x-point is by the factor of 1.5 larger than p_e at the midplane. The "momentum gain" is not explained by the calculation result of the one-dimentional fluid model. Plasma flow from the x-point to the outer divertor target may increase the velocity. Or a part of n_e^{up} may be provided from impurity ions.
T_e near the outer strike point decreases to 10 eV. Two times of p_e at the outer target (static plus dynamic pressure) is comparable to p_e at the midplane. This shows that the divertor plasma is attached. Extention of the divertor plasma detachemnet is described in Sec. 7.2.3

The reduction in T_e and increase in n_e along the field line are summarized in Fig. 4. Two values are plotted for the x-point plasma profile: one (closed circle) is at the n_e^{up} peak and another (triangle) at the separatrix from an e-folding curve excluding the n_e^{up} peak. With an increasing in $\bar{n}_e$, the reduction in T_e near the x-point and at the target is large compared to that at the midplane, and n_e at the divertor increases larger than T_e at the midplane. Under the attached divertor condition, p_e increases by the factor of 2.5 at high $\bar{n}_e$ and is saturated. Plasma detachment occures at the divertor when T_e decreases to 7 eV (at the outer divertor) and 17 eV (near the x-point) while T_e = 55 eV at the midplane. p_e decreased by 10−20% even at the midplane.

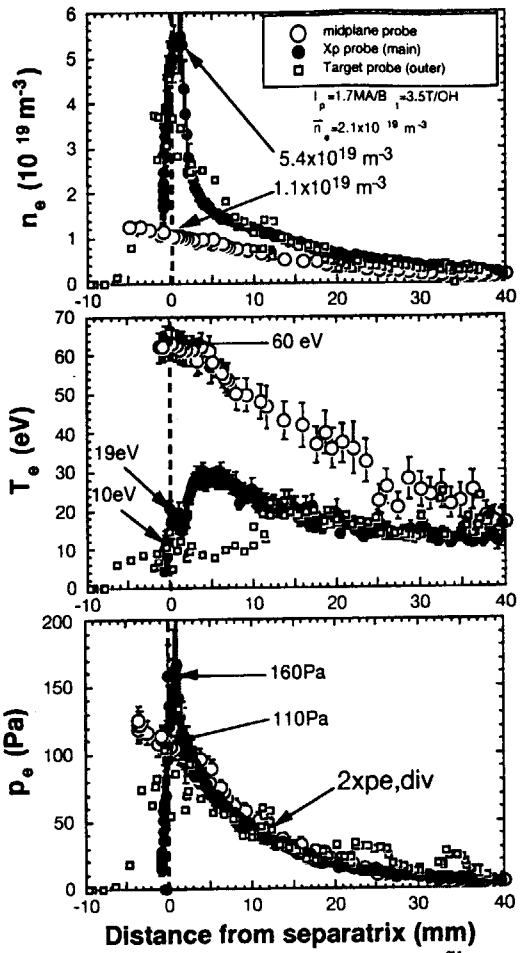

Fig. 3 Electron density, temperature, pressure profiles are measured at midplane, near x-point and outer divertor target at high density. They are mapped on the midplane radius.

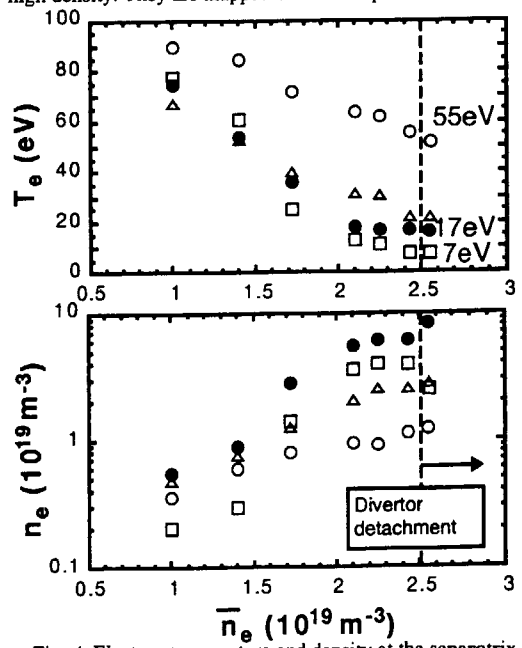

Fig. 4 Electron temperature and density at the separatrix with increasing line averaged density.

Local radiation loss and ionzation fluxes of deuterium and carbon impuriy near the x-point of the outer SOL region are evaluated by the multi-channel bolometers and spectroscopic measurements, respectively. These values are assuming the toroidal symmetry, and the results aare shown in Fig. 5. Ionization flux of deuterium atom is enhanced near the x-point, and the contribution to the radiation loss is small (~20). Most radiation power due to carbon ions such as C^{3+}, and the increase is consistent with the raduction in the local electron temperature, T_e^{up}, to 20−40eV.

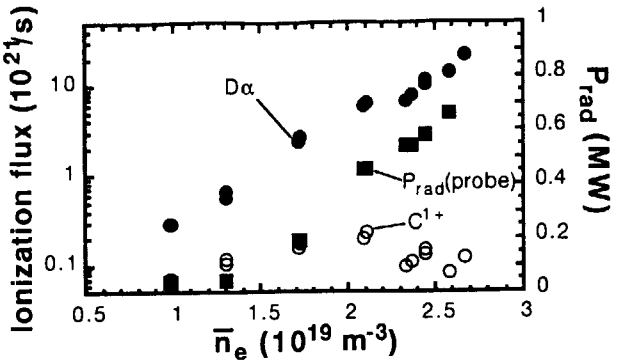

Fig. 5 Local ionization fluxes of dueterium and carbon and radiation loss from the outer SOL near x-point. Local Te and ne are used to evaluate ionization flux.

7.2.3 Divertor detachment

Figure 6 shows the ratio of down-stream electron pressure to up-stream one at the different field lines. At high $\bar{n}_e$ lower than the onset of the divertor plasma detachment, peak p_e^{up} near the x-point separatrix increase, and the ratio of p_e^{up}/p_e^{mid} becomes two. The increase in the ratio $2 \times p_e^{div}/p_e^{mid}$ is also observed at the outer divertor. With $\bar{n}_e$ increasing, region of "momentum gain" extends from the separatrix to the outer flux surfaces, while the divertor plasma is detached up to the x-point near separatrix. Candidats are underinvestigation: n_e provided from impurity ions, ion pressure at midplane larger than that near x-point and plasma flow increasing near the x-point.

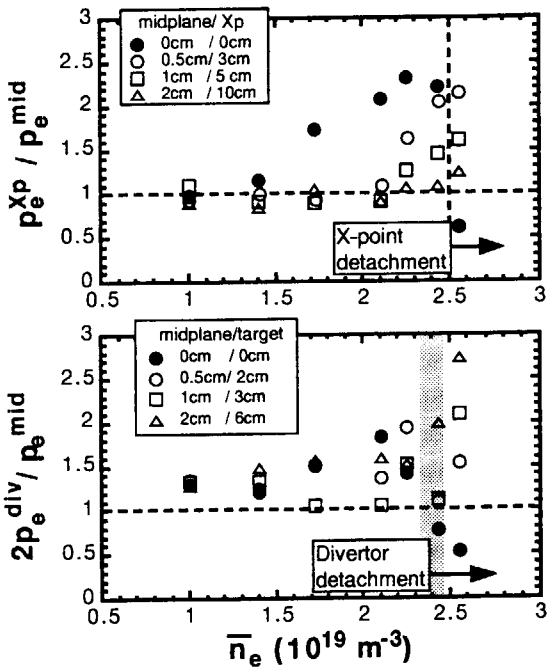

Fig. 6 Ratios of down-stream electron pressure to midplane pressure at different radius. Partial plasma detachment occurs at 2.4×10^{19} m^{-3} on the outer divertor target and at 2.5×10^{19} m^{-3} near x-point.

7.2.4 SOL width

Decay lengths of $n_{e,mid}$ and $T_{e,mid}$, λ_{T_e} and λ_{n_e}, are compared at midplane and x-point. Single e-folding length fit was used to deduce the decay length of the plamsa profiles, which are mapped on the midplane radius. Fit was applied to data in the first SOL, extending up to 30−40 mm outside the separatrix. Data at the peak n_e^{up} (~ 5 mm near x-point) was excluded for the fit.

Figure 7 shows that SOL e-folding lengths are the same between midplane and x-point from low densiy to before the onset of divertor detachment, when they maped on the same flux suefaces.

λ_{T_e} increases at high density due to a reduction in the parallel conduction of the SOL plasma, while λ_{n_e} is relatively constant or rather decreases. The ratio of $\lambda_{T_e}/\lambda_{n_e}$ increases from ~1 (low $\bar{n}_e$ = 1.0×10^{19} m^{-3}) to 1.8 (at divertor detachment: $\bar{n}_e = 2.5 \times 10^{19}$ m^{-3}).

7.2.5 Summary

SOL plasma profile was measured at the different poloidal locarions, in particular at divertor x-pont, using Langmuir probes.

(1) large peak in n_e profile appeares near the x-point at high density, and T_e decreases locally. Local p_e at the x-point became larger than p_e at the midplane.

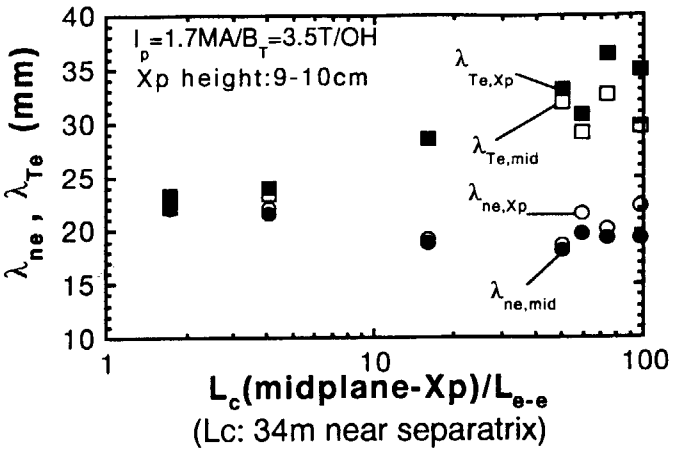

Fig. 7 e-folding lengths of n_e and T_e profiles measured with the midplane and x-point reciprocating probes as a function of electron collisionality (proportional to n_e/T_e^2).

(2) Gradient of T_e along the field linne increased at main plasma edge. T_e at the x-point decreased to ~20 eV when the divertor detachment occured.

(3) SOL e-folding length is the same between midplane and x-point when they maped on the same flux suefaces. λ_{T_e} increased at high density due to a reduction in the parallel conduction of the SOL plasma.

Effects of the divertor geometry on the decay length are summarized in the following section. The midplane reciprocating probe system is midified to Mach probe in 1998.

References

[1] N. Asakura, *et al.*, Rev. Sci. Instrum. **66** (1995) 5428.
[2] Details of the x-point probe system are shown in Sec. 8.4.
[3] B. LaBombard, *et al.*, J. Nucl. Mater. **241 – 243** (1997) 149.
[4] R.D. Monk, *et al.*, J. Nucl. Mater. **241 – 243** (1997) 397.

7.3 Effect of the divertor geometry on SOL plasma

N. Asakura and S. Sakurai

7.3.1 Introduction

Profiles of SOL and divertor plasma such as electron density, n_e, and temperature, T_e, are compared for the open and W-shaped divertor geometries. In Feb.-Mar. 1998, database of the high plasma current (I_p = 1.7 MA, B_T = 3.5 T, plasma volume V_p = 77 m^3 and triangularity δ = 0.32) was obtained in NB-heated L-mode (P_{NBI} = 4.1-4.3 MW). It was a comparable database to that analyzed in the open divertor geometry (1995), and was sent to ITER R&D profile database for the divertor/SOL study[1].

7.3.2 Divertor plasma profile

Large peak in ion saturation current profile was observed near the strike point in the W-shaped divertor. The peak profile can be measured with the spatial resolution of a few mm during a plasma x-point sweep (x-point height from the dome top was changed between 8−13 cm for 1.5 s) with keeping the same V_p and line averaged electron density of the main plasma, $\bar{n}_e$. Large peak (larger than an e-folding shape) has not been observed in the open divertor. Figure 1 shows the profiles of electron density, n_e^{div}, and electron temperature, T_e^{div}, at the outer target in the open and W-shaped divertors. At the same $\bar{n}_e = 2.3 \times 10^{19}$ m^{-3}, T_e measured with the midplane probe was 55 eV and 63-73 eV for the open and W-shaped divertors, respectively.

For the case of the W-shaped divertor, n_e^{div} near the strike point (about 2 cm) is enhanced by a factor of 2.5, and local T_e^{div} decreases to 10 eV. This result indicated that the inclined divertor target and the private dome work to condense neutrals to the separatrix. Particle recycling flux in the outer divertor chamber measured with an D_α array was slightly larger than database in the open divertor. An increment in the ion flux is about 20% of total ion flux flowing to the outer divertor target, which was not clearly observed in D_α brightness profile.

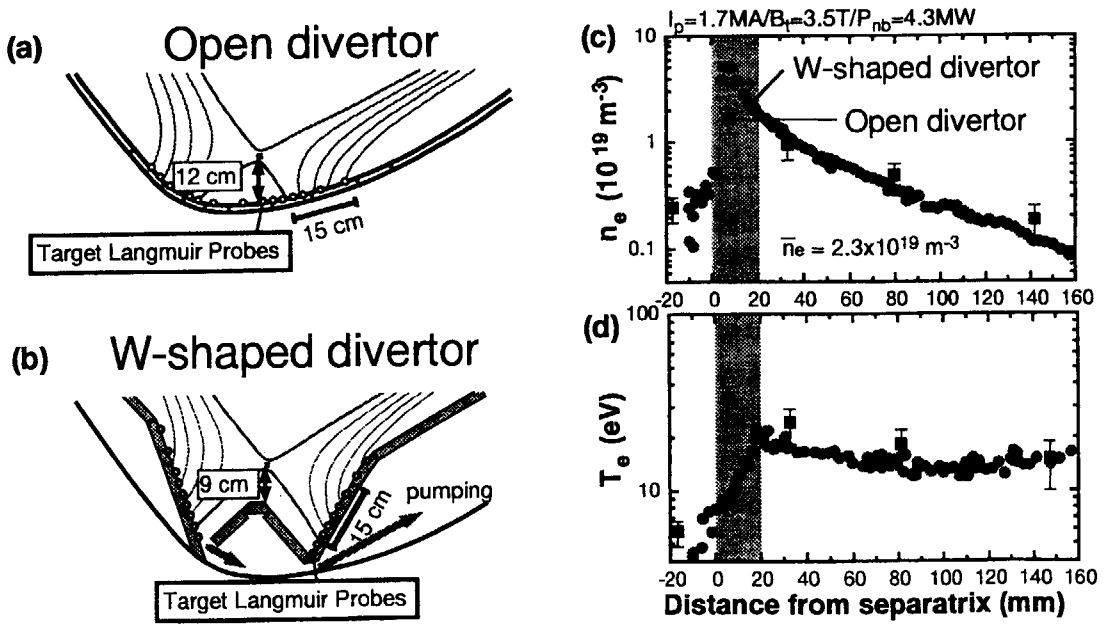

Fig. 1 Divertor geometry of (a) the open divertor, (b) the W-shaped divertor (1997/5-), and plasma configurations are shown. Comparison of (c) electron density and (d) electron temperature profiles at the outer divertor target. Circle and square symbols show the open and W-shaped divertor cases. Profiles for the W-shaped divertor were measured during x-point sweep.

7.3.3 Divertor plasma detachment

"Partial plasma detachment" was observed at high density both in the open and W-shaped divertors. Due to the larger enhancement of the ion flux near the target, radiation loss increased to 40% of P_{SOL} at lower $\bar{n}_e$, and x-point MARFE occurred at 50% of "Greenwald density". Figure 2 shows detachment locations measured with the x-point reciprocating probe and target Langmuir probes. Electron temperature near x-point (just down-stream), T_e^{Xp}, decreases with an increase in the local electron density, n_e^{Xp}, The radial width of the reduction in T_e^{Xp} is about 3.5 cm, and the magnetic flux surface agrees with the width of a reduction in T_e^{div} (2 cm) at the target. This result shows that detachment of the divertor plasma occurs simultaneously along the field line. Here, radial width of the detached region corresponds to about 0.7 cm at the outer midplane, which is slightly narrower than that for the open divertor case (about 1 cm)[1]. Divertor plasma detachment occurs in the magnetic flux region (hatched area), and, at the same time, in the outer flux surfaces T_e^{Xp} profile becomes flat and n_e^{Xp} increases. Radial diffusion of heat and particle fluxes may be enhanced at the upstream of the x-point.

Large peak in electron pressure profile near the x-point, p_e^{Xp}, (larger than the electron pressure at the midplane, p_e^{mid}) shifts to the boundary of the attached flux region. Pressure loss factor, p_e^{mid}/p_e^{Xp}, is evaluated to be 10 (= 130/13) below the X-point, and $p_e^{mid}/2p_e^{div}$ = 87 (= 130/1.5) at the outer target. Later value was larger than $p_e^{mid}/2p_e^{div} \leq 15$ for the open divertor.

7.3.4 SOL parameters at midplane

Electron density and temperature at midplane SOL, n_e^{mid} and T_e^{mid}, were measured with a reciprocating Mach probe installed at the end of 1997. Values of n_e^{mid} and T_e^{mid} were deduced with averaging those measured at upstream and downstream sides of the Mach probe. Difference of n_e was by a factor of 1.5-2.5, and that of T_e was about 10−20%.

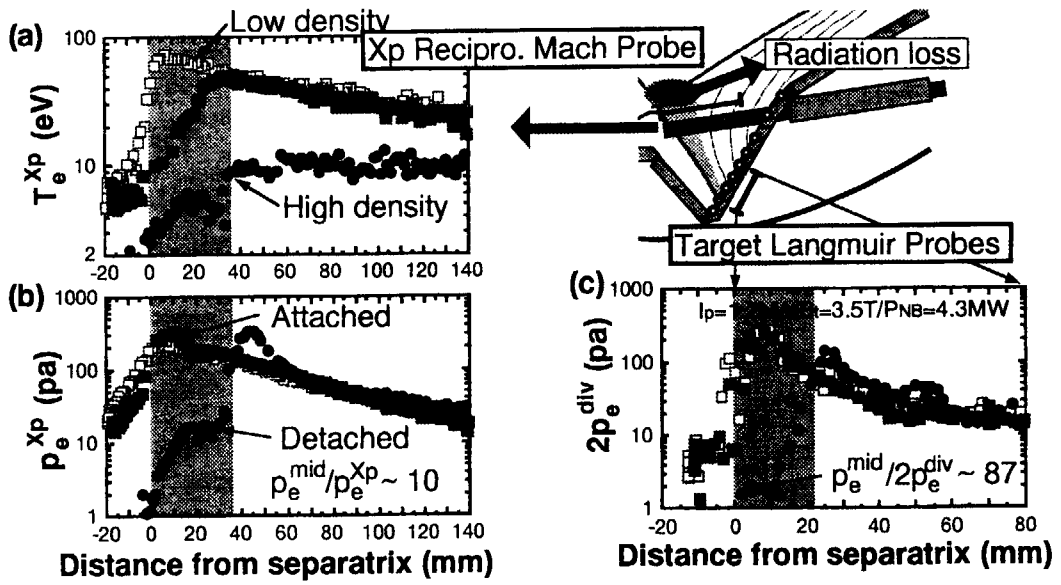

Fig. 2 Profiles of (a) electron temperature, (b) electron pressure near x-point and (c) electron pressure at the outer target. Square and circle symbols show the attached and detached divertor plasma. Hatched area shows the region, where the plasma is detached.

Figure 3 shows comparison of n_e^{mid} and T_e^{mid} profiles at the same $\bar{n}_e$ for the open (open circles) and W-shaped (closed circles) divertors. For the W-shaped divertor, field line within the midplane radius of 4.2 cm enters to the outer divertor chamber, and the outer field lines are connected to the outer baffle. Values of n_e, T_e and electron pressure, p_e, measured at low density were compared along the same field line (i.e. at the midplane, near X-point and at the outer divertor target as shown in the previous section). Those values of n_e, T_e and p_e agree on the same field line calculated by magnetic equilibrium, which confirms the accuracy of the separatrix position within ±3 mm at midplane.

At low $\bar{n}_e$ of $1.7 - 1.8 \times 10^{19}$ m^{-3}, n_e^{mid} near the separatrix is comparable. Profile of n_e^{mid} for the W-shaped divertor is broader than that for the open divertor, and n_e^{mid} in the 2nd SOL is larger by a factor of ~1.5. For the W-shaped divertor, T_e^{mid} near the separatrix (80 eV) is higher than T_e^{mid} of 60 eV for the open divertor. On the other hand, profiles of T_e^{mid} are comparable in the 2nd SOL. Therefore, over the SOL region value of p_e^{mid} is 1.2－1.5 times larger than that for the open divertor.

During the x-point MARFE (at the same $\bar{n}_e = 3.3 - 3.4 \times 10^{19}$ m^{-3}), profile of n_e^{mid} is similar in the 2nd SOL (i.e. the same n_e^{mid} and e-folding length). Profile of T_e^{mid} is similar at the 2nd SOL, while T_e^{mid} near the separatrix is higher for the W-shaped divertor.

After an installation of the divertor baffle plate in order to reduce neutral recycling in the main chamber, n_e^{mid} and decay length of the profile at the outer flux surface (2nd SOL) increased slightly under the attached divertor condition. This result is at a look contrary to our expectation.

Database of T_e^{mid}, n_e^{mid} and their e-folding lengths near the separatrix, λ_{T_e} and λ_{n_e}, is summarized in Fig. 4. Since these values at the separatrix were not measured in some profiles, values of T_e^{mid} and n_e^{mid} at 2－3 mm outer the separatrix are used. Value of n_e^{mid} increases with decreasing T_e^{mid}. Maximum n_e^{mid} of 1.6×10^{19} and 1.4×10^{19} m^{-3} are observed for the W-shaped and open divertors, respectively. Corresponding T_e^{mid} of 62 and 47 eV, below which the x-point MARFE occurs and the divertor detachment is proceeding. Values of λ_{T_e} and λ_{n_e} stay at the relatively constant levels of 2.5－3.0 cm and 1.7－2.0 cm, respectively. The values are comparable to those observed in the open divertor[1], and ratio of $\lambda_{T_e}/\lambda_{n_e}$ increases from 1.3 to 1.7 with a reduction in T_e^{mid}. Noted that at very low $\bar{n}_e$ of 1.0×10^{19} m^{-3} $\lambda_{T_e}/\lambda_{n_e}$ becomes unity.

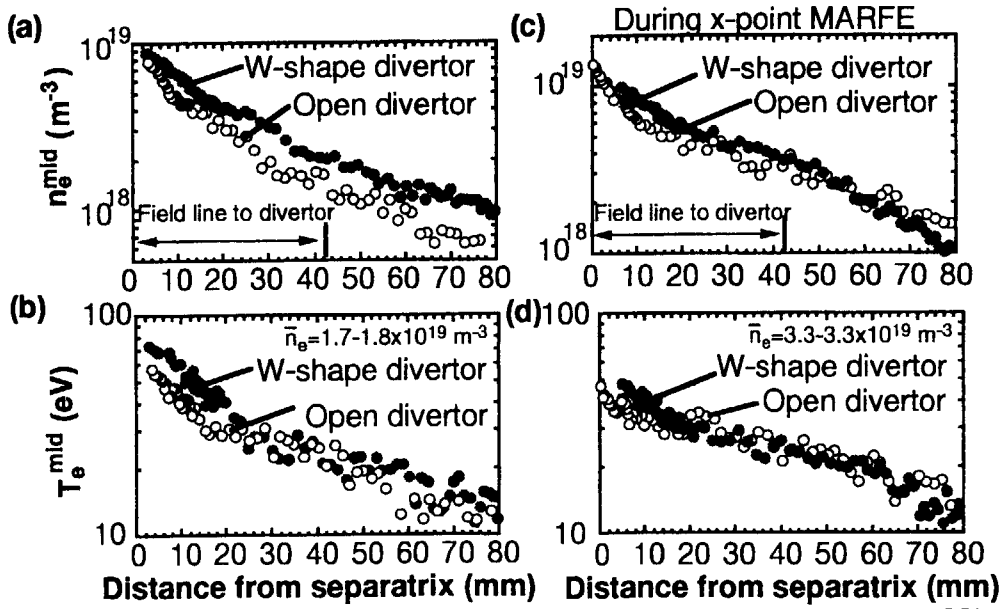

Fig. 3 Profiles of (a) and (c) electron density, (b) and (d) electron temperature at the midplane SOL measured with a reciprocating Mach probe. Line averaged main plasma density of (a) and (b) 1.7-1.8x10^{19} m^{-3}, and (b) and (c) 3.3-3.4x10^{19} m^{-3} (during x-point MARFE). Open and closed circles show the open and W-shaped divertor cases.

During the x-point MARFE, n_e^{mid} decreases when the radiation region is entering into the main plasma. The 1st SOL region becomes narrower localizing at 0.5－1.0 cm near the separatrix, and the local λ_{T_e} and λ_{n_e} increase.

Particle recycling flux in the SOL and core plasma was evaluated from a distribution of the D_α brightness[2]. Local recycling fluxes near the inner and outer baffles, $\Phi_{baf,in}^{D_\alpha}$ and $\Phi_{baf,out}^{D_\alpha}$, are compared for the W-shaped and open divertors. For the W-shaped divertor, under the attached divertor condition $\Phi_{baf,out}^{D_\alpha}$ is 40－50% larger than that for the open divertor, and during the x-point MARFE they are comparable. This result qualitatively agrees with our observation of n_e^{mid}: for the W-shaped divertor n_e^{mid} was larger than that for the open divertor. On the other hand, $\Phi_{baf,in}^{D_\alpha}$ is smaller than that for the open divertor. The result suggests that the large n_e^{mid} at the outer midplane is localized and this is caused by the larger neutral recycling flux at the outer baffle. Here, minimum distance between the outer baffle and the plasma separatrix is about 12 cm, which is larger than the local λ_{n_e} of 4.5 cm of the 1st SOL region. Neutral source due to a direct interaction between the SOL plasma and baffle structure was small.

7.3.5 Summary

SOL/divertor plasma profiles were compared for the open and W-shaped divertors.

(1) Inclined divertor target and the private dome work to condense neutrals near the separatrix. Increment of the ion flux near the divertor target is about 20% of the total ion flux to the target plate.

(2) Partial divertor detachment occurred when the x-point MARFE started, which was similar to the observation in the open divertor. However, Pressure loss factor at the outer target of 93 was larger than that for the open divertor ($\leq$ 15).

(3) Under the attached divertor condition, λ_{T_e} and λ_{n_e} at the outer midplane stay at the relatively constant levels of 2.5－3.0 cm and 1.7－2.0 cm, which were comparable to those in the open divertor. Value of T_e^{mid} near the separatrix was higher, and larger n_e^{mid} was observed at the outer SOL region: p_e^{mid} was 1.2－1.5 times larger.

References

[1] N. Asakura, *et al.*, J. Nucl. Mater., **241 － 243** (1997) 559.

[2] N. Asakura, *et al.*, Nucl. Fusion, **35** (1995) 381.

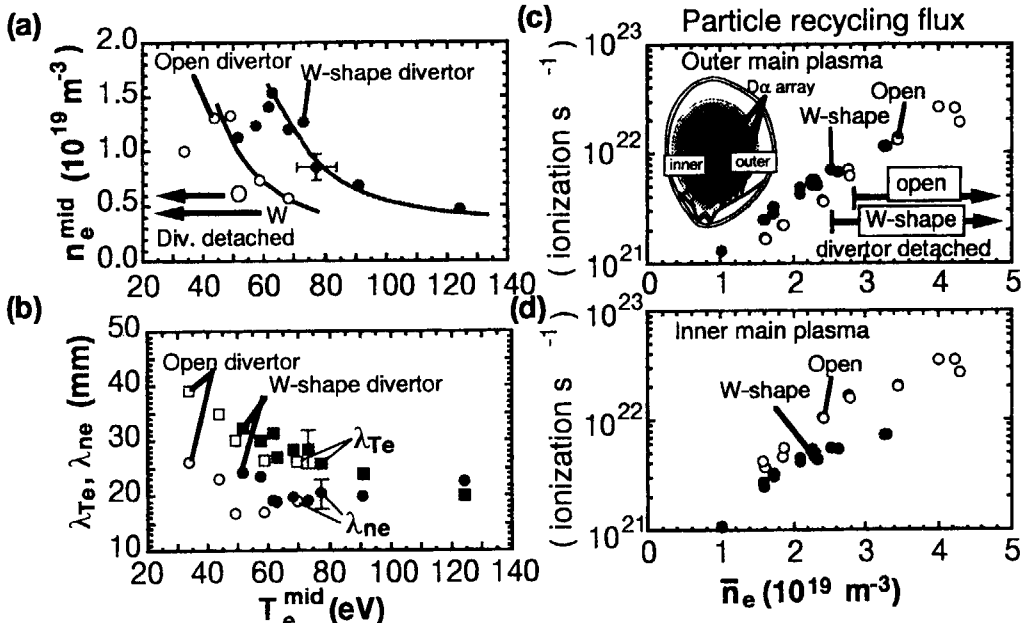

Fig. 4 (a) electron density at the separatrix, and (b) e-folding lengths of electron density (circles) and temperature (squares) at 1st SOL region (0 - 2 cm) as a function of electron temperature at the separatrix. Open and closed circles show the open and W-shaped divertors. Local recycling flux measured with Dα array is shown (c) at outer baffle and (d) at inner baffle as a function of averaged plasma density.

7.4 Divertor Radiation Control with Gas Puff

S. Konoshima, N. Hosogane, H. Tamai, R. Yoshino,
H. Kubo and T. Ishijima[1]

[1]*Tsukuba University, Ibaraki, Japan.*

Abstract

Capability of feedback control for the divertor radiation has been increased this year with addition of the divertor cryo-pump which is expected to play a role as an active particle sink term. Experimental results indicate that divertor radiation quickly decays by pumping neutrals when gas puff is turned off. Effective pumping rate including wall adsorption turns out to be similar magnitude with that of the gas puff. Stable control of radiation power was possible at any power level except near the threshold of MARFE onset. Neon seeding into L-mode plasma was also tested.

1. Introduction

Power and particle handling is a key issue for ITER divertor operation. It is important to find any stable solution of radiative divertor without loosing confinement quality [1]. Careful radiation control has brought a new approach for tokamak operation such as CDH mode [2]. A feedback control system using bolometer signals, in which measured radiation power is fed to the gas puff command, has been developed as an initial step to find a new control knob in JT-60U experiment. Initial tests were successful in obtaining stable long time sustainment of divertor radiation at modest radiation level [3]. However, because the system does not have any active particle exhaust mechanism other than passive pumping by walls, this method is limited to use only in the case of relatively slow time evolution. JT-60U divertor has been modified in 1997 from open divertor to W- shaped structure with dome and baffle plates to provide gas shielding and particle pumping capability near the inside separatrix hit point utilizing neutral beam cryo pumps. Effective pumping speed is estimated to be about 35-70 m^3/sec [4]. Effect of divertor pump and an impurity seeding results will be presented in the following section.

2. Radiation control with hydrogen gas puff and divertor pumping

Real time processor calculates an estimate of divertor radiation power, P_r-meas, from six bolometer signals of representative divertor channels with delay time of less than 1

milliseconds. Hydrogen gas throughput rate, Q_{com} is determined such that the measured radiation power, $P_{r\text{-}meas}$, is equal to that of requested, $P_{r\text{-}prog}$, in every 0.01 second with a following relation:

$$Q_{com} = G_1 (P_{r\text{-}prog} - P_{r\text{-}meas}) + G_2 T_D (dP_{r\text{-}meas} / dt)$$

Where the coefficients G_1, G_2 and T_D represent proportional gain, differential gain and the response time, respectively and 50, 1.0 - 0.3 and 0.1 are used in this experiment.

An experimental result is shown in Fig. 1(a). Hydrogen L-mode plasma with constant hydrogen neutral beam heating power at 6.5 MW is used for the experiment. Divertor radiation, $P_{r\text{-}prog}$, was given step wise waveform with 3.4, 4.7, 5.9 and 5 MW which correspond to the variation of radiative loss fraction of about 50 - 90 % of the input power. Feedback system was switched from density control mode to radiation control mode at 6 sec. A large gas command of 50 $P_a m^3/s$ is observed when $P_{r\text{-}prog} > P_{r\text{-}meas}$ satisfied at around 6.2 sec, however, because of slow response due to a long gas transmission line, divertor radiation start increase with time delay of about 0.1 sec. At the first stage of the radiation command, 3.4 MW, divertor radiation follows almost as expected, though a little larger time derivative component (G2) is used to compensate gas delay time. Fluctuation is further enhanced at the second step. Radiation power of around 70 % of the power input is a level at which MARFE (Multifaceted Asymmetric Radiation From the Edge) is normally observed in JT-60U. MARFE is a localized intense radiation zone with high density near the separatrix cross point (Fig. 1(b)) and usually believed to be a thermal instability due to a negative temperature dependence of impurity radiation [5]. At this stage, coupling between instantaneous MARFE excitation , relatively large time derivative term and rapid pumping of neutrals appears to create large amplitude oscillation as shown in Fig. 1(b). Stable MARFE is sustained in the 3rd step, though response to the command becomes quite slow. Effect played by divertor pumping is obvious at final power down phase. Radiation power goes down rapidly at around 11.6 second with a decay rate similar to that of rise times by gas puffing.

3. Neon seeding

Impurity seeding is one of candidate scenarios for ITER divertor operation [1]. Relatively small amount of neon was added to see whether seeded impurity can simply supplement the divertor radiation and therefore mitigates a heavy hydrogen gas puffing or not. Neon gas of 0.5 $P_a m^3/s$ was puffed to the same discharge as above. Figure 2 shows a result comparing with no neon case (lower box). No appreciable difference is

seen in divertor radiation, Pr(DIV), for both cases. On the other hand, neon radiation from the main plasma is evident in hydrogen like (1s2p transition) UV neon radiation, Ne X, as well as rapid increase in Pr(MAIN) signal. Line average electron density and time integrated hydrogen gas at 8.2 second were; 2.6 x 10^{19} m^{-3} and 35 Pam^3 in case with neon puff, and 2.0 x 10^{19} m^{-3} and 41 Pam^3 in case without neon, respectively. About 15 % reduction of hydrogen gas is accounted for even higher electron density of about 30 % in the neon seeding case. Additional neon impurity appears to increase electron density and main plasma radiation with divertor radiation unchanged. Mitigation of hydrogen gas puff is obtained at the expense of main plasma contamination. Different results would be expected in case of ELMing H-mode discharges.

4. Summary

Divertor cryo pump provided an efficient radiation reduction function and improved response of the feedback system. Although the pumping rate itself may only be a small part compared with total particle flux, rapid decay of the divertor radiation comparable to gas puff rate was obtained due to a larger pressure of neutrals at the divertor. As to the impurity seeding, systematic study and understanding on particle behavior in the scrape off layer including MHD activity like ELMs would be important in order to design experiment.

References

1) G. Janeschitz, et al., in Proc.16th IAEA conf. (1996)
2) O. Gruber, et al., Phys. Rev. Lett. 74 (1995) 4217. J. Winter, private comm (1994).
3) S. Konoshima, et al., "Divertor Radiation Feedback Control", JAERI Research 96-018 (1996) 190. H. Tamai, et al., submitted to Fusion Engineering and Design.
4) N. Hosogane et al., in Proc. 16th IAEA Conf.vol. 3 (1997) 555.
5) e.g. J. Drake, Phys. Fluids 30 (1987) 2429.

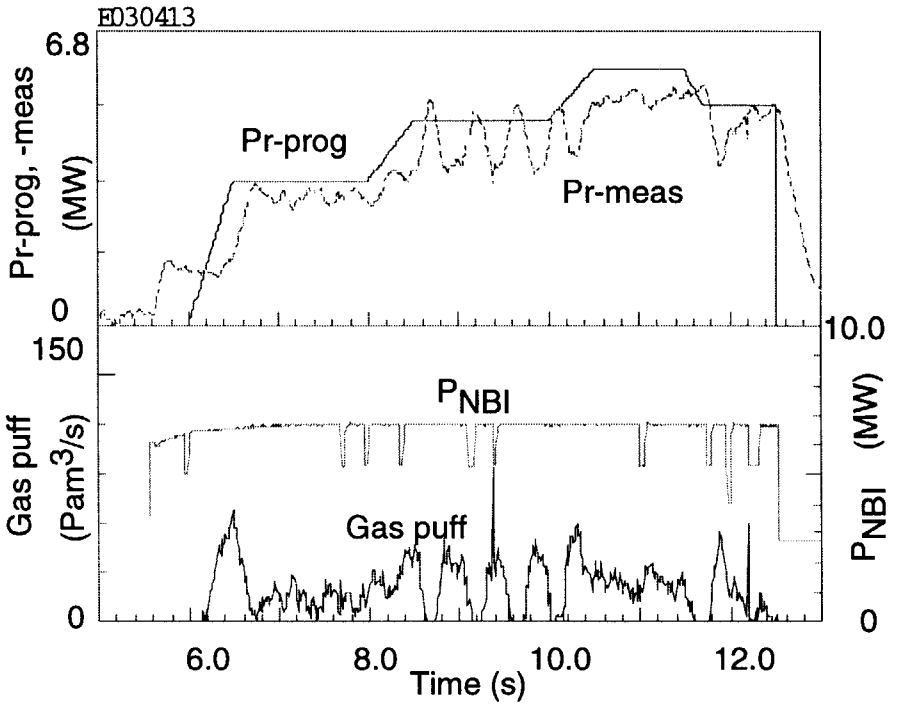

Fig. 1(a) : Feedback control of divertor radiation with gas puffing and divertor pumping. For constant hyrogen neutral beam heating of 6.5 MW, divertor radiation, Pr-prog, was given step wise waveform roughly corresponds to 50 - 90 % of the beam input.Hydrogen L-mode plasma with 1.2 MA, 3.5 tesla, and density, 2-2.5 x 10^{19} m-3 and gas puff near the divertor.

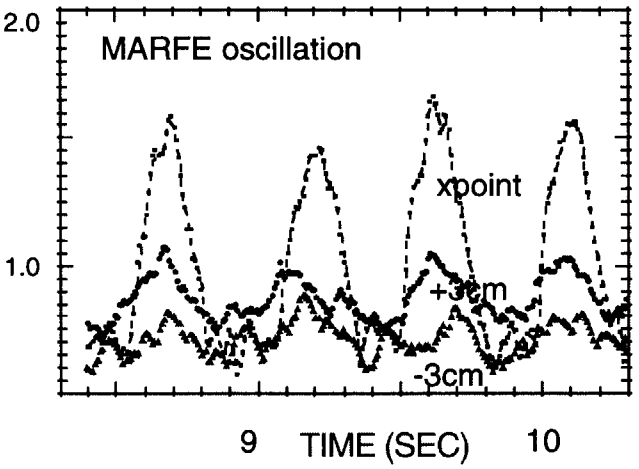

Fig. 1(b) : Profile change during MARFE on-off repetition cycle. Three chord signals of bolometer array at the x-point(broken line), 3 cm inside (triangle) and 3 cm outside (circle) the x-point indicating rapid transition to highly peaked profile near the x-point.

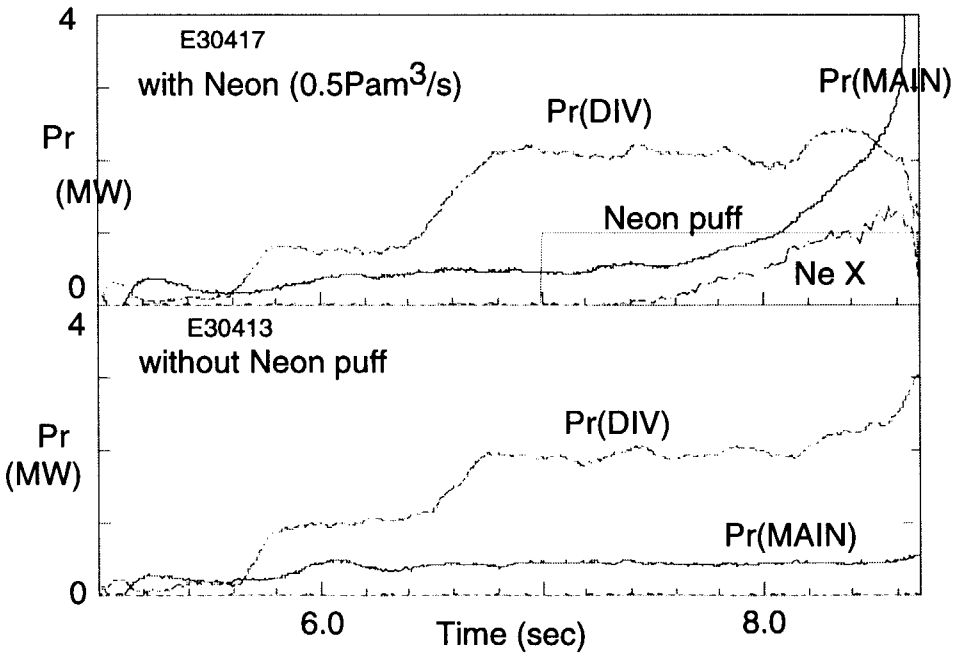

Fig. 2 Divertor radiation feedback with neon impurity seeding. Upper and lower traces correspond with neon and without neon case. Pr (DIV) (=1.7x Pr) and Pr(MAIN) are divertor and main plasma radiation power. Other conditions are the same as Fig. 1.

7.5 Volume recombination in detached divertor plasmas

H. Kubo, S. Higashijima, A. Kumagai and T. Sugie

1. Introduction

The detached divertor regime is attractive for an operation scenario of a divertor tokamak reactor such as ITER[1]. The volume recombination is considered to be important in reducing the incident ion flux and detaching the plasma from the divertor tiles[2]. The present paper describes study of the volume recombination in detached divertor plasmas by observation of Balmer lines of deuterium atoms and continuum.

2. Experimental

Figure 1 shows the diagnostics for the present divertor study. The Dα line emission was observed with a fiber array and Balmer lines (n = 2 - 5, 7, 8, 9, and 10) of deuterium atoms were observed with a visible spectrometer covering the inner and outer divertor separately. Ion saturation current, electron density and electron temperature were measured with Langmuir probes at the divertor tiles.

An L-mode discharge to be analyzed is shown in Fig. 2. During NB heating, the electron density is raised by a gas puff. A MARFE appears at 11 s., and then the intensity of C VI line from the main plasma and the radiative losses from the divertor region increase. The signal of the Langmuir probe near the outer separatrix strike point disappears, and that of the Langmuir probe just outside of the strike point increases. It indicates that the outer divertor plasma is partially detached. While the intensities of D I lines from the outer divertor increase, those from the inner divertor decrease. The inner divertor is detached immediately after beginning of the NB heating. Since it is interesting to study evolution from the attached divertor plasma to the detached one and the detachment of the outer divertor plasma is closely related to the occurrence of the MARFE, we will chiefly discuss the outer divertor.

3. Results and Discussion

Figure 3 shows a spectrum at a wavelength around the Balmer series limit obtained from the detached divertor plasma. D I lines with transitions of n = 2 - 7, 8, 9 and 10 are identified.

The populations of excited levels of deuterium atoms are attributed to two processes: ionization and recombination processes[3,4]. The population due to the ionization process results from excitation from the ground state of deuterium atoms. It decreases rapidly as the energy of the level becomes higher. On the other hand, the population due to the recombination process results from recombination from deuterium ions, and it is dominant for the high energy levels. The populations derived from the intensities of the Balmer lines are plotted for the attached and detached divertor plasmas in

Fig. 4. For the attached divertor plasma, the measured population decreases rapidly as the principal quantum number increases. The measured populations are well reproduced by calculation with assumption that the electron temperature is 50 eV, the electron density is 1×10^{19} m^{-3}, the ratio of the deuterium atom density to the electron density is 0.011, and the divertor plasma length along the viewing chord of the spectrometer is 0.08 m. The populations are dominated by the ionization process. The electron temperature and density measured with the Langmuir probe close to the strike point were 38 eV and 0.83 $\times 10^{19}$ m^{-3}, respectively. Thus the assumption in the calculation agrees with the Langmuir probe data. For the detached divertor plasma, the measured populations don't decrease so rapidly as the principal quantum number increases, compared with those for the attached one. While the outer divertor plasma is detached at the vicinity of the strike point, it is attached about 2 cm outside of the strike point. At the attached position, the electron temperature and density measured with the Langmuir probe were 19 eV and 1.7 $\times 10^{19}$ m^{-3}, respectively. Calculation on assumption that the temperature is 20 eV and the density is 2×10^{19} m^{-3} agrees with the measurement for n = 3 level but not for the higher energy levels. The sum of the populations due to the ionization and recombination processes calculated on assumption that the temperature is 10 eV and the density is 2.8 $\times$ 10^{20} m^{-3} agrees fairly with the measured population for the all levels. However, the assumed density is much higher than that observed by the Langmuir probe. Since the plasma is partially detached, a narrow layer with a very low temperature might exist near the strike point. Calculation on assumption that the temperature is 1 eV, the density is 8.9 $\times 10^{19}$ m^{-3} and the divertor plasma length is 0.02 m agrees with the measurement for the high energy levels. Therefore, the sum of the populations calculated on the first and third assumptions can fairly explain the measured populations. Further investigation with spatial resolution is necessary for detailed understanding. As a result, the populations of $n < 4$ levels are dominated by the ionization process and those of $n > 6$ levels are dominated by the recombination one.

Even in the detached divertor plasma, the ionization flux can be estimated from the Dα line intensity, because the population of the n = 3 level is attributed to the ionization process. The number of ionization events per photon of Dα line emission is about 30 at a temperature above 5 eV in this density range. On the other hand, in the detached divertor plasma, the recombination flux can be estimated from D I n = 2 - 7 line intensity, because the population of the n = 7 level is attributed to the recombination process. The number of recombination events per photon of D I n = 2 - 7 line emission is about 200 at a temperature below 15 eV. Therefore, the ratio of the ionization flux to the recombination one can be estimated from the ratio of the Dα line intensity to D I n = 2 - 7 line intensity. Time evolution of the line intensity ratio is shown in Fig. 2. The ratio increases at the onset of the detachment. From the intensity ratio, the recombination flux is estimated to be about 1 % of the ionization flux.

As mentioned above, the inner divertor was readily detached. The spectrum for the detached inner divertor plasma is similar to that for the detached outer divertor plasma. The ratio of the recombination flux to the ionization flux is estimated to be 1 - 3 %.

4. Summary

In the detached divertor plasma, the $n < 4$ levels are dominantly populated by the ionization process and the $n > 6$ levels are by the recombination process. Although the increase in the ratio of the recombination flux to the ionization flux is correlated to the onset of the detachment, the ratio is small (about 1 - 3 %) even in the detached plasma.

Acknowledgment

The authors are grateful to Dr. K. Sawada of Shinshu University for his providing them with atomic data.

References

1) Janeschitz G. et al., J. Nucl. Mater. **220-222**, 73 (1995).
2) Lumma D. et al., Phys. Plasma **4**, 2555 (1997).
3) Johnson L. C. and Hinnov E., J. Quant. Spectrosc. Radiat. Transfer. **13**, 333 (1973).
4) Sawada K., private communication.

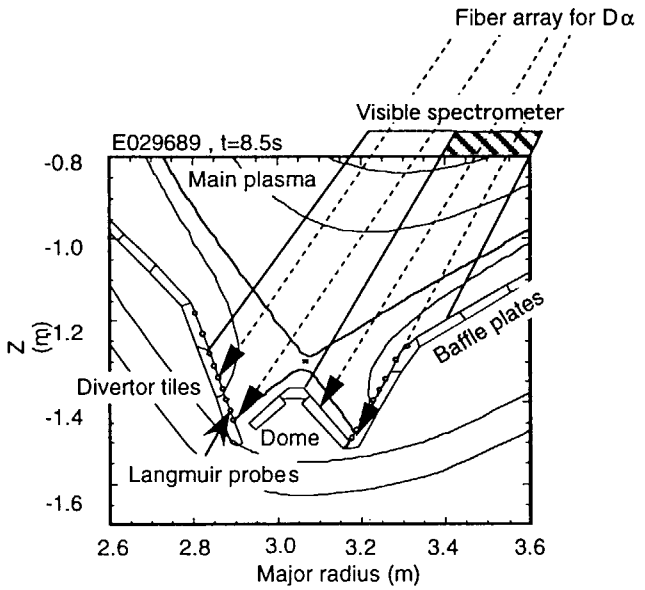

Fig. 1 Diagnostics for the present divertor study

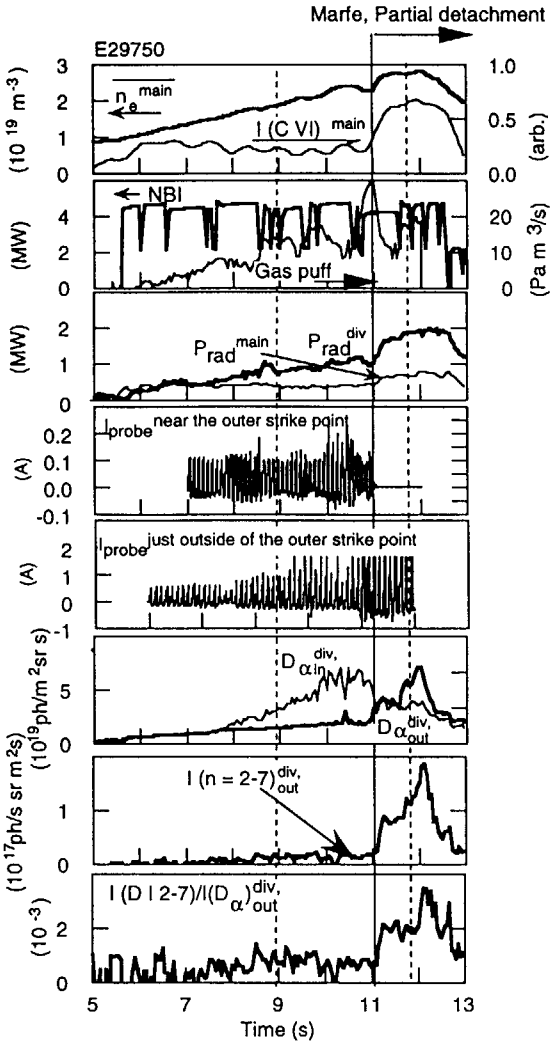

Fig. 2 Time evolution of an L-mode discharge. The plasma current was 1.2 MA and the toroidal field was 3.5 T. The first row shows the line-averaged electron density and the intensity of C VI line (3.37 nm) in the main plasma, and the second row shows the NBI power and the gas puff rate. The radiative losses in the main and divertor plasmas are shown in the third row. The forth and fifth rows show the signals of Langmuir probes located near the outer separatrix strike point and just outside of it, respectively. D α intensities from the inner and outer divertor plasmas are shown in the sixth row. The seventh shows the intensity of D I n = 2 - 7 line. The ratio of D I n = 2 - 7 line intensity to Dα line intensity in the outer divertor is shown in the bottom.

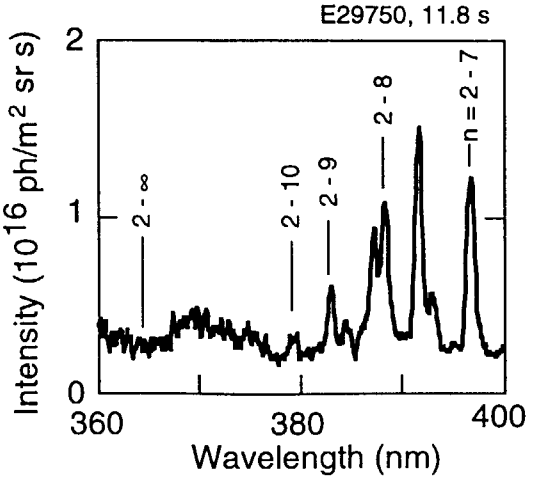

Fig. 3 Spectrum around a wavelength of the Balmer series limit obtained from the detached outer divertor plasma (11.8 s.).

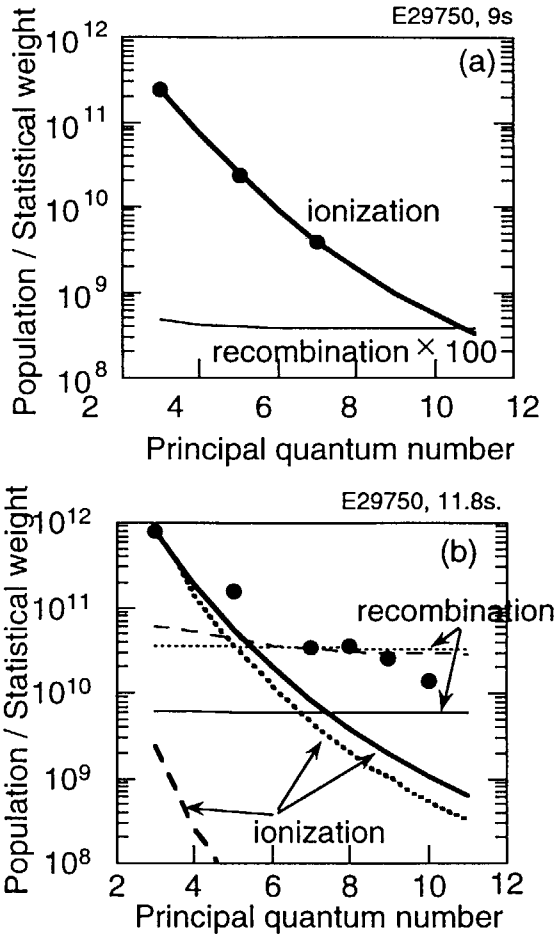

Fig. 4 Populations divided by statistical weights of excited levels of deuterium atoms in outer divertor plasmas. The points indicate the measurement and the lines indicate the calculation. The thick and thin lines indicate the populations due to the ionization and recombination processes, respectively. (a) Attached divertor plasma (9 s.). In the calculation, it is assumed that T_e = 50 eV, $n_e = 1 \times 10^{19}$ m^{-3}, n_D / n_e = 0.011 and the plasma length along the viewing chord of the spectrometer (dl) = 0.0 8m. (b) Detached divertor plasma (11.8 s.). Continuous line: T_e = 20 eV, $n_e = 2 \times 10^{19}$ m^{-3} and n_D / n_e = 0.018, dl = 0.08m. Dotted line: T_e = 10 eV, $n_e = 2.8 \times 10^{20}$ m^{-3} and n_D / n_e = 0.00052, dl = 0.08m. Dashed line: T_e = 1 eV, $n_e = 8.9 \times 10^{19}$ m^{-3} and n_D / n_e = 1, dl = 0.002 m.

8. Diagnostics

8.1 First measurement of tangential Faraday rotation of CO_2 laser wave in a tokamak plasma [1)]

Yasunori Kawano, Shin-ichi Chiba, Hiroshi Shirai, Akira Inoue, and Akira Nagashima

(Abstract)

The first measurement of the Faraday rotation of CO_2 laser wave propagating in toroidally tangential direction in a tokamak plasma has been demonstrated in JT-60U tokamak. An infrared polarimeter using a couple of photoelastic modulators has reliably detected the polarization angle of CO_2 laser wave although incident laser intensity is varied. Accuracy of measured polarization angle is found as ~0.1° so far. Feasibility of the tangential Faraday rotation for electron density measurement in large tokamaks has been confirmed.

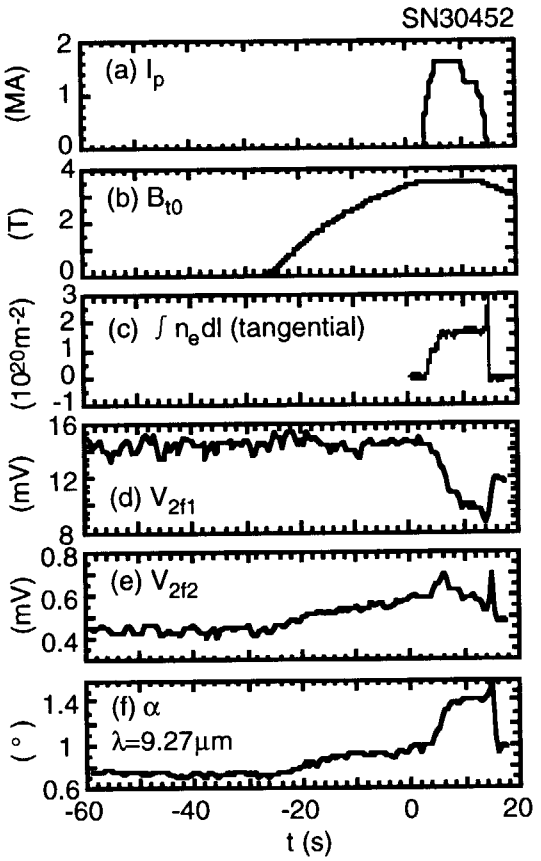

Fig. 1

Typical waveforms of the CO_2 laser polarimetry for the probing beam with wavelength 9.27 μm. The horizontal axis indicates the time defined by the JT-60U discharge sequence. The measured polarization angle α is shown in box (f). Two Faraday rotation components due to vacuum windows and the plasma are measured.

1) Y. Kawano, S. Chiba, H. Shirai, et al., submitted to Review of Scientific Instruments.

8. 2 mm-wave interferometer in divertor region[1)]

H. Takenaga, T. Fukuda, S. Sakurai, N. Hosogane, K. Kodama, K. Masaki

A mm-wave interferometer having a capability of concomitant electron temperature measurement, based on the electron cyclotron absorption (ECA) technique, has been developed for the divertor diagnostics in the W-shaped divertor of JT-60U. There are three sight lines which pass through (A) the X-point horizontally, (B) inboard side and (C) outboard side. Two color scheme with frequencies of 217 and 183 GHz was employed, in order to eliminate the spurious vibration effect. The two independent units were also arranged to enable the other applications of two chords measurement and simultaneous ECA measurement. The wave-guide and antenna were made of SUS304 because of its feasibility against the stress due to thermal expansion and electromagnetic force. Due to the complexity of the transmission line inside the tokamak and the low electrical conduction of SUS304, the insertion loss is as large as 65 dB with the sight line A. The sources were comprised of a gun oscillator and a doubler, and produce 11.0 mW at 217 GHz and 15.4 mW at 183 GHz, respectively. The output of the sources are divided into the signal and reference waves by the coupler. Receiver systems were comprised of a RX-RF unit and IF unit, and adopted a super-heterodyne detection circuitry. In the RX-RF unit, the signal and reference waves were mixed with the second harmonic wave of the local oscillator with the frequencies of 108 and 91 GHz for 217 and 183 GHz systems, respectively. The RF frequencies of 1.0 and 1.5 GHz were produced in 217 and 183 GHz systems, respectively. The RF REF output was led into the IF unit through the delay line for the phase adjustment. Forward tracking detection was adopted in the IF unit, and the IF frequencies were selected to be 2 MHz in both 217 and 183 GHz systems. Due to the low equivalent input noise of -90 dBm, the S/N ratio of about 20 dB was obtained at the chord A with 183 GHz. The measurements performed for the several types of the JT-60U discharges indicated the validity of the system and the reduction of the electron density near the X-point during the L-H transition was firstly demonstrated as shown in Fig. 1.

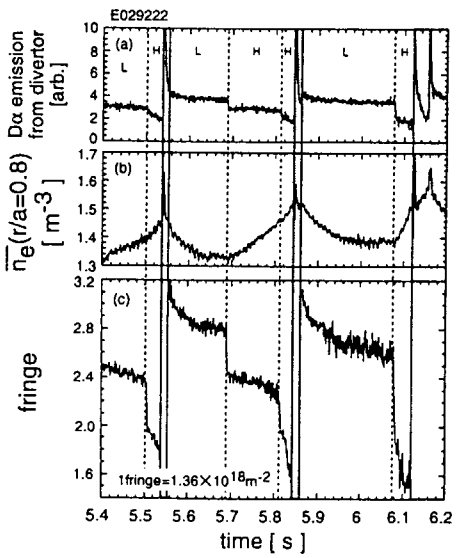

Fig. 1 Time evolution of (a) the Dα emission from the divertor, (b) the main plasma density at the edge and (c) the fringe of the interferometer. Dotted lines show the

Reference

1) H. Takenaga, et. al., to be submitted to Rev. Sci. Instrum.

8.3 Invessel Bolometer Cameras for Divertor Plasma Radiation

S. Konoshima, T. Ishijima[1], H. Tamai, N. Hosogane, T. Sasajima,
K. Masaki, K. Kodama and M. Shitomi
[1]*Tsukuba University, Ibaraki, Japan.*

Abstract

Four bolometer cameras have been installed inside the divertor chamber to monitor detailed radiation structure near the new W-shaped divertor in JT60U tokamak. This is a brief report of background, design and initial test results with an ohmic discharge.

1. Introduction

JT-60U bolometer arrays, viewing from two top diagnostic ports, one mid plane port and two side ports, have been replaced to improve spatial resolution of the divertor measurement in late 1995. By increasing number of bolometer sensors with a little smaller size, spatial resolution was increased by a factor of 2, or radial resolution from about 6 cm to 3 cm typically at divertor tiles. On the other hand, this resulted a decrease of signal to noise ratio and increased operational difficulties such as bridge circuit unbalance. Radiation shields to protect amplifiers and signal transmission electronics against neutron irradiation damage from JT-60U deuterium discharges was necessary in addition.

Divertor was modified from open configuration to W-shaped divertor with a dome and baffle plates to shield neutral particles back flow in 1997. Closed structure of the divertor chamber resulted access from diagnostic ports impossible. However, observation from many different view angles is significantly important to understand divertor radiation with asymmetric temporal-spatial variation. Since four channel bolometers of high temperature version, PTS bolometer [1-4], became commercially available, they were introduced and installed inside the divertor chamber. In the following, sight line design, installation and preliminary test results will be given.

2. Sight lines, camera design and installation

Figure 1(a) shows an overview of bolometer sight lines in JT-60U. Two top arrays have 16 chord channels in total with about 3 cm spatial resolution at tile surface covering whole divertor area through main plasma. Two mid plane arrays with 15 and 16 chords are arranged to measure upper and lower half of the main plasma plus divertor plasma. These midplane arrays are tilted about 10 degree in toroidal direction to make less sensitive to the charge exchange neutrals probably caused by orbit excursion of ripple trapped ions [5].

Details of view chords for new PTS bolometer camera installed inside the vacuum chamber are shown separately in Fig. 1(b). Three 4 channel bolometer heads are mounted inside the divertor dome. Two heads are monitoring 4 points to the divertor tiles along inner separatrix surface (ID1-4) and along outer surface (OD 1-4), respectively. Central head is looking upward aiming separatrix cross (x-) point above dome top (MD1-4). Entrance slit of a camera is located 4 cm behind a graphite tile surface and each channel are separated by plates to avoid cross talk. Another head is located to monitor x-point region horizontally (XP1-4). Slit size was determined to give a reasonable signal intensity based on existing bolometer data and laboratory test results. Glass-fiber-insulated twist-pair cables of about 5 m long were used as in-vessel wiring to the vacuum-feed-though flanges. Grounding point to the vessel potential is an entrance window of the bolometer head. Normal operating temperature of the JT-60U vacuum vessel is 300 degree C. Prior to the installation, laboratory measurements with a light source have been done on sensitivity, cooling time, effect of transmission line and so forth. Measurement indicated approximately consistent data on cooling time [6] with optical and electrical test at room temperature. These results will be discussed elsewhere including sensitivity at high temperature [4] and an analysis of transmission line [6,7].

3. Gas puffing in ohmic plasma

Figure 2 shows an example of raw signals of invessel bolometer camera during initial test using tokamak wall conditioning discharges. Electron density is increased from 0.5 x 10^{19} m^{-3} to 1 x10^{19} m^{-3} with 3 gas puffing shown in the top. Discharge mode was changed from limiter to divertor at 3 second. Reasonable signal amplitude is obtained with amplifier gain of 2000 for these low density ohmic discharges. Rough estimation of radiation power using sensitivity at room temperature gives about a factor of 5 smaller value compared with existing bolometer data, though a factor of 2 might be attributed to sensitivity decrease with temperature [4]. Time integrated bolometer signals show fairy different and interesting time evolution depend on view chord. Heavy gas puff from top port appears to cause an asymmetric evolution of density rise and neutral particle distribution. For example, signals from inside divertor and near to the divertor hit points are depressed during gas puff. Plasma disappears instantaneously at lower heat flux region due to the increased neutrals, though it recovers quickly. At this moment, a situation like 'gas blanket' might be realized locally. On the other hand, central and outside radiation increase smoothly with density rise. Two dimensional tomographic reconstruction [8] of these events would make more direct physics understanding possible.

4. Summary and additional remarks

Initial test results indicated that good quality of signals with faster response time fast enough to observe transient phenomena such as detachment and MARFE. However, after several days of measurements, many channels of the camera have damaged unfortunately during tokamak operation including disruptions. Failure investigation is ongoing with additional information and suggestions based on JET [9] and ASDEX [7] experiences, though possible candidate would be large direct (indirect) heat load and/or locally induced current during high temperature operation with disruptions.

References

1) K. F. Mast, et al., Rev. Sci. Instrum. 62 ((1991) 744.
2) Physikalisch Technische Studien GmbH, "Bolometer System for JAERI" Proj. No. 2041 (1996).
3) R. Wirth, private comm.
4) R. Reichle, et al., Proc. EPS Conf. (1995).
5) N. Hosogane, et al., Nucl. Fusion 34 (1994) 527.
6) M. Murari, et al.,private comm. (Instituto Gas Ionizzati del CNR internal report I.G.I 96/01 (1996)).
7) K. F. Mast, private comm.
8) A. W. Leonard, et al., in Diagnostics for Experimental Thermonuclear Fusion Reactors, ed. P.E. Stott, et al.,Plenum Press New York (1996) 549.
9) R. Reichle private comm.

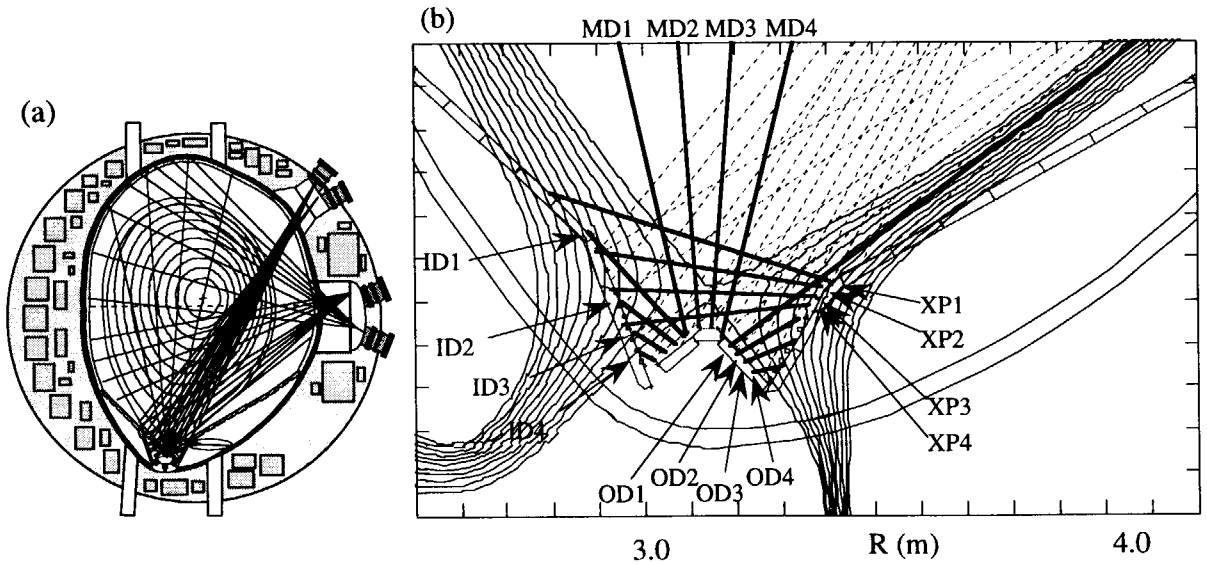

Fig. 1(a) : Bolometer view chords in JT-60U.
Fig. 1(b) : Expanded view of divertor bolometer sight lines and W-shaped divertor.

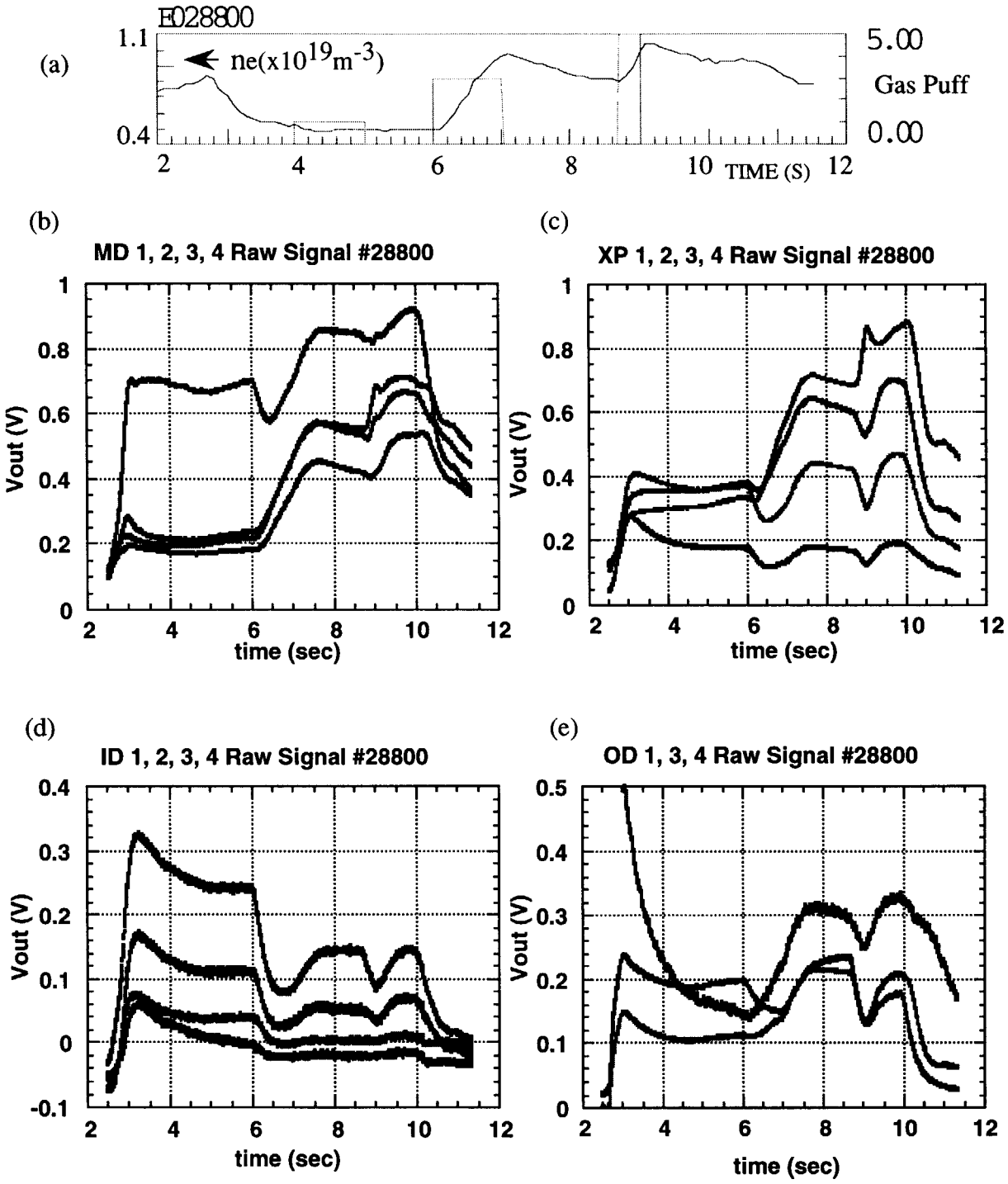

Fig. 2 Raw signals of PTS bolometer during1 MA ohmic discharge , #28800, looking from various cameras shown in Fig. 1(b). (a):Time evolution of electron density and gas puffing. Bolometer signals, (b): bottom chords looking vertically through x-point, (c): side bolometer looking x-point holizontally, (d): inside divertor along separatrix, and (e): outside divertor along separatrix. Each signal from top to bottom corresponds to channel number at 10 sec. Reasonable signal size are obtained with amplifier gain of 2000 for these ohmic discharges.

8.4 Divertor neutral pressure by fast response ionisation gauges

H. Tamai, N. Hosogane, S. Sakurai, S. Konoshima

8.4.1. Introduction

In order to investigate the divertor neutral pressure and to estimate the characteristics of divertor pumping, fast response ionisation gauges are installed at the divertor structure of JT-60U. Since the gauges are applied in the strong magnetic field, the sensitivity has to be calibrated *in situ* under the same magnetic field as that in experimental discharge. This report describes the specification of the diagnostic system, and the procedure of the sensitivity calibration.

8.4.2. Specification of diagnostic system

The gauge and its controller are developed by the ASDEX team[1), 2)]. Dominant advantage is that the sensor head can be applied in the presence of strong magnetic fields, so that the sensor head can be located very close to the plasma surroundings, which contributes to the relatively higher conductance. In actual location at the divertor described below, the time response of the gauge is estimated about 3-4ms, which is about two orders of magnitude as fast as that of conventional pressure gauges used in the vacuum vessel of JT-60U. The nominal characteristics are listed in the Table 8.4.1

Table 8.4.1 Nominal characteristics of the sensor head

Pressure Range	ultra high vacuum to several Pascal
Magnetic Field	up to 5.4 Tesla
Vessel Temperature	up to 400C
Time Response	3-4 ms

Figure 8.4.1 illustrates the sensor head and the location of the gauges installed in the vessel of JT-60U. Sensor head consists of linear tetrode with hot cathode. The direction of the normal of electrodes is set along the magnetic field line in order to gain the efficiency of electron emission and ion collection. Emission current is chopped by 500Hz, so that the minute ion current can be picked up through the lock-in amplifier.

Seven gauges are settled at divertor region in order to collect the neutral flux onto the inside baffle, the inside divertors, the dome top, the outside divertor, and the outside baffle. Another three and one are at the pumping ducts, and at the outer midplane, to collect the flux under the outer baffle, and that at the surroundings of main plasma, respectively. Each gauge has a chevron in front of the sensor head in order not to directly view the plasma and to collide the

incident particle three times at minimum for the thermalisation. The time constant including chevron is estimated about 3-4 ms.

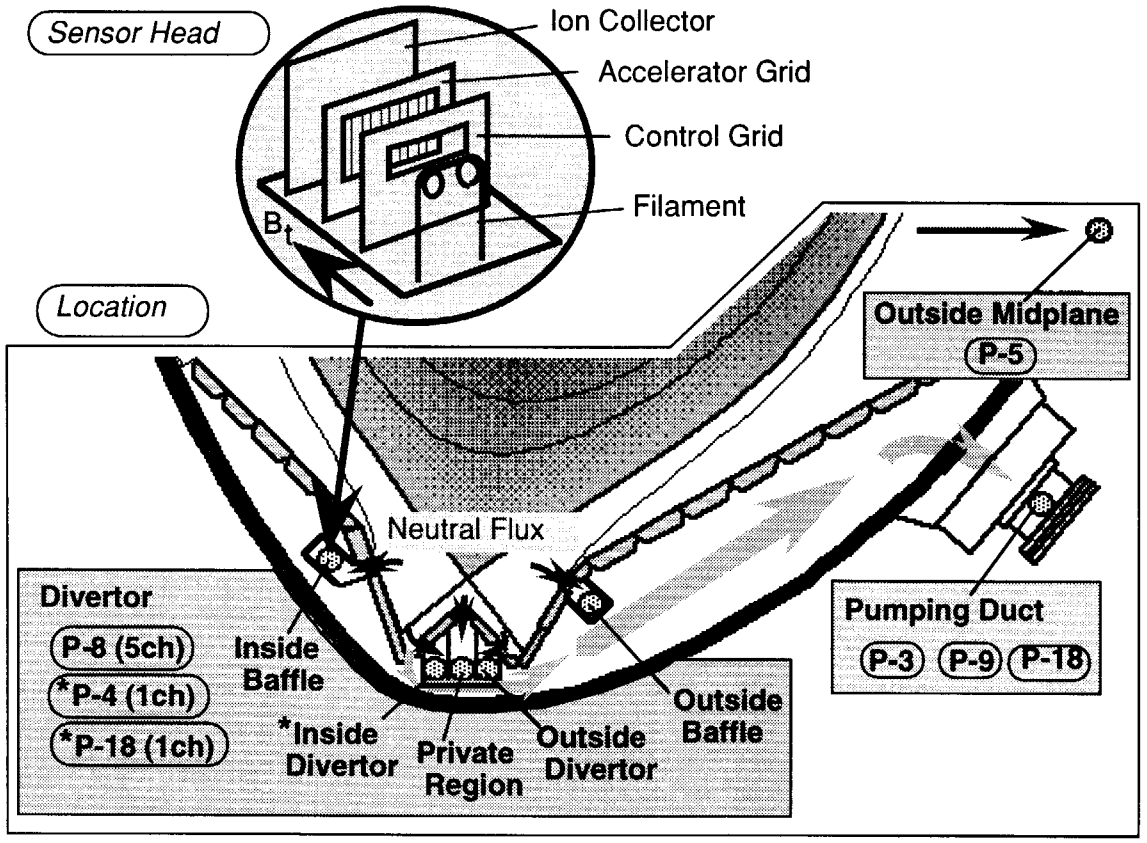

Fig.8.4.1 Sensor head of the ionisation gauge and its poloidal location.

The current control and the data acquisition system is illustrated in Fig.8.4.2. The system is supervised by the workstation, in which the control commands for the regulation of the filament and the emission current are sent via GPIB link, and the current data are collected to VME memory. Data of filament current, emission current, ion current, and neutral pressure are transferred to the ISP computer in order to produce the diagnostics database. Those data are also recorded in the backup media of the workstation (magnetic tape).

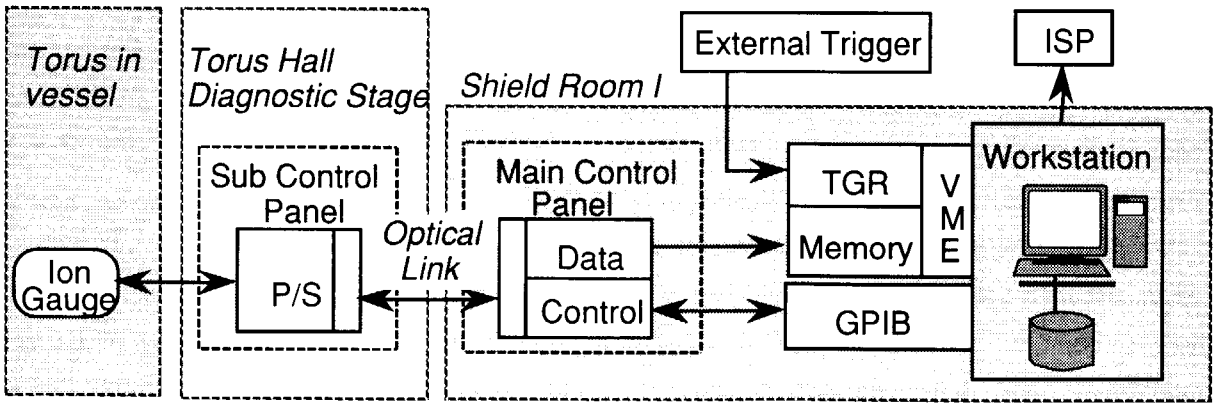

Fig.8.4.2 Block diagram of the control and the data acquisition system.

8.4.3. Calibration of sensitivity

The neutral pressure, P_o, is represented by the emission current, I_e, and the ion current, I_i, of the ionisation gauge as

$$P_o = (1 / \alpha) * I_i / (I_e - I_i), \qquad \text{Eq. 8.4.1}$$

where, α is the sensitivity of the gauge and is a function of the ionisation cross section and of the gauge geometry.

The sensitivity, α, is decided by the *in situ* calibration, in which the emission and ion current of the gauge is measured in the constant neutral pressure of the deuterium filled in the vacuum vessel under the existence of the toroidal magnetic field of 3T. Deuterium neutral pressure is obtained by the calibrated standard ionisation gauge at the pumping manifold before the application of the toroidal magnetic field.

Figure 8.4.3 plots the results of the *in situ* calibration. Ratio of output currents is plotted against the deuterium neutral pressure at 0.004Pa, 0.015Pa, and 0.097Pa, when the strength of the toroidal magnetic field reaches the flat top. Those points are fitted well in linear correlations.

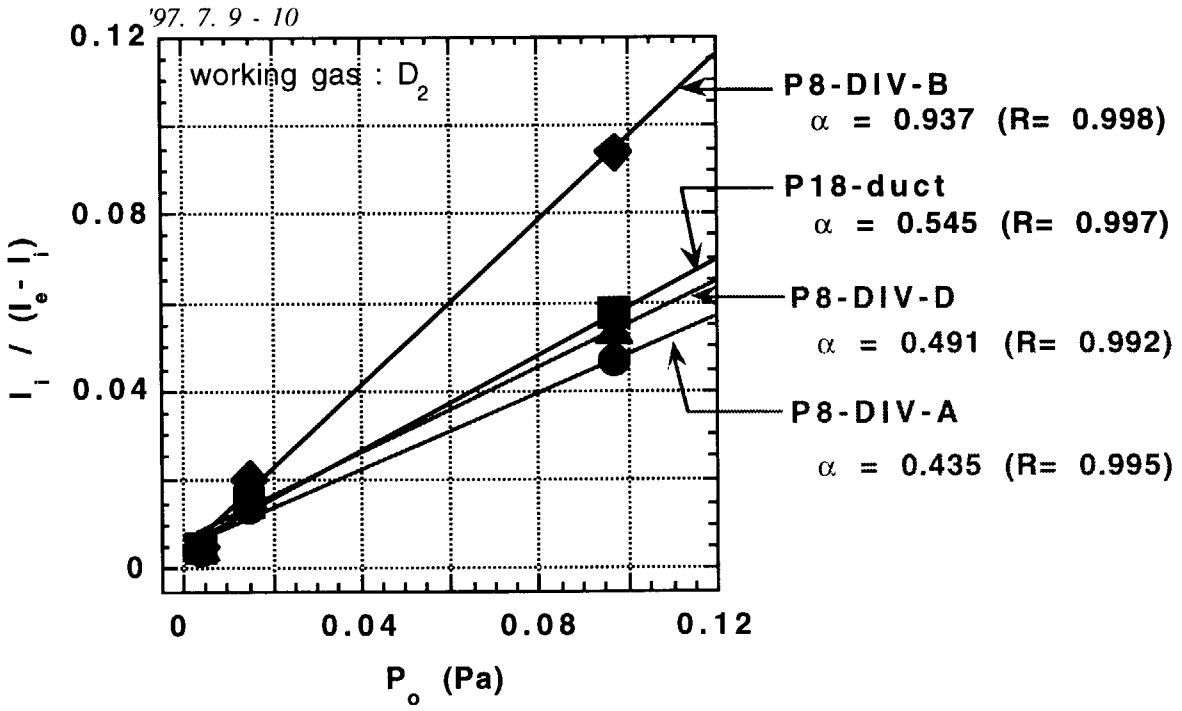

Fig.8.4.3 Typical plots for deciding the sensitivity at the in situ calibration.

The sensitivity is defined at the flat top of toroidal magnetic field. However, the emission current and the ion current gradually decrease with increase of the toroidal magnetic field, so that the sensitivity might be changed by the strength of the magnetic field. Figure 8.4.4 shows the dependence of the current ratio, $I_i / (I_e - I_i)$, on the toroidal magnetic field with flat top of 3T, and at the neutral pressure of 0.097Pa. The current ratio at B_t=1.5T is less than 5% as large as that at B_t=3T, therefore the pressure measurement is applicable to the normal

experiment discharge with toroidal magnetic field larger than B_t=1.5T within the error of 5%.

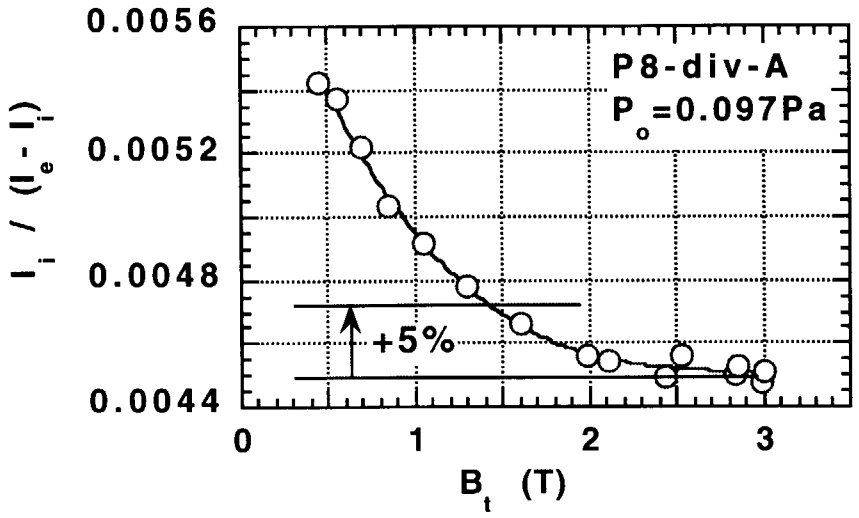

Fig.8.4.4 Dependence of the current ratio on the strength of toroidal magnetic field.

References

1) G. Haas et al., J. Nucl. Mater. *121* (1984) 151.

2) C. C. Klepper et al., J. Vac. Sci. Technol. A. *11(2)* (1993) 446

Appendix

PID name used in the diagnostics database and the precise location of each ion gauge is listed in Table 8.4.2. R, and Z in the table indicate the co-ordinate for the entrance slit of each gauge in major radius, and in vertical direction, respectively.

Table 8.4.2 PID name and the precise location of each ionisation gauge

PID	Channel	Port	Location	R (m)	Z (m)	Unit
NFA	1	P-8	Inside Baffle	2.814	-1.233	[Pa]
	2	P-8	Inside Divertor	2.919	-1.470	
	3	P-8	Dome Top	3.025	-1.360	
	4	P-8	Outside Divertor	3.119	-1.470	
	5	P-8	Outside Baffle	3.282	-1.275	
	6	P-4	Inside Divertor	2.919	-1.470	
	7	P-18	Inside Divertor	2.919	-1.470	
	8	P-3	Pumping Duct	4.589	-1.220	
	9	P-9	Pumping Duct	4.375	-1.557	
	10	P-18	Pumping Duct	4.382	-0.900	
	11	P-5	Midplane	4.820	-0.200	

8.5 Divertor reciprocating Langmuir probe

S. Sakurai and N. Asakura

1. Introduction

In order to measure plasma parameters near the X-point in a outer divertor region, a fast reciprocating Langmuir probe system was installed to the W-shaped configuration. This system was installed at an out-side lower port of vacuum vessel, and it consists of a probe and its guiding support, driving system, control and data acquisition system as shown in Fig. 1.

2. System description

A probe driving system with a pneumatic cylinder and a spring as well as data acquisition and control system by CAMAC were the same as those of the midplane fast reciprocating probe on LH launcher[1]. Maximum speed of fast reciprocating motion is about 1 m/sec, and the probe head is inserted into and extracted from the divertor plasma in about 0.4 sec respectively. Spatial resolution of 1-2mm is measured by laser position gauge. Electron temperature and density can be measured up to about 100eV and $10^{20}/m^3$ (depending on temperature) by the double probe method with the AC power supply (±200V, ~4A).

The structure of the probe and its guiding support are different from those of reciprocating probe on LH launcher as shown in Fig.2.

Mach type probe head was adopted to measure the plasma flow as well as the electron temperature and density, plasma potential. Electron temperature and ion fluxes at upside (X-point~main plasma) and downside (target plate) of the probe can be measured simultaneously by using two sets of double probes facing toward upside and downside respectively.

A guiding tube was installed under the outer baffle for supporting a drive shaft of the probe. The drive shaft is guided by front and back guide with ceramic ball bearings, which

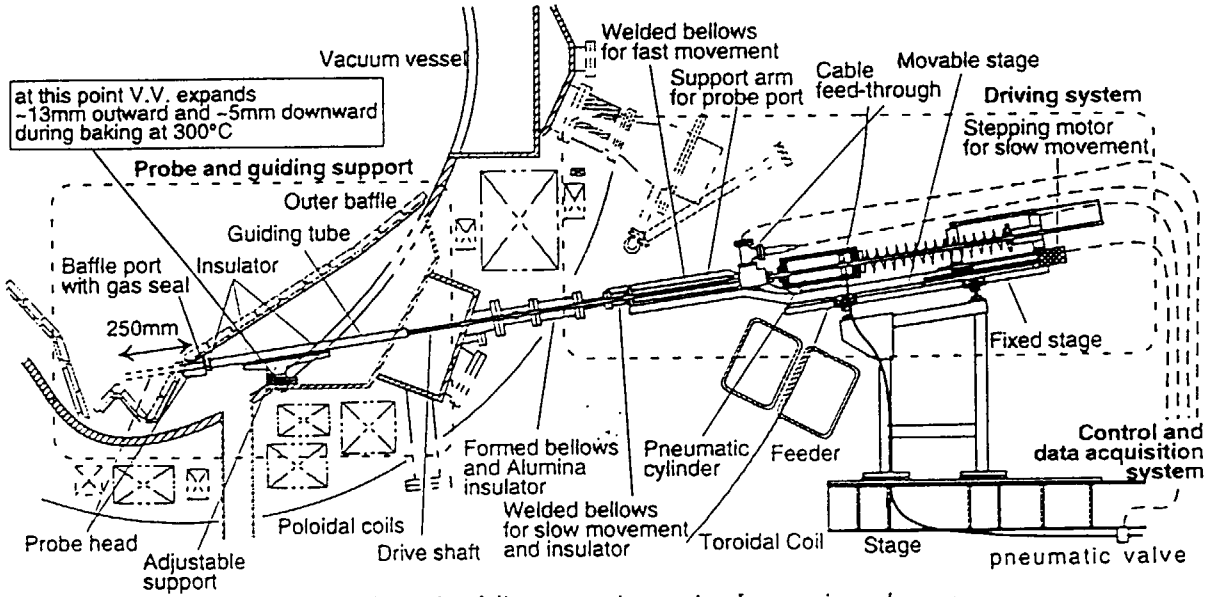

Fig. 1 Schematic of divertor reciprocating Langmuir probe system

are carefully fitted to the inside diameter of the guiding tube, to keep the small clearance (≥2~3mm) between probe head and baffle port. The driving shaft connecting between back guide and pneumatic cylinder is bent during baking of vacuum vessel at 300°C, because the guiding tube moves about 13mm horizontally and 5mm vertically due to the thermal expansion of the vessel. Although the bend of this shaft increases up to about 10mm due to the pushing force by pneumatic cylinder, the expected bending stress of 6kgf/mm^2 is much smaller than the limit of SUS304.

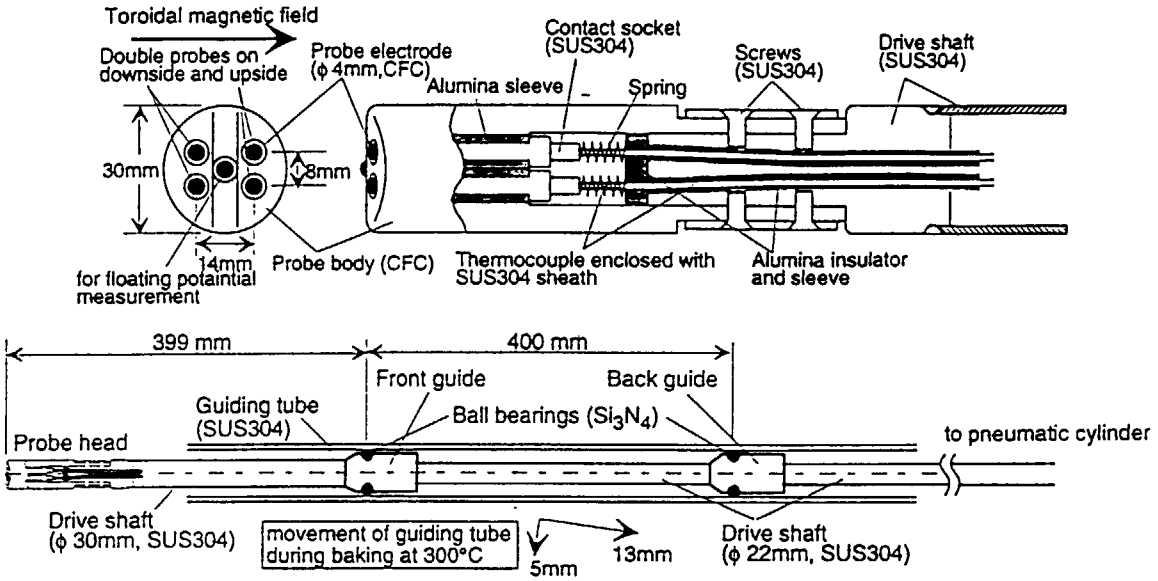

Fig. 2 Schematic of probe head and guiding system

3. Experimental results

Figure 3 shows typical profiles of plasma parameters near the X-point in ohmic heated discharges. Not only ion saturation current but also electron temperature at downside were much smaller than those at upside. It suggests that the shadow effect between probe head and divertor plate due to the short connection length along the field line should be considered to calculate the plasma flow velocity from the up/down ratio of ion saturation currents. The behavior of electron density profile in density scan of main plasma is shown in Fig.4. A large peak was observed at separatrix of outer divertor leg as well as in front of the target plate when the main plasma density exceeded about 60% of the MARFE onset density. The peak electron density exceeded the average density of main plasma. This peak was formed at the separatrix and shifted outward as the density of main plasma increased.

References

1) N. Asakura, S. Tsuji-Iio, Y. Ikeda, Y. Neyatani and M. Seki, Rev. Sci. Instrum., **66**, 5428-32, (1995)

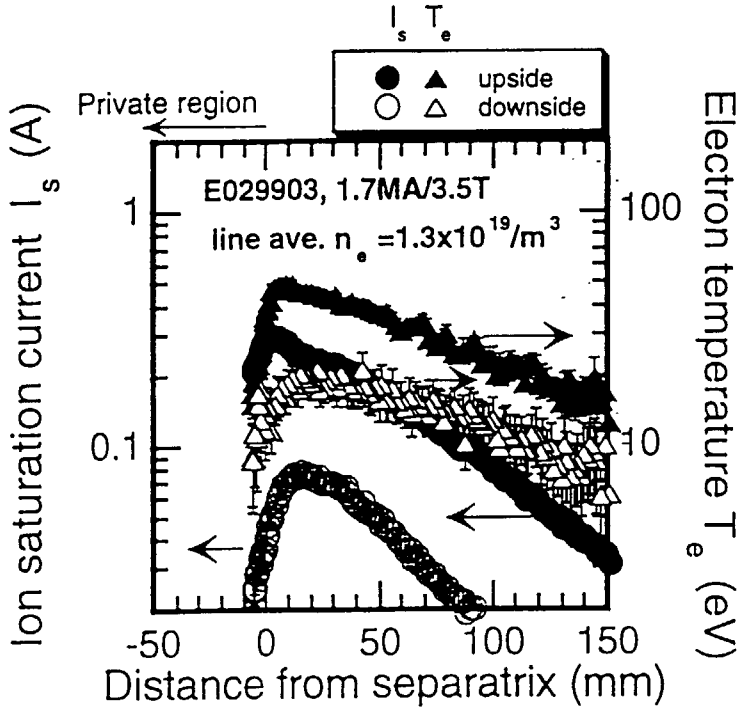

Fig. 3
Typical profiles of ion suturation current I_s and electron temperature T_e near the X-point in outer divertor. Upside means toward X-point and main plasma. Downside means toward divertor plate.

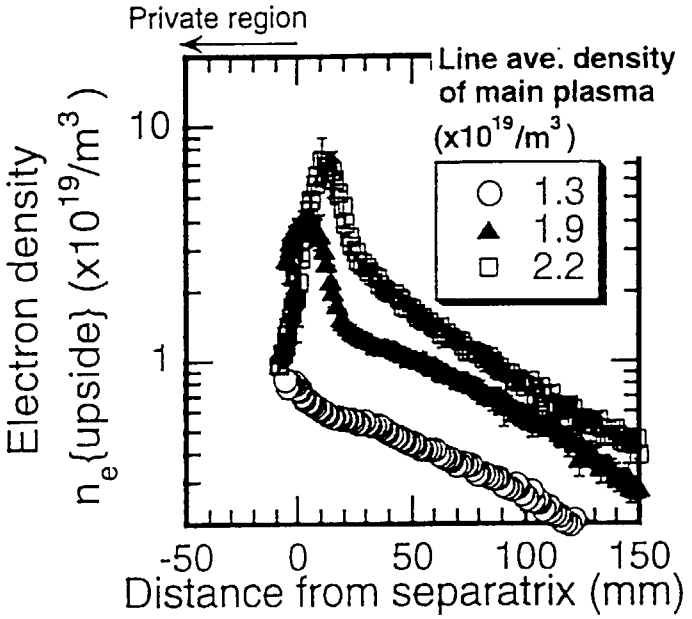

Fig. 4
The behavior of electron density profile in density scan of main plasma. Plasma current = 1.7 MA, toroidal magnetic field = 3.5 T, ohmic heated discharge.

This is a blank page.

国際単位系 (SI) と換算表

表 1　SI基本単位および補助単位

量	名称	記号
長さ	メートル	m
質量	キログラム	kg
時間	秒	s
電流	アンペア	A
熱力学温度	ケルビン	K
物質量	モル	mol
光度	カンデラ	cd
平面角	ラジアン	rad
立体角	ステラジアン	sr

表 2　SIと併用される単位

名称	記号
分，時，日	min，h，d
度，分，秒	°，′，″
リットル	l，L
トン	t
電子ボルト	eV
原子質量単位	u

1 eV = 1.60218 × 10^{-19} J

1 u = 1.66054 × 10^{-27} kg

表 5　SI接頭語

倍数	接頭語	記号
10^{18}	エクサ	E
10^{15}	ペタ	P
10^{12}	テラ	T
10^{9}	ギガ	G
10^{6}	メガ	M
10^{3}	キロ	k
10^{2}	ヘクト	h
10^{1}	デカ	da
10^{-1}	デシ	d
10^{-2}	センチ	c
10^{-3}	ミリ	m
10^{-6}	マイクロ	μ
10^{-9}	ナノ	n
10^{-12}	ピコ	p
10^{-15}	フェムト	f
10^{-18}	アト	a

表 3　固有の名称をもつSI組立単位

量	名称	記号	他のSI単位による表現
周波数	ヘルツ	Hz	s^{-1}
力	ニュートン	N	$m \cdot kg/s^2$
圧力，応力	パスカル	Pa	N/m^2
エネルギー，仕事，熱量	ジュール	J	N·m
工率，放射束	ワット	W	J/s
電気量，電荷	クーロン	C	A·s
電位，電圧，起電力	ボルト	V	W/A
静電容量	ファラド	F	C/V
電気抵抗	オーム	Ω	V/A
コンダクタンス	ジーメンス	S	A/V
磁束	ウェーバ	Wb	V·s
磁束密度	テスラ	T	Wb/m^2
インダクタンス	ヘンリー	H	Wb/A
セルシウス温度	セルシウス度	℃	
光束	ルーメン	lm	cd·sr
照度	ルクス	lx	lm/m^2
放射能	ベクレル	Bq	s^{-1}
吸収線量	グレイ	Gy	J/kg
線量当量	シーベルト	Sv	J/kg

表 4　SIと共に暫定的に維持される単位

名称	記号
オングストローム	Å
バーン	b
バール	bar
ガル	Gal
キュリー	Ci
レントゲン	R
ラド	rad
レム	rem

1 Å = 0.1 nm = 10^{-10} m

1 b = 100 fm^2 = 10^{-28} m^2

1 bar = 0.1 MPa = 10^5 Pa

1 Gal = 1 cm/s^2 = 10^{-2} m/s^2

1 Ci = 3.7 × 10^{10} Bq

1 R = 2.58 × 10^{-4} C/kg

1 rad = 1 cGy = 10^{-2} Gy

1 rem = 1 cSv = 10^{-2} Sv

（注）

1. 表1－5は「国際単位系」第5版，国際度量衡局 1985年刊行による。ただし，1 eVおよび1 uの値はCODATAの1986年推奨値によった。
2. 表4には海里，ノット，アール，ヘクタールも含まれているが日常の単位なのでここでは省略した。
3. barは，JISでは流体の圧力を表わす場合に限り表2のカテゴリーに分類されている。
4. EC閣僚理事会指令ではbar，barnおよび「血圧の単位」mmHgを表2のカテゴリーに入れている。

換算表

力	N(=10^5 dyn)	kgf	lbf
	1	0.101972	0.224809
	9.80665	1	2.20462
	4.44822	0.453592	1

粘度　1 Pa·s(N·s/m^2) = 10 P(ポアズ)(g/(cm·s))

動粘度　1 m^2/s = 10^4 St(ストークス)(cm^2/s)

圧力	MPa(=10 bar)	kgf/cm^2	atm	mmHg(Torr)	lbf/in^2(psi)
	1	10.1972	9.86923	7.50062 × 10^3	145.038
	0.0980665	1	0.967841	735.559	14.2233
	0.101325	1.03323	1	760	14.6959
	1.33322 × 10^{-4}	1.35951 × 10^{-3}	1.31579 × 10^{-3}	1	1.93368 × 10^{-2}
	6.89476 × 10^{-3}	7.03070 × 10^{-2}	6.80460 × 10^{-2}	51.7149	1

エネルギー・仕事・熱量	J(=10^7 erg)	kgf·m	kW·h	cal(計量法)	Btu	ft·lbf	eV
	1	0.101972	2.77778 × 10^{-7}	0.238889	9.47813 × 10^{-4}	0.737562	6.24150 × 10^{18}
	9.80665	1	2.72407 × 10^{-6}	2.34270	9.29487 × 10^{-3}	7.23301	6.12082 × 10^{19}
	3.6 × 10^6	3.67098 × 10^5	1	8.59999 × 10^5	3412.13	2.65522 × 10^6	2.24694 × 10^{25}
	4.18605	0.426858	1.16279 × 10^{-6}	1	3.96759 × 10^{-3}	3.08747	2.61272 × 10^{19}
	1055.06	107.586	2.93072 × 10^{-4}	252.042	1	778.172	6.58515 × 10^{21}
	1.35582	0.138255	3.76616 × 10^{-7}	0.323890	1.28506 × 10^{-3}	1	8.46233 × 10^{18}
	1.60218 × 10^{-19}	1.63377 × 10^{-20}	4.45050 × 10^{-26}	3.82743 × 10^{-20}	1.51857 × 10^{-22}	1.18171 × 10^{-19}	1

1 cal = 4.18605 J（計量法）
= 4.184 J （熱化学）
= 4.1855 J （15 °C）
= 4.1868 J（国際蒸気表）

仕事率　1 PS（仏馬力）
= 75 kgf·m/s
= 735.499 W

放射能	Bq	Ci
	1	2.70270 × 10^{-11}
	3.7 × 10^{10}	1

吸収線量	Gy	rad
	1	100
	0.01	1

照射線量	C/kg	R
	1	3876
	2.58 × 10^{-4}	1

線量当量	Sv	rem
	1	100
	0.01	1

（86年12月26日現在）